Development of an Improved PCM-to-Air Heat Exchanger for Building Envelopes - Advancement to Free Cooling Applications

Mohamed Ahmed

A Thesis
In the Department
of
Building, Civil and Environmental Engineering

Presented in Partial Fulfillment of the Requirements
For the Degree of
Doctor of Philosophy (Building Engineering) at
Concordia University
Montreal, Quebec, Canada

October 2019

CONCORDIA UNIVERSITY

SCHOOL OF GRADUATE STUDIES

This is to certify that the thesis prepared

By: Mohamed Ahmed

Entitled: Development of an Improved PCM-to-Air Heat Exchanger for Building Envelopes - Advancement to Free Cooling Applications

and submitted in partial fulfillment of the requirements for the degree of

Doctor Of Philosophy (Building Engineering)

complies with the regulations of the University and meets the accepted standards with respect to originality and quality.

Signed by the final examining committee:

_____ Chair
Dr. Ali Dolatabadi

_____ External Examiner
Dr. Umberto Berardi

_____ External to Program
Dr. Amin Hammad

_____ Examiner
Dr. Hua Ge

_____ Examiner
Dr. Fuzhan Nasiri

_____ Thesis Co-Supervisor
Dr. Fariborz Haghighat

_____ Thesis Co-Supervisor
Dr. Mohamed El Mankibi

Approved by _____
Dr. Michelle Nokken, Graduate Program Director

December 4, 2019

_____
Dr. Amir Asif, Dean
Gina Cody School of Engineering & Computer Science

ABSTRACT

Development of an Improved PCM-to-Air Heat Exchanger for Building Envelopes - Advancement to Free Cooling Applications

Mohamed Ahmed, Ph.D.

Concordia University, 2019

With high energy consumption trends in buildings, the adoption of the thermal energy storage systems toward reducing cooling load has been increased in recent years. In this study, the utilization of phase change materials (PCMs) has been comprehensively discussed for building free cooling applications. The potential and limitations of using PCM-to-Air Heat Exchangers (PAHXs) for free cooling applications were analyzed. Referring to the local climatic conditions, one of the most important operational challenges that face PAHX applications is the insufficient cooling charging energy during the PCM solidification phase. An improved PAHX type was developed in this study for building envelopes by applying the concept of thermal radiation losses to the sky during night-time to increase the cooling potential of the system. Two real-scale prototypes were designed and set-up to monitor the effect of radiative cooling on the thermal performance of the PAHX system. The experimental results indicated that exposure to the clear sky, as a cooling source, during PCM solidification increases the cooling potential of the system due to the maximized thermal losses by radiation. A 2D numerical model was developed considering the PCM thermal storage, short and long waves radiation, and convection phenomena. New thermal boundaries of long-wave radiation were developed between the system elements and the sky temperature. In addition, the 2D model considered various forms of convective heat transfer phenomenon. The experimental data and inter-model comparison were applied to validate the proposed model. The application of the developed PAHX system in the hot desert climate was assessed to evaluate its thermal performance. It was concluded that the PAHX system outlet air could be directly supplied to the indoor spaces through a direct free cooling application to satisfy the cooling loads, also it could be introduced to the mechanical cooling unit to minimize the energy consumption. The results showed that the thermal comfort levels were enhanced by up to 18% (during the direct free cooling application), and the energy consumption for cooling purposes was reduced by 18.5% (during the energy savings mode) saving an amount of energy up to about 11 kWh/week.

ACKNOWLEDGEMENTS

First and foremost, all thanks and praises are to Allah Almighty for accomplishing this modest research work, hoping that holds the good and usefulness for the scientific community.

I would like to express my deep respect and gratitude to my research supervisor Honorable Professor Fariborz Haghighat, whose wealth of knowledge that guided me in Building Engineering program, for his valuable and continuous support, motivation, and guidance through my research different stages.

I would like to acknowledge particular thanks and appreciations to my research co-supervisor Dr. Mohamed El-Mankibi for his direct help and support with which all significant, fundamental, and vital parts of the research were only possible.

Sincere thanks and appreciations to my committee members, Professor A. Hammad, Dr. H. Ge and Dr. F. Nasiri, for their valuable advices and remarks which directed me through developing the research objectives and findings.

I thank all the *Energy and Environment* team members, past and present, who have enriched and directed the research through valuable discussions and contributions. My special thanks to Dr. Karthik Panchabikesan for his valuable suggestions and remarks.

Heartfelt gratitude to the team members of *Laboratoire Génie Civil et Bâtiment – ENTPE* for their support and hospitality, with special thanks to Dr. Letizia Roccamena and Joachim Blanc-Gonnet for their appreciated contributions and helpful assistance.

I thank the Egyptian Bureau of Cultural and Educational Affairs for funding this research and for continuous support. I also thank MITACS for partially funding the experimental investigation and Concordia University (Mobility and Accelerator grants).

Finally, special thanks to my beloved family, my mother, my wife, my son, and my brothers for the great efforts, understanding, and sharing decisions and hard times through different stages of research, providing me with confidence, calmness, and serenity.

CONTRIBUTION OF AUTHORS

PCM-to-Air Heat Exchangers (Opportunities & Challenges)

Karthik Panchabikesan	Methods and structure, data organization, editing and proofing
Fariborz Haghighat	Supervisor, technical comments and proofing
Mohamed El-Mankibi	Co-supervisor, editing and proofing
Yanping Yuan	Editing and proofing

Experimental Investigation

Letizia Roccamena	Experimental prototypes design procedures and follow-up, data analysis, editing and proofing
Mohamed El-Mankibi	Co-supervisor, experimental work checking and follow-up, editing and proofing
Joachim Blanc-Gonnet	Data acquisition and analysis
Fariborz Haghighat	Supervisor, technical comments and proof reading

Numerical Modeling & Experimental Validation

Mohamed El-Mankibi	Co-supervisor, numerical modeling debugging, reviewing and proofing, editing and proofing
Letizia Roccamena	Helping in numerical modeling
Fariborz Haghighat	Supervisor, technical comments and proofing
Lubomir Klimes	Data organization, editing and proofing

PAHX Thermal Performance - Application in Hot Desert Climate

Mohamed El-Mankibi	Co-supervisor, editing and proofing
Fariborz Haghighat	Supervisor, technical comments and proofing

TABLE OF CONTENTS

LIST OF FIGURES

LIST OF TABLES

CHAPTER ONE: INTRODUCTION

1.1. Problem Overview

During the last decade, the global energy consumption rate has increased by 18% (International Energy Agency, 2017a); further increase of 30% is anticipated by 2040 (International Energy Agency, 2017b). In most developed and developing countries, there exists a gap between electricity supply and demand, due to such an increase in consumption patterns. Due to rapid urbanization and appreciable change in people lifestyle, energy consumption trend in buildings has increasing over the past few decades. According to International Energy Agency (IEA) report (International Energy Agency, 2017a), the building sector consumes around 40% of total energy. Moreover, the total energy end consumption of natural gas and electricity in the building sector has increased by 9.4% and 11.1% respectively. In low rise buildings, 30% - 45% of the energy is dedicated to HVAC and indoor environmental control systems (CCES, 2008). Such systems are not only responsible for energy consumption increase, but also act as a major contributor to carbon emissions from the building sector. In hot climates where the outdoor temperatures are exceptionally high (especially in summer), peak cooling load for residential buildings can vary from 45 to 57 W/m^2 based on the building envelope insulation properties (Pardo et al., 2012). This magnifies the energy consumption at hot and dry climates for achieving acceptable indoor conditions to reach the thermal comfort state required for human occupancy at both residential and commercial sectors.

Currently, the use of energy-intensive HVAC systems to achieve thermal comfort is becoming a greater concern in terms of increasing energy consumption and greenhouse gases (GHGs) emissions (Santamouris and Kolokotsa, 2013). Hence, it is the right time to replace the energy intensive mechanical systems by energy efficient and passive techniques. The adoption of passive techniques paves the way to reduce the heavy loads on energy networks preventing the power failure, and providing more options for re-distribution of energy capacities according to local development policies and plans (Santamouris, Mat, 2007).

Energy efficient and passive cooling strategies are concerned with enhancing the indoor thermal performance while minimizing the energy consumption. With enhanced indoor ventilation rates, integrated passive techniques are able to maintain the indoor thermal comfort, particularly in

regions with extreme conditions (Dardir, Mohamed 2017; Cui et al., 2015). One major aspect of integrating passive cooling techniques in buildings is reducing the external heat gains and the internal cooling loads. In this scenario, thermal energy storage (TES) is considered to be an efficient solution for energy conservation techniques (Haghighat, 2013; Santamouris, Mat, 2007). Originally, TES systems used the sensible enthalpy of materials as storage media where building envelope, concrete slabs, and water tanks were designed as building storage elements (Paksoy, Halime, 2007). In the past decades, interest has been raised for utilizing the heat of fusion (latent heat) of materials. In comparison with sensible heat storage, charging or discharging heat at a relatively small range of temperatures is what distinguishes latent heat thermal energy storage (LHTES) systems (Nagano et al., 2004; Agyenim et al., 2010). The heat of fusion is utilized during the change of a material's phase; those materials that have the capacity to store a high amount of energy during their change of phase are called Phase Change Materials (PCMs).

Lately, the applications of PCMs have gained much interest due to their high density, a variety of fusion temperatures, commercial availability, and flexibility of installation (Stathopoulos et al., 2016). Early applications of PCMs in enhancing indoor thermal performance were observed at mid-eighties of last century (Stritih, Uros, 2003). Applications of micro encapsulated PCM boards have been developed to enhance thermal inertia of the building envelope and, thus, to satisfy the cooling demands (Chen et al., 2008). Some experiments showed that integrating PCM boards with night ventilation (Barzin et al., 2015; Jaworski, 2014; Farid et al., 2004), or using PCM tanks in cooling cycles (Tay et al., 2012) reduced the energy consumption of active air conditioning systems during daytime operation, and enhanced the overall indoor thermal behavior (Evola et al., 2014). Further developments of using PCM shape stabilized plates as interior cladding have achieved a peak shaving of the indoor temperature when combined with night ventilation (Zhou et al., 2009).

The PCMs have been also included in buildings systems for thermal storage using the air as a Heat Transfer Fluid (HTF) inside heat exchangers called PCM-to-air heat exchangers (PAHXs). These PAHX units have been studied widely for active systems and moderate climates. However, few studies have considered the passive and free cooling applications of PAHXs in hot dry climates or for long-term operation (Waqas and Kumar, 2011; Panchabikesan, karthik 2017; El-Sawi et al., 2014). The high outdoor temperature during day and night, insufficient provided cooling energy,

year-round system operation, incomplete solidification and high relative humidity levels during solidification phase are the major challenges of using PAHXs as free cooling systems at hot and dry climates to provide acceptable thermal conditions that keep up with those provided by active means. The above-mentioned factors can formulate the operational limitations in PAHX technology that need further investigations to enable more feasible and practical applications for current system developments.

1.2. Research Gap

The research gap can be mainly identified by two points:

- The insufficient cooling energy provided to charge PAHX units, specially in hot climates, due to the insufficient difference between the inlet air temperature and PCM phase change temperature and reduced charging periods which affects the overall system performance.
- The lack of a comprehensive heat transfer model for the PAHX system that satisfies various airflow regimes (especially for low and varying air velocities representing the real conditions) and considers the radiative cooling to the night-time sky during the PCM solidification process which can increase the cooling potential in the hot desert climate.

1.3. Purpose and Objective

While the ambient air temperature does not ensure the complete PCM solidification in most cases as an existing limitation for free cooling applications, the improved PAHX design utilizes the night-time sky as an additional cooling source. The **main objective** of this research is to develop an enhanced PCM-to-air heat exchanger system for free cooling applications that makes use of the climatic potential and the PCM thermal storage capabilities to enhance the PAHX system thermal performance. The **main idea** of the present study is to make use of the radiative cooling to the sky (as a new cooling source) to increase the cooling charging energy of the PAHX system during night-time by magnifying the radiation thermal losses to the atmospheric environment during PCM solidification process. This would be achieved by exposing the PCM panels to the sky to allow the long-wave radiative heat exchange during charging phase (night-time and early morning periods). The targeted enhancements in this research are claimed to improve the stand-alone thermal performance of the system as well as enhancing the indoor thermal comfort levels and reducing the energy consumption of the building mechanical ventilation systems.

1.4. Approach & Methods

The research concept can be investigated by considering the long-wave thermal radiation to the sky and testing the effect of the developed enhancements on the charging energy of the system. To achieve that, the research follows an analytical approach to study the state-of-the-art of the PAHX system for free cooling applications. The radiative cooling effect would be studied by experimentally prototyping the developed PAHX system and tracking its thermal behavior during the charging process of the PCM. The research also follows a numerical approach for modeling the proposed system, and an experimental validation to compare the simulation predictions with those obtained by the experimental investigations. A performance analysis would be applied to assess the thermal behavior and cooling performance of the developed PAHX system. The research schema is provided by Figure 1.

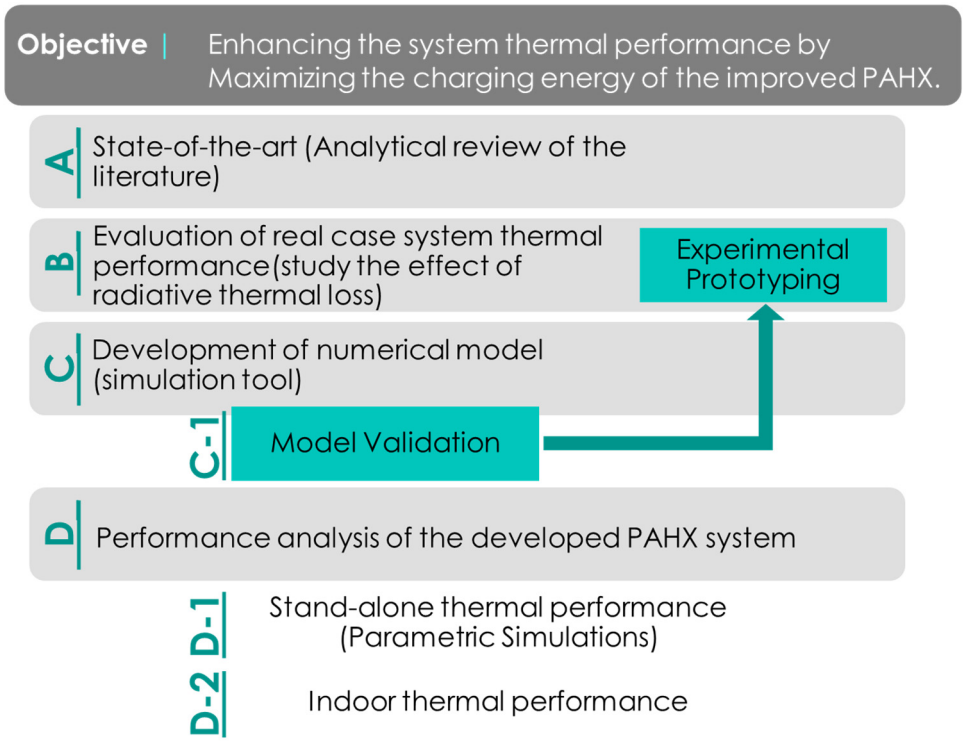

Figure 1 – Research schema

1.5. Significance & Contribution

The purpose of the developed PAHX system is to maximize the cooling charging energy of the system to increase the overall cooling potential and performance during the system operation. The significance of the improved PAHX type can be concluded as:

- During cooling applications, the cooled outlet air of the system can be supplied directly to spaces to satisfy cooling loads (a direct free cooling application).
- In case the cooled air is not within the thermal comfort range or cannot satisfy the cooling loads by direct supply, it can also be introduced to the mechanical cooling system to reduce energy consumption for cooling purposes (an energy saving application).

The novelty of this research can be concluded as:

- Development of a comprehensive model (simulation tool) for the proposed PAHX system that promotes multiple applications and provides integration flexibility with any thermal simulation platform.
- Implementation of the long-wave thermal radiation component intentionally to maximize the thermal losses (during charging) and improve the thermal performance of the PAHX system.
- Development of a comprehensive convective heat transfer component of the developed PAHX model which promotes multiple applications (real applications with varying air velocities) and various convection modes.
- Establishing ready-to-utilize experimental prototypes for the improved PAHX system which promotes the practical application and provides further potential for technological developments and implementations.

The outcomes of the research are planned to include the following:

- A comprehensive simulation tool for the developed PAHX system to be implemented and used through building design process by integration to thermal simulation platforms.
- Providing a set of experimental data for the developed PAHX unit that can be used by scientists and building researchers to develop and improve the system.

1.6. Thesis Structure

The study follows consequent steps to reach the main objective through four body chapters of the thesis:

CHAPTER TWO: (*PCM-to-Air Heat Exchangers: Opportunities & Challenges*)

This chapter highlights the existing opportunities and challenges of the PAHX system for free cooling applications to specify the research gap and the operational, climatic, and practical limitations of the PAHX systems in general. This chapter follows a detailed literature review analytical method through discussions of previous applications and investigations.

CHAPTER THREE: (*Experimental Investigation*)

This chapter presents the design concept of the developed PAHX system. The investigations were designed to study the system thermal behavior upon exposure to the night-time sky during PCM solidification period. The study in this chapter follows an experimental investigation under real ambient conditions developing two real-scale prototypes for the developed PAHX system. Special key performance indicators are proposed to efficiently analyze the experimental results and, accordingly, the thermal behavior of the developed system.

CHAPTER FOUR: (*Numerical Modeling & Experimental Validation*)

A 2D numerical model (simulation tool) is developed including the new thermal boundaries of the designed PAHX system and presented in detail in this chapter. The model develops the thermal radiation heat exchange components in-between system elements and between the system and the sky. Also, the model updates various forms of convective heat transfer between the PCM and the air. The prediction by the model was evaluated at two levels: inter-model comparison with previously developed models and comparison with the real measurements obtained by the experimental investigation.

CHAPTER FIVE: (*PAHX Thermal Performance: Application in Hot Desert Climate*)

This chapter follows a numerical investigation using the developed validated model of the PAHX system to assess its thermal performance in the hot desert climate. This chapter discusses the stand-alone performance of the system applying a parametric analysis of the system elements. Also, this chapter assesses the influence of integrating the developed PAHX system to a building ventilation system on the indoor thermal performance of an occupied space.

Lastly, the conclusions and the recommendations for future works are summarized and included in Chapter Six.

CHAPTER TWO:
PCM-to-AIR HEAT EXCHANGERS - OPPORTUNITIES & CHALLENGES

The objective of this chapter is to highlight the existing challenges of applying PAHXs in free cooling applications focusing on system limitations and constraints of the reviewed studies, as well as the technology itself. Moreover, this chapter updates and discusses the opportunities and current advancements made in PAHX system for building free cooling applications. Investigating both challenges and opportunities can come up with the required technology advancements that enhance the system's operation feasibility. An overview for free cooling concept and PCMs-based applications is presented; PAHX system parameters are also analyzed and concluded.

2.1. PCM-based Free Cooling Systems

Achieving thermal comfort by natural or passive means can be obtained through free cooling systems (Zalba et al., 2004). Based on ASHRAE Standard 55 (2013), an adaptive thermal comfort model is defined for naturally conditioned spaces according to outdoor air temperature (Equation 1). This criterion is applied for 80% acceptability limit and when no mechanical cooling or heating systems are being used. However, mechanical ventilation with outdoor air supply can be used considering air speed values (ASHRAE, 2013). According to ASHRAE standard 55, the mentioned criterion in Equation 1 is only applicable for mean outdoor air temperature between 10 ˚C and 33.5 ˚C (ASHRAE, 2013).

$$T_{comfort} = (0.31 \times T_{amb}) + 21.3\ ^{\circ}C \text{ (upper limit), or } 14.3\ ^{\circ}C \text{ (lower limit)} \quad (1)$$

Free cooling, as a passive strategy, utilizes the outdoor air as an ambient heat sink for building cooling purposes by means of ventilation (ASHRAE, 2013). Generally, direct free cooling ventilation can be achieved when the free running temperature[1] is higher than the comfort zone, and the outdoor air temperature is around the thermal comfort range of temperatures. Thus, supplied outdoor air can cool the room/space magnifying the potential of free cooling. Ghiaus and Allard (2006) and Inard et al. (2011) claimed that considering free running temperature as a

[1] The free running temperature is the indoor operative temperature of a building when no mechanical heating or cooling is being used; it depends on the outdoor air temperature and the total indoor and outdoor heat gains (Ghiaus, 2003)

threshold temperature in thermal comfort determination can increase the free cooling potential. Usually, in the hot season, outdoor ambient temperatures are higher, or extremely higher, than comfort level. In such cases and to increase the potential of free cooling, integration among passive heat dissipation techniques, such as evaporative cooling (Cuce and Riffat, 2016; Panchabikesan et al., 2017), radiative cooling (Panchabikesan et al., 2017) and geothermal heat exchanging (Ceylan et al., 2016), is recommended to maintain indoor thermal comfort. One of the efficient passive cooling concepts is utilizing night cold energy to be re-supplied during the hot period of next day; this needs involving a thermal storage process. Integrating a free cooling concept with a LHTES system can promote a cycle of temperature stability. The system then can store cold during the night and release it during the day providing a complete thermal cycle for PCM (Butala and Stritih, 2009). This concept is more feasible in climates with large temperature difference (> 15˚C) between day and night (Zalba et al., 2004).

PCMs are widely used in many applications due to their high energy storage capabilities at isothermal conditions. Also, PCMs are characterized by their high latent heat storage in comparison to other sensible heat storage materials (Zalba et al., 2004; El-Sawi, Azeldin 2013; de Gracia and Cabeza, 2015; Sharma et al., 2009). This high storage capacity of PCM enables the applicability of much smaller volume to store the same needed energy (Turnpenny et al., 2000). It is reported in the literature that 8.1 cm inorganic PCM wall possesses the same thermal storage abilities as a 40 cm concrete wall (Stritih, Uros, 2003). Other investigations reported that cooling potential of 1 kg of PCM is comparable to this of 25 kg concrete slab of high thermal mass (Turnpenny et al., 2001). Besides, some PCMs are characterized by a small change in volume during the phase change process (Darzi et al., 2013). For free cooling applications, Arkar and Medved (2007) reported that 6.4 kg of PCM per unit floor area or 1 – 1.5 kg of PCM mass for each 1 m^3/h of needed fresh air in the ventilation system, under specific conditions (Medved and Arkar, 2008), could be optimum for free cooling applications.

The working principle of PCM is the release of a large amount of energy, *latent heat of fusion*, during phase change process at a relatively constant range of temperatures called Phase Change Temperature (PCT) range. TES involving PCM is a reversible process through solidification and melting of the material (Stritih and Butala, 2007). In some LHTES systems, air is used as heat transfer fluid (HTF) to charge and discharge PCM. In free cooling, charging process (solidification

of PCM/heat release from PCM) is carried out during night-time when the ambient air temperature is lower than PCT of the material by an appropriate difference. During this process, heat transfers from the melted PCM to the incoming air; thus, PCM is solidified and subsequently, the outgoing air is warmed. Conversely, during the discharging process (heat storage in PCM), PCM is melted and the air is cooled and supplied to satisfy the cooling demand during the daytime. This process involves both conductive and convective heat transfer within the PCM itself, and convective heat transfer between PCM and air within the heat exchanger. Figure 2 illustrates the working principle of a PCM-based free cooling system.

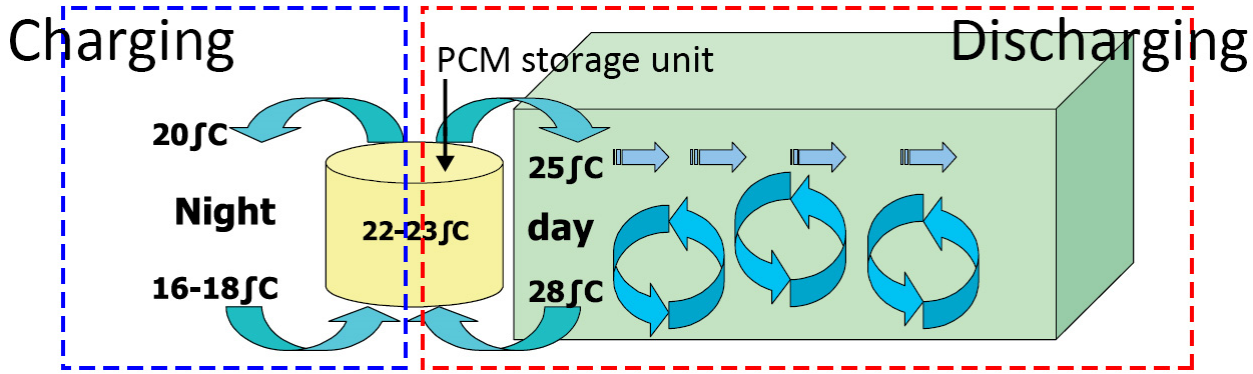

Figure 2 – Working principle of PCM based free cooling systems (Zalba et al., 2004)

Though many studies investigated the applications of free cooling using PCMs, however, few studies have considered the application of PCMs in the hot desert climate (Waqas and Kumar, 2011a). In free cooling applications, the phase change cycle is the whole day (24 hours) cycle that includes day and night periods. It is worth mentioning that daytime and night-time operations are not based exactly on the actual day and night periods, but the whole cycle is a relationship between the heat storage system and outdoor temperatures.

Generally, investigations, under different conditions, showed that the discharging process takes more time than charging considering the same airflow rate during both processes (Zalba et al., 2004). This could help to enhance free cooling performance during the summer season where higher cooling demand is needed and daytime (cooling discharge) is longer than night-time (cooling charge) (Turnpenny et al., 2000). A PCM heat storage unit was investigated by Stathopoulos, et al. (2016; 2017) using paraffin (PCT of 37 ˚C). Standalone unit thermal

performance was tested under inlet air temperatures of 44 ˚C while melting, and 26 ˚C while solidification. Results showed that, at high airflow rates, the whole cycle of melting and solidification required around 10 hours; while it could reach around 22 hours for low airflow rates. This gives a good indication for a complete whole-day cycle of charging and discharging with limited sensible heat transfer periods.

Most of the literature classified the PCMs into organic (paraffinic and non-paraffinic) and inorganic materials (Farid et al., 2004; Agyenim et al., 2010; Zalba et al., 2003). Table 1 shows the main differences between the two categories. In general, organic PCMs have higher latent enthalpy than the inorganic PCM and show more thermal stability; this could be more appropriate for free-cooling applications (Lazaro et al., 2009). Another type of PCM, called Eutectic PCM, is a mixture of different types of PCMs (organic and inorganic), or a combination of similar type (organic/organic, or inorganic/inorganic). This type forms a blend of crystals during solidification with no separation during melting (Haghighat, 2013).

Table 1 – General comparison of organic and inorganic PCMs (Zalba et al., 2003; Darzi et al., 2013; Sharma et al., 2009)

	Organic PCM	**Inorganic PCM**
Advantages	- No corrosion - Less subcooling - Higher latent enthalpy - Thermal stability	- Less volume expansion during phase change - Higher thermal conductivity (compared to organic PCM)
Disadvantages	- Lower thermal conductivity - Flammability - Lower volumetric storage capacity (compared to inorganic PCM)	- Subcooling effect - Corrosion - Lack of thermal stability

For free cooling systems, selecting the appropriate PCM for the PAHX system is one of the most important parameters for achieving better performance. Examples for suitable PCMs for free cooling applications are given in (Waqas and Ud Din, 2013). Beside the local climatic conditions, the thermal performance of PAHX system is highly influenced by PCM thermophysical properties such as PCT range, thermal conductivity and heat capacity (Thambidurai et al., 2015; Arkar and Medved, 2005). The desired PCM properties are high latent heat, high thermal conductivity, small volume expansion, least sub-cooling, chemical stability, non-toxicity and low cost (Mehling and

Cabeza 2008; Raj and Velraj, 2010). During the phase change, latent enthalpy is more dominant than sensible enthalpy forming the curve as shown in Figure 3 (Stritih and Butala, 2007).

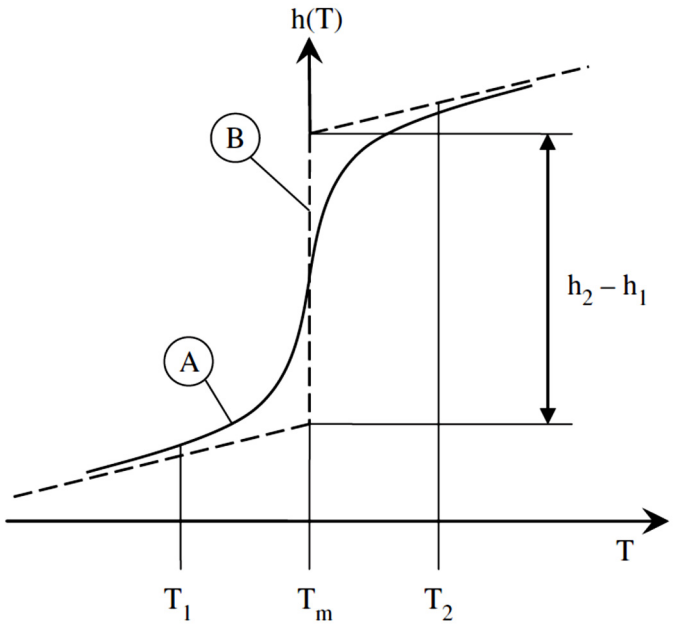

T_m: average phase change temperature (PCT), T_2-T_1: phase change range (mushy region), Δh: enthalpy change (sensible enthalpy A – latent enthalpy B)

Figure 3 – Enthalpy-temperature curve for phase change materials (Stritih and Butala, 2007)

Despite several advantages, the most important limitation of using PCM is its poor thermal properties irrespective of the types of PCM. Especially for organic PCMs, low thermal conductivity is an important limitation (Agyenim et al., 2010). Another limitation, especially in inorganic PCMs, is the sub-cooling effect (Mehling and Cabeza 2008). During solidification, PCM can be partially super-cooled before its known range of PCT (Turnpenny et al., 2000); this affects the LHTES performance. Sub-cooling effect of the organic PCM RT21 was investigated by Solomon et al. (2013); they concluded that the higher cooling rate and heat flux during solidification are, the larger the sub-cooling effect will be. This results in reducing the latent heat available for the application. Generally, impure PCMs can be introduced to limit the sub-cooling effect. Furthermore, due to thermal cycling, PCM system could have a specific lifetime. Also, corrosion between PCM and encapsulation material could threaten long-term system stability (Zalba et al., 2003). Some kinds of PCMs could be inflammable; some researches reported the

possibility of adding fire resistance additives to improve material fire resistance (Stritih, Uros, 2003).

The melting/solidification occurs at isothermal conditions in case of pure PCM. However, usually, the phase change process occurs over a range of temperatures called the mushy region (Zalba et al., 2003). Reports showed that, for building free cooling applications, better performance can be obtained using PCM of a phase change range rather than a fixed temperature which results in a broader range of temperatures and applications variety (Halawa et al., 2005). The larger this range is, the greater the free cooling potential will be (Medved and Arkar, 2008). However, every ambient temperature range has its own proper PCM where an appropriate difference between the inlet air temperature and PCT is provided during both melting and solidification. This issue still affects the performance and feasibility of long-term applications of PCM where ambient temperatures vary significantly from season to another. Also, it affects the applications of PCMs in the hot desert climate where the appropriate PCT is not within the comfort zone.

2.1.1. Influence of Local Climate on PCM-based Free Cooling Systems

Despite to PCM-based free cooling system's configurational and operational parameters, local climatic conditions are the most influential factor affecting the system performance. Selection of PCM with an appropriate PCT range corresponding to the local climatic conditions is very case sensitive (Panchabikesan et al., 2017). Ambient conditions of air temperature, relative humidity, air velocity and diurnal temperature can determine the appropriate free cooling system configuration, PCM type and design parameters. The appropriate PCM for free cooling system must have a PCT range which achieves a significant difference between solidification temperature and inlet air temperature; thus, a complete solidification of PCM is ensured. In hot climates, the appropriate PCT range of the system can be over the thermal comfort range due to the high charging temperature that may exceed the thermal comfort zone. Also, with extreme high day temperatures, cooling energy can be consumed in a short time leading to lower overall performance (Waqas and Kumar, 2011b). In warm-humid and moderate climates with a low diurnal temperature range, PCM-based free cooling systems suffer from insufficient cooling provided to the system due to the small temperature difference between PCT range and charging temperature regarding the ambient profile of a low amplitude. Thus, due to incomplete solidification, standalone PCM-

based systems may not provide good performance, especially in the warm-humid climate. Panchabikesan et al. (2018) experimentally investigated the performance of a bed packed PAHX under the moderate climate of Bangalore, India. They found that at a lower mass flow rate, the storage tank did not achieve complete solidification even after 10 hours of charging. However, Borderon et al. (2015) confirmed system acceptable performance within climates with higher daily amplitude. Also, Yanbing et al. (2003) recorded considerable enhancements in indoor thermal performance, under the moderate climate of Beijing, in terms of temperature peaks when they combined the PAHX system with a night ventilation strategy. Table 2 summarizes the effects of different local climatic conditions on the performance of a free cooling system.

Table 2 – Effects of local climatic conditions on free cooling system performance

Local climatic conditions – Advantages
- Climates with higher amplitude (the difference between maximum and minimum temperatures) could be more appropriate to solidify the PCM and to increase system cooling charging power (Borderon et al., 2015).
- Low air velocities during cooling discharging (for real applications) (Zalba et al., 2004).
- Limited cooling loads increase the system free cooling potential (Yanbing et al., 2003).
Local climatic conditions – Challenges
- Insufficient low inlet temperature during PCM solidification (insufficient charging power) (Panchabikesan et al., 2018).
- High inlet temperature during discharging (reducing system performance) (Waqas and Kumar, 2011a; Waqas and Kumar, 2011b).
- High relative humidity values (constraint specially during solidification) (Panchabikesan et al., 2018; Panchabikesan, 2017).
- High cooling loads reduce system performance and free cooling potential (Panchabikesan, Vellaisamy et al., 2017).

Using an integrated PAHX unit, Osterman et al. (2015) conducted an experimental investigation under the ambient conditions of Slovenia to study the system thermal performance for both free cooling and heating applications. During the heating season, the results showed that largest energy savings were achieved in March while the available solar energy was more, and heating demand was less. While maximum cooling potential during cooling application was possible in August and July when more fluctuations between day and night were available.

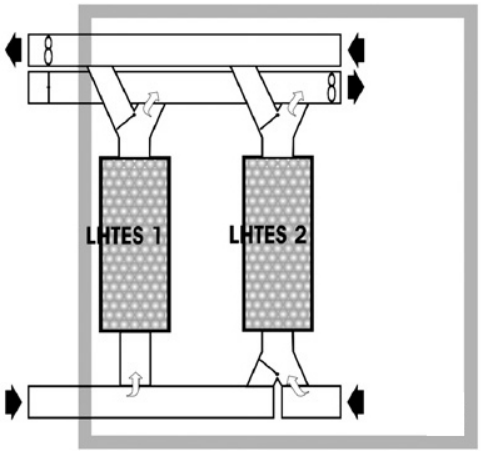

Figure 4 – Diagram of integrated mechanical ventilation system (Arkar et al., 2007)

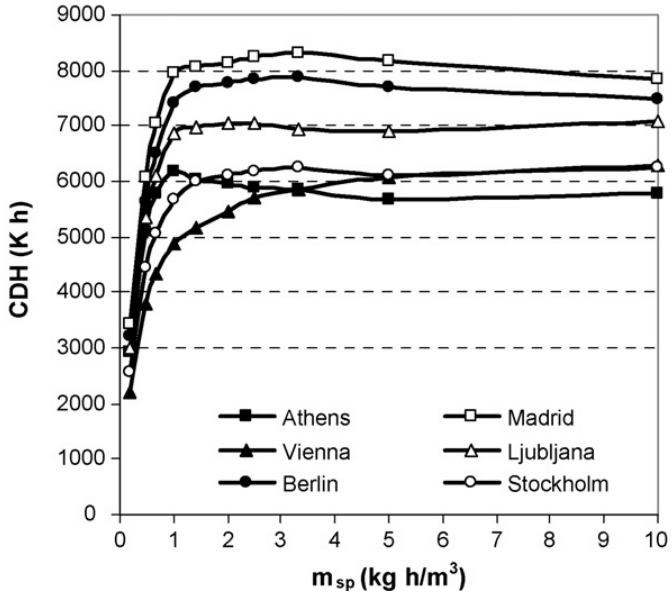

Figure 5 – CDHs in relation with difference specific PCM masses due to different locations (Medved and Arkar, 2008)

Numerical investigations were conducted by Arkar et al. (2007; 2007) using a validated two-dimensional heat transfer model utilizing the effective heat capacity method. They proposed a ventilation system, as shown in Figure 4, utilizing a packed bed configuration of a spherical encapsulation for RT20 paraffin with PCT range of 20 ˚C – 22 ˚C. They investigated the proper size of the LHTES system in terms of PCM mass in relation with ventilation rates. The researchers showed, through studying different climates, that small PCM masses depend mainly on the cooling degree hours (CDHs) of the location. After a specific mass value, there would be no great change in free cooling potential for different CDHs, as shown in Figure 5. They concluded that using a

PCM mass of around 1 or 1.5 kg for each 1 m^3/h of needed fresh air in the ventilation system would be optimum for free cooling design, under the designed conditions, as about 95% of the cooling demand maximum value can be reached using the specified PCM mass.

2.1.2. Free Cooling in Hot Desert Climate

Free cooling is most needed in hot climates where high cooling demand prevails. According to Köppen climate classification (Kottek et al., 2006), the highest recorded annual average temperatures are at the hot desert climate; this climate is featured with hot to exceptionally hot summers and dry winters. The climate is determined to be a hot desert when the annual mean temperature is greater than or equal to 18 ˚C, and the accumulated annual precipitation is less than or equal to 250 mm/year. Based on the explanation of free cooling, there are two main climatic characteristics that distinguish the hot desert climate. The first climatic feature/potential in hot desert climate is the large difference between day and night temperatures where temperature difference reaches up to 17 ˚C at some locations during summer, and even more during fall and spring seasons. This temperature swing could be very beneficial if the low night temperature is utilized for daytime cooling through an energy storage medium. In general, the hot and desert climate possesses higher diurnal temperature when compared to other climatic conditions. In most of the cases, this high diurnal temperature is beneficiary during the solidification of the PCM. However, it should be carefully noted that, when there is a high daytime temperature (for e.g. > 40 ˚C), the higher diurnal temperature may not be beneficial during the solidification of the chosen PCM. For instance, if the highest recorded day time temperature is 45 ˚C in a given hot-desert climate and the lowest night time temperature is 30 ˚C, still in this case, the diurnal temperature is 15 ˚C. But this high diurnal temperature does not guarantee the complete solidification of PCM (with the PCT of 25 ˚C to 30 ˚C), due to higher night-time temperature. This constraint should be considered while applying the PCM-based free cooling concept in the hot desert climate. In addition, the seasonal variation in temperature profile is a challenge in some locations with a continuous annual cooling demand.

The other potential in hot desert climate is the clear sky conditions. This factor provides full exposure to sky temperature during night-time when the temperature drops significantly magnifying potential of long-wave radiative heat transfer between sky and free cooling system

(Onishi et al., 2009) using the sky as the heat sink. This concept has not gained much attention from the scientific communities (Santamouris and Kolokotsa, 2013). Thermal loss by long-wave radiation can be magnified at hot desert climate with large sky temperature drop during night-time (Onishi et al., 2009) that could reach more than 15 ˚C lower than night air temperature (Adelard et al., 1998). One of the major challenges regarding this concept is the high solar gain at daytime due to system exposure to solar energy. Accordingly, a control strategy is needed to regulate passive system heat gains and losses due to application and climate (Chan et al., 2010). Dovertel and Medved (2012) proved that careful planning and optimized control strategies that are based on weather prediction for free cooling systems operation, especially when a thermal storage medium is included (Dovrtel and Medved, 2011), is highly recommended for achieving better system thermal performance. Another challenge that faces practical applications of long-wave radiative heat loss concept in hot desert climate is the high relative humidity levels at some locations during night-time along with high air temperature which stimulate the air to reach its dew point temperature during heat transfer of the cooling process. The humidity ratio in such cases can lead to increasing the probability of condensation and water accumulation on system elements (ASHRAE, 2009; Panchabikesan, 2017) reducing the free cooling potential. Practical cautions and proper design conditions should be considered. Table 3 summarizes the potential and constraints of free cooling applications in hot desert climate.

Table 3 – Potential and constraints of free cooling in hot desert climate

Free cooling potential in hot desert climate
- High amplitude climatic profile (large difference between minimum and maximum temperatures).
- Low night temperature at some locations (especially during fall and spring seasons).
- Clear sky conditions (almost all year round).
Free cooling constraints in hot desert climate
- Extremely high daytime temperature (especially during summer season).
- Insufficient low night temperature (especially during summer season).
- High relative humidity values (during night-time and early morning at some locations).
- Extremely high cooling demand (all year round at some locations).
- High solar gain during the daytime.

2.2.PCM-to-Air Heat Exchangers (PAHXs) – An Overview

Applications of PAHXs for free cooling systems can be classified into two main categories: integrated units into ventilation systems as building equipment, and integration to building envelope as ventilated facades. Both types involve convective heat transfer process between air and PCM within the heat exchanger. They differ in the number of containing plates, system dimensions, installation challenges, and allowable PCM types. They also have different boundary conditions, as the ventilated facade type could involve significant radiative component and asymmetric conditions along plate thickness (de Gracia et al., 2015; de Gracia et al., 2013; Diarce et al., 2014). The applications of PAHXs can be categorized based on system configurations such as flat plate encapsulation, packed bed encapsulation, PCM granules, and centralized units. Many studies tested the encapsulation of PCM in flat plates configuration as the flat encapsulation has a symmetric melting and freezing process, a high ratio area per volume, a less pressure drop in the air, and an easy design and installation.

Literature emphasized the significance of PAHX system parameters for identifying thermal performance. It is inferred from the literature that system governing parameters include PCT range, airflow, encapsulation rugosity, thermal conductivity, and thickness, PCM slab thickness, PCM system length, and air gap (Dolado et al., 2011). Most of the previous studies concluded that PAHXs show good performance in 24-hours cycle utilizing the concept of reversible phase change processes of PCMs that can maintain latent heat transfer for the whole duration under certain design conditions. It is reported that, the increased heat transfer rates can be achieved by greater difference between inlet air temperature and PCT range (Panchabikesan et al., 2019), higher airflow rates (Nagano et al., 2004; Dolado et al., 2011), higher thermal conductivity for encapsulation material (Dolado et al., 2011), increasing bumping, roughness or complexity of rugosity of encapsulation surface (Dolado et al., 2011), decreasing PCM slab thickness (Dolado et al., 2011; Halawa and Saman, 2011), increasing PCM system length (Mosaffa et al., 2013a), decreasing the encapsulation thickness (Zalba et al., 2004), and reducing air gap between slabs (Dolado et al., 2011; Halawa and Saman, 2011; Mosaffa et al., 2013a).

For active applications of PAHX units, some studies reported good performance of integrating PAHXs into air conditioning systems for energy saving purposes. Barzin et al. (2015) claimed that

a proper control strategy should be considered while integrating PAHX units with the air conditioning systems. Through their experimental investigation carried out under ambient conditions of 12 ˚C as a charging temperature and 22 ˚C to 26 ˚C as discharging temperatures, they proved that 73% of electricity consumption can be saved over a one-week application. They also proposed that the combination of night ventilation and free cooling can significantly improve the energy savings potential of the active systems.

Most of the studies ensured that the proper selection of PCM must be based on the local climatic conditions. Waqas and Kumar (2011a) showed that a PCM of a PCT range that falls nearly between the maximum and minimum temperatures of diurnal fluctuation leads to stabilization of outlet air temperature and better system performance. Turnpenny et al. (2000) claimed that a large temperature difference (15 ˚C or more) between air and PCT range is needed to change the phase in a practical time frame (7 to 10 hours) at low airflow rates. Mosaffa et al. (2013a) stated that PCMs with PCT of 18 ˚C – 30 ˚C are preferred for PCM-based free cooling systems.

Darzi et al. (2013) investigated a flat encapsulated PAHX configuration with 1 mm, and 2 mm thick plates filled with an inorganic salt PCM (SP22A17) (PCT range of 22 ˚C -24 ˚C, and latent heat of 150 kJ/kg). The system performance was investigated under fixed inlet conditions of 29 ˚C, 33 ˚C, and 39 ˚C. They proved that, with lower flow rates, outlet air temperature profile can be almost similar when inlet air temperature varied from 33 ˚C to 39 ˚C by doubling slabs thickness for later case. They also stated that, while discharging, in order to reduce system outlet air temperature, one of the following could be beneficial: reducing the airflow rate, reducing the inlet temperature (using an integrated passive technique), using PCM with higher latent heat of fusion, or utilizing several PCMs with various PCTs in a several-stage configuration; then the difference between air temperature and PCT in each stage can be minimized.

Investigations by Lazaro et al. (2009) stated that for free cooling applications, the proper design of the heat exchanger affects the system performance more than enhancing PCM thermal conductivity. Generally, system performance of the storage unit is more sensitive to the difference between the inlet temperature and PCT than the airflow rates (Waqas and Kumar, 2011a). In most cases, increased difference between inlet and PCT, increased airflow rates during charging,

reduced airflow rates during discharging, and using multiple PCMs in series can enhance the overall system thermal performance (Domanski and Fellah, 1996).

2.3. PAHXs For Free Cooling Applications - Opportunities

In recent years, free cooling applications of PAHX have met some achievements in enhancing indoor thermal performance. In this section, some system parameters and approaches will be discussed to assess the current opportunities of PAHX free cooling applications. These specific approaches were defined to comprehensively review PAHXs according to their importance to PAHX model sensitivity, determining system performance, and affecting outlet air temperature profile. It is worth saying that these parameters and approaches are integrated, cohesive and should be analyzed and investigated together to better assess the system performance of any PAHX configuration.

2.3.1. Temperature Driving Potential Between PCT and Inlet Air Temperature

The PAHX system cooling capacity is determined mainly by the PCM type and the difference between PCT and inlet air temperature during solidification (cooling charging process). Most of the studied investigations construed that larger difference between PCT and inlet air temperature during solidification is more efficient than providing higher air velocities (Waqas and Kumar, 2011a; Panchabikesan et al., 2017). During the discharging process, the larger the difference between PCT and inlet air temperature is, the higher the heat flux and the less duration of cooling supply will be. Panchabikesan et al. (2018; 2017) proposed a modified free cooling system of a bed packed cylindrical PCM tank integrated with a direct evaporative cooling unit. An organic PCM of a PCT range of 25.6 ˚C - 27.1 ˚C was used for an experimental investigation. They proved that integration with the evaporative cooling unit aided the PAHX unit to completely solidify at a faster rate and less charging duration by decreasing PAHX system inlet temperature (through evaporative cooling) during solidification. When the difference between PCT range and inlet temperature increased, the system showed better thermal performance. A three-dimensional model and CFD simulations were introduced by El-Sawi et al. (2013) for a metal-box unit (0.6 × 5 × 2.2 m) filled with paraffinic PCM RT20 (PCT range of 20 ˚C – 22 ˚C). The results, represented in Figure 6, showed that higher temperature difference resulted in a higher heat flux. They also

showed that the performance of LHTES unit could be enhanced when temperature difference during solidification becomes greater than 10 ˚C.

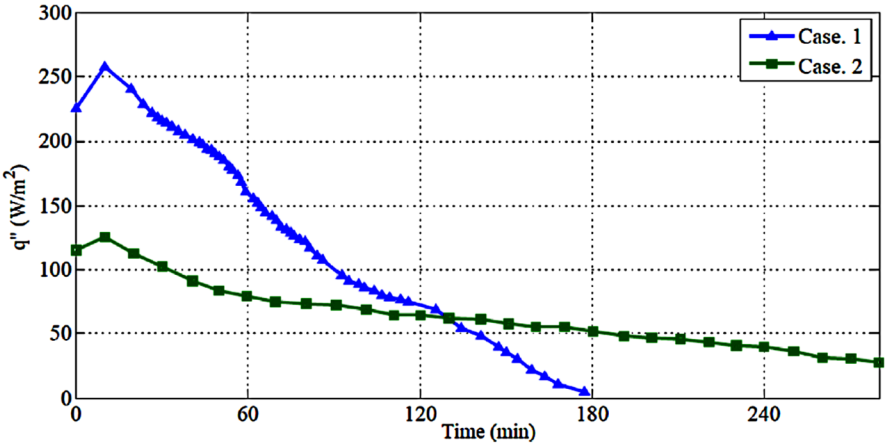

Figure 6 – Heat transfer rate during melting for temperature difference= 16 ˚C (case 1) and 6 ˚C (case 2) (El-Sawi, Azeldin, 2013)

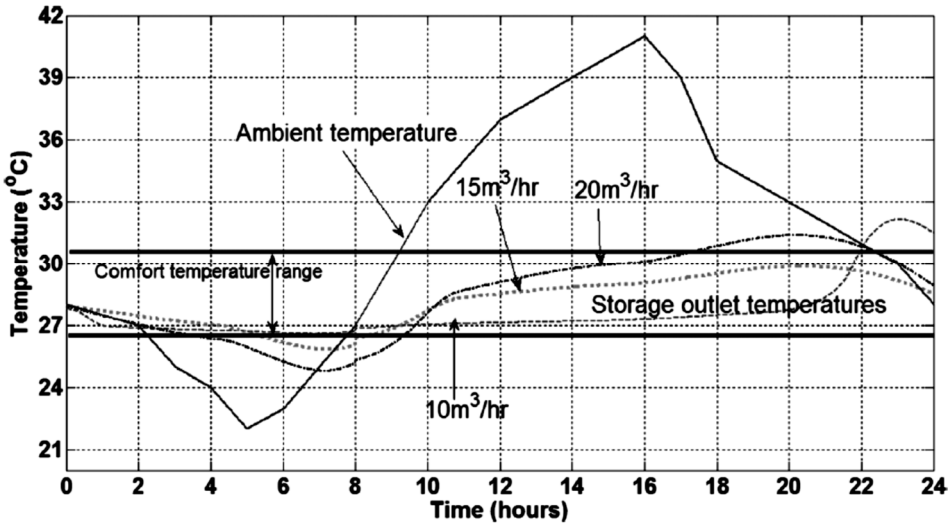

Figure 7 –Numerical results of 24-h evaluation for LHTES system performance under the ambient temperature of Islamabad, Pakistan (Waqas and Kumar, 2011a)

Waqas et al. (2011a; 2011b) tested the performance of a flat plated PAHX using salt hydrate with a PCT range of 28 ˚C – 29 ˚C. At an earlier study, a two-dimensional numerical model was developed using the enthalpy method (Waqas and Kumar, 2011a). Then, an experimental investigation was designed with given conditions to ensure system workability (Waqas and Kumar, 2011b). System thermal performance was investigated in the hot dry climate of Pakistan. The

results proved that with high diurnal temperature, lower inlet air temperature during charging leads to a better system performance (Waqas and Kumar, 2011b). In a 24-h evaluation of the system, shown in Figure 7, the authors showed that the system could achieve around 13 ˚C below the maximum temperature at relatively low flow rates (Waqas and Kumar, 2011b).

Borderon et al. (2015) investigated multiple units of flat plated PAHXs with different ventilation modes under climates of four different cities in France for summer cooling applications. Each unit consisted of 16 plates (1.2 × 1.2 × 0.015 m each) with 0.01 m air gaps and a total mass of 350 kg. Under various configurations (number of units, flow rates, PCM melting temperatures), paraffin (PCT of 21 ˚C, 23 ˚C, or 25 ˚C, and latent heat of 170 kJ/kg) was numerically investigated under moderate climatic conditions using 2D heat transfer model utilizing MATLAB for coding and TRNSYS for thermal analysis. The results showed that the cooling system could achieve a peak shaving in indoor air temperature up to 3 ˚C during day periods. Although the system had promising results, researchers showed no validation for the proposed numerical model. Muthuvelan et al. (2018) performed an experimental investigation for a flat plated PAHX unit using an inorganic PCM of a PCT range of 27 ˚C – 29 ˚C to test the indoor energy saving potential. The experiment was conducted under Indian climatic conditions of day temperature of 35 ˚C and night temperature of 22 ˚C. They concluded that the system can achieve a reduction in room temperature of 2.5 ˚C during the discharging period. Medved and Arkar (2008) tested the performance of a packed bed configuration of spherical encapsulation for RT20 paraffin with PCT range of 20 ˚C – 22 ˚C under moderate climatic conditions. Results showed that 95% of required cooling demand is satisfied. In their study, they considered the proper PCT for each location as equal to the average temperature of the hottest summer month. So, it can be expected that with changing the PCT (increasing difference between inlet and PCT range), more cooling power can be provided. This can enable system application under hotter climates.

2.3.2. Airflow Rates

For free cooling applications, low airflow rates during discharging reduce the heat transfer between air and PCM which maintains the system cooling capacity for longer periods; this enables the system to provide cool air during the long summer days when cooling demand is required. On the contrary, higher airflow rates during solidification can charge the system in a less duration which

suits better the short summer nights. It is obvious that the determination of appropriate airflow rates during both solidification and melting is a vital factor in whole system design for free cooling applications. Flat encapsulated plates of a thickness of 1.5 cm and 2.5 cm were experimentally investigated by Zalba et al. (2004) using paraffin RT25 (PCT range of 18.8 ˚C - 24.1 ˚C, and latent heat of 164 kJ/kg). Under different airflow rates, inlet temperatures were varied between 28 ˚C – 30 ˚C during melting and 16 ˚C -18 ˚C during solidification. The results, shown in Figure 8, proved that phase change has occurred slower with thicker encapsulation plates applying low airflow rates; this could be more appropriate for free cooling applications.

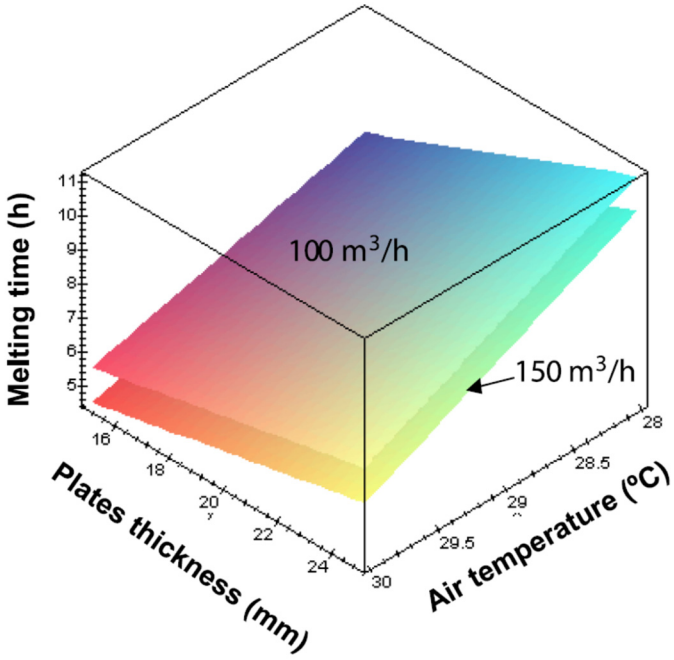

Figure 8 – Effect of airflow rates on duration of PCM melting (Zalba et al., 2004)

A flat encapsulation PCM container of 45 (0.9 × 1 m) plates was tested by Halawa et al. (2005) using calcium-chloride hexahydrate ($CaCl_2.6H_2O$) with a PCT of 28 ˚C and latent heat of 188.3 kJ/kg as an energy storage medium. With inlet temperatures of 40 ˚C and 20 ˚C, system thermal performance was numerically investigated developing a two-dimensional numerical model. The researchers validated the model using two different experiments: one was a flat slab encapsulation, and the other was conical PCM capsules (Saman et al., 2005; Halawa et al., 2010). Although the modified model showed good agreement, utilizing different geometries could be considered a drawback in the validation process. However, the researchers claimed that the same model can

predict the thermal performance of various geometries in case they have the same convective heat transfer coefficient (Halawa and Saman, 2011). The results, shown in Figure 9, proved that increased heat transfer rates can be obtained with higher airflow rates. During experimental investigations of packed bed configuration of spherical encapsulation for RT20 paraffin conducted by Arkar and Medved (2007), the results showed that embedding PAHX into a mechanical ventilation system under considerable airflow rates (2 Air Change per Hour (ACH)) during discharging could achieve similar indoor thermal comfort conditions as night cross ventilation strategy with intensive airflow rates (5 ACH).

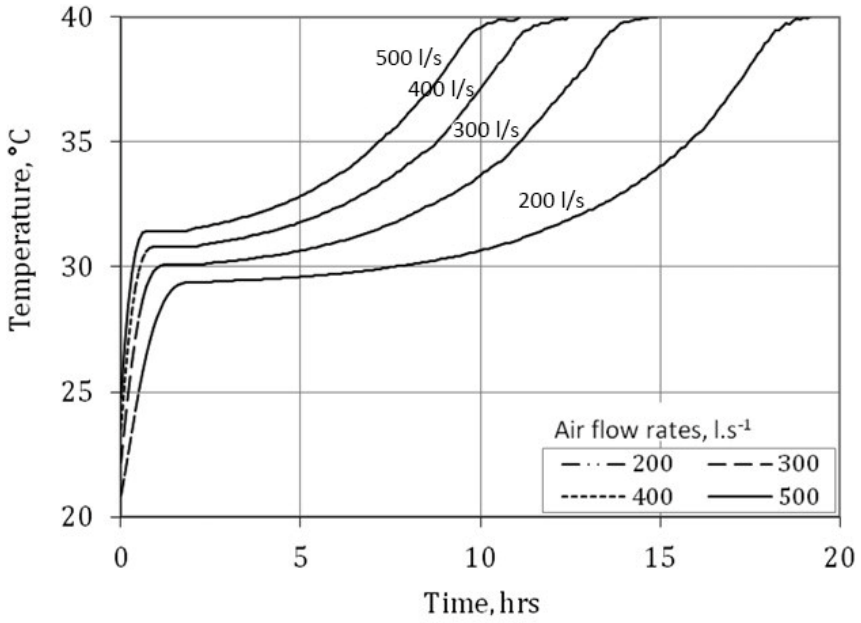

Figure 9 – Outlet air temperature profiles during melting with different airflow rates (Halawa and Saman, 2011)

2.3.3. Multi-PCM Approach

The weather of a given location keeps varying throughout the year based on the climatic season. Hence a free cooling system with the PCM having a particular or narrow range of phase transition temperature may not possess the ability to store adequate energy during its charging cycle. To resolve this, multiple PCMs with different PCT ranges that satisfy the local thermal comfort conditions can be adopted. The use of multiple PCM is also a heat transfer enhancement technique as it increases the bandwidth of the free cooling potential. Pasupathy and Velraj (2008) integrated two layers of PCM with different PCTs in the building rooftop for providing indoor thermal

comfort conditions. Peiro et al. (2015) assured the importance of using multiple PCMs configuration at medium-to-high scale thermal storage units. For PAHX applications, the multiple-PCM approach can be used in series, in the direction of airflow, where PAHX system can be divided into multiple sections of various PCMs of various PCTs. The higher PCT is situated at the inlet section, during cooling discharging process, and the lower PCT is situated at the outlet section. One limitation following this approach is that airflow direction should be reversed between charging and discharging processes, which adds some complications in system installation and operation. With an experimental application of an integrated PAHX into a mechanical ventilation system, shown in Figure 10(a), a double system, four PAHX modules each, was investigated by Zalba et al. (2004) during melting and solidification. Figure 10(b) shows that two types of PCM with different PCT ranges were used. The proposed free cooling system achieved a reduction in outlet air temperature of 4 ˚C during melting and increase of 4.4 ˚C during solidification. This could give a good indication for using the multi-PCMs approach in free cooling systems.

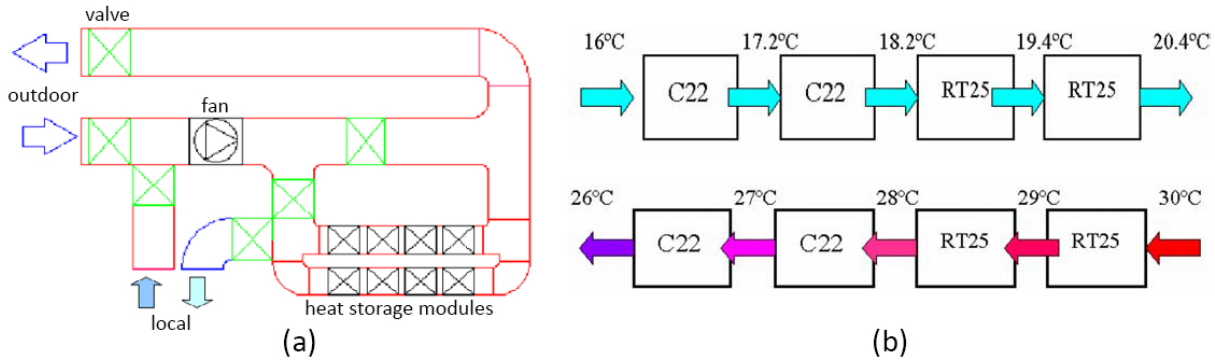

Figure 10 – Integration PCM into free cooling mechanical ventilation system (a) ventilation system configuration (b) diagram of the integrated PAHX phases performance (Zalba et al., 2004)

Numerical investigations were conducted by Vakilaltojjar and Saman (2001) for a flat plated PAHX neglecting sensible heat transfer and using two different inorganic PCMs in series ($CaCl_2.6H_2O$ with a PCT of 28 ˚C, and $KF.4H_2O$ with a PCT of 18 ˚C). Although no accurate performance evaluation could be obtained while no validation was conducted, promising results, shown in Figure 11, have supported the use of two different types of PCMs in series for more cooling potential.

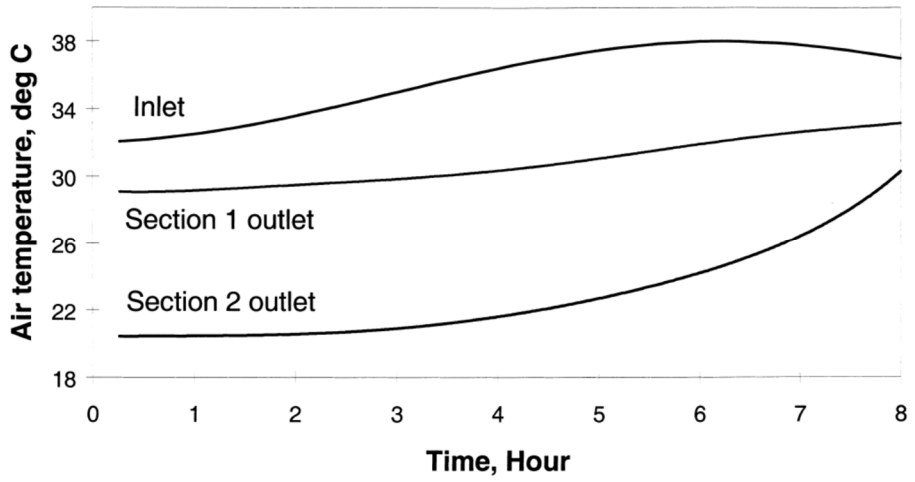

Figure 11 – Cooling potentials for using two types of PCMs in series (Vakilaltojjar and Saman, 2001)

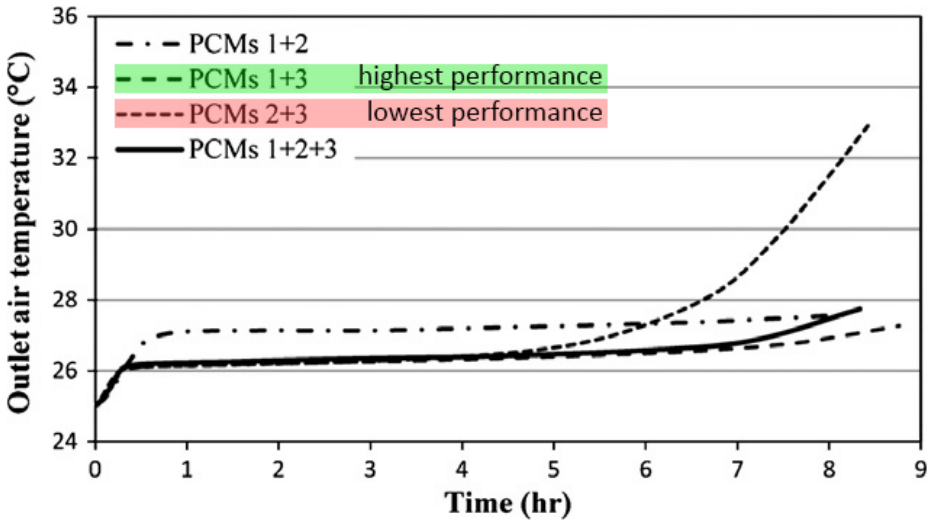

Figure 12 –Outlet air temperature profile for different combinations of PCM (Mosaffa et al., 2013a)

A flat encapsulation of 10 mm PCM slabs with 3.6 mm air gaps into (0.5 × 1.12 × 1.4 m) configuration was tested by Mosaffa et al. (2013a) to investigate the effect of multiple PCM storage at the same volume. Under fixed inlet temperatures of 36 ˚C and 25 ˚C, multiple PCMs were investigated: (1) calcium chloride hexahydrate $CaCl_2$-$6H_2O$ (PCT of 29 ˚C, latent heat of 190.8 kJ/kg), (2) paraffin C18 (PCT of 27.5 ˚C, latent heat of 244 kJ/kg), and (3) paraffin RT25 (PCT of 26.6 ˚C, latent heat of 232 kJ/kg). A validated two-dimensional heat flow model was developed utilizing the effective heat capacity method using finite element energy equations. Different combinations of PCMs were tested maintaining the same volume of the storage unit. The results,

shown in Figures 12 and 13, showed that combination of calcium chloride hexahydrate and RT25 had the best performance keeping the outlet air temperature around 27 ˚C for 8 hours (Mosaffa et al., 2013a). It can be concluded that a significant difference between PCT of different parts should be maintained to magnify performance.

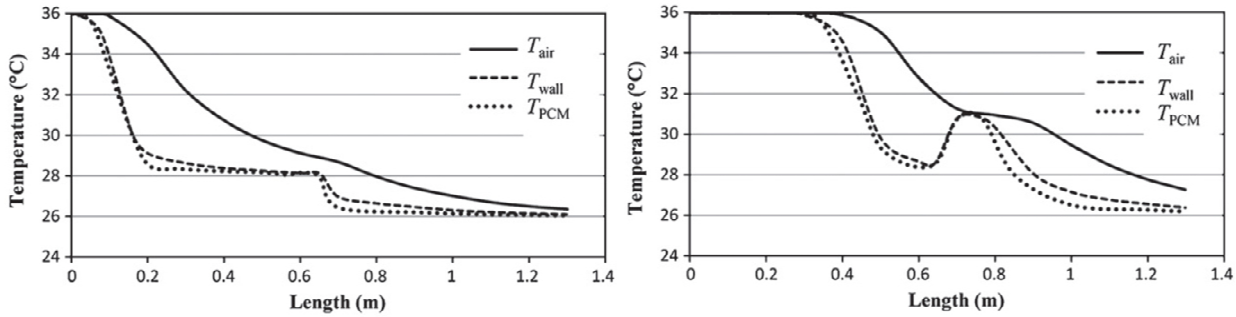

Figure 13 –Air temperature profile along system length for best performance case at Figure 12, after 4.0 hours (left) and 8.0 hours (right) (Mosaffa et al., 2013a)

2.3.4. Heat Transfer Enhancement Approach

The thermal performance of LHTES unit can be augmented through the adoption of various heat transfer enhancement techniques and thermal conductivity enhancement techniques respectively as shown in Figure 14. The use of metal fins in PCM containers with different configurations (Stritih, Uros, 2004; Solomon et al., 2013; Sparrow and Wachtler, 1978; Lacroix, M., 1993; Velraj et al., 1997), addition of graphite matrix (Marín et al., 2005), lessing rings (Velraj et al., 1999), heat pipes (Turnpenny et al., 2000), and increasing PCM fill volume ratio (Chandrasekar et al., 2015) are the commonly adopted heat transfer enhancement techniques in the PCM based storage systems. The above-said techniques enhance the thermal performance of the storage unit by increasing the heat transfer surface area without changing the thermal properties of the storage medium. Yamaha and Misaki (2006) proved that incorporated fins increase the heat transfer surface area and then the heat transfer rate between the air and PCM. In addition to the above, the dispersion of high conducting particles in nanoscale (Zeng et al., 2010; Kumaresan and Velraj, 2012; Wang and Wang, 2009; Li et al., 2013; Fan et al., 2013; Liu et al., 2009), dispersion of low density materials such as carbon/graphene fibers in the PCM (Fukai et al., 2000; Frusteri et al., 2005; Karaipekli et al., 2007; Sanusi et al., 2011), impregnation of porous mediums (Mesalhy et

al., 2005; Mills et al., 2006; Liu et al., 2014; Fleming et al., 2015) are adopted to augment the thermal properties of the storage medium and thereby increasing the overall thermal performance of the LHTES system.

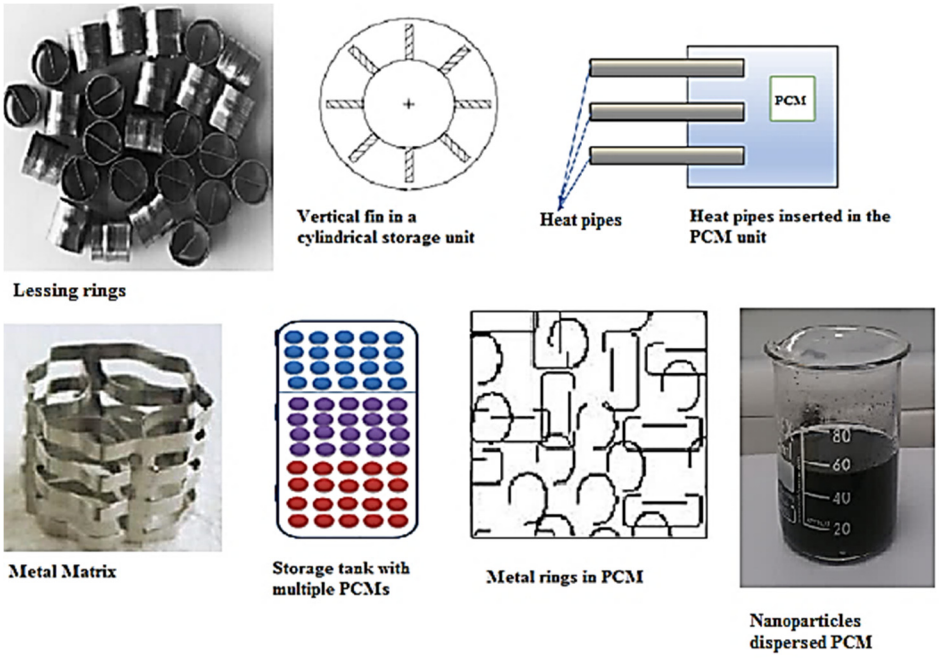

Figure 14 –Heat transfer enhancement techniques (Panchabikesan, Karthik, 2017)

One of the most effective enhancements for improving thermal conductivity and increasing the heat transfer rate of PCM is the incorporation of metal fins in the PAHX configuration (Zalba et al., 2003). Lacroix (1993) investigated the effect of integrated copper fins in PCM tubes both numerically and experimentally. The author reported that introduction of annular fins enhanced the thermal behavior of the PCM at moderate airflow rates. Velraj et al. (1997) experimentally studied the effect of internal longitudinal fin during the solidification of PCM filled in the vertical tube. The inference from the results is that the addition of fins increased the surface heat flux appreciably when compared to the no-fin configuration. With an experimental investigation for box-shaped PAHX, Stritih and Butala (2007; 2009) incorporated aluminum fins to the metal box from both exterior and interior sides. They claimed that external fins were used to increase the surface area between PCM and air and, thus, increase the convective flux. On the internal side, fins were installed in the depth of the system to increase the conduction flux inside the PCM by increasing the overall thermal conductivity. Stritih (2004) performed an experimental analysis of

the heat transfer characteristics of a box shaped PAHX with and without the fin configurations. PCM with a PCT range of 30 °C was used in this study. A reduction in solidification time up to 40% was achieved through the addition of fin configurations. The author also reported that the effect of natural convection was higher than the conduction during the melting process and hence the addition of fins had only a negligible effect during the melting of PCM.

Applying a numerical investigation to PAHX system, Stritih (2003) reported that the distance between fins is most influential than fin thickness. Solomon et al. (2013) investigated the effect of longitudinal copper fins during solidification of PCM, and also the effect of the fins on sensible cooling and subcooling of PCM. The authors indicated that during the existence of low heat transfer rate, the addition of fins suppresses the free convection effect inside the PCM and stimulates the solidification process of PCM, which in turn reduces the subcooling of PCM. During experimental investigations of a packed bed PAHX, PCM pads with heat pipes were installed by Turnpenny at al. (2001). An inorganic salt $Na_2SO_4.10H_2O$ (PCT range of 20 ˚C – 22 ˚C, latent heat of 198 kJ/kg) was used as a PCM. Under inlet temperatures of 45 ˚C during melting and 13 ˚C during solidification, a PCM unit, with a mass of 11.6 kg, was integrated into the mechanical ventilation. The system was improved by providing the heat pipes with copper fins to accelerate heat transfer; 10 PCM units were investigated experimentally in a test unit with a combination of night ventilation strategy. Investigations showed that storage cooling potential of 1 kg of PCM is equal to this of 22.7 kg of a concrete slab for thermal storage.

2.3.5. Integration Approach - Hybrid Systems

Due to the challenges of long-term applications and applications under rough climatic conditions, standalone PAHX systems do not show satisfying performance for free cooling applications. Accordingly, hybrid systems are being proposed to tackle such challenges by integrating PAHX with other techniques, like evaporative cooling systems, solar and radiative panels (Panchabikesan et al., 2017). Following an experimental investigation for PAHX free cooling unit, Muthuvelan et al. (2018) supported the idea that the integration between PAHX unit and other passive cooling technique such as evaporative or radiative cooling can achieve the same indoor thermal performance of active cooling units. Using a hybrid system of a bed packed cylindrical PAHX configuration and a direct evaporative cooling unit, Panchabikesan et al. (2017) experimentally

investigated system performance under hot dry climatic conditions of India. They monitored system cooling potential through solidification behavior of a PCM (PCT of 27 ˚C – 29 ˚C). They proved that standalone PAHXs cannot satisfy the cooling demand due to the small temperature difference between PCT and inlet temperature during solidification. Integrating PAHX with the evaporative cooler increased the cooling potential by reducing the inlet air temperature; thus, complete PCM solidification was available. They also stated that the lower the air relative humidity is, the better the system performance will be. In active applications, Walsh et al. (2013) investigated the effect of integrating a PCM storage unit with an industrial evaporative cooling system to reduce the refrigerant temperature during day peak time. They showed that the combined system achieved 67% reduction in the operation peak time of the chiller.

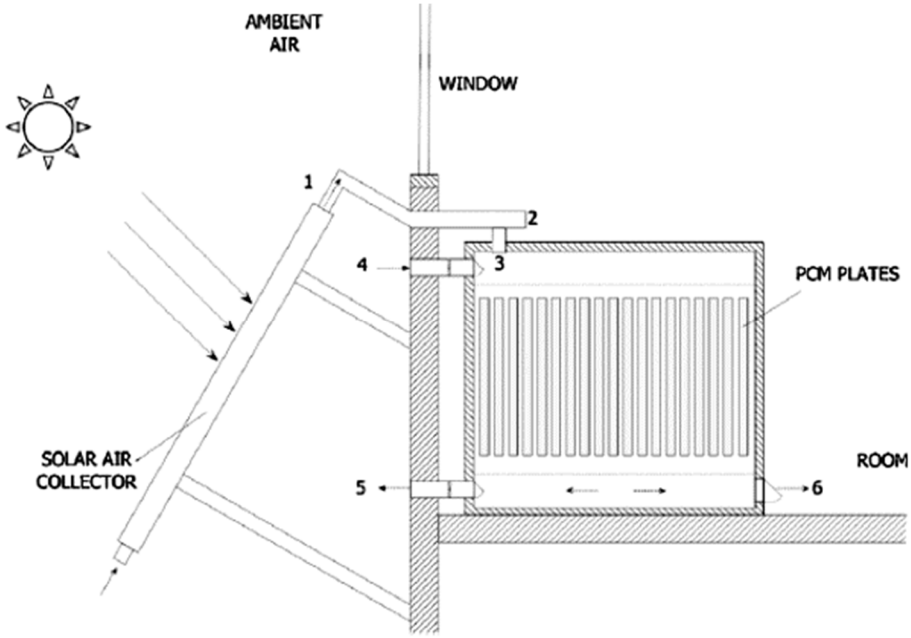

Figure 15 –System integration with solar air collector (Osterman et al., 2015)

Osterman et al. (2015) investigated a PAHX configuration of 15 polyethylene flat plates (0.3 × 0.45 × 0.015 m each), with 8 mm air gaps, in single and double units filled with paraffinic PCM RT22HC. Under the ambient conditions of Slovenia (around 17 ˚C to 25 ˚C in summer, and 0 ˚C to 15 ˚C in winter), the PAHX system was connected to a solar air collector, shown in Figure 15, for the annual operational application (both heating and cooling). The whole system showed a good annual performance with a stabilized outlet temperature around the PCT, as shown in Figure

16. Results showed that coupling standalone PAHX with other system of operation can magnify the system performance.

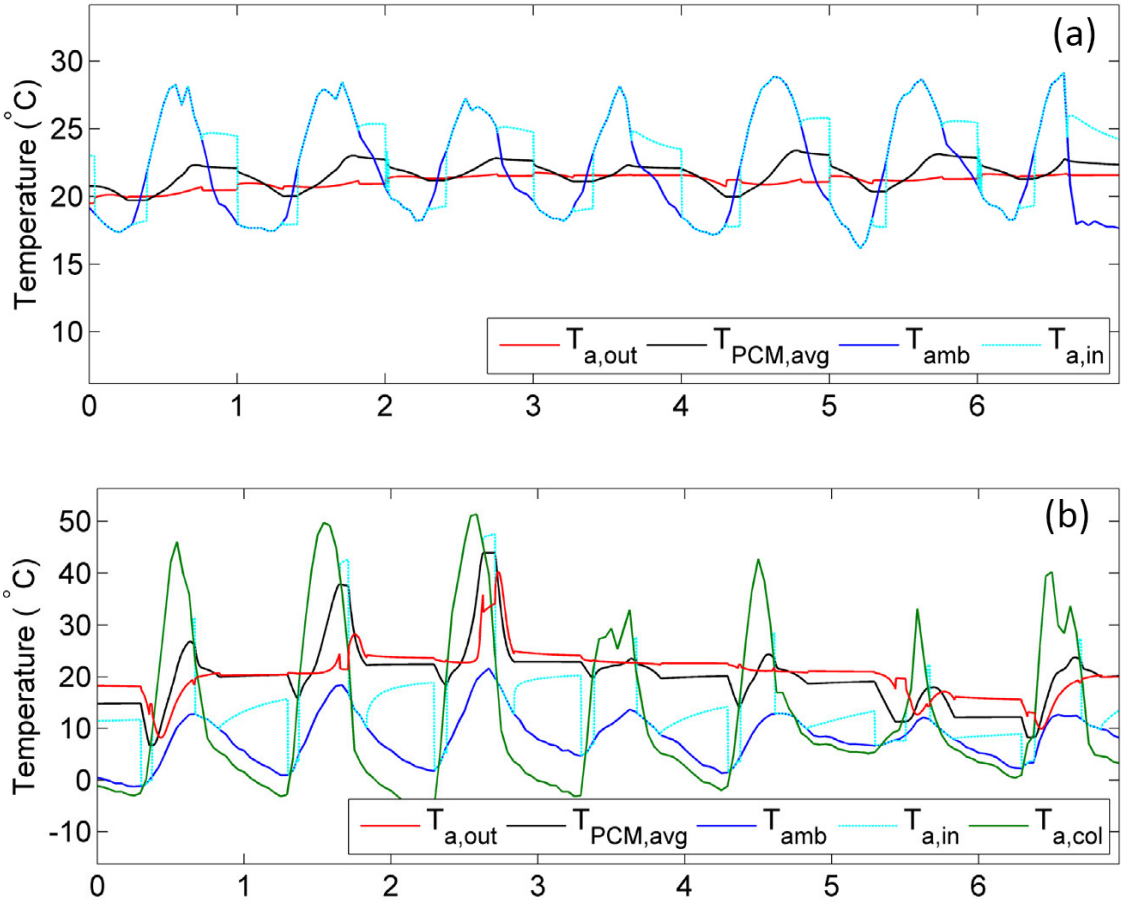

Figure 16 –Outlet temperature profile shows stabilization during (a) first week of August (cooling season) and (b) first week of March (heating season) (Osterman et al., 2015)

Utilizing long-wave radiation to the cold sky of Australia, a validated analytical model was proposed by Al-Nimr et al. (1999) to test the performance of a hybrid system of a bed packed PCM storage tank and a radiative cooling system using water as a HTF. During the night, water was cooled through the radiative panel, which was cooled by long-wave thermal radiation to the sky temperature. The cold water was used to charge the PCM storage tank. The results showed that the system performed better when the radiator panel area was increased, and the mass flow rate was elevated. However, the closed-loop system provided higher cooling rates than open-loop one. Following the same concept, a microencapsulated PCM slurry storage tank was combined with a radiative cooling panel. The hybrid system, designed by Zhang and Niu (2012), was investigated

to evaluate its energy saving potential for five Chinese cities. Using an energy simulation platform, the hybrid unit was connected to an air conditioning system. The results showed that energy saving potential can reach up to 77% at some locations for low-rise buildings. The authors recommended system applications in moderate climates, as the high ambient temperature and relative humidity during night in hot humid climates can affect the system performance. Other hybrid system enhancements were proposed by Lu and Yan (1995) by adding solid silica gel beds to the radiative panels to ensure system workability in humid areas. Following an analytical approach, Ali (2013) investigated the feasibility of applying a radiative cooling solar collector system for thermal comfort applications in the hot arid climate of Egypt. The results showed that, with low airflow rates, the system provided an outlet air temperature 5.5 ˚C – 7 ˚C lower than the ambient temperature.

2.4. PAHXs For Free Cooling Applications – Challenges

For free cooling systems, PAHX applications face a lot of complications and challenges; most of these difficulties are related to local climatic conditions and ambient environment. These challenges affect system performance, its year-round operation, and the resulted outlet air temperature from PAHX units. The following section discusses the challenges of the previous studies of PAHX free cooling applications through analysis of system parameters and design conditions.

2.4.1. Phase Change Temperature Range

Selecting the proper PCT range of the PAHX systems is one of the vital factors affecting the thermal performance of the system, especially in the climates of extremely hot conditions. In these climates, the suitable PCM of the system usually is of a PCT range over the thermal comfort range. Also, in warm-humid, moderate climates with low amplitude, sufficient cooling power may not be provided to the system due to the incomplete charging process of the system regarding the small difference between PCT range and charging temperature. Under moderate climatic conditions, Borderon et al. (2015) numerically investigated a flat plated PAHX. The results of the investigated configuration showed that the system could not satisfy thermal comfort during the whole summer season. The low cooling performance of the system was due to the small difference between PCT

and inlet temperature, especially during the solidification process. Furthermore, Arkar and Medved (2007) showed that the insufficient difference between PCT range and inlet temperature during charging, as shown in Figure 17, affected the system storage abilities and performance. A metal-box unit (0.6 × 5 × 2.2 m) filled with paraffinic PCM RT20 (PCT range of 20 ˚C – 22 ˚C) was tested by Stritih and Butala (2010; 2007) under ambient conditions of around 25 ˚C as a maximum temperature and 21 ˚C as a minimum temperature. The results, shown in Figure 18, proved that outlet temperature profile did not show stabilization. Instead, it followed the inlet temperature profile. This means that the system storage capacity was low due to the reduced charging energy due to the improper selection of PCM according to this inlet profile.

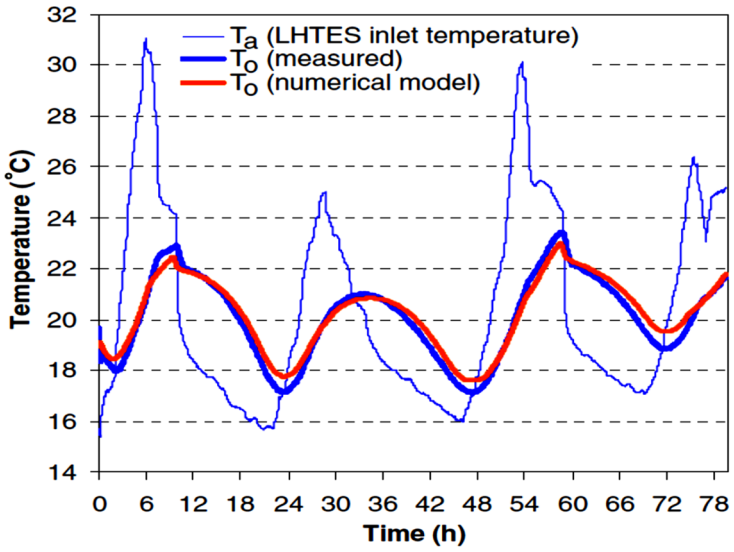

Figure 17 – Insufficient difference between Inlet and phase change temperatures (PCT range 20 ˚C – 22 ˚C) leads to relative stabilization of outlet profile (Arkar and Medved, 2007)

A cylindrical configuration using floor bed PCM granules was developed by Takeda et al. (2004) and Nagano et al. (2004) with porosity percentage of 42.8% to evaluate heat transfer between PCM and air. Commercial PCM granules (GR25-RUBITHERM GmbH) were used with the composition of 65% porous ceramics and 35% paraffin wax (Nagano et al., 2004). The granules were 1 mm – 3 mm in diameter with a PCT of 23.5 ˚C - 24.9 ˚C, a latent heat of fusion of 41.9 kJ/kg, and thermal conductivity of 0.13 W/m.K (Takeda et al., 2004). A small prototype (600 mm in length, and 50 mm in diameter) was experimentally investigated; in conjunction, the one-dimensional model was developed utilizing finite difference energy equations using enthalpy method. Although a good

agreement was obtained between the experimental and numerical results, the incomplete cycles of phase change due to the small difference between PCT and inlet profile, with the relatively small range of PCT could lead to an inaccurate indication about system performance. However, the outlet air temperature profile showed stabilization around PCT.

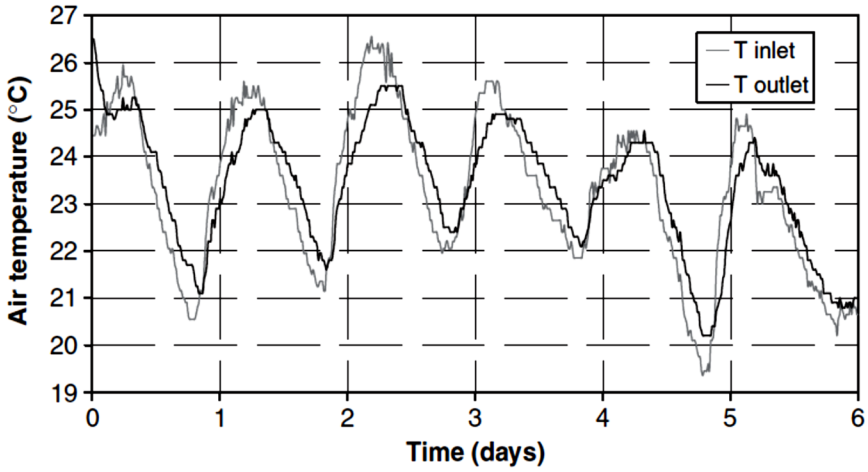

Figure 18 –Improper selection of PCM leads to the insufficient cooling performance of PAHX (Stritih and Butala, 2007)

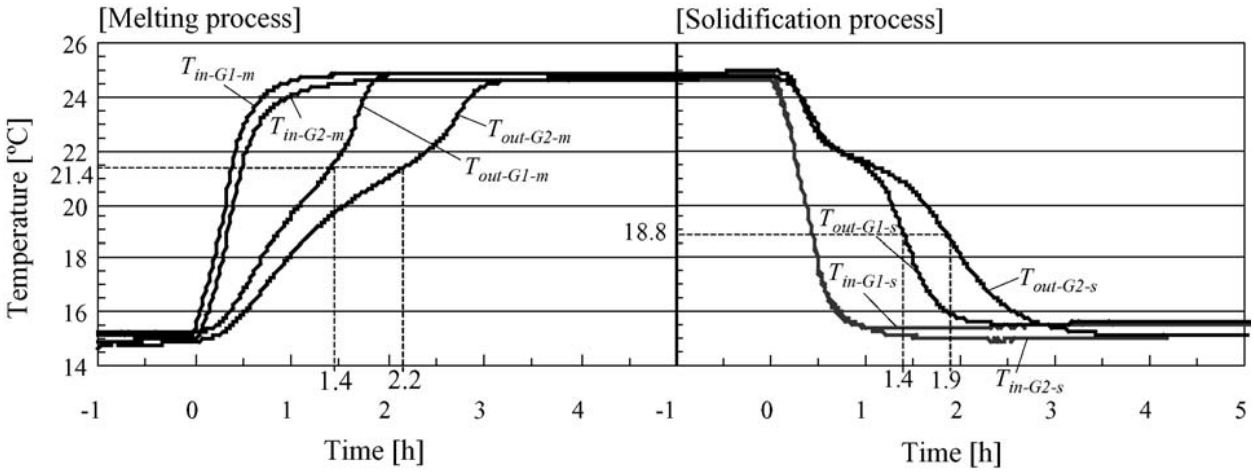

Figure 19 – Inlet and outlet air temperature of PCM floor bed during melting and solidification at different airflow rates (Nagano et al., 2006)

Other investigations by Rady (2009a; 2009b) using granular phase change composites of two different kinds of granules (GR27, PCT range of 21 ˚C – 29 ˚C, a latent heat of fusion of 64.9 kJ/kg; and GR41, PCT of 31 ˚C – 45 ˚C, a latent heat of fusion of 65.9 kJ/kg) showed that system storage capacity, represented by latent heat, has a more significant effect on the system

performance than the PCT range. Further configuration developments were experimentally investigated by Nagano et al. (2006). A permeable PCM granules floor bed was merged with building thermal mass and air conditioning system. Granules of PCT range of 17 ˚C – 22 ˚C were used with inlet temperatures that varied from 15 ˚C to 26 ˚C. As shown in Figure 19, the phase change occurred within around 2 hours (under high airflow rate) and 3 hours (under low airflow rate) in both melting and solidification which indicates system low capacity. The results also showed that provided heat storage could not satisfy the cooling load along the day; this is due to system size, relatively small latent heat storage, and the small difference between PCT and inlet temperatures, especially during the solidification process. This ensures the importance of the proper selection of PAHX configuration and PCT range due to the application.

2.4.2. Inlet Air Temperature

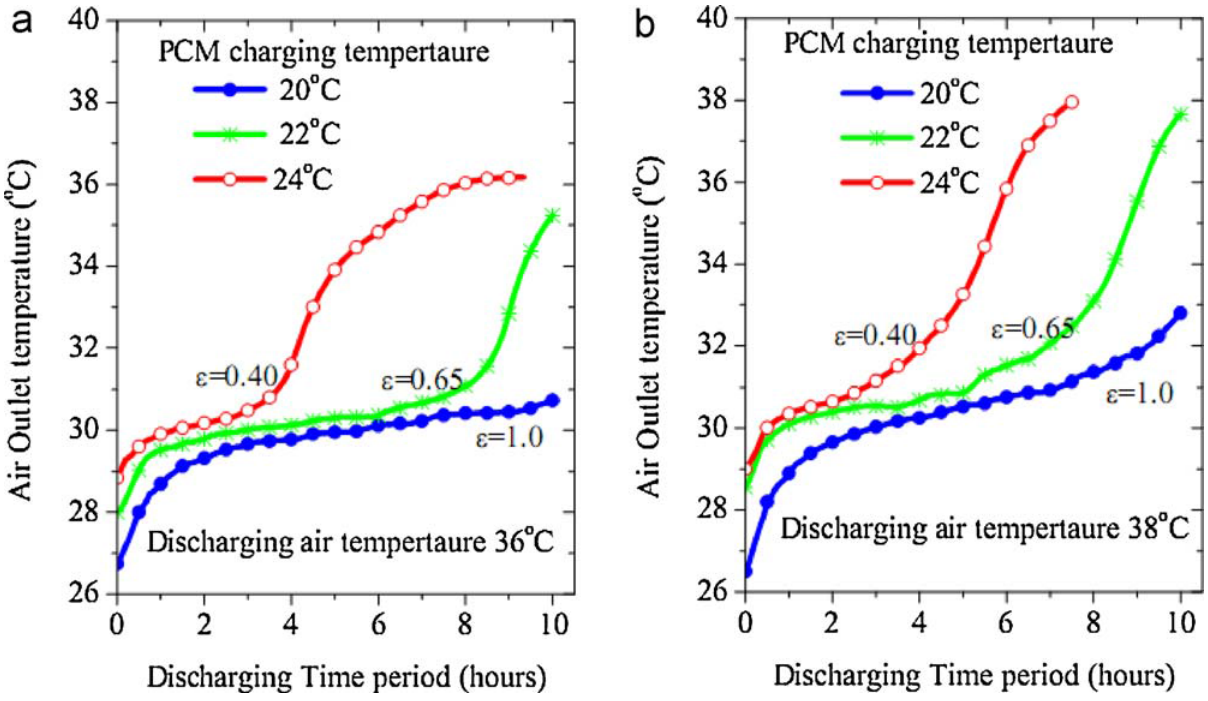

Figure 20 – Outlet air temperature for inlet temperature of (a) 36 ˚C, and (b) 38 ˚C with different charging temperatures (Waqas and Kumar, 2011b)

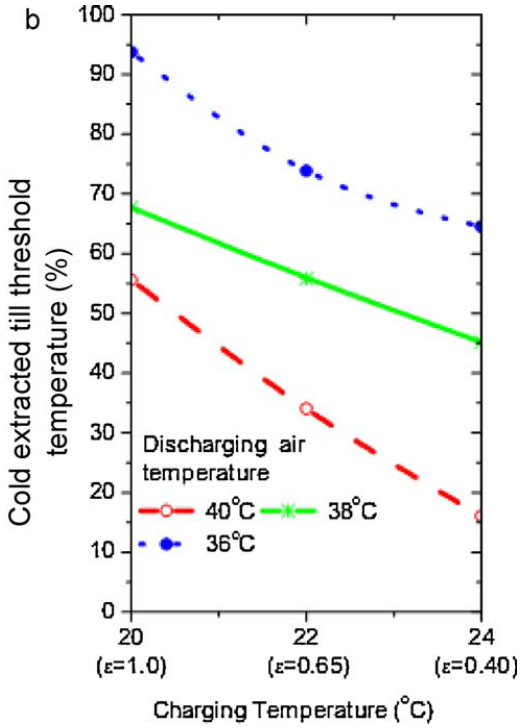

Figure 21 – Extracted energy due to different charging and discharging temperatures (Waqas and Kumar, 2011b)

Several studies reported the effect of changing the inlet air temperature during melting and solidification on PAHX performance while maintaining the same PCT range of the system. Flat encapsulated configuration was tested by Waqas et al. (2011a; 2011b) using salt hydrate PCM with melting range of 28 ˚C – 29 ˚C, a latent heat of 180 kJ/kg, a thermal conductivity of 0.6 W/m.K, and a PCM mass of 13 kg. System thermal performance was investigated in the hot dry climate under inlet temperatures that varied from 20 ˚C to 24 ˚C during solidification, and from 36 ˚C to 40 ˚C during melting. It is reported that best performance of the system was observed at charging/discharging of 20 ˚C / 36 ˚C (difference of 16 ˚C); lowest performance was observed at charging/discharging of 24 ˚C / 40 ˚C (also difference of 16 ˚C). From this result, it is inferred that the inlet air temperature is an important parameter to evaluate system performance. An adaptive thermal comfort profile was proposed by Waqas and Kumar (2011a). The researchers studied the effect of different charging and discharging temperatures on system performance. As shown in Figures 20 and 21, they proved that, with the large temperature difference between charging and discharging, higher discharging temperature results in less system performance. Yanbing et al. (1999) used a packed bed storage unit of a fatty acid PCM of PCT range of 22 ˚C – 26 ˚C to

evaluate indoor thermal performance under ambient conditions of Beijing. They concluded that circulated air temperature did not drop below the PCT range as the charging temperature reached only 20 ˚C as a minimum. This means that the charging temperature was insufficient to completely charge the system.

2.4.3. Airflow Rates Strategy

It is important to choose the appropriate airflow rates during both the charging and discharging processes, particularly during the charging process. As choosing a lower flow rate might lead to incomplete solidification of the chosen PCM; whereas, having a higher flow rate (more than required) might end up in increased power consumption of the whole system. The other problem of having an undesirable high airflow rate is that the temperature of charging air might raise up to 1°C due to the heat generated by the operation of the fan. Fan operation and power consumption were being considered to regulate system airflow rates due to the expected increased power consumption of the provided high airflows, especially in summer seasons (Osterman et al., 2015).

Most of the studies concluded that relatively high airflow rates during charging and low airflow rates during discharging are the most appropriate operational conditions for PAHX free cooling applications. Furthermore, they concluded that high airflow rates during discharging can lead to lower system performance. The performance of a PAHX was investigated by Darzi et al. (2013) for a flat plated PAHX during the melting process; a validated two-dimensional numerical model and CFD simulations were utilized to investigate the system performance through various airflow rates. The results ensured that higher flow rates reduce the duration needed for the complete system discharging. They also showed that, with increasing airflow rates, the system consumes its storage power rapidly; this can affect the resulted outlet air temperature for practical applications.

Some of the investigations studied the PAHX performance under fixed airflow rates during both melting and solidification. Arkar and Medved (2007) showed that preferable outlet air temperature can be attained with higher airflow rates during the daytime. At evening time, a sharp increase in outlet profile, that follows the inlet air temperature profile, is occurred due to the consumed cooling power of the system, as shown in Figure 22. This depicts that the proper selection of PCM and airflow rates controls system storage abilities and performance.

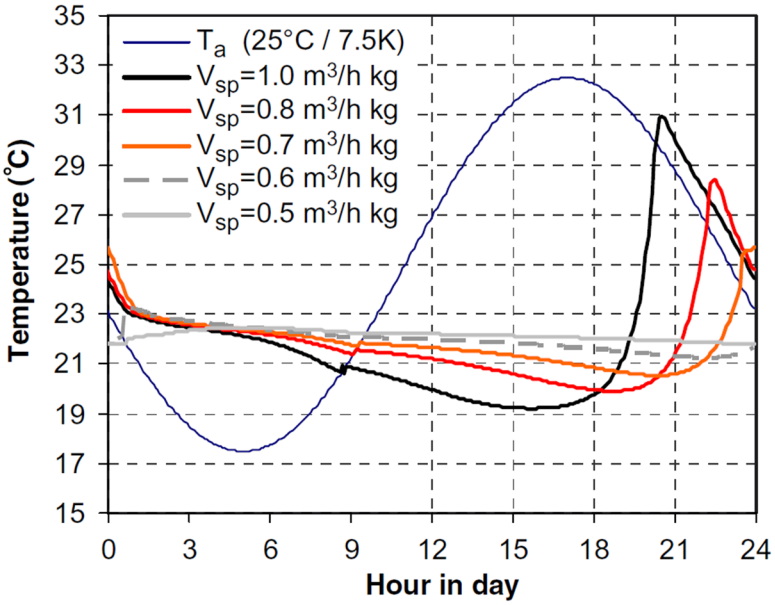

Figure 22 –outlet air temperature profiles due to various airflow rates (Arkar and Medved, 2007)

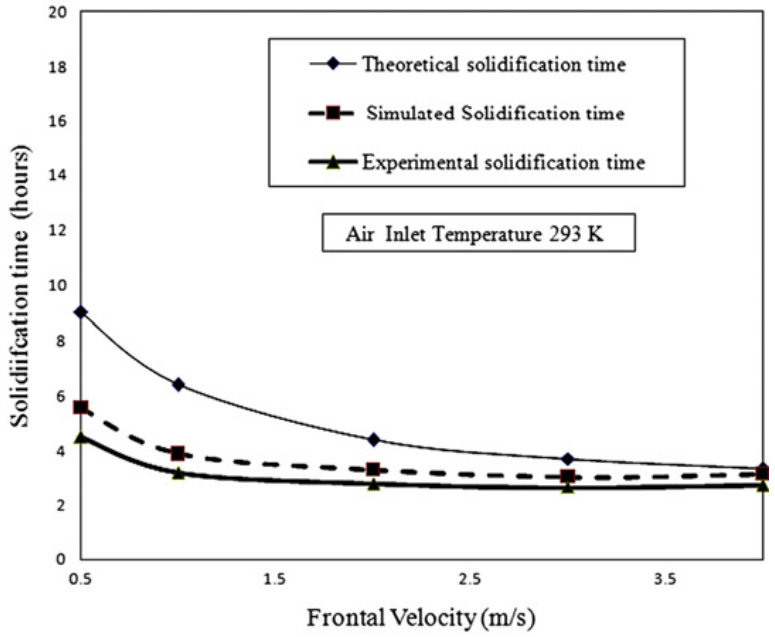

Figure 23 – Effect of various air velocity on solidification time (Antony Aroul Raj and Velraj, 2011)

A modular PAHX was developed by Antony Aroul Raj and Velraj (2011) to test the effect of airflow rates on the duration of solidification. Experimental, analytical and CFD investigations were conducted; their results, shown in Figure 23, revealed that, with lower airflow rates, solidification time increases, heat transfer characteristics improve, and system free cooling

potential increases. One observation from the figure is that the more the values of air velocities decrease, the more the error between analytical and experimental results increases. This may be due to applying the same convection model with various air velocities, which represent various conditions of convective heat transfer. Predicting system performance under only forced convection conditions, even with very low air velocity values, neglecting free or mixed convection modes, where buoyancy forces play a role at low airflow patterns, could be a strong limitation of performance prediction of PAHXs.

2.4.4. Year-Round Thermal Management

Although many achievements were made regarding increasing the PAHX thermal performance, long-term applications and year-round thermal performance are still significant limitations of system practical applications (Gowreesunker et al., 2013). The degree hours are defined to determine the cooling and heating demand of the building (ASHRAE, 2013). Cooling/heating degree hours (CDH/HDH) represent the required energy to cool/warm the indoor environment to reach the comfort zone. The higher the degree hours, the higher the cooling/heating demand, and the greater the energy required to maintain indoor thermal comfort conditions (Thambidurai et al., 2015). For annual applications, most of the locations have different values for CDHs and HDHs. Under these conditions, PAHX system must deal with both cooling and heating demands for year-round applications. At some locations with extreme hot climates, year-round cooling demand is required with high CDH values. The ambient temperature profile results in an extreme high cooling demand in the hot season and high to moderate cooling demand in warm and cool seasons. In all situations, thermal management is a strong limitation for standalone PAHX systems for passive applications.

Rouault et al. (2016) tested the effect of integrating two latent storage units with the ventilation system of a residential space on the indoor air temperature. The authors used RT21 (PCT range of 17 ˚C – 19 ˚C, latent heat of 134 kJ/kg) as a PCM. The storage units were used as a cooling system within the whole control system of the test unit. The investigation was conducted for around two weeks of the summer season of Bordeaux, France. Although the system showed some achievements in temperature profile peak shaving, the storage system did not show the required

performance to maintain the system outlet air temperature within the comfort range of temperatures.

For longer-term real applications, maintaining system performance is a strong challenge due to the fluctuated ambient profile. Waqas and Kumar (2011a) tested the PAHX performance in a 24-h evaluation under ambient conditions. The results showed that the system achieved 13 ˚C below the maximum temperature, but as the multi-day evaluation was not investigated, the long-term performance of the system would be a limitation of the study. They also developed the thermal storage system in (Waqas and Kumar, 2013) for only a space heating application in the winter season by connecting the PAHX unit with a solar air collector. Jaworski, Maciej (2014) presented a new structure of a ventilated ceiling panel made of a composite of a gypsum mortar and 27% of microencapsulated PCM. The whole ceiling system worked as a PAHX free cooling system combined with night ventilation. A PCM of a PCT range of 23 ˚C – 24 ˚C was used to investigate the system thermal performance. Investigations under longer-term real conditions were performed; the results showed that when the ambient profile was lower than the PCT range, PCM did not undergo a phase change and its thermal capacity was not used, as shown in Figure 24. Also, when the ambient profile was higher than the PCT range, PCM was not charged and the system showed no thermal performance. The author recommended further optimization in terms of system parameters.

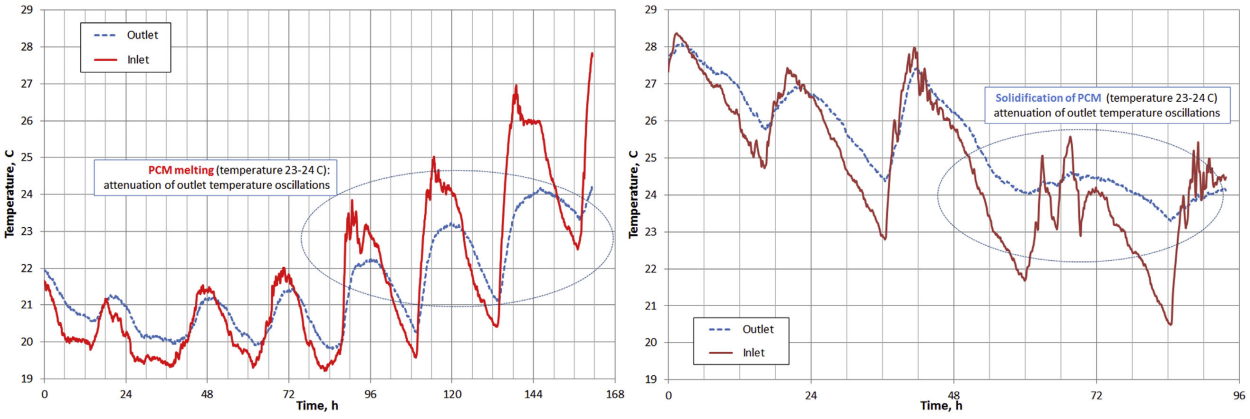

Figure 24. Effect of several-day ambient air profile on system performance (melting and solidification) (Jaworski, Maciej, 2014)

2.4.5. Auxiliary Power Consumption

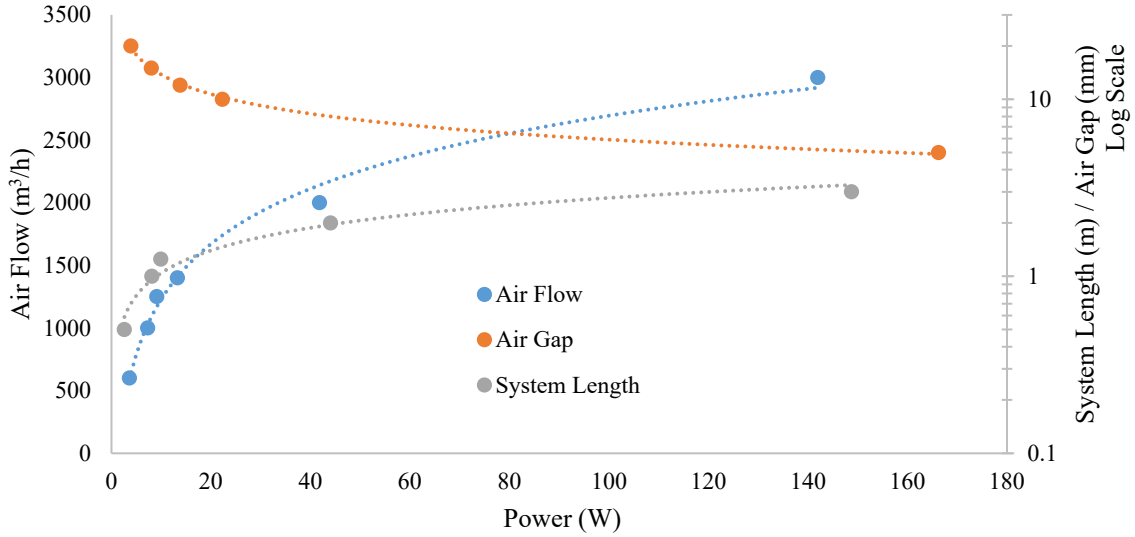

Figure 25 – Effect of airflow, system length, and air gap on fan power consumption (Dolado et al., 2011)

System power consumption is an important factor in identifying system performance and the potential of energy savings. Many studies investigated the system behavior with respect to the power-based performance. For free cooling applications, the power consumption comes mainly from the fan operation (P_{fan}). Coefficient of performance was developed by the term (Q_{pcm}/P_{fan}) to represent PAHX performance, where Q_{pcm} is the total energy absorbed by PCM (Mosaffa et al., 2013a). A developed term, air exergy (available energy supplied by air), was proposed instead of Q_{pcm} to express system efficiency (Mosaffa et al., 2014). In mechanical ventilation systems, the electricity consumption refers to fan power. The three main parameters that affect fan power in PAHX system are airflow, system length and air gap between PCM slabs. Figure 25 is based on a numerical investigation conducted by Dolado et al. (2011) for a proposed flat encapsulation configuration; it shows that there was an exceptional increase in power consumption when air gap was less than 10 mm. Also, this increase appears when airflow rate was greater than 2000 m^3/h, and when PAHX system length was more than 2 m. Considering power consumption factor in designing PAHX system is important in whole system performance evaluation.

2.4.6. Economic Feasibility of PAHXs Free Cooling Applications

Most of the carried-out studies investigating the economic feasibility of PAHXs free cooling applications were conducted in climatic conditions where the daytime temperature is moderately high (for e.g. ~30 °C). In such climates, the free cooling potential is increased specially in warm seasons (Bulut and Aktacir, 2011; Panchabikesan et al., 2017; Waqas and Ud Din, 2013). Also, most of the conducted studies were carried out under fixed or simulated inlet temperature within controlled environment (Waqas and Kumar, 2011b; Mosaffa et al., 2013a; Arkar and Medved, 2007), which affects the prediction of the economic feasibility study of the PCM-based free cooling system applications under real-case conditions. Zalba et al. (2004) considered an application of integrated free cooling multi-PCM PAHX units with a ventilation system under inlet temperatures of 30 °C during discharging and 16 °C during charging. The authors conducted an economic study for material and installation initial cost for the system and compared it with a conventional active unit. They reported that, with a payback period of 3 - 4 years, the free cooling system achieved 9% additional initial cost and 9.4 times less power consumption than the active cooling unit. They also stated that PCM costs 17% of the total system initial cost. Considering both initial and operational cost, Thambidurai et al. (2015) conducted an economic analysis of applying PCM based free cooling system in tropical climates using PCM with a PCT of 20 °C – 25 °C and with latent heat storage capacity of 185 kJ/kg . The authors reported that total investment costs, as well as the annual equivalent total cost savings, increase and the simple payback period decreases with the increase in the storage capacity of the LHTES system. It is to be noted that, most of the studies available in the literature that reported the economic analysis of free cooling system was carried out in European countries or in the places where the ambient temperature is relatively low (< 25°C). However, for hot dry climates, only limited real time experimental studies have been carried out and in specific, no studies reported the economic feasibility of PCM-based free cooling systems. Also, only limited studies have discussed the climate-based energy saving potential for active cooling systems in this climate (Budaiwi, I.M., 2001). In hot desert climate, the year-round operation of the free cooling system is still a challenge during the summer season due to high ambient temperature even at night time and hence it might not be feasible to completely solidify the PCM within the PCT range of 25 °C – 30 °C. Also, the potential for achieving energy savings is relatively less compared to the other climates. Hence, in hot-desert climate, it is highly

recommended to initially conduct the feasibility study for the year-round operation of the free cooling system that can support a real case economic analysis of PCM-based free cooling system.

2.5. Discussion

Most of previous studies concluded that PAHXs show good performance in 24-h cycle utilizing concept of reversible phase change processes of PCMs that can maintain latent heat storage for whole duration under certain design conditions. Table 4 proposes a design guidelines checklist for the mandatory parameters of any PAHX system and system enhancement parameters. The guidelines checklist includes all the design parameters and decisions that must be checked and designed for system implementation.

Table 4 – PAHX system design guidelines checklist

System Primary Parameters	System Enhancing Parameters
• Local climatic conditions	• Incorporation of fins, metal matrix, …
• System configuration	• Multiple PCMs / cascaded system
• Phase change temperature range	• Hybrid system/integration with other passive systems
• PCM thermophysical properties	
• Inlet air temperature profile	• Nano-additives approach
• Airflow rates	• Dispersion of carbon fibers
• Encapsulation geometry	
• Encapsulation material	
• PCM fill volume ratio	
• Percentage of porosity (for packed beds)	
• System insulation material thickness	

A proper management of system design parameters could enhance the heat transfer process within PAHXs. Generally, increased heat transfer rates can be achieved by:

- Greater difference between inlet and phase change temperatures (during charging) (Panchabikesan et al., 2019).
- Higher airflow rates (during charging) (Nagano et al., 2004; Dolado et al., 2011).
- Higher thermal conductivity for encapsulation material (Dolado et al., 2011).

- Increasing bumping, roughness or complexity of rugosity of encapsulation surface (Dolado et al., 2011).
- Decreasing PCM slab thickness (Dolado et al., 2011; Halawa and Saman, 2011).
- Increasing PCM system length (Mosaffa et al., 2013a).
- Decreasing the encapsulation thickness (Zalba et al., 2004).
- Reducing air gap between slabs (Dolado et al., 2011; Halawa and Saman, 2011; Mosaffa et al., 2013a).
- Integration of suitable passive cooling concepts with PAHX (Panchabikesan et al., 2018; Panchabikesan et al., 2017).

Tracking the outlet air temperature for free cooling systems is very challenging, as the outlet temperature profile is not separately responsive to each system parameter. Instead, it is a function of all the governing parameters simultaneously. However, sufficient difference between inlet and PCT range leads to a temperature stabilization of the outlet air around the PCT. Moreover, the outlet air profile shows more stabilization with lower airflow rates (Waqas and Kumar, 2011a). Thus, the proper selection of PCM and airflow rates controls system storage abilities and performance (Arkar and Medved, 2007). For all the previous parameters, generally, Table 5 summarizes the effect of each PAHX system parameter on the cooling power provided by the system, the duration needed for complete melting and solidification, and the outlet air temperature. Tables 6 and 7 summarize the reviewed configurations and investigation results of PAHXs. Most of the investigated studies were under a controlled environment inside laboratories with warm to temperate simulated climatic conditions. Only few studies investigated the thermal behavior of the system under hot climatic conditions or using real case experimental prototypes.

Table 5 – Effect of PAHX parameters on cooling energy, heat transfer duration, and outlet air temperature

Increasing Parameter	**Affected Outputs**		
	Cooling Power*	Heat Transfer Duration	Outlet Air Temperature**
Difference between Inlet air temperature & PCT	Increasing (Zalba et al., 2004; Dolado et al., 2011; Waqas and Kumar, 2011b)	decreasing (Zalba et al., 2004; Dolado et al., 2011; Waqas and Kumar, 2011b)	- increasing (with increasing inlet temp.) (Waqas and Kumar, 2011b) - decreasing (with decreasing PCT) (Waqas and Kumar, 2011b)
Airflow rate	increasing (Nagano et al., 2004)	decreasing (Nagano et al., 2004)	- decreasing (initial periods) (Arkar and Medved, 2007)

			- increasing (last periods) (Arkar and Medved, 2007) - stabilizing (low flow rates) (Arkar and Medved, 2007)
Encapsulation thermal conductivity	increasing (Dolado et al., 2011)	decreasing (Dolado et al., 2011)	- decreasing (initial periods) - increasing (last periods)
Encapsulation surface rugosity	increasing (Dolado et al., 2011)	decreasing (Dolado et al., 2011)	- decreasing (initial periods) - increasing (last periods)
Encapsulation thickness	decreasing (Zalba et al., 2004)	increasing (Zalba et al., 2004)	Increasing
PCM slab thickness	decreasing (Dolado et al., 2011; Halawa and Saman, 2011)	increasing (Dolado et al., 2011; Halawa and Saman, 2011)	decreasing (Mosaffa et al., 2013a)
PCM system length	increasing (Mosaffa et al., 2013a)	decreasing (Mosaffa et al., 2013a)	decreasing (Mosaffa et al., 2013a)
Air gap between slabs	decreasing (Dolado et al., 2011; Halawa and Saman, 2011; Mosaffa et al., 2013a)	increasing (Dolado et al., 2011; Halawa and Saman, 2011; Mosaffa et al., 2013a)	Increasing
Latent enthalpy	increasing (Dolado et al., 2011)	increasing (Dolado et al., 2011)	Decreasing

** Cooling energy amplitude not cumulative cooling energy over time*

*** During melting. Trend here is not directly responsive to single parameter and is a function of other parameters*

Table 6 – PCM-to-air heat exchangers configurations of reviewed studies

Researcher	**Year**	**Configuration**	**PCM**	**PCT**	**Volume m³**	**Inlet temperatures**		**Encapsulation Material**
Zalba et al. (2004)	2004	Flat plate encapsulation	molecular alloy	19.5 - 22.2 ˚C		*melt*	28-30 ˚C	HDPE (15 /25 mm thickness)
			Paraffin RT25	20 - 24 ˚C		*solid*	16-18˚C	
Turnpenny et al. (2000; 2001)	2001	PCM pads with heat pipes	Glauber's Salt	20 - 22 ˚C		*melt*	~45˚C	
						solid	~13˚C	
Arkar et al. (2005; 2007; 2007)	2007	Packed bed (spherical encapsulation)	RT20 paraffin	20 - 22 ˚C				1.0mm polyethylene
Stathopoulos et al. (2016; 2017)	2016	Flat plate encapsulation	Paraffin Mikrotek 37D	37 ˚C	1.05 x 0.75 x 0.25	*melt*	44˚C	Aluminum (18 mm)
						solid	26˚C	
Dolado et al. (2011)	2011	macro-encapsulation slabs	organic PCM	26.5 ˚C				

Nagano et al. (2004)	2004	cylindrical packed bed granules	granules GR25	23.5 - 24.9 ˚C		various		1-3 mm in dia. ceramic granules
Waqas and Kumar (2011a; 2011b)	2011	Flat plate encapsulation	Salt hydrate SP29	28 - 29 ˚C	0.5 × 0.5 × 0.01	*melt* *solid*	36-38-40˚C 20-22-24˚C	galvanized steel
Stritih and Butala (2007; 2010)	2010	Centralized unit	RT20 paraffin	20 - 22 ˚C	0.09 × 0.5 × 0.22	various		metal box
Panchabikesan et al. (2018; 2017)	2017, 2018	Packed bed (spherical encapsulation)	RT 28 PCM & HS 29 PCM	25.6 – 27.1 °C & 27 – 29 °C	-	various		High Density Polyethylene (HDPE)
Osterman et al. (2015)	2015	Flat plate encapsulation	RT22HC paraffin	21 - 23 ˚C	0.3 x 0.45 x 0.015	various		Polyethylene
Halawa and Saman (2011)	2011	Flat plate encapsulation	Salt hydrate	28 ˚C	0.9 x1.0	*melt* *solid*	40˚C 20˚C	
Mosaffa et al. (2013a; 2013b; 2014)	2013	Flat plate encapsulation	Salt hydrate Paraffin C18 Paraffin RT25	29 ˚C 27.5˚C 26.6 ˚C	0.5 x 1.12 x 1.4	*melt* *solid*	36˚C 25˚C	
El-Sawi et al. (2013; 2014)	2014	Centralized unit	RT20 paraffin	20 - 22 ˚C	0.22 × 0.22 × 0.5	various		metal box

The literature review has revealed some drawbacks and limitations in PAHX free cooling applications, especially in the region of hot desert climate. Based on the literature, the research gaps of PAHXs for free cooling applications were identified, and are summarized below:

- None of the reviewed studies has conducted experiments by considering the potential of night-time sky radiation during solidification process. This consideration can speed up the solidification process or increase the system cooling abilities. Also, using PCM with low PCTs can be promoted to enhance the system cooling performance.
- Maintaining an outlet air temperature that promotes the indoor thermal comfort is a system limitation, especially in extremely hot climates. The high inlet air temperature affects the resulted outlet temperature because the average temperature of day and night fluctuation (PCT of the system), even the night temperature itself during summer season at some locations, is still higher than the comfort temperature range.
- Regarding the previous issue, applying same PCM does not meet the temperature seasonal variations. This affects the long-term system performance due to changing of ambient

temperature profiles with various seasons. However, some investigations showed that combining PAHX system with other techniques could maintain the system performance during annual applications.

- Other investigations assured the potential of using multiple-PCM approach within the PAHX system; this ensures system workability with high inlet temperatures. However, there is a limitation following this approach; the airflow direction should be reversed between melting and solidification processes, which puts some constraints in system operation.

Table 7 – Achievements and drawbacks of reviewed studies

Researcher	Methodology	Achievements	Limitations
Turnpenny et al. (2000; 2001)	-Experiment -1D heat transfer model	-Higher heat transfer rate with higher difference between inlet air temperature and PCT.	-One-dimensional mathematical model of the heat transfer. -Neglecting temperature gradient along heat pipes. -Neglecting the convection heat transfer between PCM and indoor environment (insulation properties). -Neglecting pressure distribution around heat pipes.
Stathopoulos et al. (2016; 2017)	-Experiment -2D heat transfer model (apparent heat capacity)	-Complete whole-day cycle of charging/discharging. -Reduced airflow rates increase the duration of melting/solidification processes. -Different heat capacity values along the PCM unit.	-Insufficient discharge period to assess the heating capacity of the PCM unit. -Neglecting thermal losses observed in experiment.
Zalba et al. (2004)	-Experiment -Empirical model	-Increased encapsulation thickness slow down heat transfer. -Reduced airflow rates increase the duration of melting/solidification processes. -Decreased ΔT increase the duration of melting/solidification processes. -Effect of air flow is greater while solidification.	
Marin et al. (2005)	-Experiment	-Using low conductivity encapsulation material with paraffin while ΔT is small to slow down heat transfer. -Reduction in outlet temperature of 4.0˚C during melting. -Achieving 9% additional initial cost and 9.4 times less power consumption.	-Using graphite matrix to enhance heat transfer while using low conductivity material as encapsulation.
Arkar et al. (2005; 2007; 2007)	-Experiment -2D heat transfer model (effective heat capacity)	-Considering heating/cooling rates in the apparent heat capacity model. -2.0 ACH LHTES system equals intensive night ventilation strategy. -1.0 – 1.5 kg of PCM per 1.0m^3/h of needed fresh air for free cooling. -6.4 kg of PCM per unit floor area for free cooling.	-Assumption of porous percentage for spheres encapsulation. -Not efficient for long-term application.

Dolado et al. (2011)	-1D heat transfer model - Enthalpy method	-Relationship between heat transfer and most of system parameters. -Considering the heat transfer through encapsulation layer.	-Neglecting the temperature gradient in air flow direction (1D model).
Nagano et al. (2004)	-Experiment -1D heat transfer model - Enthalpy method	-Maximum heat energy obtained during melting is proportional to ΔT.	-Small latent heat storage of granules. -Model showed some differences in temperature change while phase change.
Waqas and Kumar (2011a; 2011b)	-2D heat transfer model (enthalpy)	-Performance is a function of inlet and phase change temperatures. -Outlet temperature stabilized around thermal comfort in hot dry climate.	-Short term investigation (24h). -Adaptive thermal comfort model.
Stritih and Butala (2007; 2010)	-Experiment -2D heat transfer model (enthalpy)	-Enhanced performance with temperature difference during charging greater than 10.0˚C.	-Low system storage capacity due to reduced charging energy.
Osterman et al. (2015)	-Experiment -2D heat transfer model (enthalpy) -CFD modelling	-Both heating and cooling performance (annual application). -Reduction of 142kWh of annual energy consumption.	
Mosaffa et al. (2013b; 2014)	-2D heat transfer model (effective heat capacity)	-Significant difference between PC temperatures of different parts of multi-PCM system should be satisfied to maintain system performance.	
Panchabikesan et al. (2018; 2017)	Experiment	- Conduct of charging experiments under real time ambient conditions of hot-dry and moderate climate respectively. - Integration of evaporative cooling unit with the PAHX and increased the temperature driving potential between the PCM and the inlet air (heat transfer fluid).	- Not considering the auxiliary power consumption of fan and the pump.

CHAPTER THREE: EXPERIMENTAL INVESTIGATION

3.1.Research Concept

One of the possible effective passive techniques is utilizing the radiative cooling during PCM solidification using the sky as the heat sink; this concept has not gained much attention from the scientific communities especially in the hot desert climate. The full exposure to the sky promotes long-wave radiative heat exchange between the sky and the free cooling system. Thus, thermal losses during cooling charging of the system can be magnified by long-wave radiation under clear sky conditions, specially with large drop of the sky temperature that could reach more than 15˚C lower than ambient air temperature during night-time and early morning periods (Onishi et al., 2009; Adelard et al., 1998). Some advancements were obtained by utilizing the long-wave radiation to the cold sky as previously indicated in Section 2.3.5. The reviewed studies in Chapter two reported the insufficient cooling charging energy of the PAHX units during the solidification phase of the PCM which affects the overall system performance. The main idea of the ongoing research is to develop a PAHX unit for building envelope applications to increase the cooling charging energy by magnifying the radiation thermal losses to the atmospheric environment during PCM solidification process.

The developed PAHX idea is more appropriate for building envelope applications which promote better exposure to the sky. It is worth mentioning that the system is not a part of building envelope construction. However, it can be applied and integrated with newly constructed envelopes and existing envelopes in renovation projects as well. One of the limitations of this concept is the large solar gains during daytime. Accordingly, a proper operational control strategy is essential to ensure the system workability for cooling purposes. In this chapter, experimental investigations were conducted to study the effect of system exposure to the night-time sky during PCM solidification period on the cooling charging energy of the system. The thermal behavior of the developed PAHX system was evaluated utilizing different operational modes. Special key performance indicators were proposed to analyze the experimental results and conclude the experimental findings.

3.2. Developed PAHX System Design

The proposed system is a PAHX unit that consists of PCM panels in contact with an internal air channel where the air flows and the desired heat exchange occurs. The used panels can consist of

macro or micro-encapsulated PCMs in dependence to the application. The main concept of the system, presented in Figure 26, is to arrange the PCM panels side by side to face the sky to magnify the effect of thermal radiation exchange between the PCM panels and the sky (radiative discharging to the sky). An external air cavity can be created by adding a glazing panel over the PCM panels to limit the effect of the convection heat transfer between the panels and the ambient environment; thus, the study of the stand-alone effect of the thermal (long-wave) radiation can be relevant and reliable. Therefore, as shown in Figure 27, two configurations were proposed: 1- exposed to the Ambient conditions configuration (config-A) which allows both convection and thermal radiation exchange between the PCM panels and the ambient environment, and 2- Glazed configuration with an air cavity (config-G) which allows the thermal radiation exchange with limited convection heat exchange with the ambient environment. The targeted heat exchange between the PCM panels and air occurs at the internal air channel. The proposed system can be used for horizontal (roof applications) and vertical (facade applications) orientations.

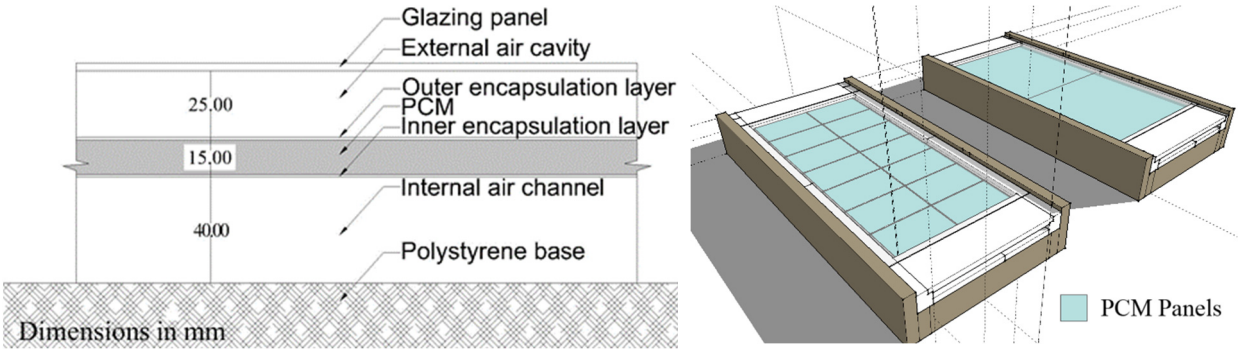

Figure 26. The developed PAHX system for building envelope applications

The system is mainly designed for free cooling applications where the layout of the panels allows the radiative thermal losses to the sky. The purpose of the developed design is to maximize the cooling charging energy of the system (during PCM solidification process during night-time and early morning) to increase the overall cooling performance during the system operation. During cooling applications (cooling discharging/melting of the PCM), the solar radiation should be blocked by means of insulation; thus, the heat transfers between the air and the PCM inside the air channel resulting in cooled air that can be supplied directly to spaces to satisfy cooling loads (direct free cooling application). In case the cooled air is not within the thermal comfort range or cannot satisfy the cooling loads by direct supply, it can also be introduced to the mechanical cooling

system to reduce energy consumption for cooling purposes. It is worth mentioning that the PCT of the system should be carefully selected according to the ambient air temperature profile during operation of the system.

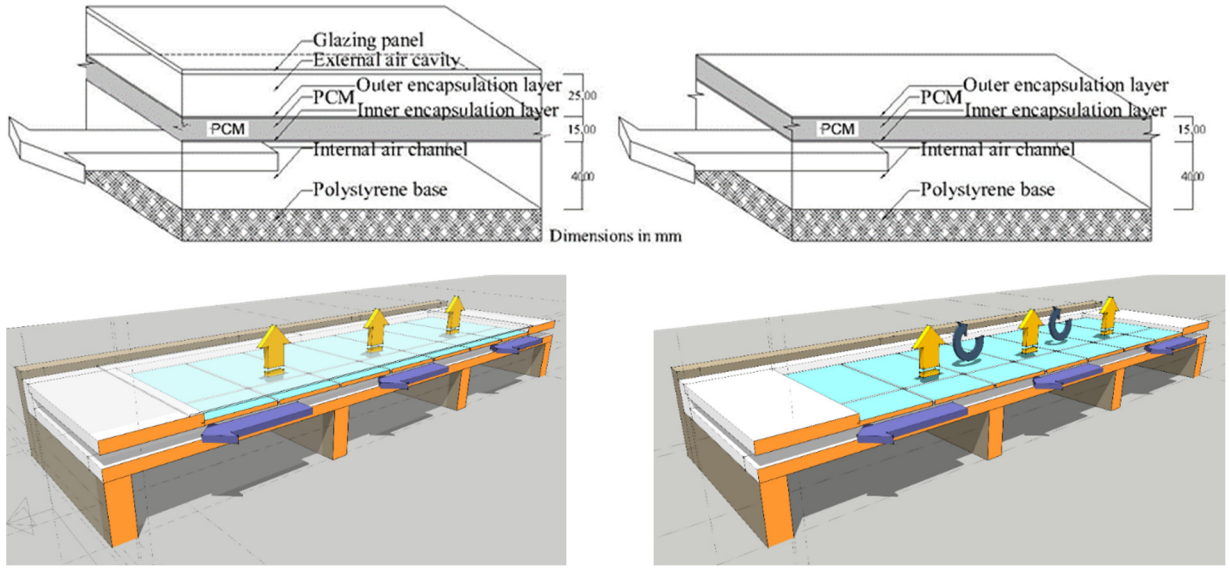

Figure 27. The configurations of the proposed PAHX system: config-G (left), config-A (right)

3.2.1. Prototype Design

Two full-scale prototypes were proposed for the developed PAHX system to investigate the thermal behavior of the new PAHX type applying the concept of thermal radiation losses to the sky. The two prototypes were designed using two different kinds of PCMs with different PCT ranges. The two prototypes were identical in terms of construction materials, dimensions and configuration. The type of PCM panels was the only difference between the two prototypes which were distinguished by the notation 'prototype 01' and 'prototype 02'. Organic PCM RT44HC was used in prototype 01; microencapsulated PCM composite panels were used in prototype 02. Full design and dimensions are provided in Figure 28. The external dimensions of the two prototypes were 2,610 × 1,210 mm. The internal air channel was 1,060 mm in width and 40 mm in height. Entry and exit regions were designed to regulate the supply airflow. In the current experimental investigation, the airflow was let to be natural under wind-driven forces. The glazing panels were 3 mm transparent polymethyl methacrylate (PMMA) thick panels (BLOX, 2019) with dimensions of 2,100 × 1,000 mm. The PMMA panels were designed to totally cover the PCM panels and form an airtight cavity with a thickness of 25 mm. Thus, the exposed PCM panels to the ambient

environment (without the glazing panels) were used in the configuration (config-A), and the glazing panels were applied to the system to form the configuration (config-G). Both configurations were applied to the two prototypes.

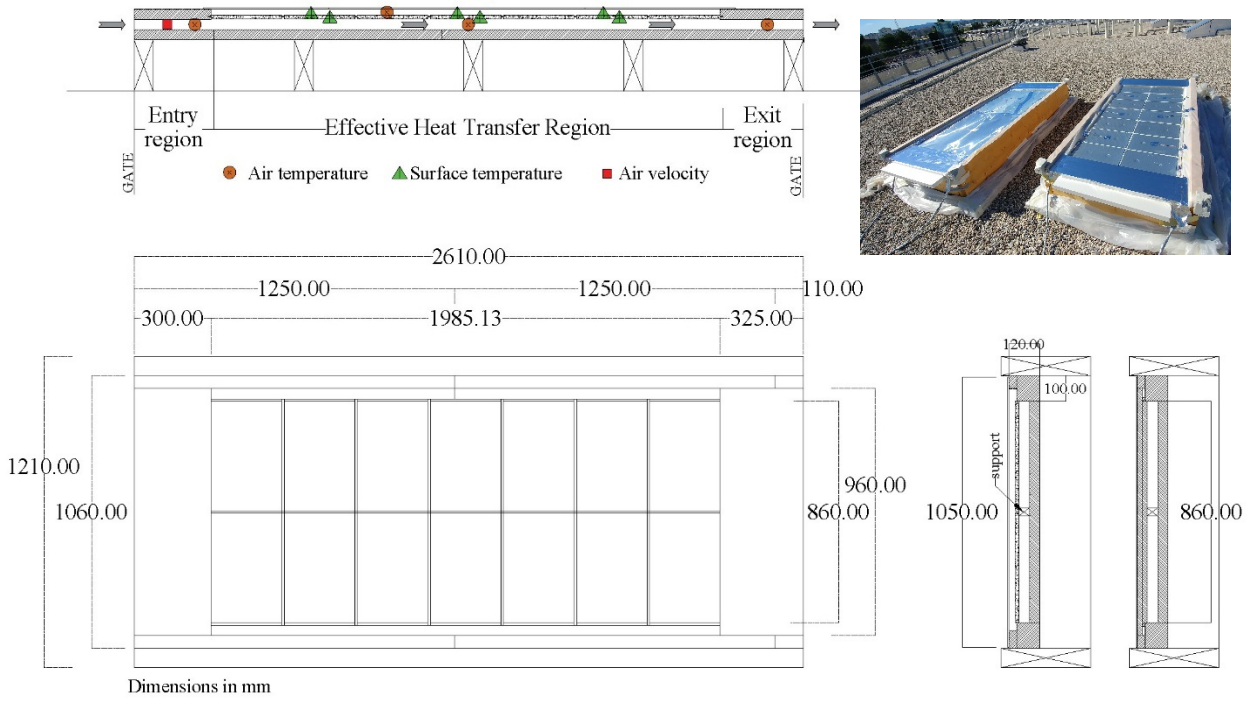

Figure 28. Design and dimensions of the proposed prototypes

The two prototypes were constructed from wood frames as main structure elements and polystyrene sections, as shown in Figure 29. The wood sections were designed to minimize the effect of wind and gusts on the system. They also kept the system away from direct contact with the roof floor to limit the effect of condensation during rainy days. All the wood sections were painted with an anti-humidity overlay to reinforce their surfaces against the outdoor weather conditions. Furthermore, the polystyrene sections were used as secondary structural elements to support the PCM panels in both prototypes and to keep the internal air channel with the needed dimensions. The polystyrene sections were chosen with appropriate thermal insulation properties to thermally insulate the system through undesired directions. The PCM panels were kept supported with the help of small wooden sections to maintain the internal air channel with a height of 40 mm and prevent any bending effect in panels. A protective layer was applied to all exposed polystyrene sections to increase their resistance to the weather conditions. A silicon paste was used in-between all the connections of the system to ensure the airtightness of the internal air channel

and external air cavity and to protect them from any possible water leakage during rainy days. A 50 mm layer of Rockwool insulation sheet (thermal resistance of 2.85 m²K/W) was selected to be applied to the top of the system to control the undesired thermal losses and gains by radiation and convection to and from the ambient environment respectively.

Figure 29. Main construction elements (wood and polystyrene sections) for both prototypes

3.2.2. Phase Change Material

- *Macro-encapsulated PCM panels*

Table 8. Thermal properties of RT44HC (Rubitherm, 2019)

Melting range (*heating*)	41 – 44 (*peak of 43*)	˚C
Solidification range (*cooling*)	44 – 40 (*peak of 43*)	˚C
Thermal storage capacity*	250 (±7.5%)	kJ/kg
Heat capacity	2	kJ/kg.K
Density	800 (*solid*)	kg/m^3
	700 (*liquid*)	kg/m^3
Thermal conductivity	0.2	W/m.K
Volume expansion	12.5	%

**Combination of latent and sensible heat in a temperature range of 35˚C to 50˚C*

The PCM used in prototype 01 was a macro-encapsulated organic PCM into Compact Storage Modules (CSM), a product of RUBITHERM (2019). The used PCM panels were aluminum cases filled with an organic PCM RT44HC with a PCT range of 40 ˚C – 44 ˚C. They were used due to their assembling flexibility that enables a variety of applications. One of the strongest advantages of using these modules was that the phase change occurs within the case volume. This enables a ready-to-use system component in building applications with a stable and strong housing. Besides, the aluminum, as an encapsulation material, ensured a high thermal conductivity. The housing also provided inner and outer anticorrosive coating, quick installation, fixed volume, and easy cleaning. The overall dimensions of a single panel were 450 × 300 mm. The effective area filled with PCM

was 425 × 275 mm, with a thickness of 15 mm. In the current study, 14 PCM panels were used in prototype 01. The average weight of the used panels was 1.382 kg/panel at their solid state. The organic PCM RT44HC provided high thermal storage capacity with stable thermal and chemical behaviors. Detailed properties are provided in Table 8. Figure 30 shows the enthalpy cooling and heating curves provided by PCM manufacturer. These curves will be used for further numerical modeling investigations for prototype 01.

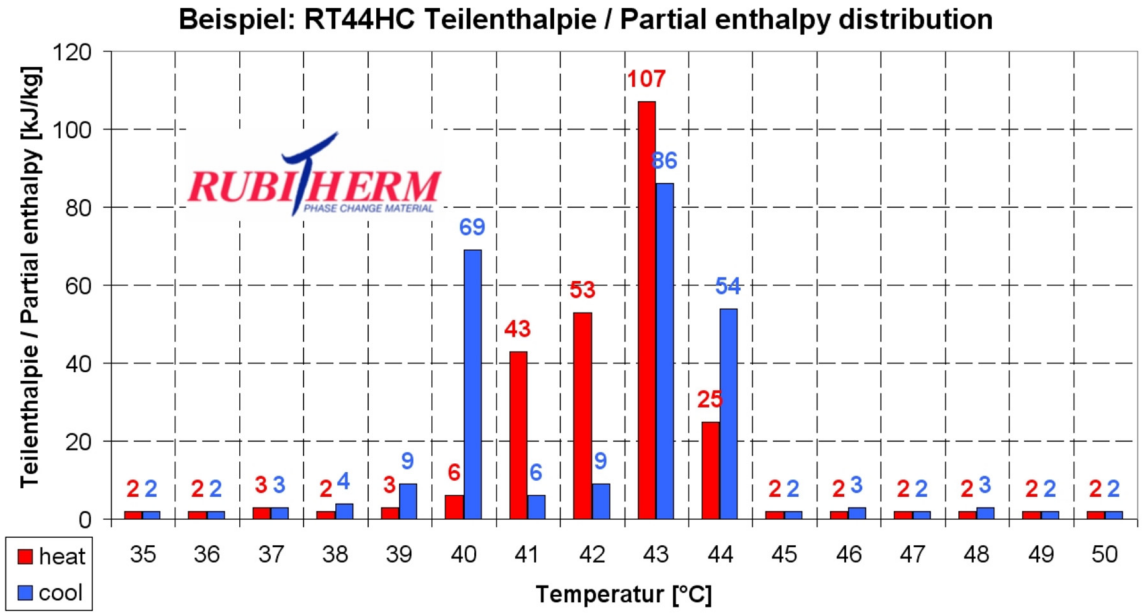

Figure 30. Enthalpy-temperature curves (heating and cooling) for RT44HC (Rubitherm, 2019)

- *PCM composite wallboards*

In prototype 02, a different type of PCM panels, *DuPont™ Energain®* (Kuznik and Virgone, 2009; Joseph A. King Jr., 2010; DuPont, 2012; Borderon, Julien, 2012), was used. The used PCM panels were composite wallboards that consisted of a mixture of 60% microencapsulated paraffin-based PCM and 40% ethylene-based polymer. The mixture was encapsulated in aluminum laminated highly reflective sheets of a thickness of 0.1 mm. The overall dimensions of the panels were 1,000 × 1,000 × 5 mm. Detailed thermophysical properties of the panel are provided in Table 9. Originally, this kind of panel is used for interior cladding to increase the thermal mass of the building envelope to enhance the indoor thermal performance. However, in this study, the panels were used directly in the PAHX system. Therefore, every two panels were attached together to form one panel of the thickness of 10 mm in order to increase the panel rigidity and thermal

storage. This kind of panels is distinguished with flexibility of installation, fire resistance and shape stabilizing where there is no possible leakage during melting phase due to the microencapsulation technology of the PCM. Figure 31 shows the enthalpy cooling and heating curves. These curves were experimentally obtained by the research group of Lleida University, Spain with a heating/cooling rate of 0.5 ˚C/min (Borderon, Julien, 2012).

Table 9. Thermal properties for *Energain* panels (DuPont, 2012; Borderon, Julien, 2012)

Phase change range	18 – 24	˚C
Latent heat storage capacity	72	kJ/kg
Thermal storage capacity*	140	kJ/kg
Heat capacity	2.5	kJ/kg.K
Density	900	kg/m^3
Thermal conductivity	0.22 (*liquid*)	W/m.K
	0.18 (*solid*)	W/m.K

**Combination of latent and sensible heat in a temperature range of 15˚C to 30˚C*

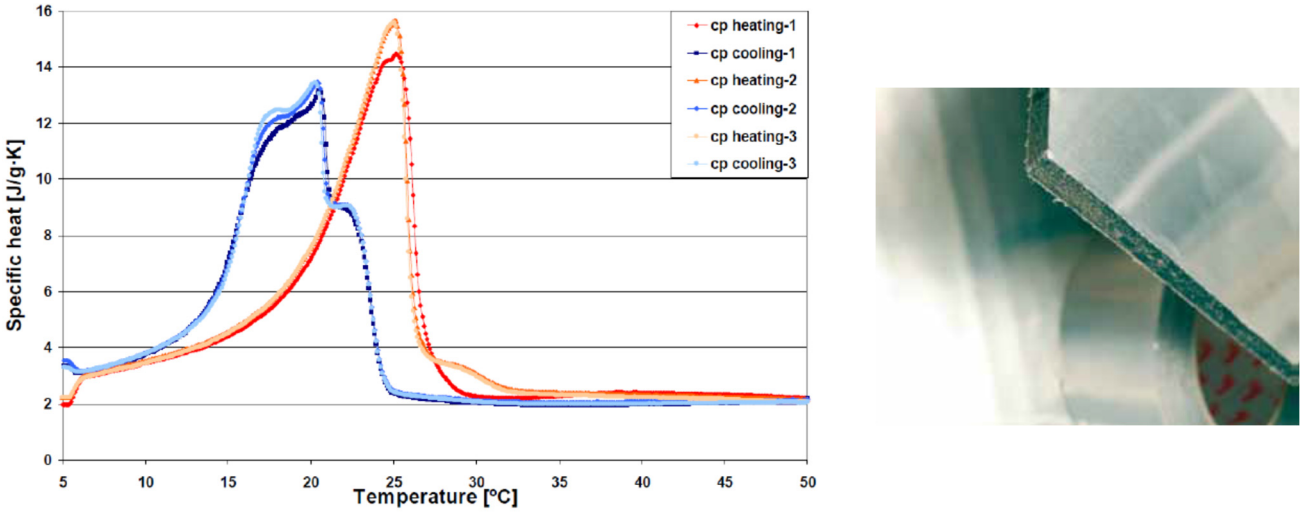

Figure 31. Enthalpy-temperature curves (heating and cooling) for *Energain* panels (Borderon, Julien, 2012)

3.3. Experimental Setup

3.3.1. Location and Climate

The experiment was conducted during the summer and fall seasons of Lyon, France. According to Köppen-Geiger climate classification (Kottek et al., 2006), Lyon is classified as *Cfb* climate which is characterized with a warm temperate climate and a warm and humid summer. It is worth mentioning that the experiments did not aim to evaluate the cooling or heating performance of the system under the temperate climate. Instead, they investigated the thermal behavior of the system

under a real case application that could promote the system application in hotter and drier climates. All the weather measurements and records were monitored by IDMP weather station (Station IDMP: Vaulx-en-Velin, 2019) which is located at the following coordinates: latitude: 45° 46' 43" N, longitude: 4° 55' 21" E, and an elevation of 170 m above the sea level. Solar radiation, air temperature, relative humidity, wind direction, and wind velocity were measured by the weather station. All the weather data were measured every 1 minute as a time step. The preparation, design, and construction of the experiments started in April 2018 for investigations during the summer and fall seasons. The experimental prototypes were constructed to provide a direct contact with the ambient environment and full exposure to sky conditions (with minimum obstacles to the sky), and where the system monitoring and electrical and data connections were available.

3.3.2. Instruments and Measuring Tools

Three parameters were monitored in the experiments to evaluate the thermal behavior of the system: PCM panels surface temperature (inner and outer surfaces), the air temperature, and the air velocity in the internal air channel. In total, 28 temperature sensors were used in both prototypes. 20 of them were assigned to measure the surface temperature of the panels, and 8 were assigned to monitor the air temperature in the internal air channel and the external air cavity. The temperature sensors were applied to the inner and outer surfaces of the panels measuring the surface temperature with the distribution shown in Figures 32 to 34. Also, six temperature sensors were installed at the inlet, middle, and outlet of both air channels of the two prototypes. Additionally, two sensors were applied at a middle position of the exterior air gap (directly under the glazing) of the two prototypes.

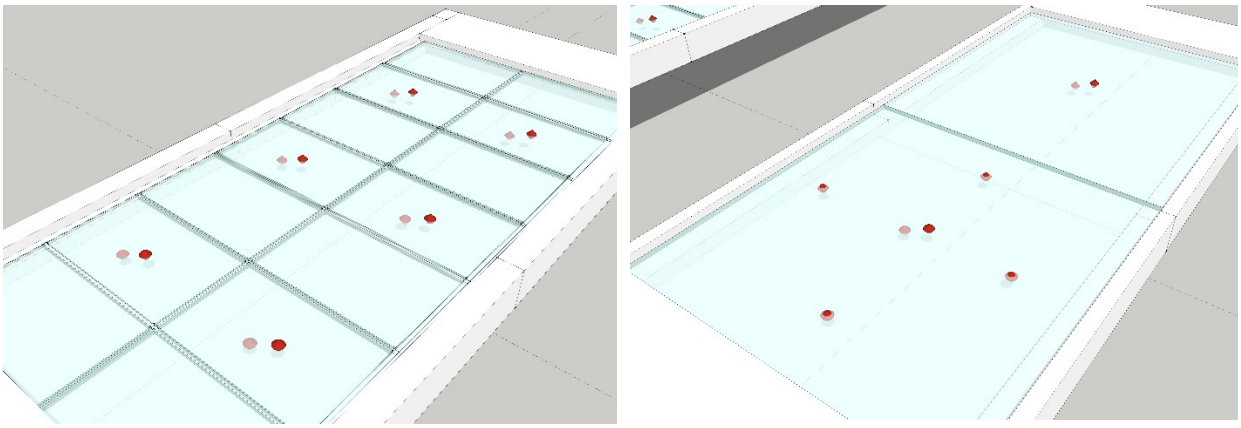

Figure 32. Sensors distribution plan for prototype 01 (left) and prototype 02 (right)

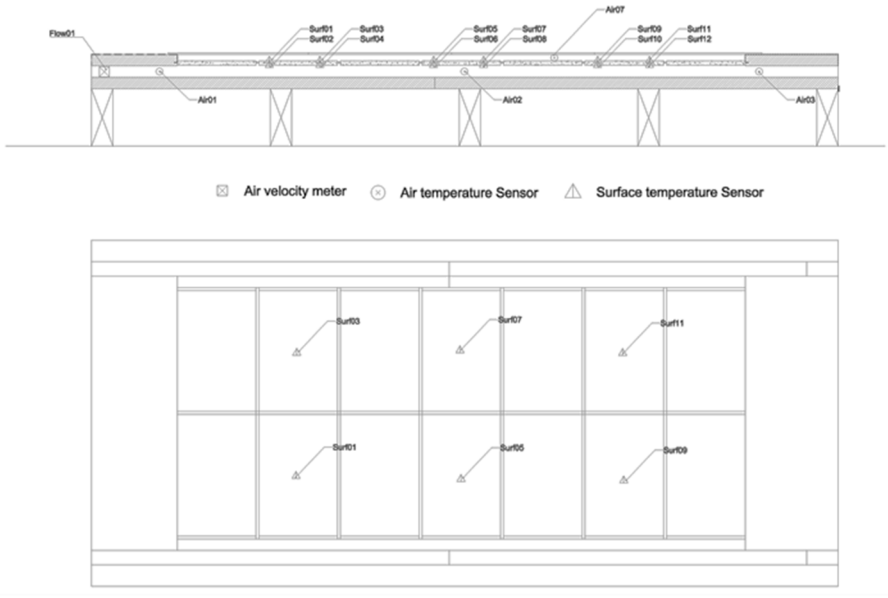

Figure 33. Detailed sensors distribution plan for prototype 01

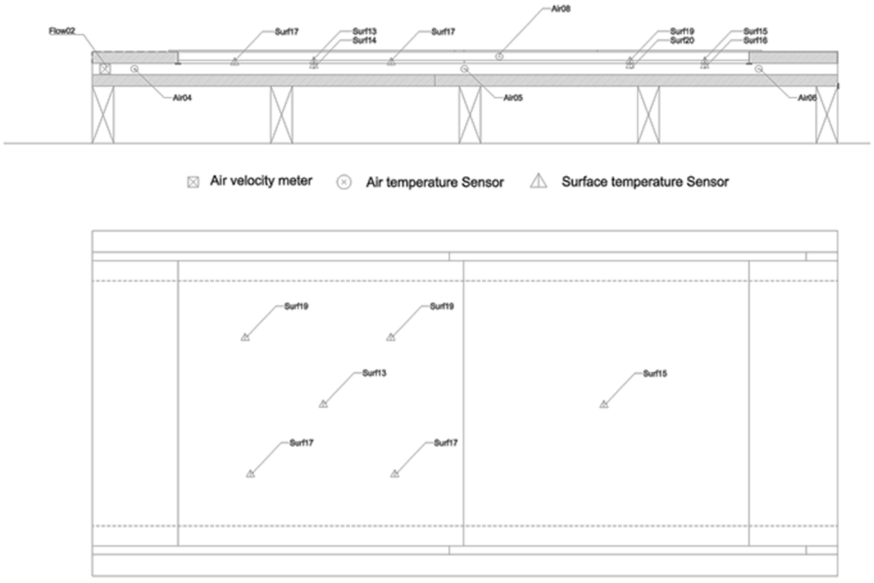

Figure 34. Detailed sensors distribution plan for prototype 02

All the used temperature sensors were Resistance Temperature Detectors (RTDs) PT100[1] – 3 wires sensors. The used RTD PT100 sensors had an accuracy of ± 0.1˚C (between -10.0˚C and 85.0˚C) (Bahrar, Myriam, 2018). In addition, two air velocity meters were installed at the inlet of the air channels of the two prototypes. The used velocity meters were omnidirectional air velocity

[1] Platinum RTD with a resistance of 100 ohms at 0°C

transducer (model 8470, by TSI Inc.) with maximum detection speed range of 5 m/s (TSI-Incorporated, 2019). The sensors were connected to temperature input modules[2] that were connected to a compact data acquisition platform that transmitted the signals of the sensors with a time step of 20 seconds to the LabVIEW software. The software used a customized graphical interface to include all the measured data from both prototypes as shown in Figure 35. An illustration of the entire data acquisition system is shown in Figure 36. Due to different time steps between the weather station and the data acquisition system, a linear interpolation was applied to the obtained weather data to match the time interval of the experiments time step.

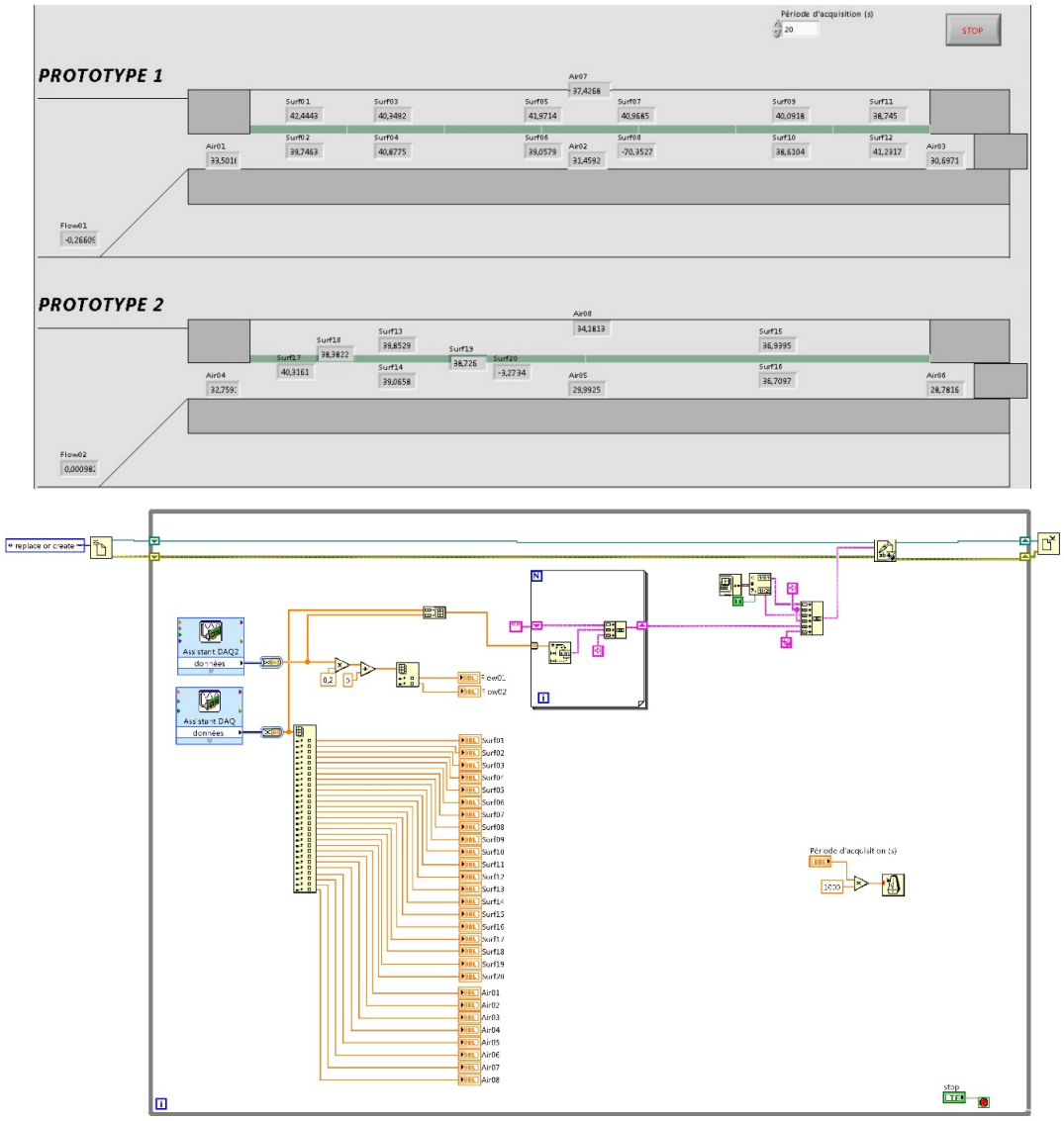

Figure 35. LabVIEW interface as data acquisition software

[2] C series temperature input modules - National Instruments ™ NI-9217

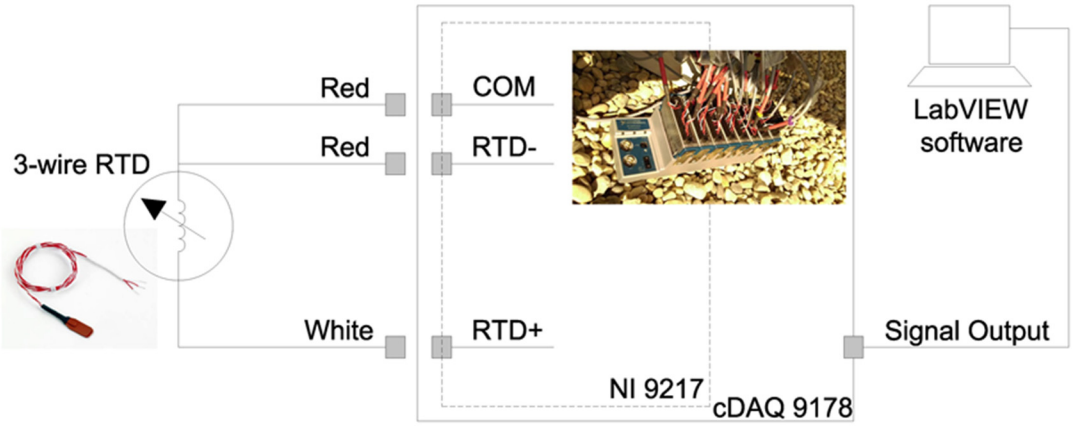

Figure 36. Data acquisition system

3.3.3. Experimental Scenarios

Several experimentation scenarios were investigated with different system configuration, internal airflow scenarios, and operating modes. For each prototype, the configuration without the glazing panel (config-A) and the configuration with the glazing panel (config-G) were considered. Also, the airflow inside the air channel was controlled by opening or closing both inlet and outlet of the air channel. The opening and closing of the air channel were manually operated by designed polystyrene sections. Also, the insulation sheet could be attached to the top of the system. Referring to the above-mentioned variables, six different scenarios were considered in the study of the thermal behavior of the system. The six scenarios are shown in Figure 37. The exposed configuration (config-A) had two different scenarios: the closed and the opened air channel (scenarios 1 and 2). The glazing configuration (config-G) had four scenarios: with the closed (scenarios 3 and 5) and with the opened (scenarios 4 and 6) air channel, and with the insulation layer attached (scenarios 5 and 6) or removed (scenarios 3 and 4).

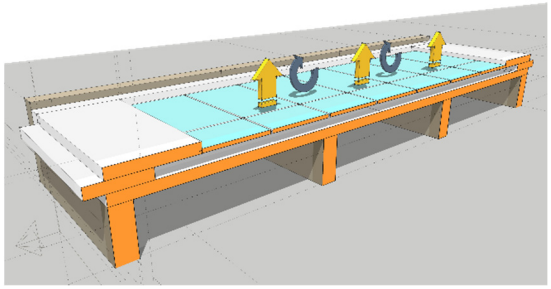

Scenario 1
- Config-A
- Air channel: closed
- Insulation: NO

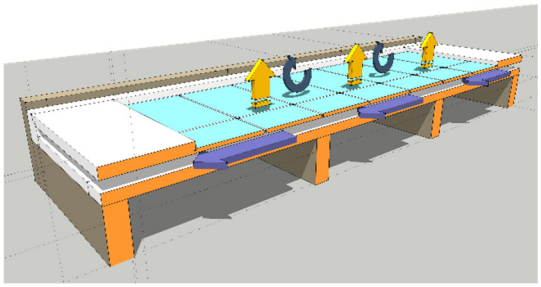

Scenario 2
- Config-A
- Air channel: open
- Insulation: NO

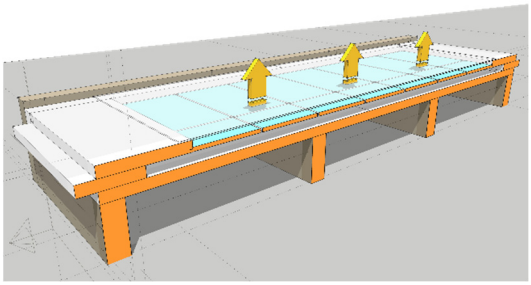

Scenario 3
- Config-G
- Air channel: closed
- Insulation: NO

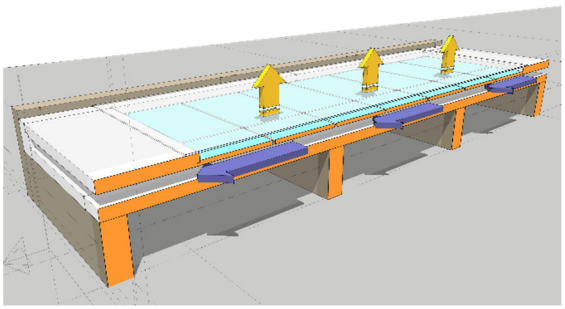

Scenario 4
- Config-G
- Air channel: open
- Insulation: NO

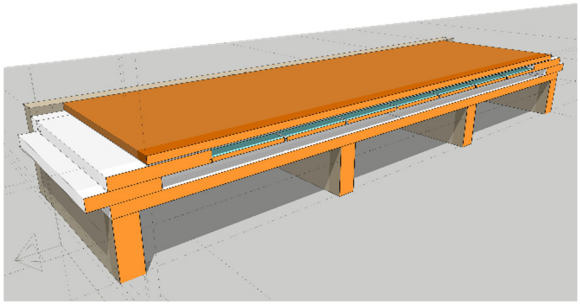

Scenario 5
- Config-G
- Air channel: closed
- Insulation: YES

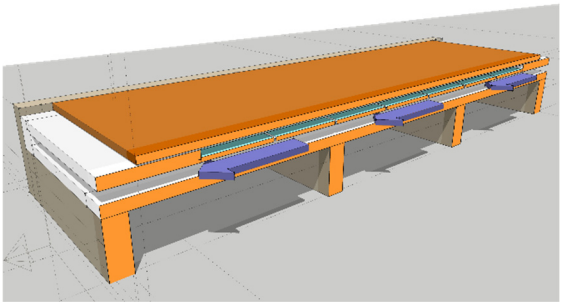

Scenario 6
- Config-G
- Air channel: open
- Insulation: YES

Figure 37. Experimental scenarios for field experimentation

3.4. Data Analysis - Key Performance Indicators (KPIs)

The experimental investigations were focused on the charging energy process during the cooling charging period including the PCM solidification. In order to evaluate the performance of the developed PAHX system, specific indicators were proposed based on previously identified Key Performance Indicators (KPIs) in (Del Pero et al., 2018) and (Haghighat, 2018). Prior to illustrate the analysis KPIs, some important definitions need to be clarified to better understand the data analysis procedure:

Cooling source: (or the heat sink) the source/environment to which the energy transferred from the system elements while solidification of the PCM. This cooling source differs due to the operational conditions of the experiment. It can be the ambient air, the atmospheric layer (the sky), or a combination of these sources.

Charging Latent storage capacity (C_l): the total latent energy that is stored in the system during PCM solidification (charging process) regardless the cooling source.

Storage capacity regarding the ambient air ($C_{t\text{-}amb}$): the maximum possible amount of energy (latent and sensible) that the system can store during charging process considering only the ambient air as the cooling source. This definition is important to be compared with the actual recharge energy that the system stores to elaborate the added energy to the system regarding other cooling sources (the sky).

PCM temperature (T_{pcm}): the average temperature of the inner and outer surface temperatures of the PCM panel. While the measuring sensors were only fixed on the panel surfaces, this average is considered to represent the PCM temperature inside the panel.

Solidification/Melting rate (˚C/h): the average rate of PCM solidification/melting considering the hourly average PCM temperature. The solidification/melting rate was taken for the whole period of the charging process regardless the charging duration.

Free heating mode: the experimental case in which the air channel was intentionally opened to warm up the inlet air. The experimental case was considered as free heating mode when the outlet air temperature was warmer than the inlet air temperature.

Standby mode: the condition in which the insulation layer was attached to the system and the air channel was closed (scenario 5 in the experimental scenarios). This mode aims at energy conservation of the system by minimizing the heat gain by convection and solar radiation or the heat loss by convection and thermal radiation.

The following proposed KPIs allow to evaluate and analyze the experimental data to better understand the behavior of the PAHX system. The KPIs were customized to meet the experiments objective and the certain operational modes of the experiments.

3.4.1. Latent Charging Power (P_l)

The latent charging power is the rate of the released energy (kW) of the system during the phase change of the cooling charging process regardless the cooling source. The latent charging power of the system was used considering the solidification rate to compare the charging behavior of various configurational conditions of the experiments. Due to different weather, operational, and

configurational conditions during the experiments, the solidification periods varied for each case. Accordingly, the total amount of latent energy (charging latent storage capacity) cannot be used for comparison between several cases. Instead, latent charging power can represent the storage abilities of the experimental cases. Regarding the experimental time step (Δt), the latent charging power (P_l) can be expressed as:

$$P_l = [\sum_{i=1}^{L} (m \,.\, Cp_i \,.\, (Tpcm_{i+\Delta t} - Tpcm_i))] / L \quad (kW) \tag{2}$$

Where m is the total PCM mass of the PAHX system, Cp_i is the heat capacity at a specific temperature and a time instance, $Tpcm_i$ is the PCM temperature during the phase change at a time instance, i is the time instance, and L is the duration of phase change in seconds. The Cp values were obtained using the apparent Cp method as will be illustrated in detail in the next chapter. This method assumes one fixed rate of cooling/heating along the system. The latent enthalpy of the material during its phase change was represented by the change in the Cp values during the solidification ($Cp_{cooling}$) and melting ($Cp_{heating}$) according to temperature-enthalpy curves of the material. By tracking the evolution of the PCM temperature, Cp values were calculated every experimental time step according to Equation 3. $Cp_{cooling}$ and $Cp_{heating}$ were obtained from the PCM temperature-enthalpy curves, and their values were interpolated over the entire range of temperatures.

$$Cp_i = \begin{cases} Cp_{cooling} & if\ Tpcm_i \geq Tpcm_{i+1} \\ Cp_{heating} & if\ Tpcm_i < Tpcm_{i+1} \end{cases} \tag{3}$$

3.4.2. Cooling Recharge Energy (C_r)

The recharge energy (kWh) is the total energy (both latent and sensible) that is stored in the system during the cooling charging process. The cooling recharge energy differed due to the cooling source, charging duration, and operational and configurational conditions. In contrast to storage capacity regarding ambient air ($C_{t\text{-}amb}$), the cooling source affects the value of the recharge energy (C_r). The total recharge energy (C_r) can be represented as:

$$C_r = \sum_{j=1}^{n} [\sum_{i=1}^{j} (m \,.\, Cp_i \,.\, (Tpcm_{i+\Delta t} - Tpcm_i))]/3600 \text{ (kWh)} \tag{4}$$

Where $Tpcm_i$ is the PCM temperature during the entire charging process at a time instance, j is the number of the measurements for one hour, and n is the duration of the charging process in hours.

3.4.3. Charging Performance Indicator (CPI)

Another important KPI for investigating the charging abilities of the PAHX system is the Charging Performance Indicator (CPI). CPI can be defined as the ratio between the actual stored energy during charging process (C_r) and the maximum storage capacity regarding the ambient air ($C_{t\text{-}amb}$), as illustrated in Equation 5. This KPI declares the increased charging energy that was stored in the system due to other cooling sources than the ambient air (sky temperature in case of cooling charging process). CPI is important to evaluate the idea of the developed type of PAHX that was claimed to increase the cooling charging abilities by the exposure to the sky temperature during the cooling charging process. Thus, CPI could give an indication for the storage abilities and performance of the whole system when is used for cooling applications.

$$CPI = C_r / C_{t\text{-}amb} = [(Tpcm_{j(max)} - Tpcm_{j(n)}) / (Tpcm_{j(max)} - Tamb_{j(min)}) \times 100] - 100 \ (\%) \quad (5)$$

In Equation 5, $Tpcm_{j(max)}$ is the hourly average temperature of the PCM for the first hour of the charging process which represents the maximum value of PCM temperature, $Tpcm_{j(n)}$ is the hourly average temperature of the PCM for the last hour (n) of the charging process which represents the minimum value of PCM temperature. $Tamb_{j(min)}$ is the minimum hourly average temperature of the ambient air during the charging process. For practical applications, $Tpcm_{j(n)}$ and $Tamb_{j(min)}$ may not be within the same hour. Whereas the objective of this indicator was to indicate the increased charging energy regardless the duration of the charging process, the calculations considered the minimum values of the PCM and ambient air temperatures whether they were during the same hour or not.

3.4.4. Increased Charging Energy

This KPI is related to the previous indicator (CPI); it indicates the added energy to the system regarding the sky temperature as an extra cooling source. The increased charging energy is the difference between the actual stored energy during charging process (C_r) and the maximum storage capacity regarding the ambient air ($C_{t\text{-}amb}$), as indicated in Equation 6. The temperature difference between the minimum hourly average temperature of the PCM and the minimum hourly average

temperature of the ambient air during the charging process was the indicator of the increased charging energy to the system.

$$C_r - C_{t\text{-}amb} = m \,.\, Cp \;.\; \left(Tamb_{j(min)} - Tpcm_{j(n)}\right) / 3600 \text{ (Wh)} \quad (6)$$

3.4.5. Discharging Performance

The performance of the discharging was indicated by the effective temperature difference between the hourly average temperature of the outlet air ($Ta_{j(outlet)}$) and the hourly average temperature of the inlet air ($Ta_{j(inlet)}$) during discharging regardless the thermal losses from the system. The rate of discharging (δT) was defined regarding the duration of discharging (n) as:

$$\delta T = \left(\sum_{j=1}^{n} \left(Ta_{j(outlet)} - Ta_{j(inlet)}\right)\right)/n \quad (^{\circ}C/h) \quad (7)$$

3.5. Experimental Results and Discussion

The investigations were conducted using some experimental scenarios to monitor the system temperature during the PCM solidification phase. The temperature of the air channel and the surface temperatures of the PCM panels (outer and inner surfaces) were monitored. The investigations were conducted to mainly assess the cooling charging energy of the system. Generally, the lower the panel surface temperature could reach in the system, the higher the charging energy achieved by the system.

3.5.1. Results of **Prototype 01**

The experimental scenario 1 (config-A (exposed to ambient) with a closed air channel) was applied under clear sky conditions. The experiment started when the PCM was in the mushy phase with a temperature of around 43 ˚C, where the PCT range of prototype 01 is (40 ˚C - 44 ˚C). The phase change (PCM solidification) continued for 3 hours under both effects of radiation and convection thermal losses due to the exposure to the ambient conditions. As noticed in Figure 38, at the beginning of the experiment, the ambient temperature was around 14 ˚C lower than the PCM temperature. It can be noticed that panel and channel temperatures dropped below the ambient profile by up to 4 ˚C after 5 hours of the cooling charging process. During a cooling charging time of 10 hours (during night and early morning), the system maintained its temperature lower than the ambient air temperature. The increase in cooling charging energy was calculated regarding

PCM and ambient air temperatures as it will be discussed later. The minimum recorded panel temperature was 15.8 ˚C when the ambient air temperature was 19.7 ˚C.

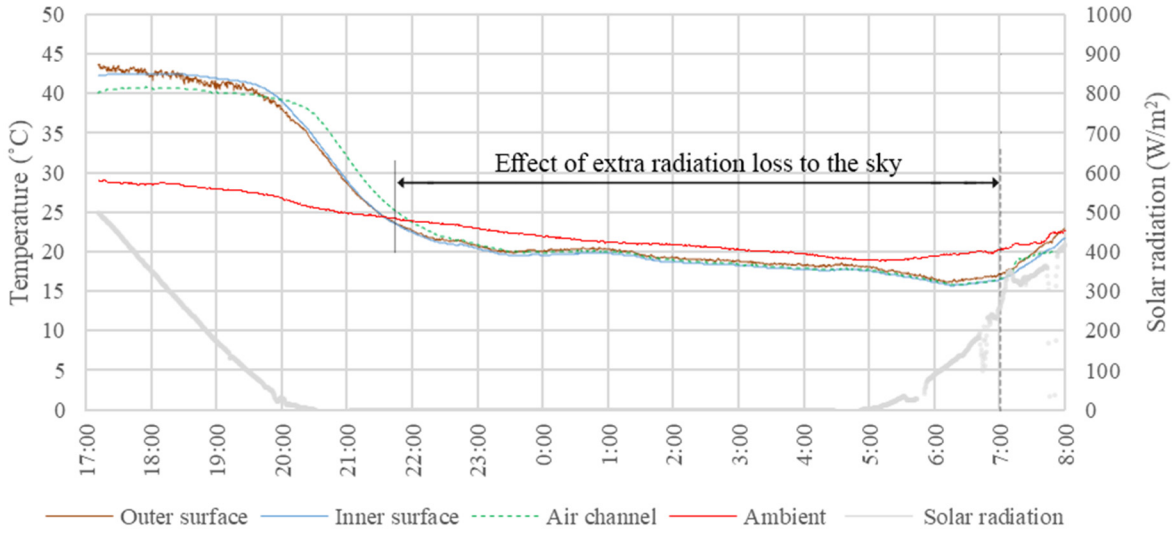

Figure 38. Cooling charging investigation for prototype 01 _ scenario 1

The cooling charging investigation was repeated applying scenario 2 (config-A and opened air channel) under cloudy conditions. As expected, the convection effect was magnified (due to the internal airflow) and the radiation effect was limited (due to limited exposure to clear sky). Therefore, it can be noticed in Figure 39, that the PCM panel temperature respected the ambient air profile without an extra effect of the radiation losses to the sky during the charging period (night-time and early morning).

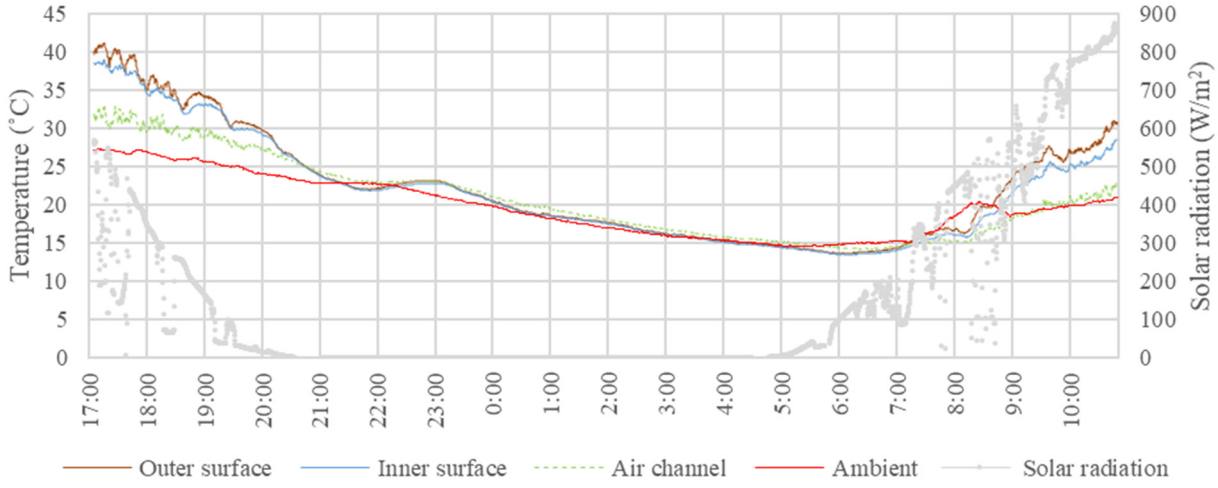

Figure 39. Cooling charging investigation for prototype 01 _ scenario 2

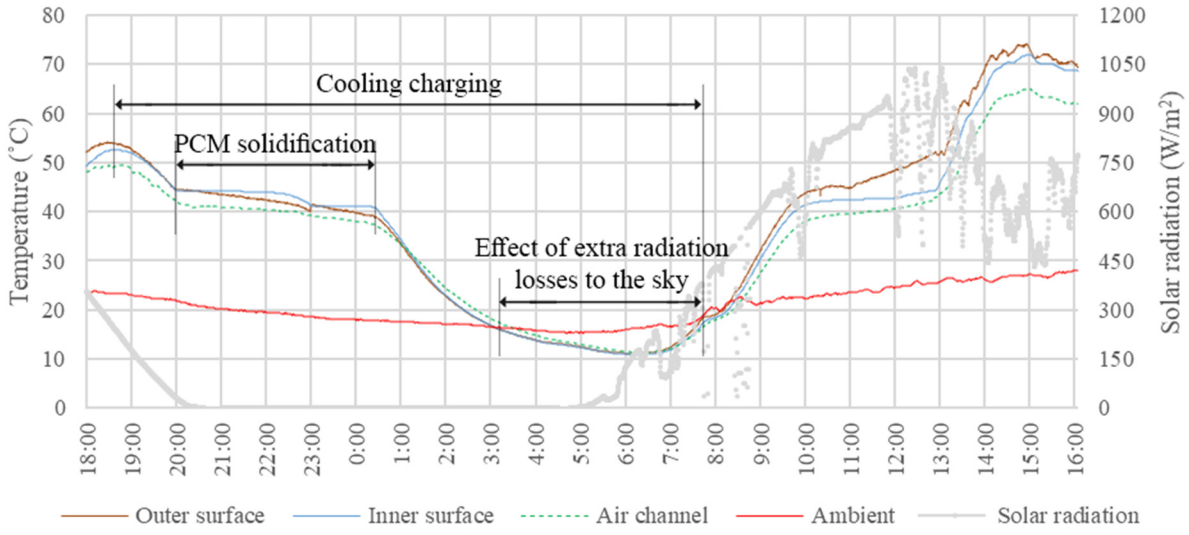

Figure 40. Cooling charging investigation for prototype 01 _ scenario 3

Scenario 3 (glazed configuration, config-G, and closed air channel) was applied under clear sky conditions. During the cooling charging period, prototype 01 showed a better performance in terms of the low temperature the system could reach due to the radiation thermal losses to the sky. The overall charging process was slower than config-A due to the glazing effect. However, both the panel and air channel temperatures reached up to 5 ˚C lower than the ambient air profile, as noticed in Figure 40. The minimum temperature during charging process was 10.8 ˚C while the ambient air temperature was 16.2 ˚C. It can be concluded that, due to the greenhouse effect, extra heat gains during the daytime, and the nature of radiation heat transfer, the rate of heat transfer/thermal loss was reduced where the system required a longer duration to solidify the PCM than scenario 1. However, more charging power can be expected if longer charging duration is available. This means that with longer night periods (the case of hot desert climate for example), the system is expected to gain more cooling charging power during cooling charging process.

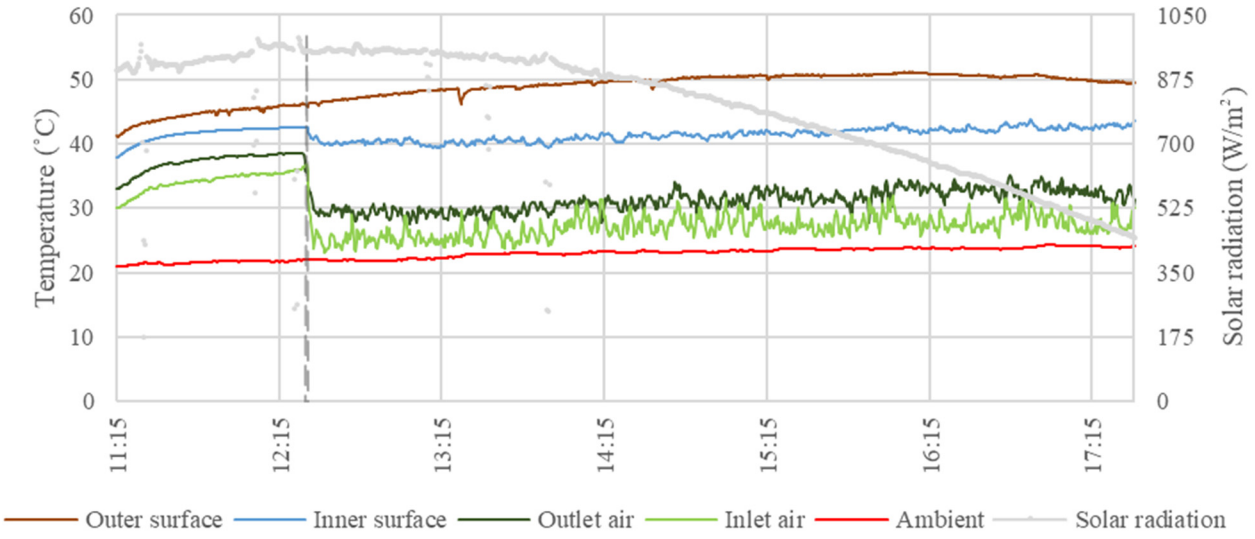

Figure 41. Free heating investigation for prototype 01 _ scenario 4

Scenario 4 (config-G and opened air channel) was applied during the daytime for a free heating application. Figure 41 shows that during 5 hours of application, the continuous heat gain by solar radiation maintained the panel temperature compensating the thermal losses by convection to the ambient air. During this application the inlet air temperature was around 22 ˚C, while the outlet air temperature reached up to 5 ˚C warmer than the inlet profile. When the insulation was added to the system (scenario 6) during the PCM solidification, the thermal behavior of the system was assessed for another free heating application, as shown in Figure 42. During around 14.5 hours of application (from 18:15 to 08:45), the system maintained the outlet air temperature warmer by up to 14 ˚C than the inlet temperature profile. It can be noticed that the phase change occurred within 10 hours (from 19:00 to 5:00) till complete solidification due to the reduced heat transfer to the environment and the blocked thermal radiation exchange to the sky due to the insulation layer. The higher heating performance of the system can be noticed with lower air velocity inside the air channel, as shown in Figure 43. During the charging process between 22:30 to 7:30, the average air velocity was 0.3 m/s.

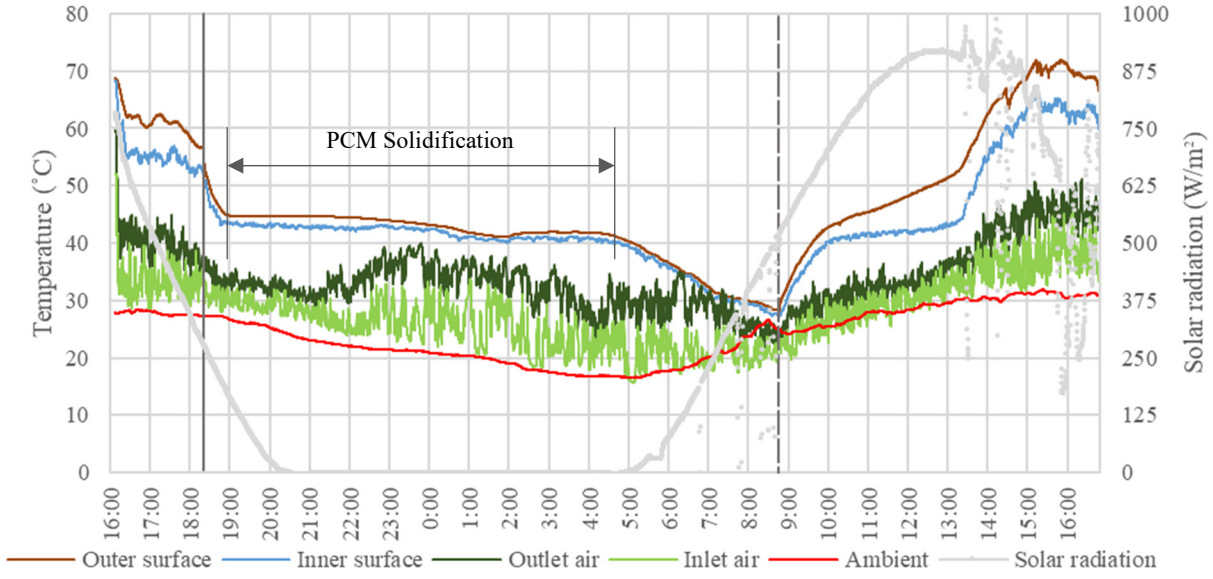

Figure 42. Free heating investigation for prototype 01 _ scenario 6

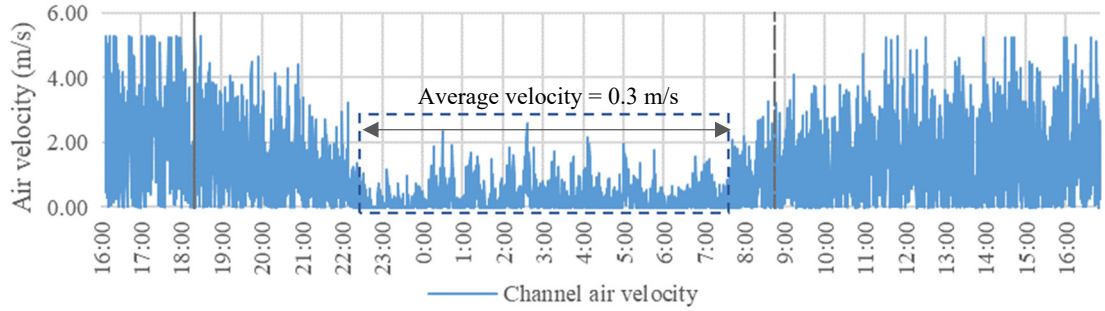

Figure 43. Air velocity inside the air channel for the application in Figure 42

3.5.2. Results of **Prototype 02**

Generally, the low thermal properties of prototype 02 were due to the microencapsulation technology used in the panels manufacturing. Accordingly, it can be noticed while applying scenario 1 (config-A and closed air channel), as shown in Figure 44, the inner surface temperature of the panel was warmer than the outer surface temperature. Although the application was under clear sky condition, the ambient temperature was not as low as required to charge the system, as the difference between the PCT range of the PCM panels and the ambient air profile (minimum temperature of 18.8 ˚C) was insufficient to completely solidify the PCM. When scenario 2 was applied (config-A and opened air channel), the experiment was under partially cloudy conditions. However, the magnified effect of the convection thermal losses to the ambient air and the sufficient low ambient air temperature profile (minimum of 14.5 ˚C) maximized the thermal losses during

the cooling charging process allowing complete solidification for the PCM panel. As illustrated in Figure 45, the phase change occurred during around 5 hours of the application.

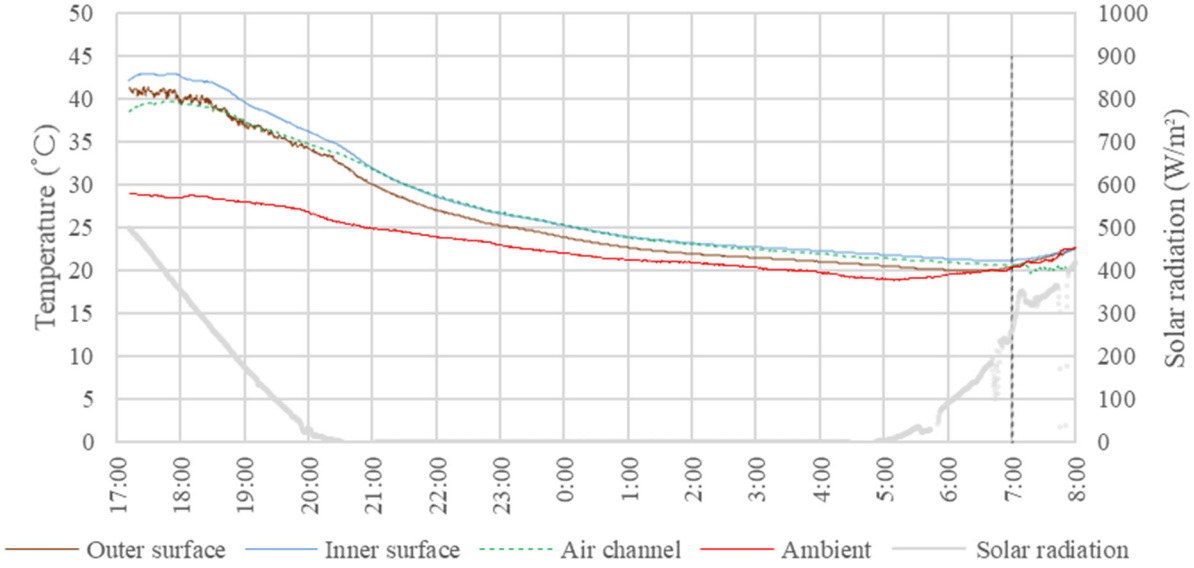

Figure 44. Cooling charging investigation for prototype 02 _ scenario 1

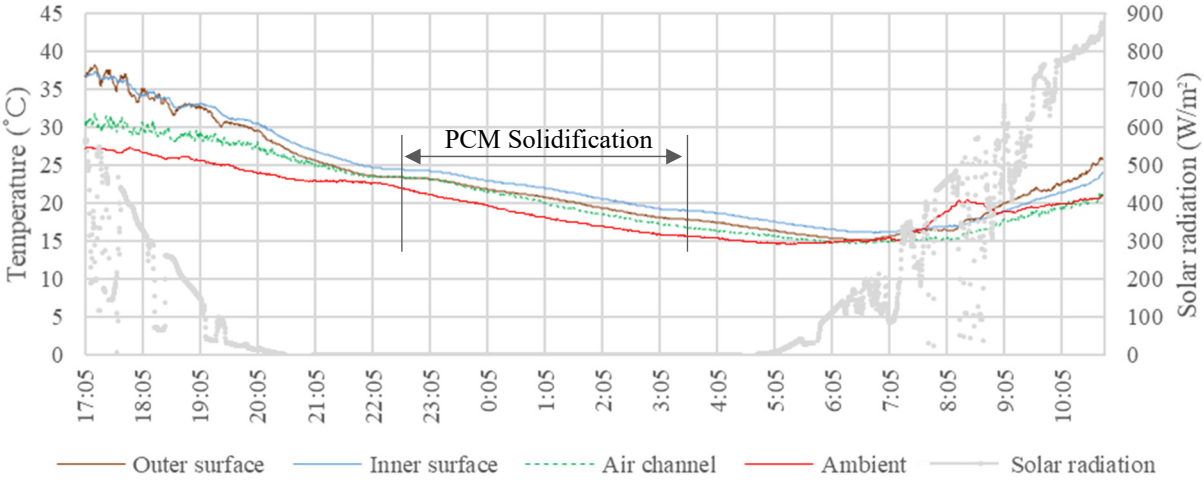

Figure 45. Cooling charging investigation for prototype 02 _ scenario 2

Scenario 3 (config-G with closed air channel) was applied under clear sky conditions during the cooling charging process. Due to the low rate of heat transfer related to the glazed configuration, the duration of solidification extended to around 8 hours till the complete solidification of the PCM panels. As noticed in Figure 46, it can be noticed that only the temperature of the air inside the external cavity reached a temperature up to 8 ˚C lower than the ambient temperature during the early morning period. It promotes the cooling potential for further developments of the system to

utilize the air cavity in cooling applications as an extra channel for air supply during cooling discharging process. The standby mode (scenario 5) was applied by adding the insulation layer to the system when its temperature was 17 ˚C to conserve the energy and minimize the heat gain to the system. The standby mode was applied for 8 hours; the system temperature increased to around 22 ˚C when the ambient temperature was around 27 ˚C. For this case, the rate of thermal losses during standby mode was 0.58 ˚C/h.

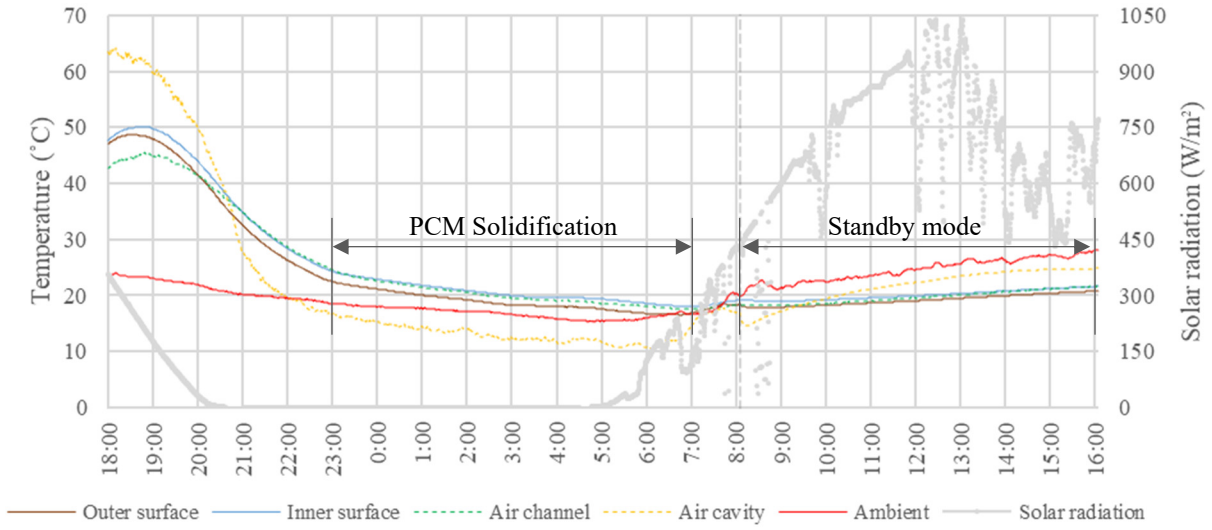

Figure 46. Cooling charging investigation (scenario 3), and standby mode (scenario 5) for prototype 02

During an investigation of cooling discharging, scenario 6 (insulated system and opened air channel) was applied to investigate the cooling performance during daytime. As shown in Figure 47 (from 16:00 to 18:20), due to small difference between PCM panel temperature and ambient profile, and the relatively high values of air velocities inside the air channel, shown in Figure 48, where the average air velocity was 2.3 m/s, the outlet air temperature was only reduced up to 2.5 ˚C lower than the inlet air temperature. During the period from 18:20 to 07:30, prototype 02 went into another cycle of cooling charging (including the solidification of PCM) utilizing scenario 4 (config-G and opened air channel) under cloudy conditions. While the ambient air profile was sufficient to charge the PCM, the airflow through the air channel accelerated the solidification process (5.5 hours till complete solidification) which was faster than scenario 3.

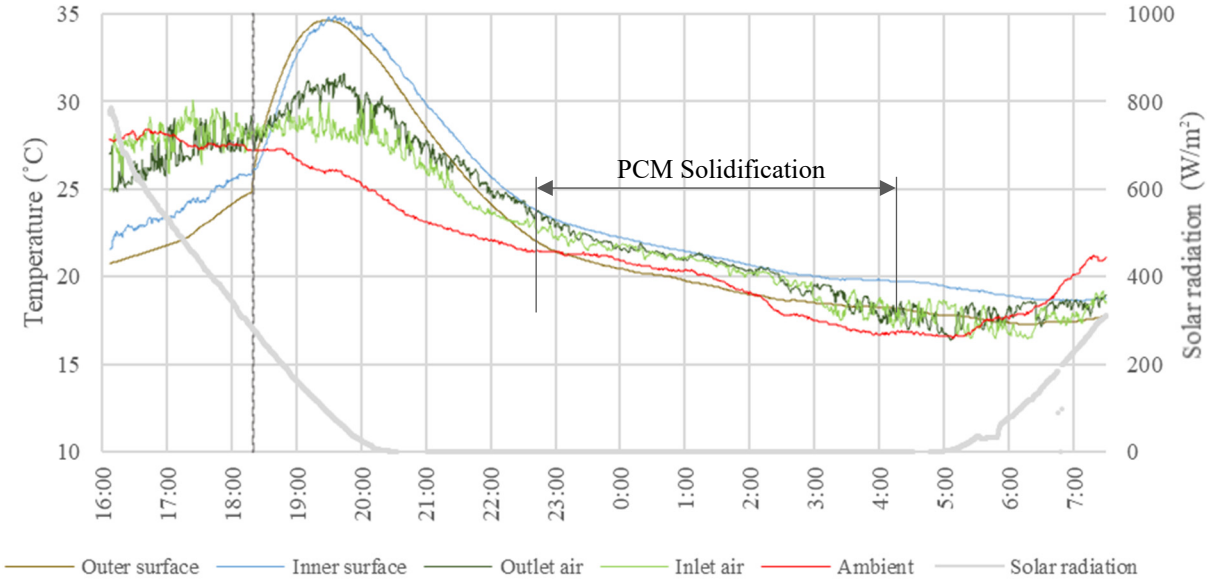

Figure 47. Cooling charging and discharging investigations for prototype 02 (scenarios 4 and 6)

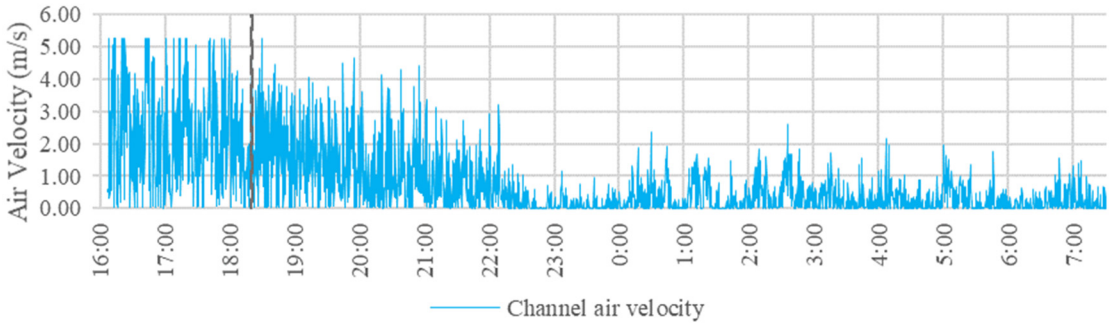

Figure 48. Air velocity inside the air channel for the application in Figure 47

Scenario 4 was applied for a free heating application during the daytime, as presented in Figure 49. During 5 hours of the application (from 12.30 to 17.30), when the inlet air temperature was around 22 ˚C, the outlet air temperature was up to 10 ˚C warmer than the inlet air temperature. During this application, the thermal losses by convection to the ambient air were compensated by the solar radiation during the day.

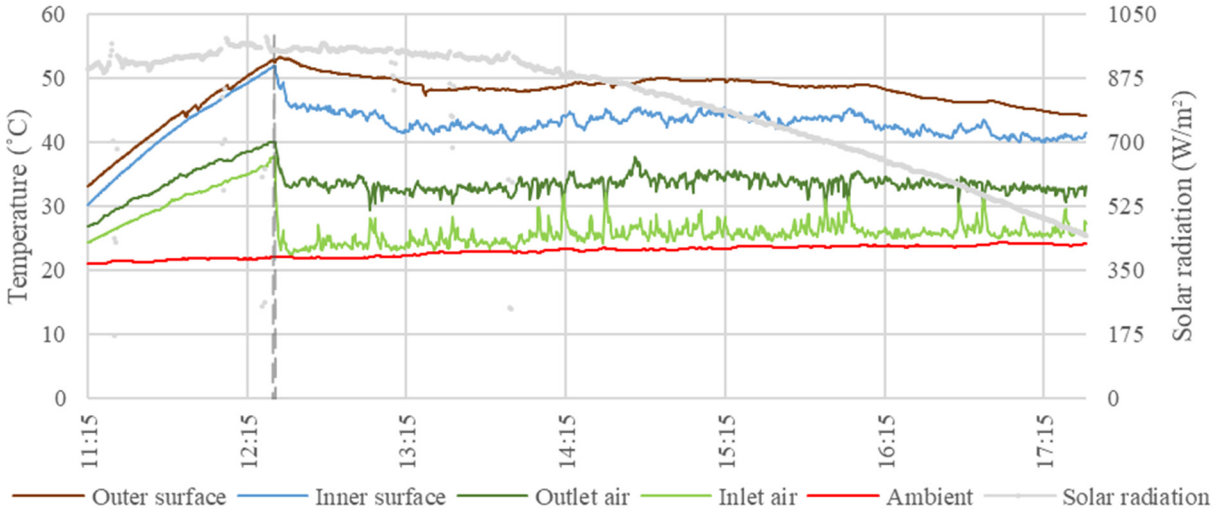

Figure 49. Free heating investigation for prototype 02 _ scenario 4

3.6. Experimental Results Analysis

3.6.1. Latent Charging Power

The latent charging power (P_l) is used to evaluate the rate of the latent storage for several experimental scenarios under different weather conditions. The two prototypes were investigated applying the previously mentioned scenarios. Regarding the latent charging power inside the two prototypes, shown in Figures 50 and 51, it can be noticed that, generally, P_l of prototype 01 was greater than prototype 02 in all the cases. This was due to the higher thermal properties and latent storage capacity of the organic PCM (RT44HC) in prototype 01. For prototype 01, it can be noticed that P_l while applying config-A under clear sky conditions (scenario 1 on July 09) recorded the highest value among all other cases. It means that the glazing layer (config-G) had a negative effect on the rate of latent storage which was decreased in scenario 3. It is important to mention that the cloudy conditions on July 10 while applying scenario 2 affected the overall charging power of the system where P_l decreased about 68% of its value under clear sky conditions. On the other hand, in prototype 02, it can be noticed that the config-G helped the system to increase the latent charging power specially in scenario 4 (when both radiation and convection thermal losses were in charge). It can also be noticed that in the days of lower ambient air temperature profiles during cooling charging, P_l was increased regardless the scenario (as noticed in the difference between scenarios 1 and 2). Moreover, as expected, the standby mode (scenario 5) showed the least P_l; however, the thermal losses were considerable due to the manually operated insulation technique.

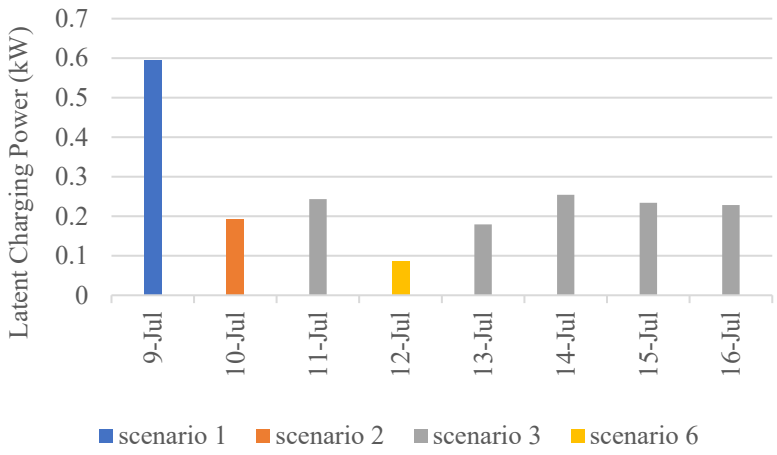

Figure 50. Latent cooling charging power for prototype 01

It can be concluded that the difference between PCT of the system and the ambient temperature is an important factor in controlling the charging power. The larger this difference is, the greater the latent charging power will be. When this difference is large enough to charge the system, the exposed configuration (config-A) is expected to achieve higher P_l. When this difference is insufficient (in case of PCM wallboards of a PCT of 18 ˚C – 24 ˚C), then the glazed configuration (config-G) can be more appropriate to charge the system. In the latter case, the cooling source during the solidification will be mainly the sky temperature and the charging process will mainly occur due to radiation thermal losses. However, in all the cases the clear sky conditions magnify the charging abilities increasing the rate of the latent storage of the system.

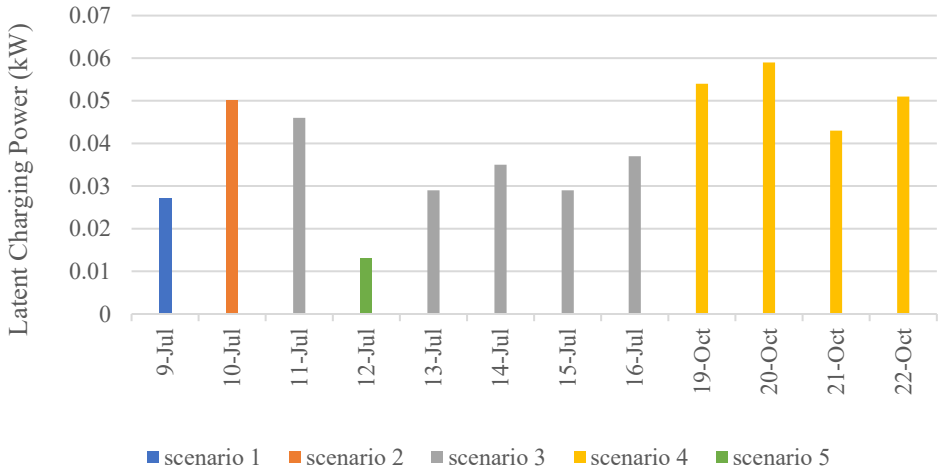

Figure 51. Latent cooling charging power for prototype 02

3.6.2. Cooling Recharge Energy

The investigations were conducted to monitor the total amount of charging energy (both latent and sensible) stored in the system during cooling charging process. Generally, the lower PCM temperature the system reaches, the higher the charging energy the system stores. The investigations were conducted using both prototypes and various scenarios. The hourly average cooling recharge energy (C_r) was calculated to evaluate all the cases.

- *Prototype 01 – Scenarios 1 and 2*

The charging process was evaluated while applying scenario 1 (config-A and closed air channel) under a clear sky condition. It can be noticed that, during phase change (PCM solidification), C_r achieved the highest values that reached 0.73 kWh, as shown in Figure 52. The phase change was accelerated due to the thermal losses by convection regarding the direct exposure to the ambient environment and the magnified effect of the radiation thermal losses to the clear sky. As observed, although the radiation thermal losses magnified the thermal losses of the PCM, the ambient air temperature affected the evolution of the PCM temperature during the night-time and early morning due to the direct contact between the PCM panels and the ambient environment.

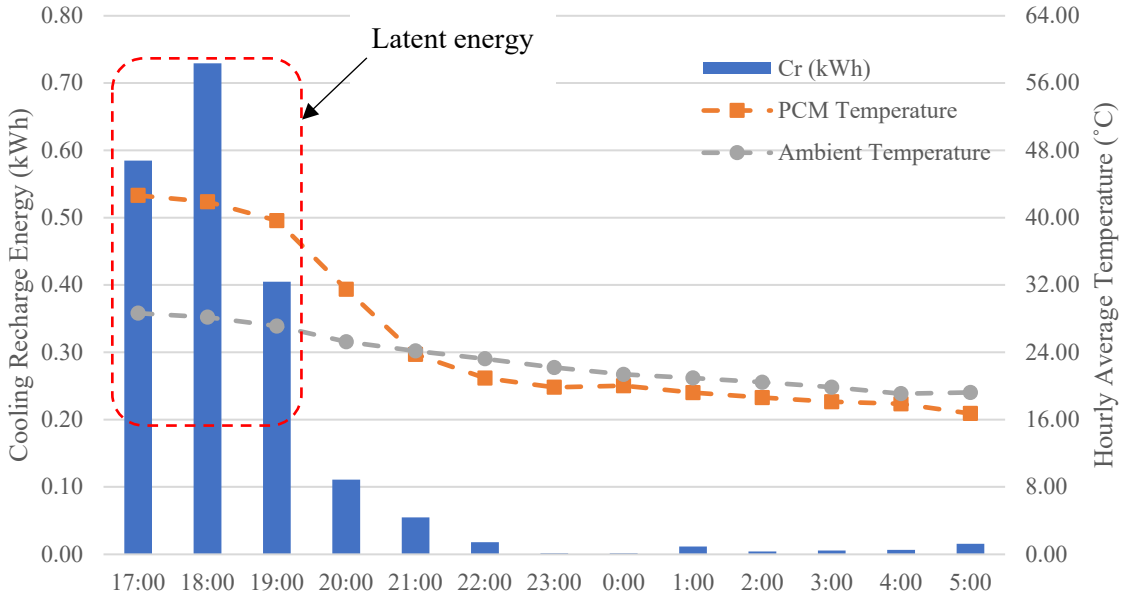

Figure 52. Cooling charging energy for prototype 01 – scenario 1

However, when it was cloudy while applying scenario 2 (config-A and opened air channel), it can be remarked in Figure 53 that the total cooling recharge energy was affected by the reduced radiation thermal losses. Moreover, the convection effect was magnified, by opening the air channel, and the ambient profile was totally dominating the evolution of the PCM temperature without extra radiation losses from the PCM to the sky due to the cloudy conditions.

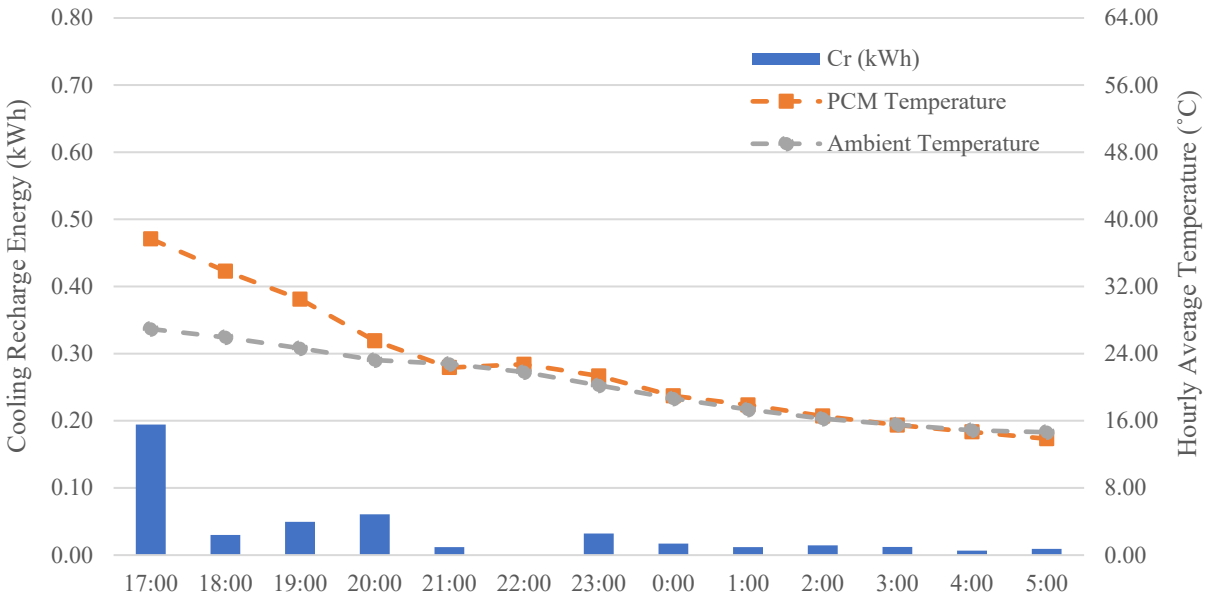

Figure 53. Cooling charging energy for prototype 01 – scenario 2

- *Prototype 01 – Scenario 3*

When scenario 3 (config-G and closed air channel) was applied under clear sky condition, the convection thermal losses were limited, and the charging process was mainly occurred by the radiation thermal losses to the sky temperature during night-time and early morning. In Figure 54, it can be noticed that the recharge latent energy was reduced almost to the half when compared to scenario 1 and the solidification process was decreased. However, the ambient air profile had less impact on the evolution of the PCM temperature. As a result, the PCM reached a lower temperature than the ambient air profile increasing the overall charging energy of the system.

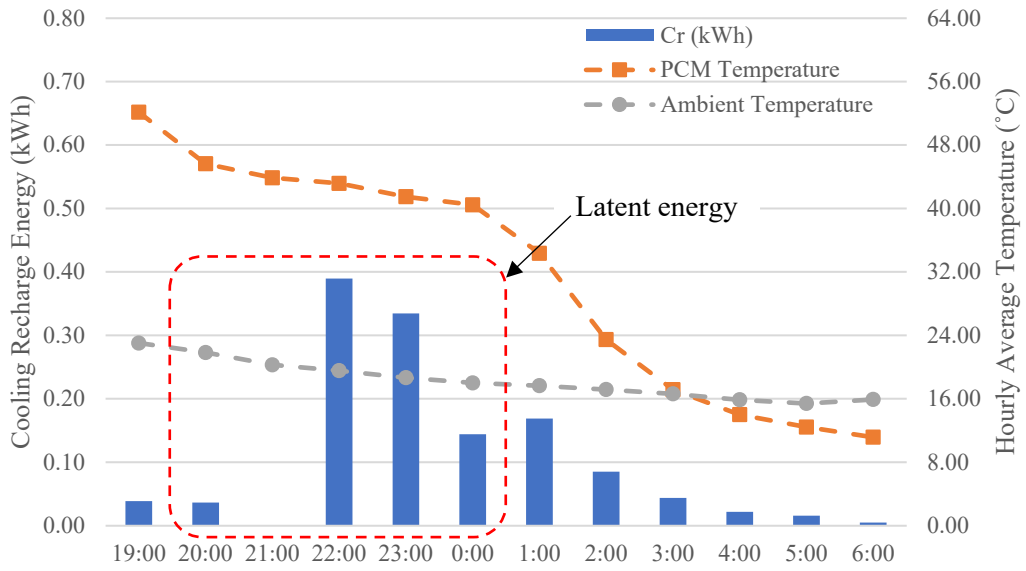

Figure 54. Cooling charging energy for prototype 01 – scenario 3

- *Prototype 01 – Scenario 6*

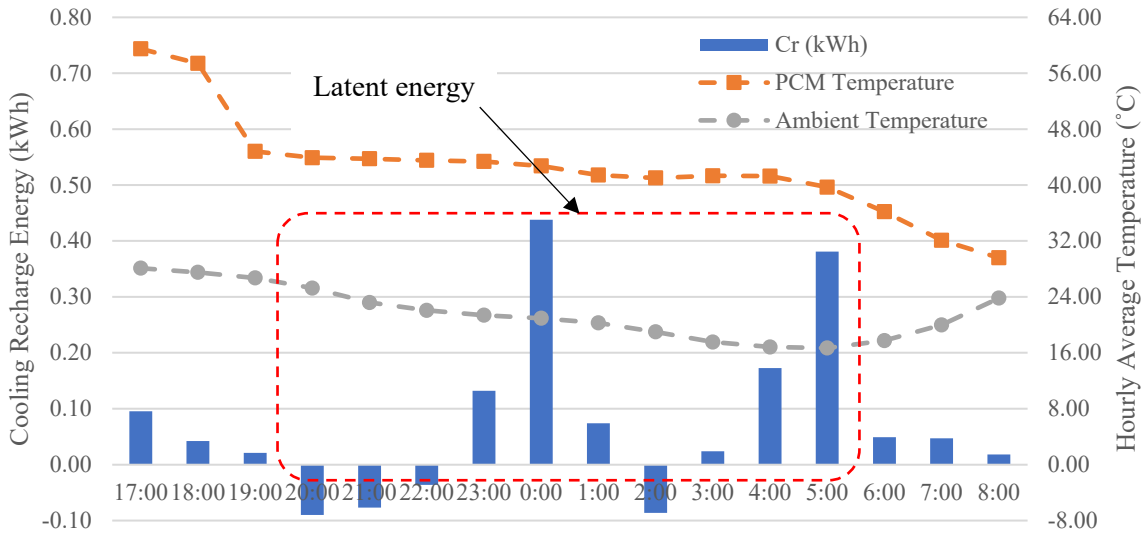

Figure 55. Cooling charging energy for prototype 01 – scenario 6

When the insulation layer was added, and the air channel was opened (scenario 6) during the charging process, the duration of the PCM solidification recorded the longest period as shown in Figure 55 (10 hours of phase change). Although the difference between the ambient air temperature profile and PCT range was sufficient to solidify the PCM, the low air velocity at this night (shown in Figure 43) and the blocked radiation thermal losses to the environment reduced the recharge energy increasing the solidification duration.

- *Prototype 02 – Scenarios 1 and 2*

In general, the cooling recharge energy in prototype 02 was lower than prototype 01 due to the thermal properties of the used PCM panels. Scenario 1 was applied under clear sky conditions in prototype 02. As the ambient profile (minimum of 19 ˚C) was insufficient to charge the PCM (PCT range of 18 ˚C – 24 ˚C), it can be observed, as remarked in Figure 56, that the recharge latent energy was not as high as the sensible energy where the difference between the ambient air profile and the PCM temperature was larger. This resulted in an overall low charging performance as will be indicated later in the analysis of the charging performance. It can be inferred that the thermal radiation losses did not increase the charging power of prototype 02. This could be due to the thermal properties of the PCM panels and the PCT range of the used PCM.

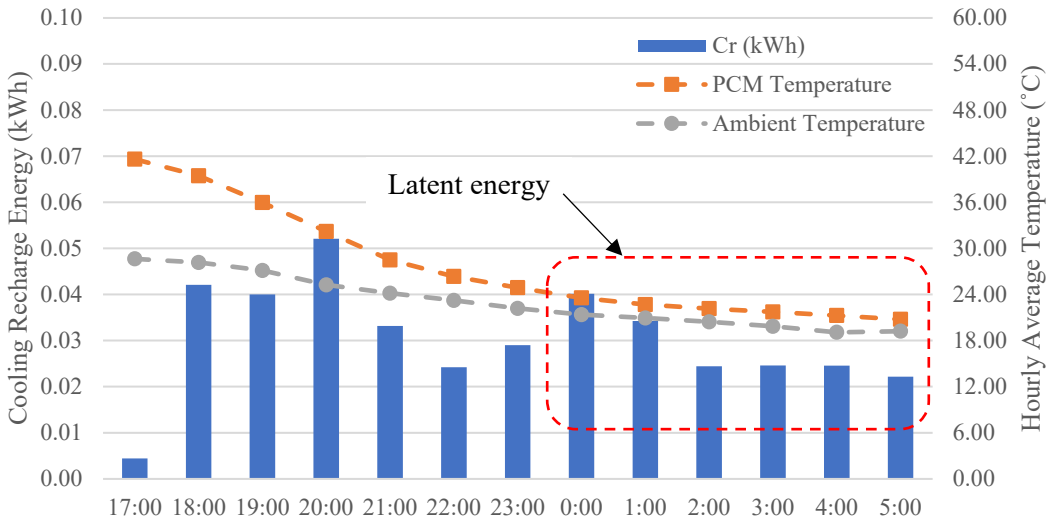

Figure 56. Cooling charging energy for prototype 02 – scenario 1

However, when scenario 2 (config-A and opened air channel) was applied under cloudy conditions, Figure 57 shows that the charging latent energy was almost doubled due to the increased effect of the convection thermal losses and the relatively larger difference between the ambient air profile (minimum of 14.6 ˚C) and the PCT range which allowed the complete solidification during charging process. It can be concluded that, with using the microencapsulated PCM panels of prototype 02, when convection is dominating, the radiation thermal losses did not contribute efficiently in increasing the charging energy of the system.

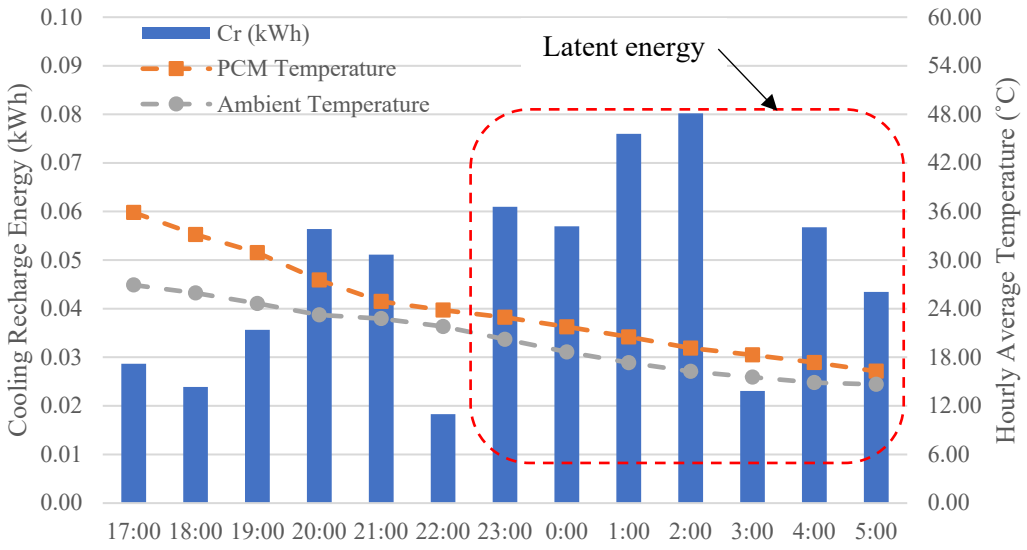

Figure 57. Cooling charging energy for prototype 02 – scenario 2

- *Prototype 02 – Scenario 3*

When scenario 3 (config-G and closed air channel) was applied under a clear sky condition, it can be remarked in Figure 58, at the beginning of the charging process, that recharge sensible energy increased due to the large difference between PCM temperature and the ambient temperature. However, during PCM solidification, the charging process was slowed down, and the duration of the solidification increased in comparison with scenario 2.

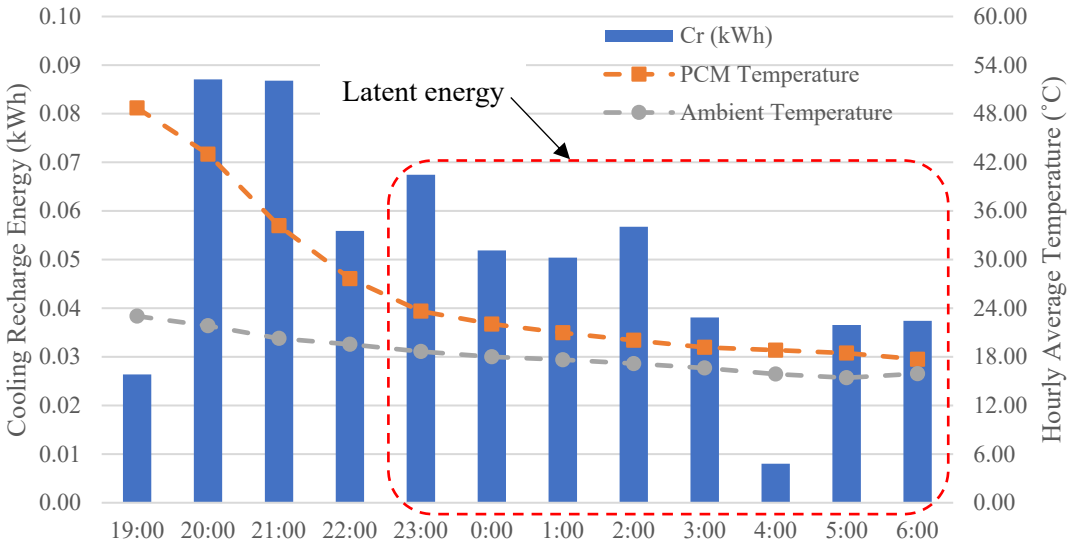

Figure 58. Cooling charging energy for prototype 02 – scenario 3

- *Prototype 02 – Scenario 4*

When the air channel was opened while config-G was applied (scenario 4), both latent and sensible recharge energies increased. Due to the maximized effect of radiation thermal losses to the sky and the convection losses to the ambient air, it can be noticed from Figure 59 that the PCM was completely solidified and the PCM temperature reached up to 3 ˚C lower than the ambient air temperature profile. Another important reason for this high performance during charging is the sufficient difference between the ambient air temperature profile and the PCT range of the microencapsulated panels during charging process.

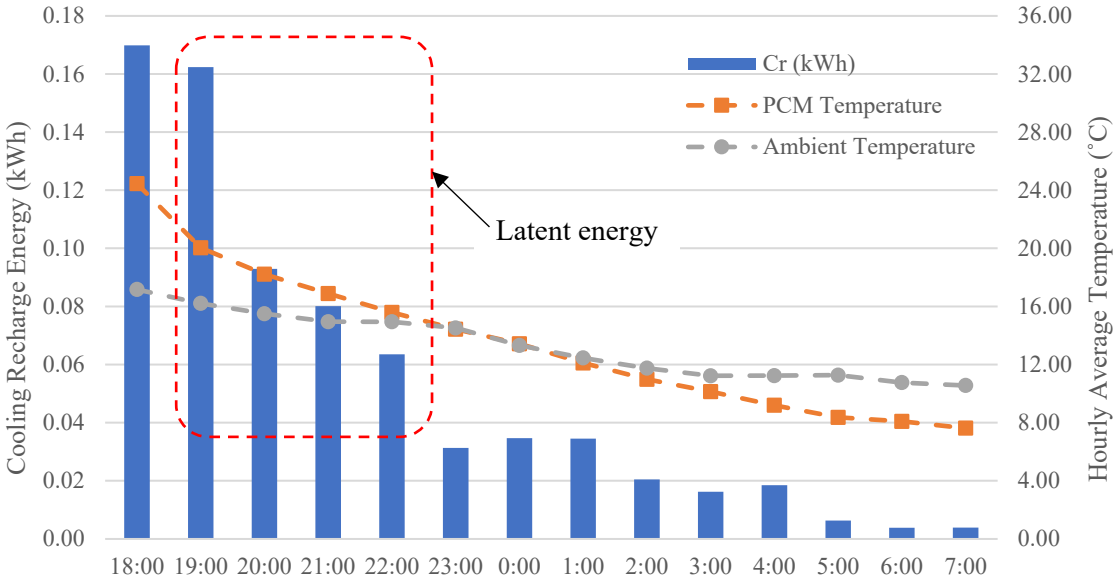

Figure 59. Cooling charging energy for prototype 02 – scenario 4

- *Prototype 02 – Scenario 5*

When the insulated configuration (scenario 5) was applied for a standby mode, the system achieved the least released energy as indicated in Figure 60. The PCM temperature increased 3.2 ˚C in 7 hours of the standby application. All the energy during the application of scenario 5 was related to the latent energy of the system.

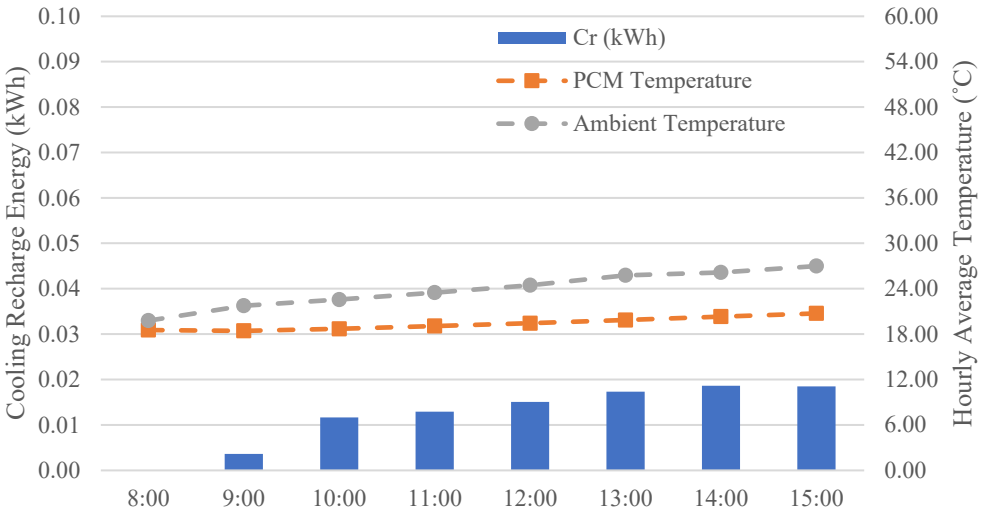

Figure 60. Cooling charging energy for prototype 02 – scenario 5

3.6.3. CPI and Increased Charging Energy

This indicator is a relationship between the total energy that the system stored during charging regarding all possible cooling sources (C_r) and the maximum possible energy that the system could store regarding only the ambient air as a cooling source ($C_{t\text{-}amb}$). CPI represents the increased released energy regarding radiation losses that is added to the maximum released energy to the ambient air. The higher the CPI is, the higher the cooling charging potential of the system will be regarding the radiation thermal losses to the sky. For a quantitative evaluation, the increased charging energy was calculated for each cooling charging process. All the investigated cases of the experimental scenarios were included regarding the different weather conditions during the applications. Beside the ambient air temperature, the related weather conditions to the charging performance were the relative humidity (RH) and the sky condition. Over a qualitative scale, cloudiness cover and RH were redefined by three spectra according to Table 10. It is worth mentioning that the proposed scale was based on the weather data provided by the weather station.

Table 10. The proposed qualitative scale for cloudiness cover and RH value

Cloudiness cover (%)	Clear	Partially cloudy	Cloudy
	0-40	41-70	71-100
RH (%)	Low	Medium	High
	0-40	41-70	71-100

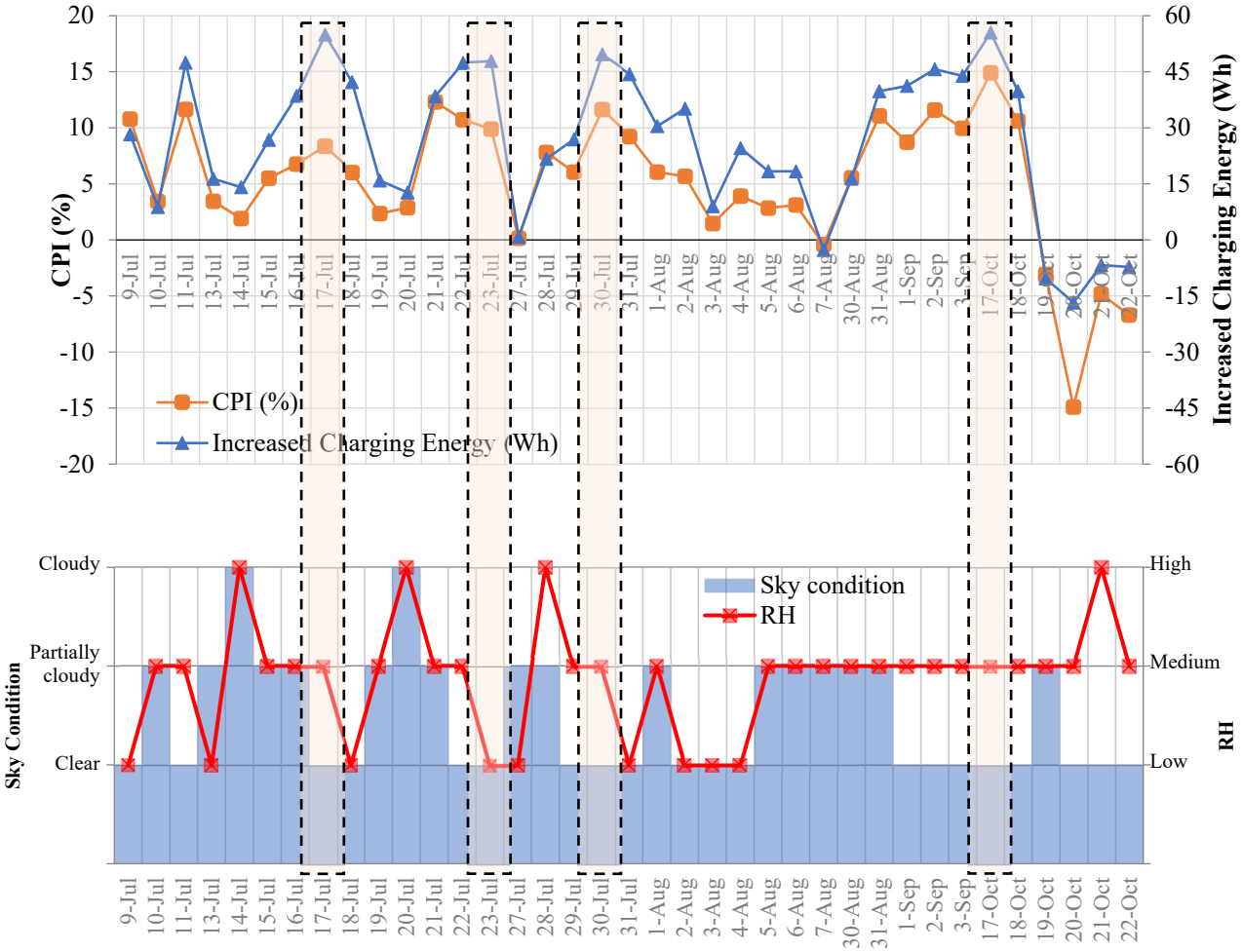

Figure 61. CPI and increased charging energy for prototype 01 regarding RH and sky condition

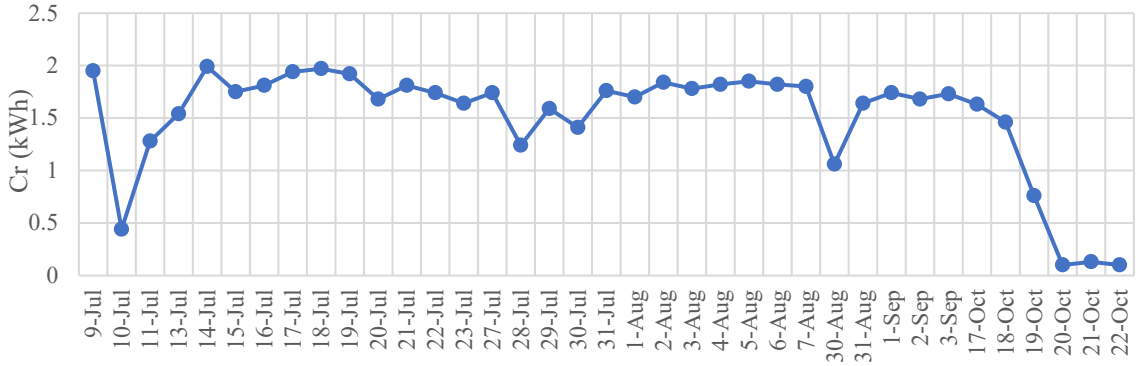

Figure 62. Total cooling recharge energy for prototype 01

For prototype 01, Figure 61 represents the CPI and the increased charging energy values regarding the ambient conditions. Most of the investigated cases in prototype 01 were while applying scenario 3 (config-G and closed air channel). It can be remarked that at most cases CPI recorded

positive values that reached up to 14.86% with an increased charging energy up to 55.33 Wh. The highest values of CPI can be noticed during clear sky conditions and while RH values were low to medium. However, it can be remarked that when scenario 6 (insulated configuration) was applied for the last four cases, the total recharge energy stored inside the system, represented by Figure 62, did not reach the maximum possible charging energy regarding the ambient air temperature. This was due that the exposure to the sky temperature was blocked by the insulation reducing the charging performance. In this case, the ambient air was the only heat sink to charge and discharge the system which is the case for conventional PAHX units.

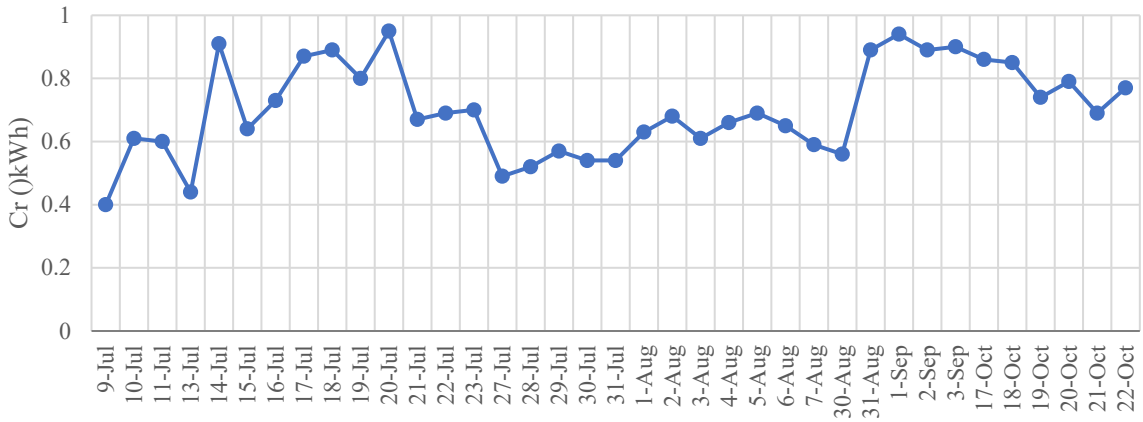

Figure 63. Total cooling recharge energy for prototype 02

Regarding prototype 02, the overall recharge energy, represented in Figure 63, was lower than prototype 01 regardless the applied scenario due to the thermal properties of the PCM panels. As inferred by Figure 64, the highest values of CPI were noticed while applying scenario 4 when there was a sufficient difference between the ambient air profile and the PCT range of the panels. The highest recorded CPI value was 22% with a maximum increased charging energy value of 48 Wh. Again, it can be noticed that the best charging performance was occurred with clear sky conditions and low to medium RH values.

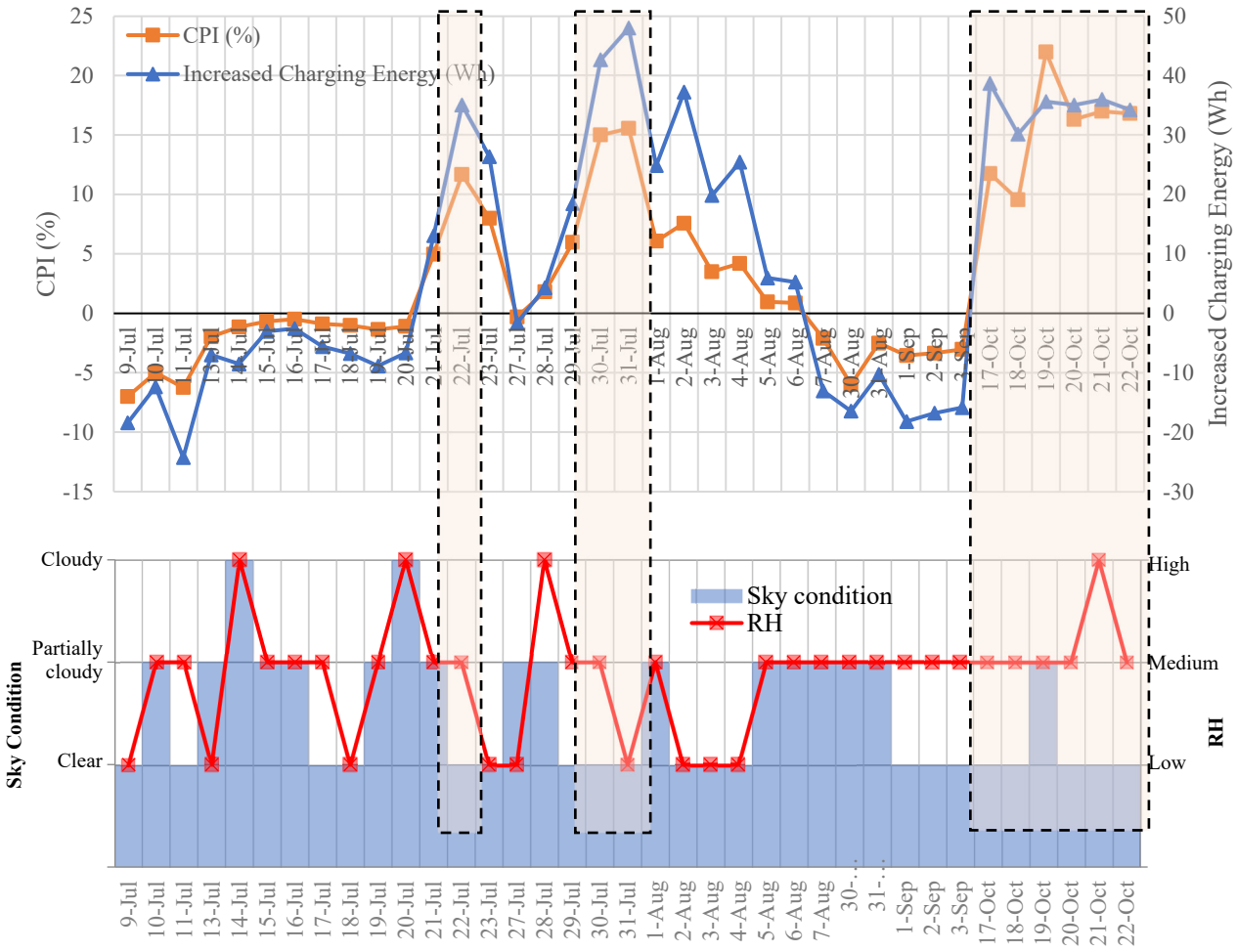

Figure 64. CPI and increased charging energy for prototype 02 regarding RH and sky condition

3.6.4. Rate of Discharging

The cooling discharging investigation was conducted using prototype 02. Due to the low thermal properties of the PCM panels, the maximum hourly average temperature of the outlet air recorded 1.8 ˚C cooler than the inlet air temperature. Both prototypes were investigated for heating discharging applications. Regarding prototype 01, applying scenarios 2, 4, or 6 with an opened air channel while free heating mode resulted in a warmer outlet air of the system. These cases were considered to be assessed as heating discharging cases. The hourly average outlet air temperature was evaluated regarding the inlet air temperature. The rate of heating discharging was calculated for prototype 01, as shown in Figure 65. The maximum value of the discharge rate was 10.6 ˚C/h with a maximum recorded hourly average outlet air temperature of 15 ˚C warmer than the inlet air temperature. For prototype 02, the maximum value of the discharge rate was 15.8 ˚C/h, as shown

in Figure 66, and the maximum hourly average outlet air temperature was 22.5 ˚C warmer than the inlet air temperature. In general, it is worth mentioning that better performance was noticed with lower air velocity values inside the air channel. Generally, according to the results of both prototypes, the difference between the inlet air temperature and the PCM temperature (PCT range of the system) during discharging is a critical factor that needs to be designed intentionally to control the performance of the system.

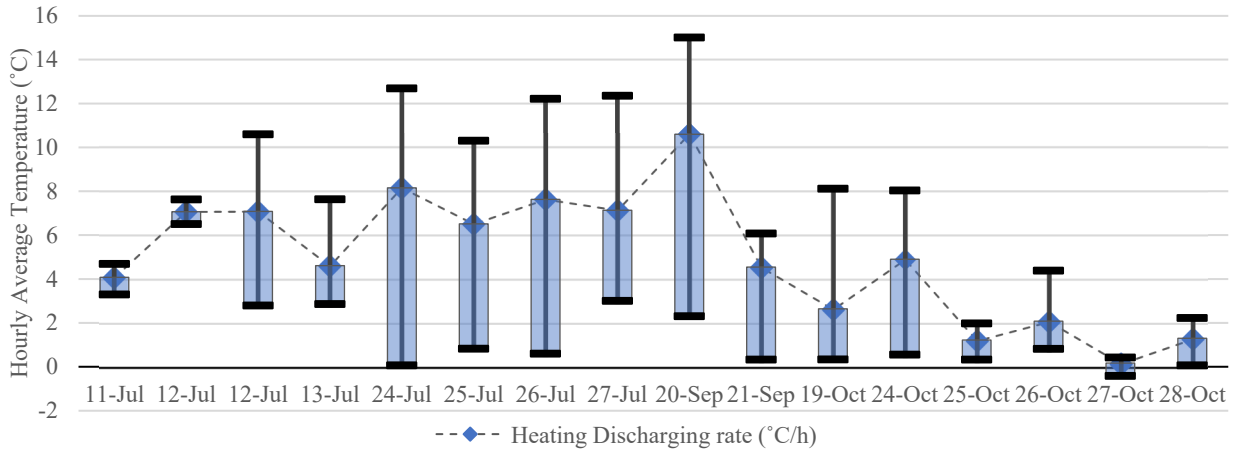

Figure 65. Rate of heating discharging for prototype 01

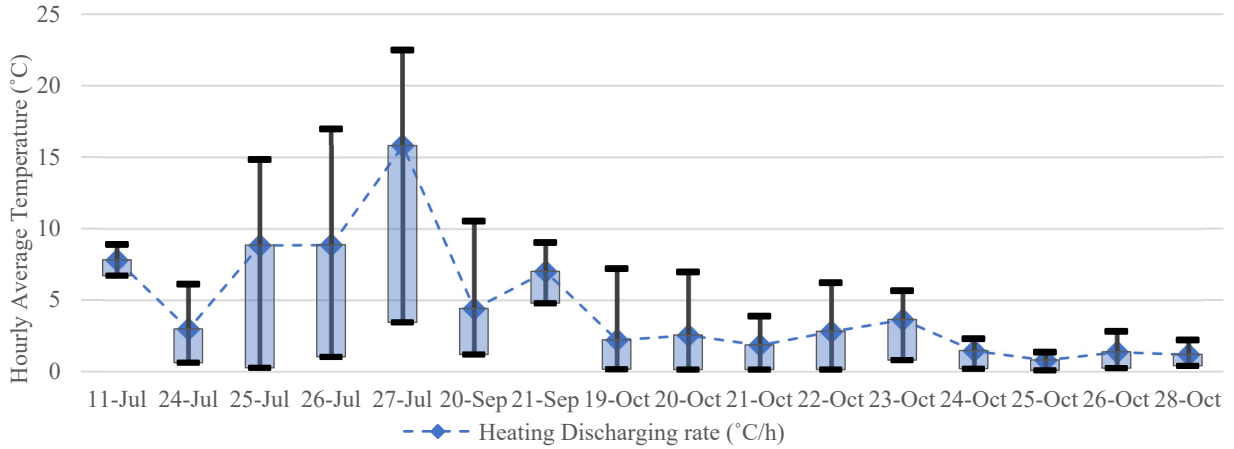

Figure 66. Rate of heating discharging for prototype 02

3.7. Discussion

The experimental results showed that when the difference between the ambient air profile and the PCT range of the system was sufficient to solidify the PCM, it is better to apply configuration A (exposed to ambient) during charging to allow the thermal losses by both convection and radiation to the ambient environment. In case the system reached the maximum charging energy related to

the ambient air as a cooling source, or the ambient air profile was not low enough to charge the system, then configuration G (glazed configuration) would be more appropriate to minimize the convection heat transfer and maximize the radiation thermal losses to the sky temperature which can increase the cooling charging energy during the charging process. However, a proper control strategy as well as an energy management plan is required with respect to the operational mode and the duration of the application to maximize the charging power and the overall cooling performance of the system. The following conclusions can be inferred from the results analyses:

- It can be inferred that due to the thermal properties of PCM wallboards in prototype 02, the cooling charging power in prototype 02 was lower than prototype 01 in general.
- With cloudy conditions (limited thermal radiation losses) and when the PAHX system was exposed to the ambient environment with an opened air channel, the convection thermal losses were dominating the heat transfer process. This means that no extra charging energy is expected beyond these related to the ambient air temperature.
- It can be concluded that the exposure to the clear sky, as a cooling source, increases the charging energy of the system. Moreover, the charging power of the system can be increased by applying the exposed configuration to the ambient (config-A).
- Regarding the previous point, the limited exposure to the sky with real conditions can be a limitation of practical applications. Further configuration developments are recommended to investigate practical implementations and vertical configurations.
- The difference between the PCT range of the system and the ambient air profile during charging process is a key factor in determining the cooling performance of the system. The larger this difference is, the greater the charging power and, thus, the cooling potential of the system will be.
- Another key factor of the determination of the cooling charging energy of the system is the clear sky conditions which magnify the cooling charging energy of the system especially when combined with a sufficient low ambient air temperature.
- It can be claimed that applying the concept of the radiation thermal losses to the clear sky during the cooling charging increased the charging energy by up to about 15% in prototype 01, and about 22% in prototype 02 in specific conditions which increases the cooling potential of the application of the developed PAHX system.

CHAPTER FOUR: NUMERICAL MODELING & EXPERIMENTAL VALIDATION

4.1. Modeling for PAHXs

Generally, the heat transfer within PAHXs is divided into two main processes based on the mode of heat transfer: convective heat transfer from PCM to air, and heat transfer inside the PCM itself (Osterman et al., 2015). The mathematical expression of the convective heat transfer varies due to the configuration of PAHX where different formula for the Nusselt number are used. The average mass flow rate inside the PAHX unit indicates the nature of the convective heat transfer mode whether it is forced, free, or mixed convection. With respect to heat transfer between air and PCM inside the heat exchanger, most of the literature formulated the heat transfer model under forced convection conditions, even with very low air velocity values (Waqas and Kumar, 2011; de Gracia et al., 2013b). Limited studies considered the free or mixed convection modes of heat transfer in free cooling PAHX applications. This could be a strong limitation for predicting the system performance under free or mixed convection modes where buoyancy forces play a role in heat transfer at low airflow regimes. It should be mentioned that limited studies tackled the convection model with free convection conditions due to the challenging operational conditions related to changing air velocities during system operation. Instead, all the studied systems were under forced convection conditions with controlled airflow rates.

The heat transfer inside PCM is expressed by conduction or both conduction and convection models. The mushy region is expressed by the liquid fraction during phase change. Considering the free convection within the liquefied part in PCM model is highly debatable in most of the studies. Many investigations showed the importance of considering natural convection in the melting phase at spherical encapsulations, box and central unit configurations (Lamberg et al., 2004; El-Sawi, Azeldin, 2013). Regarding flat plates encapsulation, Mosaffa et al. (2013) showed that considering free convection could only be beneficial in vertical configurations with considerable PCM slab thicknesses. In horizontal configurations, gravity and liquid stratification could reduce the effect of natural convection. However, due to the nature of heat transfer during phase change process, it is hard to formulate a generalized model for all different boundary conditions, configurations and geometries of the proposed system (Halawa and Saman, 2011).

Mainly, the thermal energy storage inside PCM is expressed by two methods: enthalpy method and heat capacity method (Haghighat, Fariborz, 2013).

Borderon et al. (2015) numerically investigated the PAHX thermal performance using a 2D heat transfer model utilizing the apparent heat capacity method considering forced convection conditions. Waqas and Kumar (2011) investigated the performance of a flat encapsulated configuration using a 2D numerical model utilizing the enthalpy method for both laminar and turbulent flows. Darzi et al. (2013) studied the performance of a flat plated PAHX during the melting process under various airflow rates using a 2D numerical model and CFD simulations. Stathopoulos et al. (2016; 2017) used a 2D numerical model to study the thermal performance of a flat plated PAHX unit assuming the convective heat transfer coefficient as a constant calibration factor. They studied the thermal performance and the effect of the proposed heat transfer enhancements (internal fins) inside the prototype solving the convection problem under forced convection conditions. de Gracia et al. (2013) examined the integration of macro-encapsulated PCM panels inside the air channel of a ventilated facade. A 2D numerical model of the system was utilized to investigate the performance of the system during different weather conditions in (de Gracia et al., 2013a) and (de Gracia et al., 2013b); the enthalpy method was applied in these studies. The numerical model considered the thermal radiation exchange between system elements. The authors assumed a constant external convective heat transfer. The internal convective heat transfer coefficients were calculated using empirical correlations of Nusselt number for forced convection conditions. The thermal radiation to the ambient environment was considered as thermal losses of the system applying a simple model for the determination of the sky temperature, which depended only on the ambient air temperature. The authors also proposed a simpler PCM model in (de Gracia et al., 2015) with more simplified assumptions. They claimed that the simple model is beneficial for the system implementation for building applications. Jaworski et al. (2014) presented a numerical model for a ventilated ceiling panel assuming a constant external convective heat transfer coefficient. The internal heat transfer coefficient was calculated based on a Nusselt number correlation for internal turbulent flow under forced convection conditions. Evola et al. (2014) developed a numerical model for a ventilated partitioning wall of micro-encapsulated PCM wallboards assuming that the flow is

laminar within the ventilated cavity. They experimentally obtained the correlation of Nusselt number for rectangular cavities.

Based on the previous review, the research gap in the numerical modeling for PAHXs can be identified by the lack of a generalized numerical model for PAHXs that fulfills various convection modes (free, forced, or mixed) and considers the radiative component. This chapter describes the development of a comprehensive model for simulating the developed PAHX system described in Chapter three for free cooling applications and its integration into the building envelope. The model considers various forms of convective heat transfer (natural or forced) and thermal radiation heat exchange. The prediction by the model was evaluated at two levels; inter-model comparison and comparison with the experimental measurements illustrated earlier in Chapter three.

4.2. Model Development

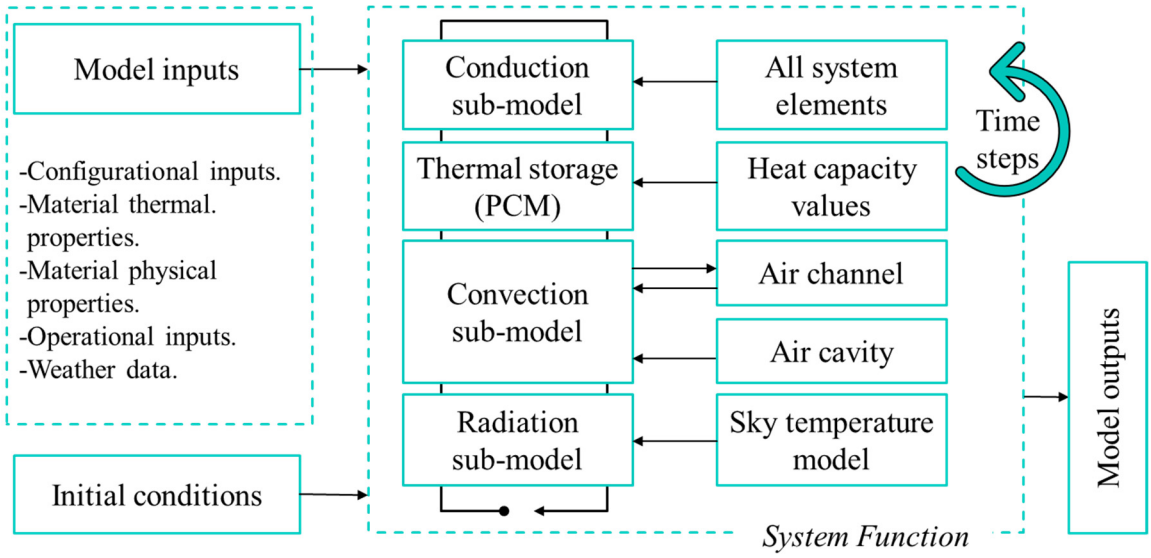

Figure 67. Graphical illustration of the structure of the proposed PAHX model

The proposed numerical model considers, mainly, four phenomena (sub-models), as shown in Figure 67: conduction, radiation, convection, and thermal energy storage. The long-wave radiation sub-model was developed to represent the heat exchange in-between the system elements and between the system elements and the sky. Accordingly, the sky temperature is an essential parameter that affects the accuracy of the model. A procedure for the determination of

the sky temperature was developed and integrated into the radiation sub-model. The convective sub-model was developed mainly between the storage medium (PCM) and both the internal air channel and the external air cavity. The free, forced, and mixed airflow regimes were regarded in the convection model to satisfy various convection modes. The convection sub-model was developed to automatically identify the appropriate convection mode at each time step regarding the air velocity, air and PCM temperatures, and the system configuration. Accordingly, the calculations of the convective heat transfer coefficient during simulations are being updated at each time step. The thermal storage inside the PCM was modeled by the apparent change in the heat capacity of the PCM during its phase change, the so-called apparent heat capacity method, as will be illustrated below. The sub-models were coded in the MATLAB environment using the energy balance approach. The finite difference technique was followed with an implicit method to ensure the model stability regardless of the value of the time step.

4.2.1. Energy Balance Approach

The energy balance approach (often referred to as the control volume method) depends on defining a number of control volumes of the spatial domain (Haghighat, Fariborz, 2013). The basic assumption of this approach is that the heat entering the control volume equals to the sum of heat leaving the control volume and the stored amount of heat in the material. Other important assumptions are that each control volume can be represented by a single value of temperature, and that the temperature value is assumed identical for the whole volume of the control element. In such case, each control volume can be represented by one node. The accuracy of this approach depends on the number of control volumes which are used for the spatial discretization of the domain. The whole heat transfer domain can be represented by the nodal discretization in either single or multi-dimensional analysis grid or mesh. The general formulation of conduction heat transfer is:

$$\left({}^{1}/_{\alpha}\right) {}^{\partial T}/_{\partial t} = \nabla.(\nabla T) \tag{8}$$

The first order differential term $(\partial T/\partial t)$ is the temperature change in the time domain; the second order differential term $\nabla.(\nabla T)$ is related to heat fluxes in the multi-dimensional space domain, and α is the thermal diffusivity defined as $k/\rho\, c_p$, where k is the thermal conductivity,

ρ is the density, and c_p is the heat capacity. The heat transfer Equation (8) can be rewritten into the 2D form as:

$$\rho\, c_p \,\partial T/\partial t = k\left(\partial^2 T/\partial x^2 + \partial^2 T/\partial y^2\right) \tag{9}$$

4.2.2. General Apparent Heat Capacity Method

The apparent heat capacity method assumes a constant rate of heating/cooling during the phase change for determining the value of the heat capacity in respect of the nodal temperature (Stathopoulos et al., 2017; Haghighat, Fariborz 2013). The apparent change in specific heat capacity (c_p) values was monitored by tracking the change in temperature corresponding to the change in latent heat during phase change. Various values of heat capacity can be inferred according to Equation (10).

$$C_p = \begin{cases} C_s & T_{pcm} < T_s \quad solid\ phase \\ L/(T_s - T_l) + (C_s + C_l)/2 & T_s < T_{pcm} < T_l \quad mushy\ region \\ C_l & T_{pcm} > T_l \quad liquid\ phase \end{cases} \tag{10}$$

where C_s, C_l are the heat capacities in the solid and liquid phases, respectively, T_s, T_l are temperature limits of the PCT range, and L is the latent heat of fusion/crystallization during the phase change or the latent enthalpy. The main assumption of this method is that the heat of fusion is uniformly released/absorbed during the entire phase change process (Haghighat, Fariborz, 2013). Referring to the experimentally obtained values of heat capacity, this approach presents one curve of heat capacity values during the solidification process, and another curve during the melting process based on a specific heat transfer rate.

However, in an experimental investigation of a flat plated PAHX, Stathopoulos et al. (2017) obtained the values of the heat capacity for the PCM Mikrotek 37D using Differential Scanning Calorimetry (DSC). They found that the measured values of heat capacity are highly dependent on the cooling/heating rates. It means that when the cooling/heating rates change, the values of c_p vary, but with the same integrated area below the curves of c_p which is equal to the latent heat of fusion. They also claimed that the heating and cooling rates of PCM depend on the location of measurement inside the heat exchanger (close to inlet, middle or close to outlet) where the air temperature changes, and thus also the temperature difference between air and PCM, along the

heat exchanger. They proved that heat transfer rate decreases as the distance from the inlet increases. They proposed an improved method that depends mainly on the availability of experimental measurements for determination of c_p values. The improved method proposed various heating/cooling rates in respect to the location inside the PAHX unit. This was claimed to be more accurate in determining heat capacity values inside PAHX units. A 2D numerical model for a flat plated PAHX was proposed and experimentally validated by Stathopoulos et al. (2016) based on experimentally measured heat capacity values. The authors utilized six curves of c_p of PCM Mikrotek 37D, as shown in Figure 68, (three curves for three different cooling rates, and another three for different heating rates) based on measured data to represent heat transfer inside the PAHX unit. The authors in (Stathopoulos et al., 2017) divided the PAHX system to three consequent parts (inlet, middle and outlet) assigning different cooling and heating curves for each part. Both cooling and heating curves for heat capacity were determined based on different cooling and heating rates of DSC measurements. Although this procedure provided better model accuracy, this dependency on the experimental data obstructed the model applicability for other research investigations instead of a single case study.

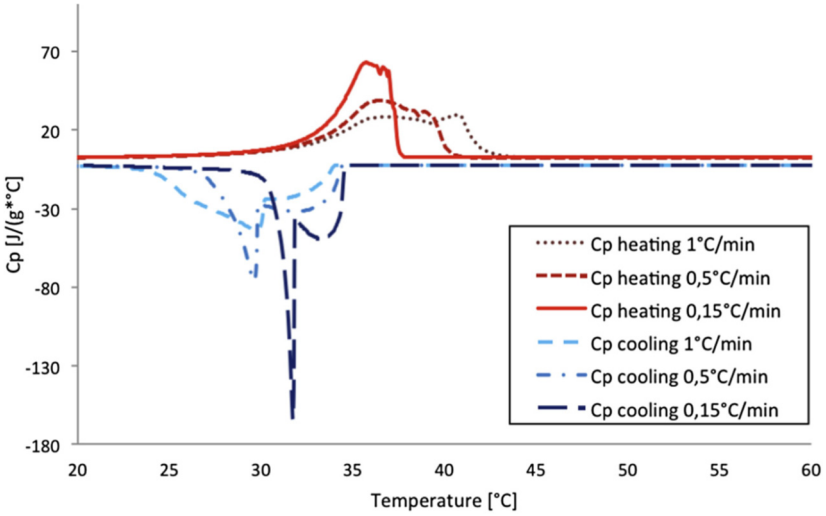

Figure 68. The experimentally obtained c_p values by Stathopoulos et al. (Stathopoulos et al., 2016)

In this section, a general apparent c_p method is presented assuming one fixed rate of cooling/heating along the system for the generalization of the heat capacity method. This generalized approach can be beneficial to formulate a general method for further investigations, in case of unavailability of the experimental measurements, due to the commercial availability of the apparent c_p cooling and heating curves by PCM suppliers. An investigation was conducted to

test the accuracy of the general apparent c_p method in comparison with the improved apparent c_p method presented by Stathopoulos et al. (2016; 2017).

- *Justification of general apparent heat capacity method*

Numerical developments were conducted in terms of generalization of the model of Stathopoulos et al. (2017) to be applicable to broad investigations. The general approach assumes one fixed rate of cooling/heating along the system, as shown in Figure 69, which is the original assumption of apparent heat capacity method. This approach can be beneficial to formulate a design platform for PCM selection; thus, any PCM type can be easily tested. The prediction of the general apparent heat capacity method will be compared to the experimental data discussed in (Stathopoulos et al., 2016).

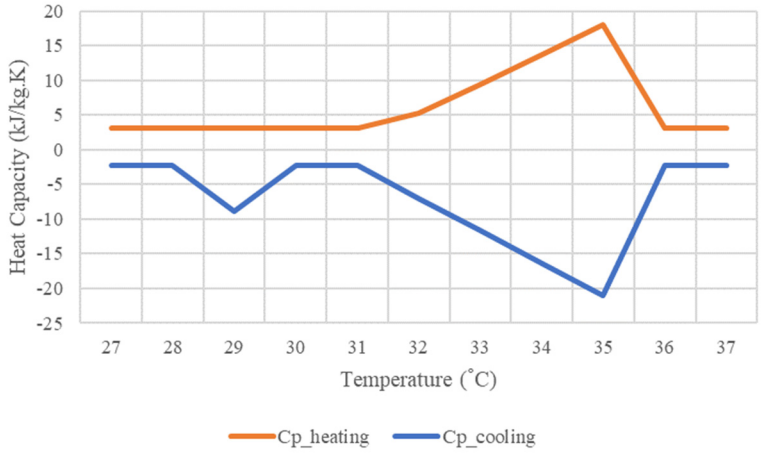

Figure 69. Simplified c_p values for general apparent heat capacity method

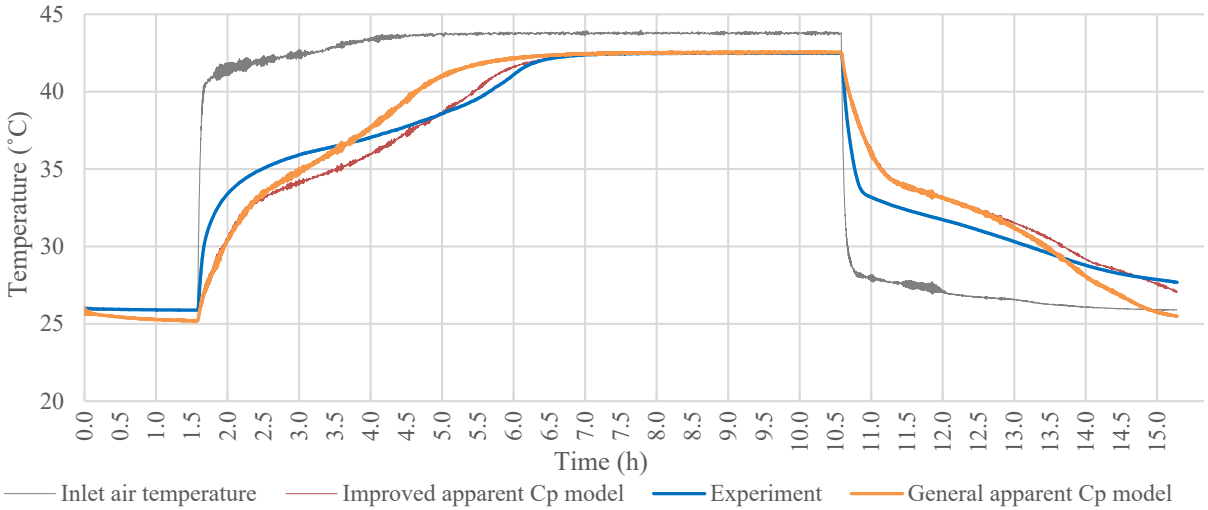

Figure 70. Validation of the general apparent heat capacity method

Figure 70 presents the results of the comparison of the general apparent c_p method against the experimental results. The figure shows the evolution of the system outlet air temperature under volume airflow rate of around 300 m^3/h during both PCM melting (cooling discharging) and solidification (cooling charging). The general method was also compared with the improved apparent c_p method mentioned in (Stathopoulos et al., 2016) using the experimentally obtained values of heat capacity. The operational conditions, variables, and other input values of the two models were identical with the experiment. The results show that the general apparent heat capacity method showed an expected discrepancy with the improved method and the experimental results due to the simplified approach of heat capacity determination. However, it shows the same behavior. The discrepancy can be noticed nearly at the end of each process (melting or solidification). It means that with the simplified approach the system tends to consume its storage capacity faster than the actual behavior.

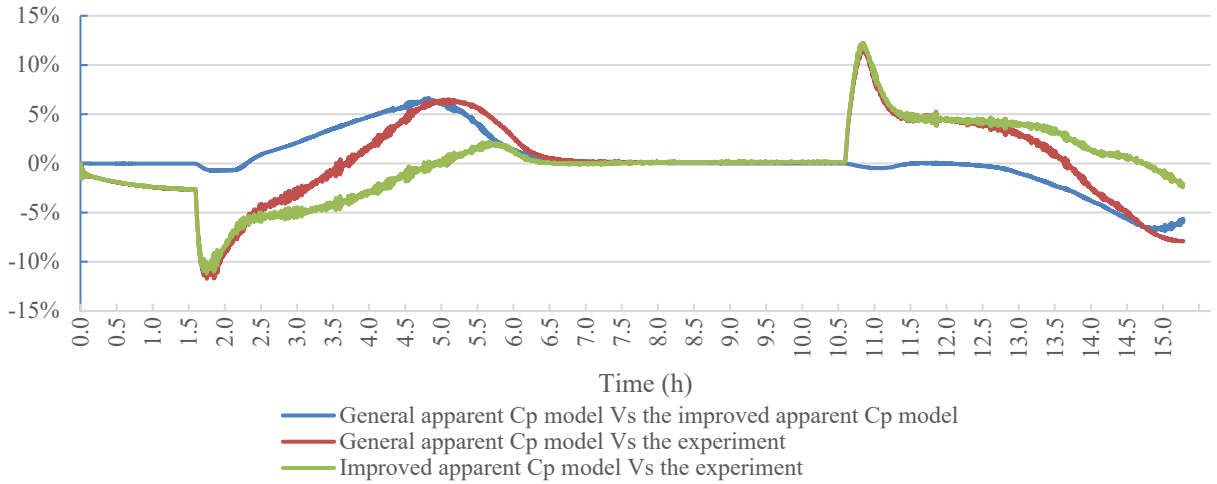

Figure 71. Percent error analysis of the general apparent heat capacity method

In order to determine the discrepancy level of the general approach, a percent error test was conducted for the general and the improved apparent c_p methods tracking the difference between predicted and measured data. Figure 71 shows the percentage of error of the general and the improved apparent c_p methods compared to the experimental data. The results show that both general and improved methods exceeded 10% of error percentage with the experimental data only at the start of each phase change process. Otherwise, the error in both methods remained below 10% with the experimental data. Comparing to the improved method, the general method showed 7% as a maximum value of error percentage. It can be inferred that the general method

showed up to 10% as a level of discrepancy with the experimental data, especially at the end of the phase change process where the system storage capacity is about to be consumed. However, it is still of an acceptable agreement with both experimental results and the improved apparent c_p method. In terms of the average error, the improved apparent c_p method showed average errors of 3.2% and 3.7% during melting and solidification respectively with the experimental data. While the general apparent c_p method showed average errors of 3.9% and 4.6% during melting and solidification respectively with the experimental results.

4.3. Numerical Modeling

In this section, a detailed description of the numerical model is presented. All the energy balance equations of the different layers of the system are shown. The main parts of the model are discussed in detail. Also, the assumptions and potential of the numerical model are discussed.

4.3.1. Nodal Discretization

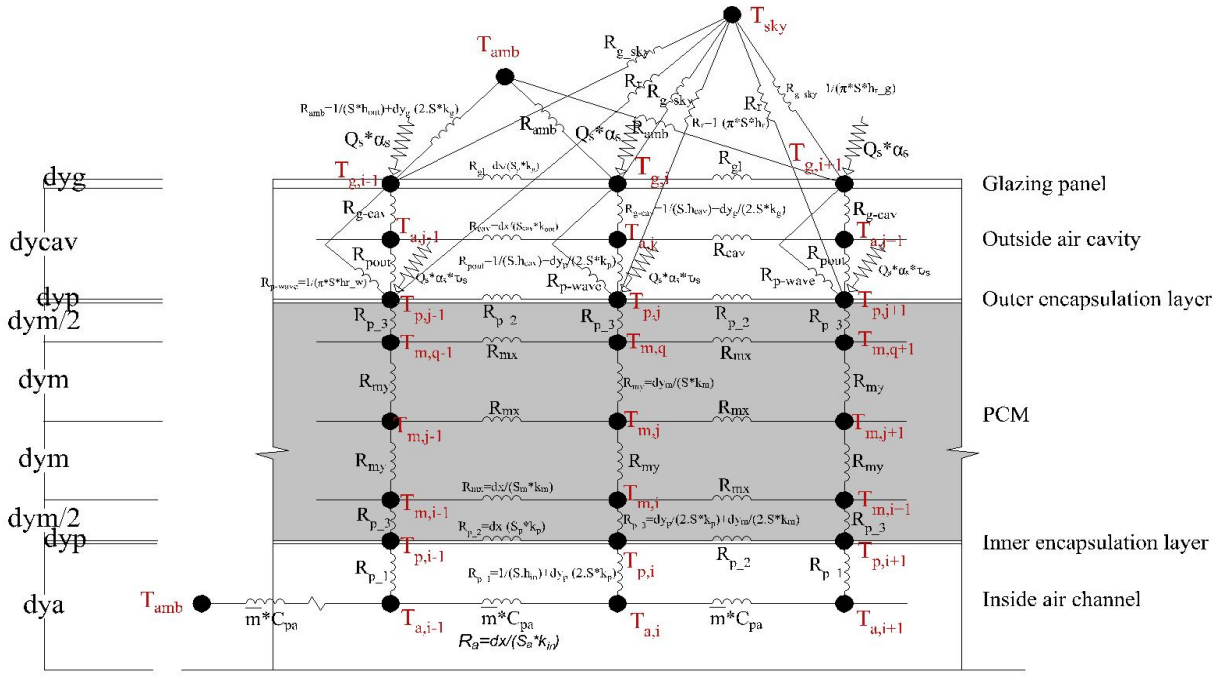

Figure 72. Nodal discretization and thermal network for config-G

The formation of the nodal discretization was developed for all heat transfer media. The model was analyzed in two dimensions: *X* direction (direction of airflow), and *Y* direction (perpendicular to airflow). The model was discretized into *n* number of nodes in the *X* direction,

and *m* number of nodes in the *Y* direction. The resolution of the mesh was represented by discretization lengths in both *X* and *Y* directions. Thicknesses of the air channel, encapsulation layers, air gap, and glazing layer were represented by one node for each layer in the *Y* direction. The PCM discretization length, *dym*, was determined as (PCM thickness / *m*). The discretization length in the *X* direction, *dx*, was an input to the model and defined as 0.1 m. The number of nodes in the *Y* direction of the PCM layer, *m*, was an input to the model and was initially represented by 5 nodes. The number of nodes in the *X* direction, *n*, was calculated in the model according to the total length of the system (*L*) and *dx* as (*L/dx*). Generally, the model considers the system full height as a single discretized length in the *Z* direction assuming that there is no change in the temperature along the *Z* direction. The nodal discretization and the thermal network of the config-G and config-A are presented in Figure 72 and Figure 73, respectively.

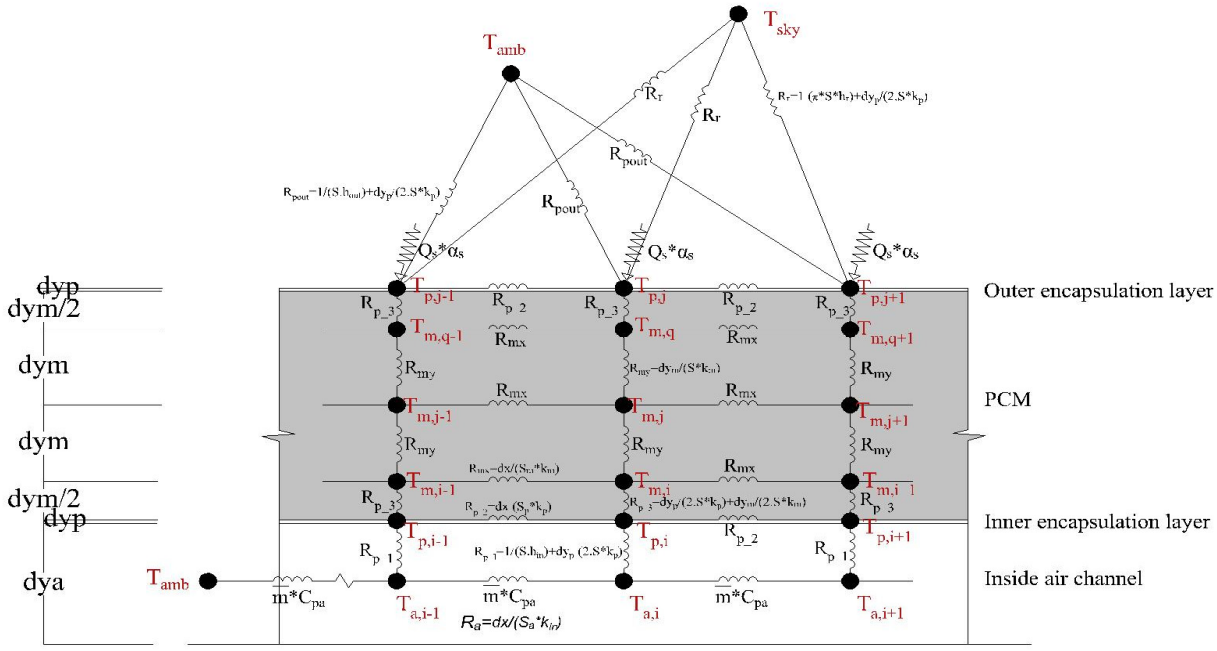

Figure 73. Nodal discretization and thermal network for config-A

4.3.2. Thermal Network

The thermal-electrical analogy is used to represent heat transfer among system elements. The thermal boundary conditions for heat transfer, and accordingly the thermal network, differ according to the configuration. Regarding the config-G presented in Figure 72, the heat transfer media are the internal air channel, encapsulation layers, the PCM, the external air cavity and the

glazing layer. The external thermal boundaries are the thermal radiation and convection to the ambient environment, and solar radiation components. The thermal network includes convective and fluid flow boundaries inside the air channel, conductive thermal resistances through the PCM and encapsulation, convective boundaries between the outer encapsulation and the air cavity, and both convective and radiative boundaries between the glazing layer and the ambient environment. The long-wave radiation heat exchange is taken into consideration between the outer encapsulation layer and the glazing layer, and also between the outer encapsulation and the sky temperature considering the long-wave radiation transmissivity value of the glazing layer, if there is any, according to the type of glazing. The solar transmittance and absorptance values of the glazing are also considered in the determination of the solar gain to the system. Similarly, for the config-A shown in Figure 73, all the energy factors and thermal boundaries are modified to satisfy the changes in the configuration and system elements. All the energy factors are coded in a way which calculates them automatically at the beginning of the simulation when the configuration is identified.

4.3.3. Energy Balance Equations

The finite difference method was used to approximate the spatial derivatives of the energy equations utilizing the implicit technique for solving sets of the energy equations. The implicit technique provides the unconditional model stability regardless of the value of the time step. The average temperature method was introduced to identify the unknown temperature after a specified time interval. The average temperature (T) is the temperature at the mid of the time interval between the current known temperature (T^{t-dt}) and the future unknown temperature (T^{t}) and it can be identified using Equation (11). The consideration of the average temperature increases the model stability and the simulation convergence (Stathopoulos et al., 2016).

$$T = (T^{t-dt} + T^{t})/2 \tag{11}$$

All energy balance equations were formulated with the respect of the average temperature. The energy balance equations for the heat transfer media of the complete system (config-G) are presented by Equations (12) : (20) in Table 11. Details about the formulation and solution of the energy balance equations are presented in Appendix - A.

Table 11. Energy balance equations for all proposed system layers

Internal air channel energy balance equation (in case of airflow):

$$\frac{2 .\rho_a . Cp_a . V_a}{dt}(T_{a,i}-T_{a,i}^{t-dt}) = \dot{m} . Cp_a .(T_{a,i+1}-T_{a,i}) + h_{in}. S .(T_{p,i}-T_{a,i}) \quad (12)$$

Internal air channel energy balance equation (in case of no airflow):

$$\frac{2 .\rho_a . Cp_a . V_a}{dt}(T_{a,i}-T_{a,i}^{t-dt}) = \frac{T_{a,i-1}- 2 .T_{a,i}+T_{a,i+1}}{R_a} + h_{in}. S .(T_{p,i}-T_{a,i}) \quad (13)$$

Inner encapsulation layer energy balance equation:

$$\frac{2 .\rho_p . Cp_p . V_p}{dt}(T_{p,i}-T_{p,i}^{t-dt}) = \frac{T_{a,i}-T_{p,i}}{R_{p_{-1}}} + \frac{T_{p,i-1}-2 .T_{p,i}+T_{p,i+1}}{R_{p_{-2}}} + \frac{T_{m,i}-T_{p,i}}{R_{p-3}} \quad (14)$$

PCM layer energy balance equations:

$$\frac{2 .\rho_m . Cp_m . V_m}{dt}(T_{m,i}-T_{m,i}^{t-dt}) = \frac{T_{p,i}-T_{m,i}}{R_{p_{-3}}} + \frac{T_{m,i-1}-2 .T_{m,i}+T_{m,i+1}}{R_{mx}} + \frac{T_{m,j}-T_{m,i}}{R_{my}} \quad \text{Inner row} \quad (15)$$

$$\frac{2 .\rho_m . Cp_m . V_m}{dt}(T_{m,j}-T_{m,j}^{t-dt}) = \frac{T_{m,j-1}-2 .T_{m,j}+T_{m,j+1}}{R_{mx}} + \frac{T_{m,i}-2 .T_{m,j}+T_{m,q}}{R_{my}} \quad \text{Middle rows} \quad (16)$$

$$\frac{2 .\rho_m . Cp_m . V_m}{dt}(T_{m,q}-T_{m,q}^{t-dt}) = \frac{T_{p,j}-T_{m,q}}{R_{p_{-3}}} + \frac{T_{m,q-1}-2 .T_{m,q}+T_{m,q+1}}{R_{mx}} + \frac{T_{m,j}-T_{m,q}}{R_{my}} \quad \text{Outer row} \quad (17)$$

Outer encapsulation layer energy balance equation:

$$\frac{2 .\rho_p . Cp_p . V_p}{dt}(T_{p,j}-T_{p,j}^{t-dt}) = \frac{T_{m,q}-T_{p,j}}{R_{p_{-3}}} + \frac{T_{p,j-1}-2 .T_{p,j}+T_{p,j+1}}{R_{p_{-2}}} + \frac{T_{a,j}-T_{p,j}}{R_{pout}} + \frac{T_{sky}-T_{p,j}}{R_r} + \frac{T_{g,i}-T_{p,j}}{R_w} + (C1 .Q_s.\alpha_s.\tau_s) \quad (18)$$

External air cavity layer energy balance equation:

$$\frac{2 .\rho_a . Cp_a . V_a}{dt}(T_{a,j}-T_{a,j}^{t-dt}) = \frac{T_{p,j}-T_{a,j}}{R_{pout}} + \frac{T_{a,j-1}-2 .T_{a,j}+T_{a,j+1}}{R_{cav}} + \frac{T_{g,i}-T_{a,j}}{R_{g-cav}} \quad (19)$$

Glazing layer energy balance equation:

$$\frac{2 .\rho_g . Cp_g . V_g}{dt}(T_{g,i}-T_{g,i}^{t-dt}) = \frac{T_{amb}-T_{g,i}}{R_{amb}} + \frac{T_{g,i-1}-2 .T_{g,i}+T_{g,i+1}}{R_{gl}} + \frac{T_{a,j}-T_{g,i}}{R_{g-cav}} + \frac{T_{p,j}-T_{g,i}}{R_g} + \frac{T_{sky}-T_{g,i}}{R_{sky}} + C2 .Q_s.\alpha_s \quad (20)$$

In the previous equations, $T_{location}^{time\ step}$ is the node temperature, dt is the time step, dx is the discretization length in the X direction, and S is the node surface area. Regarding the internal air channel layer (Equations (12 - 13)), ρ_a is the air density which is calculated as a function of air temperature, Cp_a is the air heat capacity, V_a is the air node volume, $\dot{m}$ is the air mass flow rate, h_{in} is the convective heat transfer coefficient for air channel, and $R_a = dx / (S_a \times k_{in})$ where S_a is the cross-sectional area of air channel node ($Y \times Z$), and k_{in} is the air thermal conductivity. The model automatically selects one of the two air channel equations regarding the airflow condition inside the air channel. Regarding the inner encapsulation layer, Equation (14), ρ_p is the encapsulation density, Cp_p is the encapsulation heat capacity, V_p is the encapsulation node volume, $R_{p-1} = dy_p / (2 \times S \times k_p) + 1/(S \times h_{in})$, $R_{p-2} = dx / (S_p \times k_p)$, $R_{p-3} = dy_p / (2 \times S \times k_p) + dy_m / (2 \times S \times k_m)$ where dy_p, dy_m are the discretization lengths of the encapsulation and PCM in the Y direction, k_p, k_m are the encapsulation and PCM thermal conductivity, S_p is the cross-sectional area of the encapsulation node ($Y \times Z$). Regarding the PCM layer (Equations (15) : (17)), ρ_m is the PCM density, Cp_m is the PCM heat capacity, V_m is the PCM node volume, $R_{mx} = dx/(S_m \times k_m)$, $R_{my} = dy_m/(S \times k_m)$, $T_{m,i}$ is the PCM temperature of the inner row nodes, $T_{m,j}$ is the PCM temperature of the middle rows nodes, and $T_{m,q}$ is the PCM temperature of the outer row nodes. Regarding the outer encapsulation layer, Equation (18), $R_{pout} = 1/(S \times h_{cav})+dy_p/(2 \times S \times k_p)$, $R_r = 1/(\pi \times S \times h_r)+dy_p/(2 \times S \times k_p)$, $R_w = 1/(\pi \times S \times h_w) +dy_p/(2 \times S \times k_p)$, where h_{cav} is the convective heat transfer coefficient for the outer cavity and it is calculated according to the convection model, h_r is the radiative heat transfer coefficient to the sky component (in case of thermal transmittance value of the glazing), h_w is the radiative heat transfer coefficient to the glazing layer, $C1$ is the encapsulation node capacitance, Q_s is the solar gain (W/m^2), α_s is the solar absorptance of the encapsulation layer, and τ_s is the solar transmittance of the glazing layer. All the radiative heat transfer coefficients are calculated according to the thermal radiation sub-model. The mentioned energy balance equation for the outer encapsulation is for config-G. In case of config-A, the thermal radiation component with the glazing layer is eliminated, the convection component with the external air cavity temperature is replaced by the convection with the ambient temperature. Regarding the external air cavity layer, Equation (19), $R_{g-cav} = 1/(S \times h_{cav}) + dy_g/(2 \times S \times k_g)$, $R_{cav} = dx/(S_{cav} \times k_{out})$, where dy_g is the discretization length in the Y direction, k_g is the glazing thermal conductivity, S_{cav} is the cross-sectional area for the

external air cavity, and k_{out} is the air thermal conductivity inside the air cavity. For the glazing layer, Equation (20), ρ_g is the glazing density, Cp_g is the glazing heat capacity, V_g is the glazing node volume, $C2$ is the node capacitance, $R_{amb} = 1/(S \times h_{out}) + dy_g/(2 \times S \times k_g)$, $R_g = 1/(\pi \times S \times h_w) + dy_g/(2 \times S \times k_g)$, $R_{sky} = 1/(\pi \times S \times h_g)$, $R_{gl} = dx/(S_g \times k_g)$, where h_{out} is the convective heat transfer coefficient for the ambient air calculated by the convection sub-model, h_g is the radiative heat transfer coefficient to the sky temperature determined by the radiation sub-model, α_s is the glazing solar absorptance, and S_g is the cross-sectional area for the glazing layer.

4.3.4. Convection Heat Transfer Sub-model

The convective heat transfer coefficients were calculated for the inner channel (h_{in}), the outermost layer of the system (the encapsulation layer in config-A and the glazing layer in config-G) (h_{out}), and the external air cavity, in case of config-G, (h_{cav}) according to the general Equation (21).

$$Nu_D = h \,.\, D_h / k \tag{21}$$

where D_h is the hydraulic diameter, and k is the air thermal conductivity. The model is configured to adapt the determination of the convective heat transfer coefficients according to the air velocity values, system configuration, system orientation, and the wind direction. The Nusselt number is evaluated in each time step according to the driving forces (buoyancy and wind-driven forces). Regarding the calculations of the free convection, Rayleigh (Ra) and Grashof (Gr) numbers are evaluated regarding the temperature difference between the surface (T_s) and heat transfer fluid (T_{HTF}) as shown in Equations (22) and (23).

$$Ra = Pr \,.\, Gr \tag{22}$$

$$Gr = g \,.\, \beta \,.\, |(T_s - T_{HTF})| \, L^3 / \upsilon^2 \tag{23}$$

where Pr is the Prandlt number, g is the standard gravity, β is the volumetric thermal expansion coefficient, L is the characteristic length, and υ is the kinematic viscosity. Various empirical correlations for the determination of the Nusselt number regarding free convection forces are presented in Table 12. The proposed correlations are based on conditions mentioned by Cengel, Yunus, (2003) and Incropera et al. (2007) regarding the system configuration and airflow conditions. In case with no airflow inside the air channel, the model considers the internal air

channel as an enclosure. In case of non-zero airflow, empirical correlations for natural convection over flat surfaces are used to determine the heat transfer condition.

Table 12. Correlations for Nusselt number for free convection (Cengel, Yunus, 2003; Incropera et al. 2007)

In case of horizontal closure (no airflow)		
when $T_{HTF} \geq T_s$	$Nu_{nat}=0.195\times Ra^{1/4}$	$Ra < 4\times10^5$
	$Nu_{nat}=0.068\times Ra^{1/3}$	$Ra \geq 4\times10^5$
when $T_{HTF} < T_s$	$Nu_{nat}= 1$	
In case of vertical closure (no airflow)		
	$Nu_{nat}=0.2\left(\frac{Pr\,.\,Ra}{(0.2+Pr)}\right)^{0.28}\left(\frac{H}{L}\right)^{-1/4}$	
In case of the horizontal channel/external layer (airflow)		
when $T_{HTF} \geq T_s$	$Nu_{nat}=0.54\times Ra^{1/4}$	$Ra < 10^7$
	$Nu_{nat}=0.15\times Ra^{1/3}$	$Ra \geq 10^7$
when $T_{HTF} < T_s$	$Nu_{nat}= 0.27\times Ra^{1/4}$	
In case of the vertical channel/external layer (airflow)		
	$Nu_{nat}=0.59\times Ra^{1/4}$	$Ra < 10^9$
	$Nu_{nat}=0.1\times Ra^{1/3}$	$Ra \geq 10^9$

Regarding the forced convection mode inside the air channel, the empirical correlations for the Nusselt number are presented in Table 13. When the model considers the airflow inside the channel as forced convection, turbulent and laminar flow regimes are considered according to the value of Reynolds number (Re) which depends mainly on the air velocity value (V) and hydraulic diameter (D_h), and is calculated according to Equation (24). The flow is considered laminar if ($0 < Re \leq 2000$), and turbulent when ($Re > 2000$). The transitional flow regime is assumed to be calculated as the turbulent regime. For turbulent flow regime, the friction coefficient (f) is calculated inside the air channel as in smooth channels according to Equation (25).

Table 13. Correlations for the Nusselt number for forced convection in the internal air channel (Çengel, Yunus, 2003; Incropera et al. 2007)

Turbulent flow	$Nu_{for}=\frac{\left(\frac{f}{8}\right)(Re-1000)\,Pr}{1+12.7\left(\frac{f}{8}\right)^{1/2}(Pr^{2/3}-1)}$

Laminar flow	$Nu_{for\_d} = 7.54 + \frac{(\frac{0.03\, D_h}{L})\, Re\, Pr}{1+0.016\,[(\frac{D_h}{L})\, Re\, Pr]^{2/3}}$	Developing flow
	$Nu_{for\_f} = 7.54$	Fully developed flow
	If $0.2\, L \leq L_t < L$	$Nu_{for} = \frac{(Nu_{for\_d} + Nu_{for\_d})}{2}$
	If $L_t \geq L$	$Nu_{for} = Nu_{for\_d}$
	If $0.2\, L > L_t$	$Nu_{for} = Nu_{for\_f}$

$$Re = V \,.\, D_h \,/\, \upsilon \tag{24}$$

$$f=(0.79 \;\; ln\, Re - 1.64)^{-2} \tag{25}$$

Regarding laminar flow calculations inside the air channel, the entry thermal length (L_t) is considered to identify whether the flow is developing or fully developed. The thermal length is calculated by Equation (26). Referring to Table 13, if $0.2\, L < L_t < L$, both developing and fully developed flows are considered assuming half of the system length to behave as a developing flow. Otherwise, either developing or fully developed flow is considered.

$$L_t = 0.05\, Re\, D_h \tag{26}$$

Regarding the convection over the system outermost surface, both natural and forced convection are considered. The Reynolds number is recalculated regarding the ambient conditions, and the flow regime is considered as an external forced convection over plates taking into account the system orientation. The wind direction is considered for two cases: 1- wind is parallel to the system characteristic length (case-1), and 2- wind is perpendicular to the system characteristic length (case-2). The empirical correlations for the Nusselt number for forced convection over flat plates are used as shown in Table 14.

Table 14. Correlations for the Nusselt number for ambient forced convection (Cengel, Yunus, 2003; Incropera et al. 2007)

Horizontal configuration	$Nu_{for\text{-}amb} = [(0.037\; Re_{out}^{0.8}) - 871]\, Pr^{1/3}$	$Re_{out} \geq 5\times10^5$
	$Nu_{for\text{-}amb} = 0.664\; Re_{out}^{1/2}\, Pr^{1/3}$	$0 < Re_{out} < 5\times10^5$
Vertical configuration	Wind direction (case-1)	
	$Nu_{for\text{-}amb} = [(0.037\; Re_{out}^{0.8}) - 871]\, Pr^{1/3}$	$Re_{out} \geq 5\times10^5$

	$Nu_{for\text{-}amb}=0.664\ Re_{out}^{1/2}\ Pr^{1/3}$	$0 < Re_{out} < 5\times10^{5}$
	Wind direction (case-2)	
	$Nu_{for\text{-}amb}=0.228\ Re_{out}^{0.731}\ Pr^{1/3}$	

In all cases, the correlations of Nusselt number for both free and forced convection are calculated and the ratio (Gr/Re^2) is evaluated; where Gr is the Grashof number representing the free convection driving forces, and Re is Reynolds number representing the forced convection driving forces. As shown in Table 15, in the case of (Gr/Re^2) >10, the free convection mode is dominating and is only considered. In the case of (Gr/Re^2) <0.1, the forced convection mode is dominating and is only considered. In case of 0.1< (Gr/Re^2) <10, then the mixed convection mode is considered; as it can be claimed that both driving forces have a contribution in the heat transfer process. Accordingly, convective heat transfer coefficients are determined regarding the associated Nusselt numbers which are recalculated in each time step and updated according to the air velocity and the temperature difference between the air and the surface temperature of the PCM panel.

Table 15. Determination of the Nusselt number for free, forced, and mixed convection conditions (Cengel, Yunus, 2003; Incropera et al. 2007)

If $Re = 0$		$Nu_{in} = Nu_{nat}$	*(Free convection)*
If $Re > 0$	if $Gr/Re^2 > 10$	$Nu_{in} = Nu_{nat}$	*(Free convection)*
	if $Gr/Re^2 < 0.1$	$Nu_{in} = Nu_{for}$	*(Forced convection)*
	if $0.1 \le Gr/Re^2 \le 10$	$Nu_{in} = (Nu_{for}^3 + Nu_{nat}^3)^{1/3}$	*(Mixed convection)*

4.3.5. Radiation Heat Transfer Sub-model

The whole system has three long-wave radiative heat transfer components: h_r (the radiative heat transfer coefficient between the outer encapsulation layer and the sky in case of glazing thermal transmittance), h_g (the radiative heat transfer coefficient between the glazing and the sky), and h_w (the radiative heat transfer coefficient between the outer encapsulation layer and the glazing). All the radiative heat transfer coefficients are calculated according to the Stefan-Boltzmann equation (Cengel, Yunus, 2003; Incropera et al. 2007) . The radiative heat exchange is considered by the

radiative power (Q_r) assuming the encapsulation layer and the glazing layer as grey surfaces, and the sky as a black body. The radiative heat transfer coefficients are calculated by Equations (27): (29) included in Table 16.

Table 16. Calculations of radiative heat transfer coefficients (Cengel, Yunus, 2003; Incropera et al. 2007)

The radiative heat exchange between the encapsulation layer and the sky $Q_{r\text{-}r} = \varepsilon_p.\tau_g.\sigma.F.(T_p^4 - T_{sky}^4)$ $Q_{r\text{-}r} = h_r.A.(T_p - T_{sky})$	(27)
The radiative heat exchange between the glazing layer and the sky $Q_{r\text{-}g} = \varepsilon_g.\sigma.F.(T_g^4 - T_{sky}^4)$ $Q_{r\text{-}g} = h_g.A.(T_g - T_{sky})$	(28)
The radiative heat exchange between the encapsulation layer and the glazing layer $Q_{r\text{-}w} = \varepsilon_p.\varepsilon_g.\sigma.F_1.(T_p^4 - T_g^4)$ $Q_{r\text{-}w} = h_w.A.(T_p - T_g)$	(29)

In Table 16, ε_p is the surface emissivity of the encapsulation layer, ε_g is the surface emissivity of the glazing layer, τ_g is the glazing long-wave transmittance (in case of config-G), σ is the Stefan-Boltzmann constant, which is equal to 5.67×10^{-8} W/m^2.K^4, F is the sky view factor which assumed to be 1 and 0.5 for horizontal and vertical configurations respectively, F_1 is the view factor between the glazing and encapsulation parallel surfaces which is assumed to be 1, A is the hemispherical area of the node where the multi-directional radiative exchange occurs (it is assumed to be equal to $\pi.S$ (Incropera et al. 2007)), where S is the node surface area, T_p, T_{sky}, and T_g are the temperatures of the encapsulation layer, the sky, and the glazing layer, respectively. Mostly, the glazing transmittance is set to zero because most of the glazing types are opaque to long-wave thermal radiation.

4.3.6. Determination of Sky Temperature

The effective sky temperature refers to the temperature of the lower atmospheric layer. The main three parameters that affect the determination of the effective sky temperature are the ambient air temperature, the moisture content of the air, and the cloud cover. The exposure to the clear sky during dry conditions promotes the concept of radiative cooling. Thus, the lower the cloud cover,

the relative humidity, and the ambient air temperature, the greater the radiative cooling potential in a given location (Adelard et al., 1998; AL-Lami et al., 2017) . The correlation in Equation (30) proposed by Adelard et al. (1998) is used for the determination of the sky temperature (T_{sky}) considering the ambient air temperature (T_a), the water steam pressure (P_w), and the cloud cover (N).

$$T_{sky}=(L/\sigma)^{0.25} \tag{30}$$

$$\text{Where:} \quad L=L_o(1+0.01\,A)+(BC(8-N)/8)$$

$$L_o=3.6\,T_a+231$$

$$A=10.1\,\ln(P_w)-12.3$$

$$B=1.7\,T_a+107$$

$$C=-0.22\,\ln(P_w)+1.25$$

The water steam pressure in air is ascertained due to the value of the relative humidity (RH) using Equation (31) based on ASHRAE psychrometric calculations (ASHRAE 2009) .

$$RH=P_w/P_{ws}\,.100\% \tag{31}$$

$$\text{Where:} \quad P_{ws}=d\,.\,10\text{^}(m.\,T_a/(T_a+n))$$

In Equation (31), T_a is the air temperature in ˚C, P_{ws} is the water steam saturation pressure, RH is the relative humidity, $d, m,$ and n are constants determined according to Table 17 considering the air temperature.

Table 17 –Constants for Equation (31) (ASHRAE 2009)

Air temperature	*d*	*m*	*n*
-20˚C: +50˚C	6.116441	7.591386	240.7263
+50˚C: +100˚C	6.004918	7.337936	229.3975

4.3.7. Model Potential and Assumptions

The set of energy balance equations is numerically solved using MATLAB 2015. The numerical model is linked to SimuLink environment as a model interface. All ambient conditions are used as inputs in the MATLAB program; ambient conditions can be user-defined or real data from a

weather data file. The system configuration (config-A or config-G), the orientation (horizontal or vertical), wind direction (parallel or perpendicular), system dimensions and time step must be determined at the beginning of each simulation. All other model variables are automatically calculated. The thermal properties of the air and PCM are functions of the temperature; a linear interpolation of thermal properties values over the temperature is applied. The number of system nodes is calculated according to system inputs; this enables dividing the PCM panel into parts promoting the application of using multiple PCM approach with different properties for each part. The numerical model is flexible in terms of providing various applications as it is adapted to various convection conditions which promote real applications with varying air velocities. The model automatically handles different cases of free, forced, or mixed convection scenarios according to the air velocity, system configuration, system orientation, and wind direction. The model shows flexibility in terms of applying different heating/cooling heat capacity curves according to applications and availability of data. The model shows a good simulation stability in terms of simulation convergence regardless of the time step. The whole numerical model is presented as a stand-alone model for the PAHX system for building envelope applications. This model can be coupled with building ventilation systems into whole building models in any thermal simulation platform.

The model applies some simplifications; it neglects natural convection inside the PCM in terms of tracing the solid/liquid interface during the phase change. This assumption was justified in the literature as the natural convection effect can be neglected in the flat encapsulation of relatively small thicknesses, especially in horizontal configurations (Mosaffa et al., 2013). A linear interpolation of the PCM thermal conductivity from the solid to liquid phase is considered to represent the phase change; no effective thermal conductivity method is followed. Another important assumption is that the model considers the convective heat transfer coefficient with an average value along the system length by getting the average of the calculated values of all the nodes inside each air layer. Thus, one value of the convective coefficient is provided in each time step. The air velocity value in the internal air channel is a model input. This is considered as a limitation in designing the system under wind-driven airflow conditions without experimental prototyping. In such cases, providing the ambient air velocity to represent the internal air velocity is not an accurate assumption due to pressure and temperature differences. However,

developing a correlation between the internal and ambient air velocities is recommended for designing the system under natural airflow conditions.

The model is limited to the PAHX envelope type with boundary conditions related to thermal radiation and convection. It cannot be directly used for other PAHX types. Also, the current model supports only horizontal and vertical configurations; the inclined configuration is not supported. One practical limitation of the proposed application is that the air (inside the air channel or the ambient air in contact with the outer surface) could reach its dew point temperature due to cooling which could lead to some condensation which may reduce the system efficiency. This can be a limitation of the application in hot and humid climates; this practical issue should be considered in further developments of the model and follow-up studies of the system.

4.4. Model Validation

The validation of the developed model described in Section 4.3 was conducted in two phases: the validation of the entire model against data acquired experimentally with the use of prototypes described in Sections 3.2 and 3.3, and the inter-model validation, in which some sub-models of the entire developed model were compared with other models under identical conditions. The radiation and sky temperature sub-models were considered in the process of the inter-model validation to assess their accuracy and the level of calibration.

4.4.1. Validation of The Model Against Experimental Data

The validation investigations were conducted according to the ASHRAE Guideline 14 for energy measurements (ASHRAE, 2002). This guideline proposes data validation criteria for the comparison of the numerical results with reference (experimental) data. The proposed criteria were discussed in (Roccamena et al., 2019) applying a PCM-based thermal storage system. The guideline describes the uncertainty of numerical models using two criteria: Normalized Mean Bias Error (NMBE) and Coefficient of Variation of Root Mean Square Error (CVRMSE). The definitions of the NMBE and CVRMSE criteria are presented in Equation (32) and Equation (33), respectively.

$$NMBE = \Sigma_{i=1}^{n}(y_{s(i)} - y_{ref(i)}) / (\bar{y}_{ref} \times n) \times 100 \quad (\%) \tag{32}$$

$$CVRMSE = \left[\sqrt{\Sigma_{i=1}^{n} (y_{s(i)} - y_{ref(i)})^2 / n} \right] / \bar{y}_{ref} \times 100 \quad (\%) \tag{33}$$

For detailed data simulations, this guideline claims that the numerical models can be considered as calibrated with the reference data when the NMBE is within the range ±10%, and the CVRMSE is below 30%. Furthermore, another criterion - the maximum deviation - was applied for the identification of the maximum deviation of the hourly-average simulated data from the reference data. The time step of the model was set to 20 seconds, and the hourly-average data were selected to avoid discrepancies in the detailed data set. The maximum deviation was determined according to Equation (34).

$$Max\ Dev. = Max \left\{ {}_{1}^{m} \left| \Sigma_{i=1}^{j} y_{s(i)} - \Sigma_{i=1}^{j} y_{ref(i)} \right| \right\} \ (^{\circ}C) \tag{34}$$

Referring to the previous equations (32), (33), and (34), y_s is a numerically simulated value, y_{ref} is a reference value from the experimental measurement at the same time instance, $\bar{y}_{ref}$ is the average value of the measured values y_{ref}, n is the total number of the measurement samples, j is the number of the measurement samples per hour, and m is the number of measured hours included in the investigated dataset. All simulated and experimental temperatures used in the evaluation of NMBE and CVRMSE were in degrees of Celsius (˚C). The validation of the entire model was conducted by means of the comparison of numerical results with experimentally obtained data for both the configurations (config-A and config-G), for both the prototypes, and for various experimental scenarios (discussed earlier in Section 3.3.3). This means that the validation process of the PAHX model was performed using two different types of the PCM having distinct thermophysical properties.

Generally, the numerical simulation was designed to meet the identical setup of the scenario, orientation, configuration, and procedures with the experimental investigation. The weather data (the ambient air temperature, the relative humidity, the ambient air velocity, and the intensity of solar radiation) for the considered days of the experiments were linked to the numerical model as inputs. The percentage of the cloud cover was estimated as a constant value during each experiment. The estimation of the cloud cover was according to the observation of the sky conditions and the interpretation of the weather data during the experiments. It is worth mentioning that the model did not consider the changes in cloudiness during a certain

experiment/simulation. Accordingly, the sky temperature was calculated by the sub-model according to the relative humidity, ambient air temperature, and the estimated cloud cover. The thermophysical properties of the PCM were provided by the PCM manufacturers. Moreover, the surface properties (emissivity, absorptivity, and transmissivity) of the panel and glazing layer were assumed with regard to the materials used in the experiment.

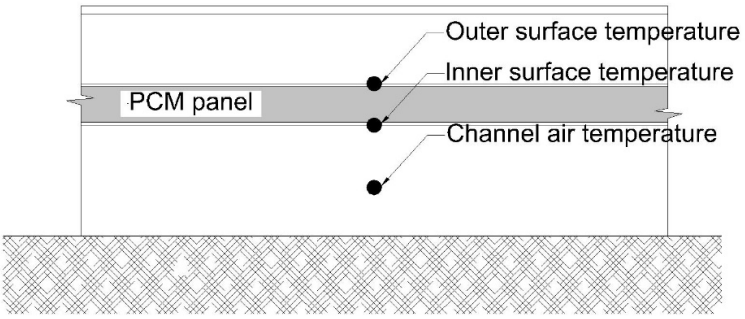

Figure 74. Nodal temperatures used in the comparison between simulation and experiment

Table 18 – NMBE, CVRMSE, and maximum deviation values for the model validation results

Prototype	Experimental Scenario	Duration of Experiment	n	NMBE (%)			CVRMSE (%)			MAX DEV. (˚C)		
				Inner surface Temp.	Outer surface Temp.	Air channel Temp.	Inner surface Temp.	Outer surface Temp.	Air channel Temp.	Inner surface Temp.	Outer surface Temp.	Air channel Temp.
1	1 & 2	23h:47min	4284	1.39	-0.6	2.1	6.48	6.08	6.36	5.98	3.47	3.15
	3	22h:29min	4048	-1.7	-3.6	4.3	7.1	14.6	8.5	5.71	8.5	5.25
	4 & 6	24h:42min	4448	-3.3	0.9	-6.6	6.1	9.2	11.2	8.79	10.12	5.43
2	1 & 2	23h:47min	4284	-9.5	-4.2	-5.3	10.6	6.5	8.2	5.59	3.7	3.93
	3	20h:03min	3610	0.3	4.2	7.6	10.1	8.6	10.4	8.63	4.77	6.36
	3 & 5	22h:30min	4050	0.1	4.4	3.6	7.3	9.3	4.4	5.22	4.2	2.29

The internal air velocity and the inlet air temperature to the air channel were obtained directly from the experimental measurements and provided to the model. The experimental investigations were carried out for several days. Every experimental investigation was conducted for a complete cycle of the solidification and melting, which resulted in almost a 24-hour investigation. For each investigation three nodal temperatures, shown in Figure 74, were compared with three experimentally determined reference temperatures (the temperature of the

inner surface of the PCM panel, the temperature of the outer surface temperature of the PCM panel, and the air temperature inside the air channel). The validation results are summarized in Table 18. In prototype 01, experimental scenarios 1, 2, 3, 4, and 6 were applied for comparison with the experimental data.

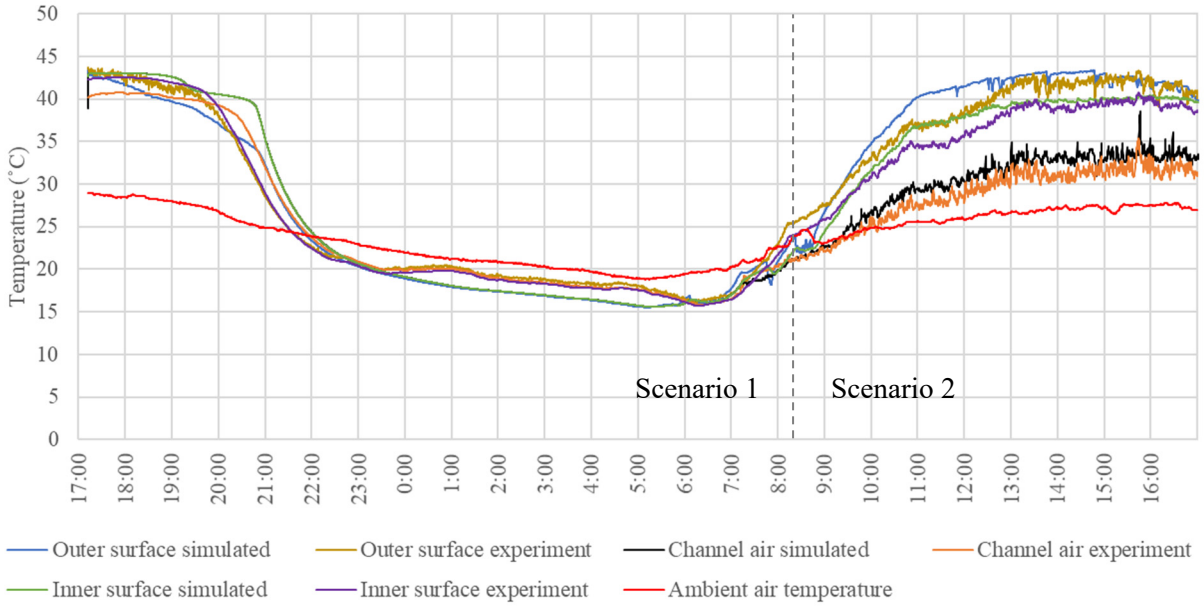

Figure 75. Validation results for prototype 01, scenarios 1 and 2

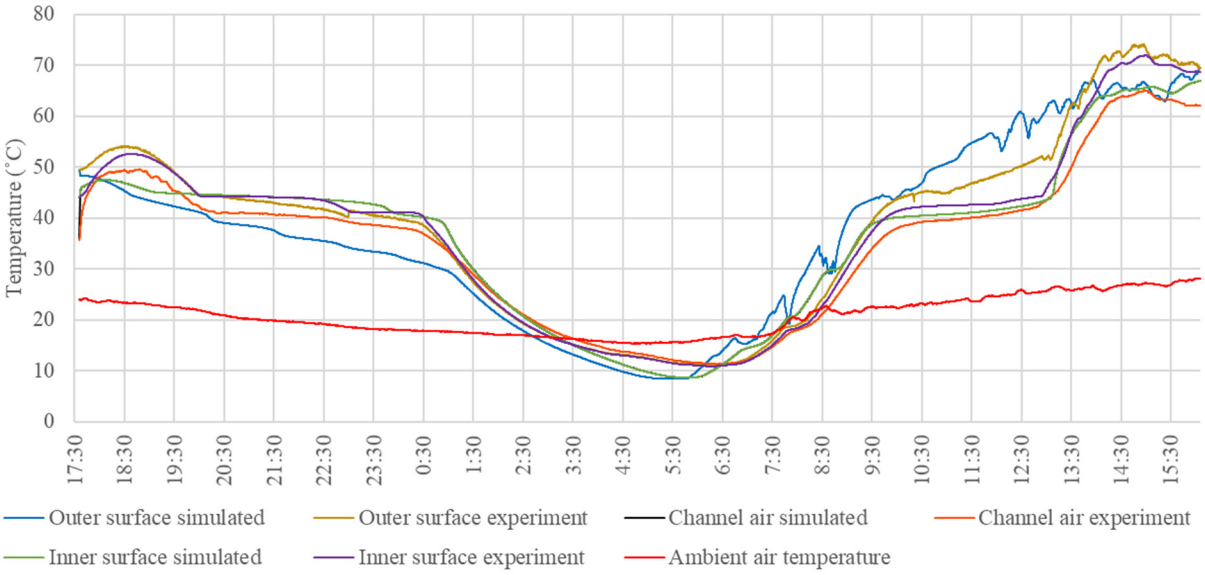

Figure 76. Validation results for prototype 01, scenario 3

Figure 75 shows the validation of the numerical results for scenario 1 (config-A with closed air channel) during night-time and early morning (cooling charging) and scenario 2 (config-A with

the opened air channel) during daytime. Figure 76 shows the temperature evolution of the three nodes in comparison with the measured data for these nodes for scenario 3 (config-G with closed air channel). Figure 77 shows the validation of the numerical results for scenario 4 (config-G with the opened air channel) during daytime, and scenario 6 (config-G with an insulation layer and opened air channel) during the night-time and early morning periods.

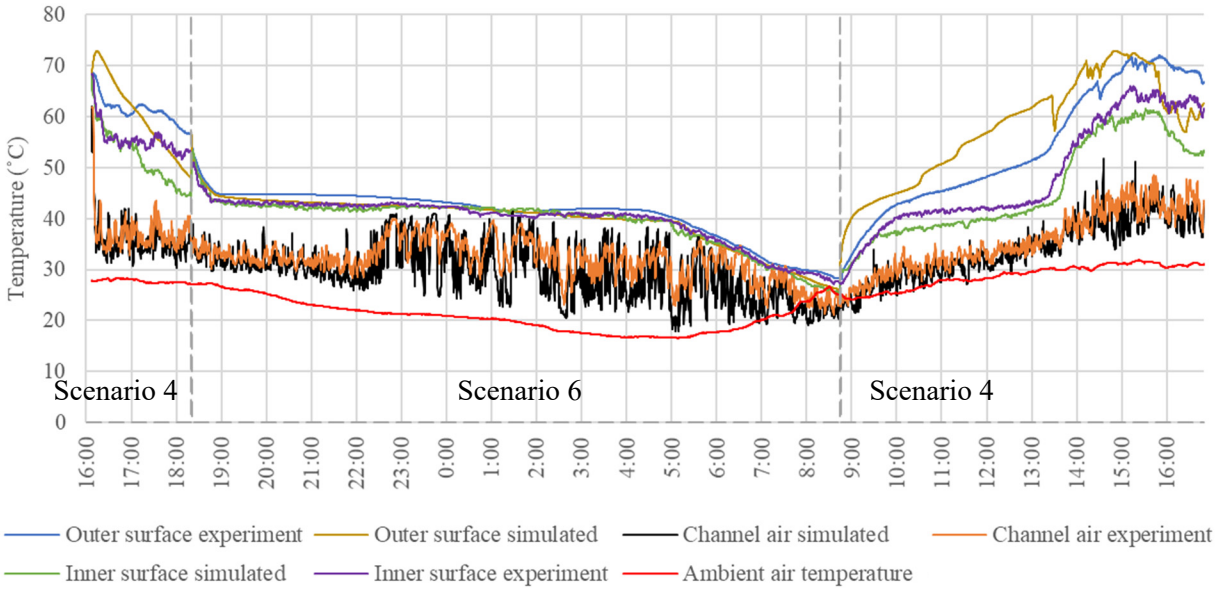

Figure 77. Validation results for prototype 01, scenarios 4 and 6

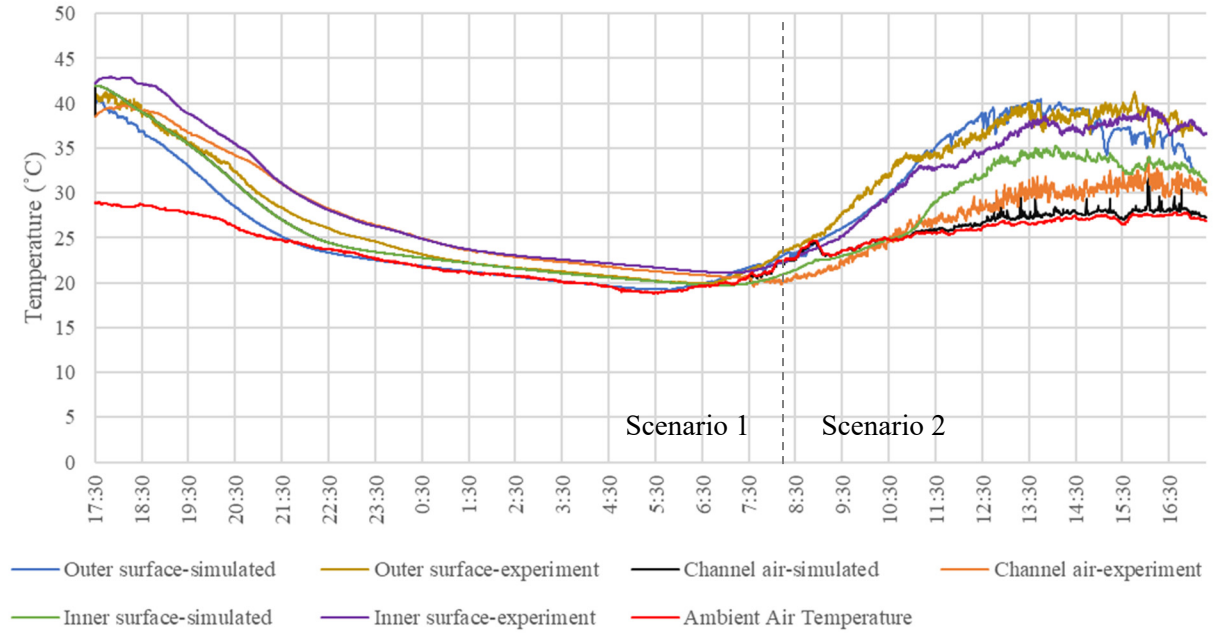

Figure 78. Validation results for prototype 02, scenarios 1 and 2

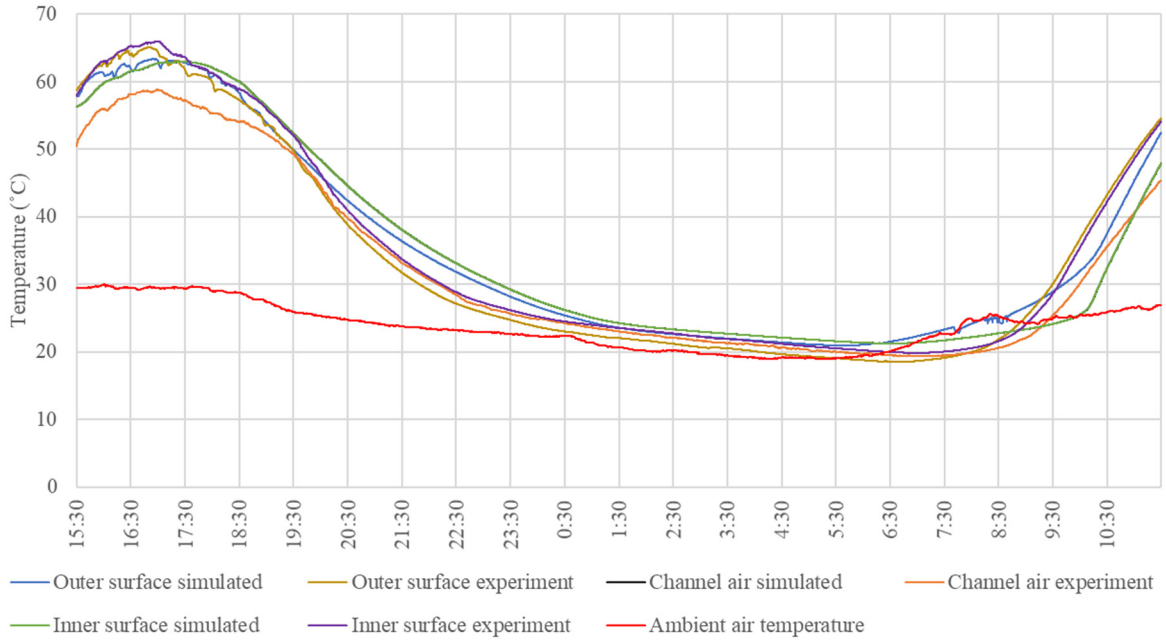

Figure 79. Validation results for prototype 02, scenario 3

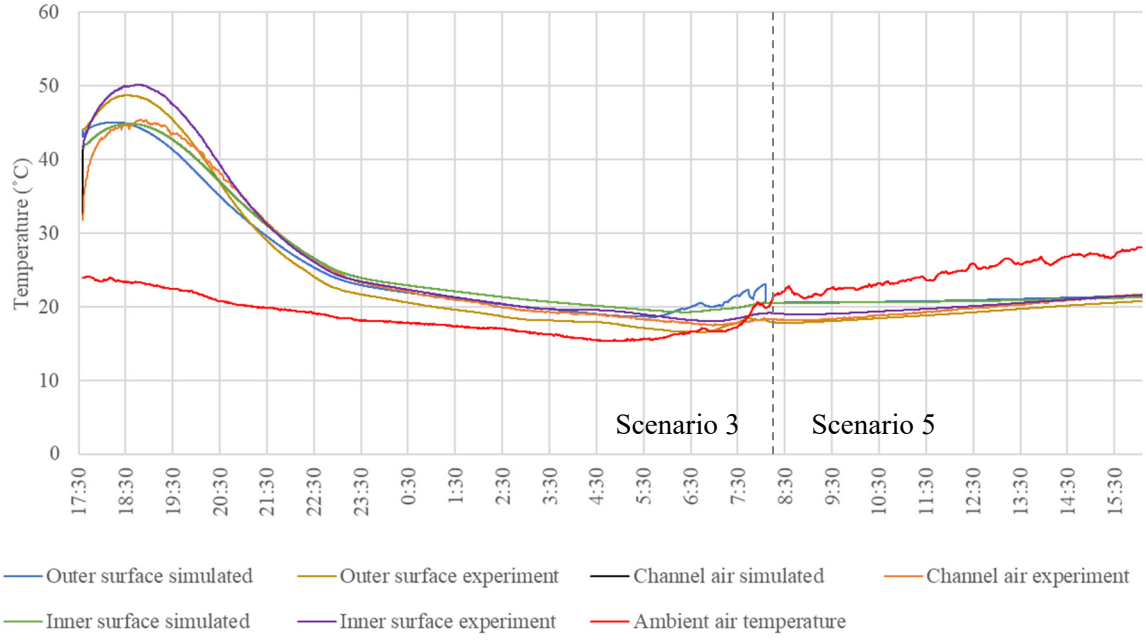

Figure 80. Validation results for prototype 02, scenarios 3 and 5

In prototype 02, experimental scenarios 1, 2, 3, and 5 were applied for validation investigation. Figure 78 shows the validation results for scenario 1 (config-A with closed air channel) during cooling charging (night-time and early morning) and scenario 2 (config-A with open-air channel) during daytime (cooling discharging). Figure 79 shows the validation results for scenario 3

(config-G with closed air channel). Figure 80 shows the validation of scenario 3 during cooling charging (night-time and early morning) and scenario 6 (config-G with an insulation layer and closed air channel) applying an energy preservation strategy during daytime. In all cases of no airflow, it can be noticed that the temperature of the air channel was identical to the temperature of the inner surface of the PCM panel in the numerical model calculations. This is due to the ideal equilibrium of heat transfer in the model which is not achieved in the real condition.

4.4.2. Inter-Model Validation

The inter-model validation was conducted to calibrate the thermal radiation exchange sub-model and the sky temperature sub-model. Regarding the thermal radiation exchange sub-model, COMSOL Multiphysics software (COMSOL-AB, 2017) was used to compare the developed sub-model, described in Section 4.3.5, with the radiation model included in COMSOL. The COMSOL uses a surface-to-surface radiation heat transfer model to calculate the radiation exchange in dependence to the surface radiosity as:

$$\dot{Q}_i = A_i.\varepsilon_i / (1-\varepsilon_i) \,.\, (J_i - E_i) \quad (W) \tag{35}$$

where $\dot{Q}_i$ is the net rate of radiation heat transfer from the surface i, A_i and ε_i are the area and the emissivity of the surface, respectively. The surface radiosity J_i is the total radiation energy leaving the surface per unit area and per unit time, and E_i is the incident radiation on the surface i, which equals to $(n^2.\ \sigma.\ T_i^4)$; where n is the refractive index, and T_i is the temperature of the surface. A specific configuration was designed to investigate the radiation heat exchange between two parallel plates with the dimensions of 3×2 m^2 and an air gap of 0.05 m between the plates. The same configuration was adopted in both the models in terms of dimensions, spacing, and materials. The plates were made of aluminum (representing the PCM panel) and glass (representing the glazing layer). Both models used identical physical, optical, and thermal properties of the layers. The boundary and initial conditions were set to be identical as well. The two models simulated the radiation heat exchange between the two plates, conductive heat transfer through the plates, and convective heat transfer in the air layer. Neither the transmissivity of the glazing layer nor the sky temperature was considered. The same criteria (NMBE and CVRMSE) as in case of the validation of the model against experimental data were used to evaluate the model in the inter-model validation process. Figure 81 shows the

temperature behavior of the plates for a 2.5-hour simulation. The NMBE and CVRMSE were calculated for both the surfaces. For the encapsulation layer (aluminum), the NMBE was -1.57%, and the CVRMSE was 2.43%. For the glazing layer (glass), the NMBE was 4.36%, and the CVRMSE was 5.1%. According to ASHRAE Guideline 14, the inter-model comparison shows that the developed radiative heat exchange sub-model is within the acceptable limits for the model calibration.

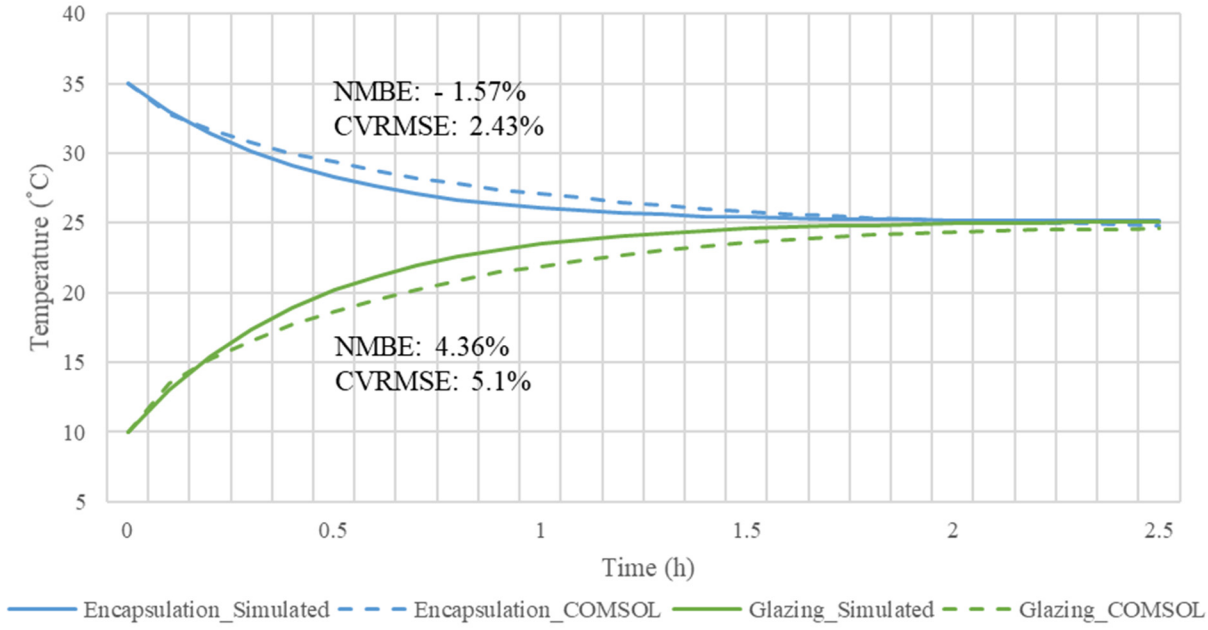

Figure 81. Temperature behavior of encapsulation and glazing layers under thermal radiation exchange

For another specific validation of the proposed sky temperature sub-model discussed in Section 4.3.6, another model-to-model calibration process was conducted. The developed sky temperature sub-model was compared with the Swinbank model of the sky temperature (Swinbank, W.C. 1963). The model advised by Swinbank, and improved by Cole (Cole, R.J. 1976) proposes a sky temperature model that depends on the ambient temperature (T_a), the cloud cover (C), and the apparent emissivity of the atmospheric layer (ε_c). Equation (36) represents Swinbank model; the value of the cloud cover ranges from 0 for a clear sky to 1 for a cloudy sky.

$$T_{sky}^4 = 9.365574\times10^{-6}(1-C)\,T_a^6+(T_a^4.\,C.\,\varepsilon_c)$$

$$\varepsilon_c=(1-0.84\,C)(0.527+0.161\,exp(8.45(1-273/T_a)))+0.84\,C \quad (36)$$

Considering the same range of the ambient air temperatures, the sky temperature was simulated using both models under clear sky and cloudy conditions. Again, the NMBE and CVRMSE were applied to evaluate the inter-model comparison. Figure 82 shows that for the clear sky investigation, NMBE was 8.05% and CVRMSE was 15.74%. For cloudy conditions, the investigation reveals that NMBE was 4.01% and CVRMSE was 4.09%. This means that the developed sky temperature sub-model is within the accepted range of model calibration when compared to the Swinbank model for determining the sky temperature.

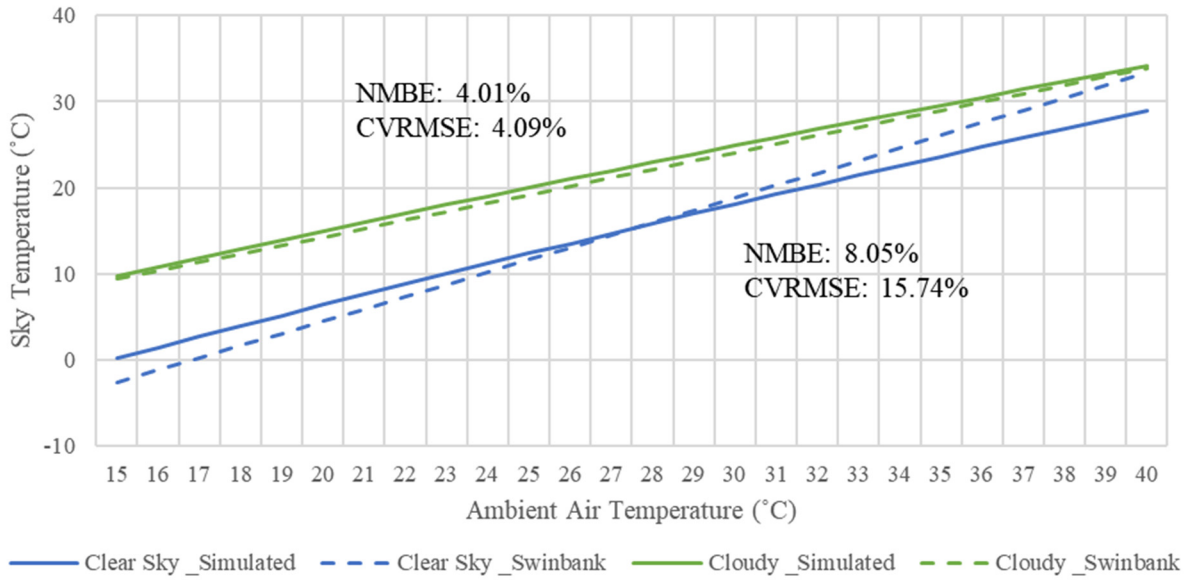

Figure 82. Determination of the sky temperature under clear and cloudy conditions

4.5. Parametric Investigation

A numerical analysis was conducted to assess the thermal response of the developed model to system parameters of the air velocity inside the air channel and the ambient/inlet air temperature to test the model response towards the sensitive changes of inlet air temperature and velocity values. The glazed configuration (config-G) with the horizontal orientation was considered for the developed PAHX system using Rubitherm RT44HC with the PCT range of 40 ˚C - 44 ˚C. The investigation assumed 36 hours of operation (solidification – melting - solidification processes) under clear sky conditions. In the first part of the analysis, the thermal behavior of the PCM panel was tracked under different values of the air velocity inside the air channel. The initial temperature of the system was 25 ˚C, and the inlet air temperature was considered

identical to the ambient air temperature. Values of the air velocity inside the air channel from 0 to 1 m/s were applied with the step of 0.2 m/s, while other parameters were kept constant. It is worth mentioning that when the air velocity was set to zero, the model assumed the condition with the closed channel at both its ends and with no direct contact between the air in the channel and the ambient air. In the second part of the analysis, the variable ambient/inlet air temperature was considered to test the dynamic thermal behavior of the system. The initial air temperature of the system of 25 ˚C was considered with the constant air velocity of 0.2 m/s. The inlet air temperature was assumed variable from 10 ˚C to 30 ˚C with the step of 5 ˚C, while other inputs and parameters of the model were kept unchanged.

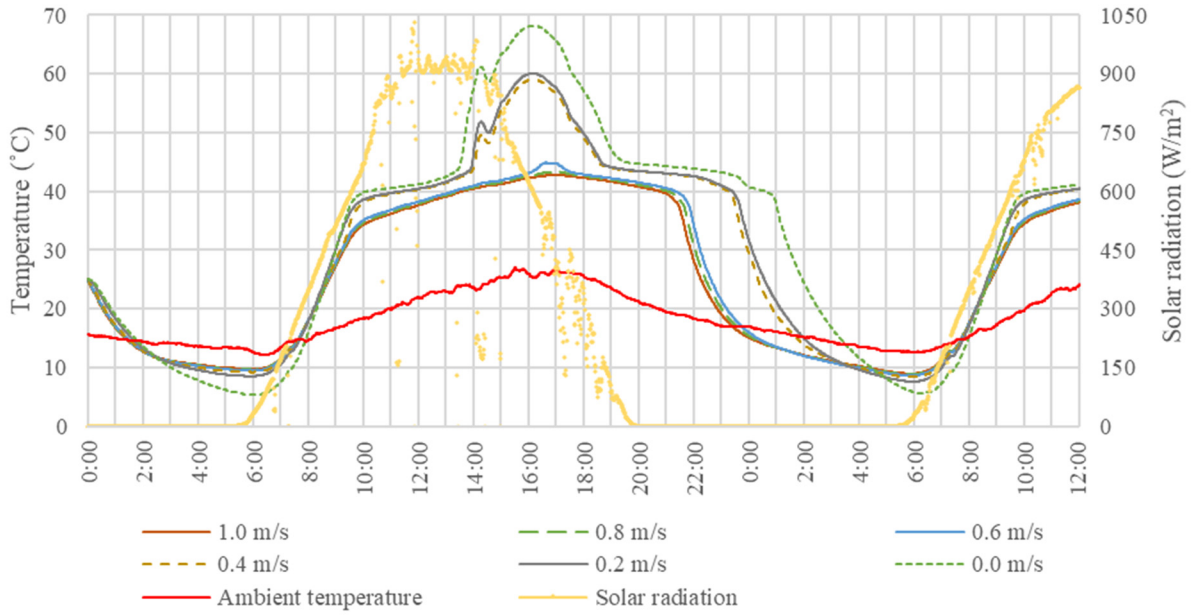

Figure 83. Influence of the air velocity in the air channel on the PCM panel inner surface temperature

Figure 83 shows the simulated thermal behavior of the PCM panels applying various air velocities inside the air channel. The thermal response is represented as the change of the temperature of the surface of the PCM panel facing the air channel. The figure shows that lower air velocities promote longer solidification periods, a lower system temperature during cooling charging, and a higher system temperature during melting. Figure 84 presents the influence of the inlet air temperature on the inner surface temperature of the PCM panel. It shows that the higher the inlet air temperature, the higher the surface temperature of the PCM panels. It can be noticed that during the cooling charging at the early morning period with the inlet air

temperature of 10 ˚C, the temperature of the PCM panel reached about 2.5 ˚C. While the inlet air temperature was 30 ˚C, the temperature of the PCM panel reached about 25 ˚C. It can be concluded through applying several inlet air profiles that the larger temperature difference between the inlet air temperature and the PCT range of the PCM promotes higher cooling charging potential. As with a larger difference, the temperature of the PCM panel could achieve a larger drop in temperature during the cooling charging process. It can also be noticed that the duration of the phase change is affected by this temperature difference. Unlike the first part of the analysis, it can be observed that the temperature behavior across all the cases is homogenous. This is because all the cases were investigated under identical conditions of the convection model due to the constant air velocity in the channel, while in the first part of the analysis there were changes in the calculations of the convection sub-model due to the changes in the air velocity inside the air channel.

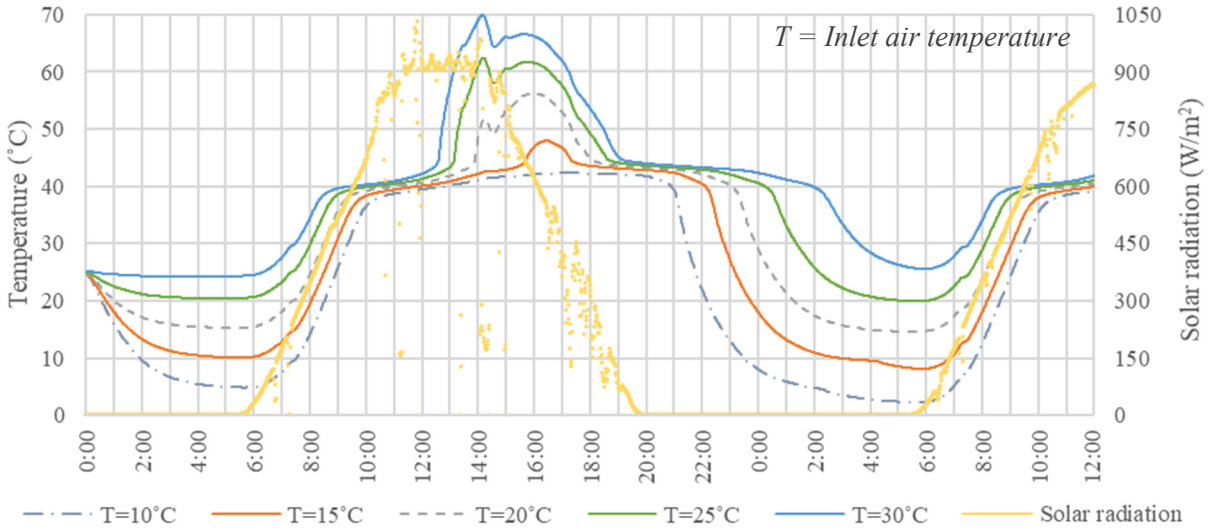

Figure 84. Influence of the inlet air temperature (T) on the PCM panel inner surface temperature

4.6. Discussion

4.6.1. Experimental Results

Referring to the cooling charging experimental investigations and both the considered configurations (config-A and config-G), the PAHX system showed an increased storage ability during the charging process as the temperature of the PCM panels dropped up to 5 ˚C (applying config-G) below the ambient air temperature. It can be inferred from the results that the long-

wave thermal radiation from the PCM panels to the sky during night-time and early morning amplified the total thermal losses of the PAHX system during the charging process (cooling) of the PCM. For the glazed configuration (config-G), it can be concluded that due to the glazing effect, extra heat gains during the daytime, and the nature of radiation heat transfer, the solidification rate of the PCM was slower than in case of the config-A. It can be expected that with longer night-time periods, the system could promote additional cooling charging potential during the solidification of the PCM. It can be inferred that the difference between the PCT and the ambient air temperature, and properties of the PCM have strong impact on the charging process (cooling) of the system.

4.6.2. Validation Results

Referring to the validation results, it can be claimed that the behavior of the model was in a good agreement with the variation of the air velocity inside the air channel. It can be concluded that the convection model can cope with low, moderate, and high air velocity values inside the air channel. Furthermore, the model shows an acceptable performance for changes in the configuration (config-A, config-G, and the insulated configuration) which required the modification of boundary conditions and of the nodal size of the system. The model showed a sufficient stability regarding those changes in boundary conditions during the validation process. Furthermore, the use of two different types of PCM panels with different thermophysical properties in the prototypes 01 and 02 gives more reliability to the validation results.

The results of the model validation against experimental data shown in Table 18 reveal that the NMBE values were for all cases between -9.5% and 7.6%, while the CVRMSE values were equal or lower than 14.6%. This indicates that all the cases were within the accepted calibration range of the ASHRAE Guideline 14. The numerical results in Table 18 are visualized in Figure 85 and Figure 86. From these figures, it can be inferred that there is no systematic error regarding the temperature profile of the three nodes used for comparison. However, the discrepancy level between the experimental and simulated data is more significant in the case of prototype 02, especially for NMBE values. The reasons can be the simplifications and assumptions adopted in the model in regard to thermal properties of the microencapsulated PCM panels. Referring to the results of the maximum deviation, the outer surface temperature in prototype 01 and the inner surface temperature in prototype 02 recorded the highest values of the

maximum deviation. It can be expected that with more accurate assumptions for the thermophysical properties of the PCM and panel surfaces in both prototypes, the discrepancies in the comparison results could be reduced and controlled. In all the cases, the air temperature in the channel achieved an acceptable agreement with the reference data recording the lowest values of maximum deviation. Also, the model is sensitive to the percentage value of the cloud cover, which is an essential variable in the calculations of the sky temperature. The cloud cover was estimated in the model as a constant value during each application. As the cloud cover was changing during the experiment, this could lead to the observed discrepancies in the comparison between the simulation results and reference data. Besides, the actual properties of the PCM panels might be affected, as they were previously already used in another investigation.

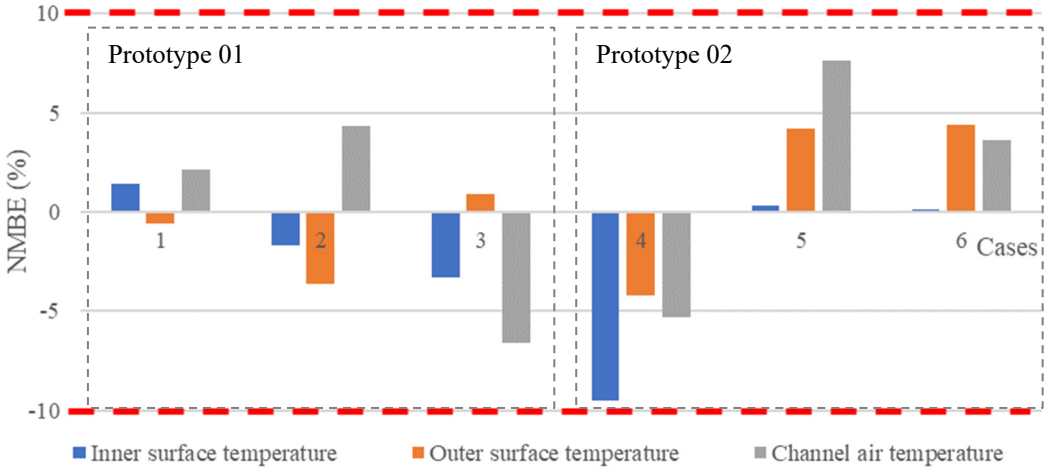

Figure 85. NMBE results for all the cases of the validation investigations

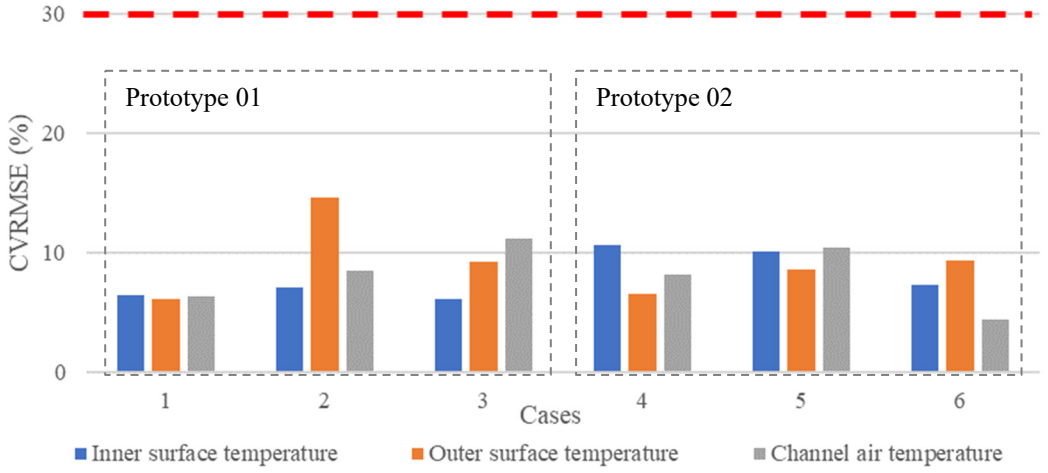

Figure 86. CVRMSE results for all the cases of the validation investigations

4.6.3. Parametric Analysis Results

Regarding the parametric analysis, it can be concluded that the developed PAHX model is well responsive to both the air velocity and the ambient/inlet air temperature, which are considered the main driving forces dominating the heat transfer process inside the PAHX unit. Regarding the air velocity, it can be inferred from Figure 83 that when the glazed configuration was applied during the cooling charging of the PCM during night-time and early morning, heat transfer was magnified by the thermal radiation losses to the ambient environment, especially in case with no airflow, in which the effect of convection was limited. This promotes the cooling potential of applying the PAHX system for building envelope applications under an insufficiently low air temperature during the PCM solidification with no airflow condition. Also, during the heating charging process of the PCM with no airflow in the air channel, solar gains increased the temperature of the system minimizing the thermal losses by convection to the ambient environment. This increases the heating charging potential of the system during the daytime periods. It can be noticed from Figure 83 that with air velocity values lower than 0.6 m/s, the behavior of temperature profiles is slightly different than for higher values of air velocity. This is due to the change of the convective heat transfer sub-mode. At lower air velocities, the model considers that free convection contributes to the heat transfer process and dominates in some periods regarding the temperature difference between the PCM panel and the air channel. At higher air velocities, the model considers the mixed convection mode where free as well as forced convection driving forces have an impact on the heat transfer process.

As for the ambient air temperature, which is considered as the inlet air temperature to the system, it can be inferred from Figure 84 that during all cases of cooling charging, the surface temperature of the panel was around 5 ˚C to 7.5 ˚C lower than the proposed ambient air temperature due to the effect of the radiation thermal losses during the solidification of the PCM. These results are supported by the experimental results for the scenario 3 and the prototype 01 in Figure 40 in Section 3.5.1. The sky temperature is assumed to be a function of the ambient air temperature, where the lower the ambient air temperature, the lower the sky temperature. That is the reason why the drop of the surface temperature of the panel with the PCM with respect to the ambient air temperature is greater for lower ambient air temperatures.

The developed PAHX system promotes the cooling potential of the PAHX unit for envelope-integrated applications under insufficiently low air temperatures during cooling charging periods through the utilization of the effect of the thermal radiation loss. Referring to the charging processes, the proposed PAHX system has confirmed good potential for both cooling and heating charging abilities. However, a proper control strategy is needed in terms of the heat gain/loss control and the duration of the operation to maximize the charging energy of the system. Also, a proper airflow strategy during the charging and discharging processes is mandatory to regulate heat transfer between the air channel and the PCM panels.

CHAPTER FIVE:

PAHX THERMAL PERFORMANCE - APPLICATION IN HOT DESERT CLIMATE

5.1.Developed PAHX in Hot Desert Climate

Generally, the thermal performance of the PAHX units was claimed to be enhanced in climates with large daily temperature amplitude (Waqas and Kumar, 2011b; Borderon et al., 2015). Also, most of the studies construed that larger difference between PCT range and inlet air temperature during PCM solidification is more effective for improving the system performance than providing higher air velocities (Waqas and Kumar, 2011a; Panchabikesan et al., 2017). El-Sawi et al. (2013) showed that the thermal performance of the PAHX unit can be enhanced when the temperature difference between PCT range and inlet temperature during the PCM solidification is greater than 10.0˚C. Waqas and Kumar (2011a; 2011b) investigated the thermal performance of a PAHX unit utilizing a salt hydrate PCM in the hot dry climate applying various inlet temperatures. The researchers proved that better thermal performance could be achieved by applying lower inlet temperatures during cooling charging.

The developed PAHX units were proposed to ensure the workability of the system under hot climates. Muthuvelan et al. (2018) claimed that the integration between the PAHX unit and other passive cooling techniques such as evaporative or radiative cooling can improve the indoor thermal performance. Panchabikesan et al. (2017) studied the integration of a bed packed cylindrical PAHX tank with a direct evaporative cooling unit in a moderate climate. They proved that this integration aided the PCM to be completely solidified at a faster rate by decreasing the PAHX system inlet temperature during PCM solidification. The proposed system showed better thermal performance with higher difference between the inlet air temperature and the PCT range. The approach of using multiple phases of PCM types inside the PAHX system was investigated by Zalba et al. (2004) using two types of PCMs with different PCT ranges. The system achieved 9.4 times less power consumption comparing to a conventional cooling unit. Mosaffa et al. (2013) investigated the multi-PCM approach using a flat plated PAHX. They concluded that a significant difference between PCT of different parts should be designed to magnify the system thermal performance. Jaworski, Maciej, (2014) presented a new structure of a ventilated ceiling panel composed of gypsum mortar and 27% of microencapsulated PCM. The whole ceiling system

worked as a PAHX free cooling system combined with night ventilation. The results showed that the system achieved a good performance in terms of peak shaving.

This chapter presents an investigation of the thermal performance of the developed PAHX system in the hot desert climate. One of the limitations regarding the application in the hot desert climate is the large solar gains during daytime. Accordingly, an operational control strategy was proposed to ensure the system workability for cooling purposes in the hot desert climate. The stand-alone performance of the system was investigated using a parametric analysis for the system elements. Also, this chapter discusses the influence of integrating the PAHX unit to the building ventilation system on the indoor thermal performance of an occupied space.

5.1.1. Control Strategy

This study focuses on the investigation of the thermal performance of the developed PAHX system in the hot desert climate where the high cooling demand prevails, and free cooling is most needed. The hot desert climate (BWh climate according to Köppen classification (Kottek et al., 2006)) is distinguished with hot to exceptionally hot summers with the highest recorded annual average temperature (Kottek et al., 2006). The large diurnal swing between day and night temperatures and the clear sky conditions are the main climatic characteristics of the hot desert climate that promote free cooling applications. However, one of the major challenges regarding this climate is the high solar gain during the daytime. Regarding the PCM-based free cooling systems, a control strategy is needed to regulate the system heat gains and losses especially during cooling discharging (the melting of PCM during daytime).

For the current application of the PAHX system, an operational control strategy was proposed to minimize the heat gains during the daytime application (cooling discharging). The experimental scenarios illustrated in Section 3.3.3 were utilized to identify the operation control plan. During the cooling charging (night-time and early morning), scenarios 1 and 2 were applied identifying the exposed configuration to the ambient environment (config-A). Scenarios 3 and 4 were applied identifying the glazed configuration (config-G). The inlet and outlet of the air channel were controlled to provide an airflow through the air channel (scenarios 2 and 4) or to achieve a no airflow condition (scenarios 1 and 3) during the charging process. During the cooling discharging (daytime), scenario 6 was applied by adding the insulation layer to protect the system from the

exceeding solar gains during the application. Practically, adding the insulation layer could be mechanically operated. The air velocity inside the air channel was initially proposed to be 0.3 m/s during cooling discharging (during applying scenarios 2 and 4). The control strategy considered the value of the solar radiation as the control parameter that switches between the two operational modes (cooling charging and discharging) with a threshold of 100 W/m^2 as presented by the algorithm shown in Figure 87. The threshold was selected to be 100 W/m^2 to allow the system charging during the early morning to make use of the low ambient air temperature and the low sky temperature during this period.

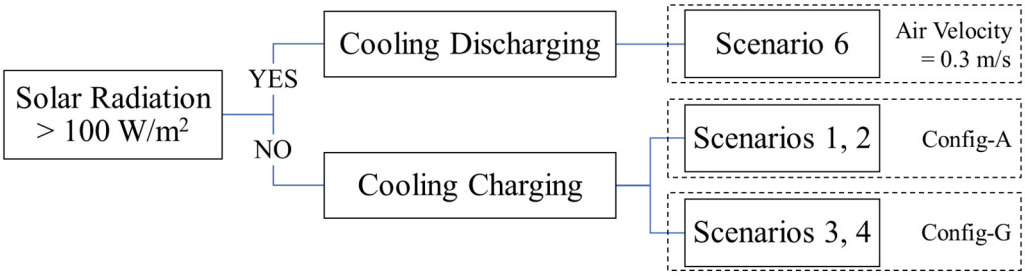

Figure 87. The operational control strategy of the developed PAHX in respect of solar radiation

5.2. Thermal Performance of The Reference Case

The reference case, or the base case, is the preliminary assumed variables for the proposed PAHX system in terms of dimensions, orientation, and PCM type. The horizontal orientation was applied for the reference case. No-airflow condition was applied during cooling charging (scenario 1 for config-A or scenario 3 for config-G). The assumed system variables are summarized in Table 19. A parametric investigation was conducted to specify the location and the type of PCM for the study.

Table 19. System variables of the reference case

Variables	Value	Unit
System length	2	m
System width	0.9	m
PCM panel thickness	0.015	m
Air channel height	0.04	m
Air velocity (during discharging)	0.3	m/s

5.2.1. Location-Based Analysis

Several locations were initially proposed to figure out the changes in the system performance within the same climatic region in respect of the location. Six cities were chosen within the hot

desert climate with different average ambient air temperature and relative humidity to assess the thermal performance of the reference case. The six locations, shown in Table 20, were represented by various weather data systems which differ according to the weather station (EnergyPlus, 2019). PCM RT26 with the thermal properties shown in Table 21 was initially used to assess the performance of the system in the six locations. The first week of summer (June 21st: June 27th) was selected to represent the typical weather behavior of the cooling season in the hot desert climate.

Table 20. The weather data codes of the locations of the study (EnergyPlus, 2019)

	Location	Coordinates	Weather Data Code
01	Cairo	(N 30° 7') (E 31° 23')	623660 _ ETMY
02	Asyut	(N 27° 2') (E 31° 1')	623930 _ ETMY
03	Aswan	(N 23° 58') (E 32° 46')	624140 _ ETMY
04	Riyadh	(N 24° 42') (E 46° 47')	404380 _ IWEC
05	Kuwait	(N 29° 13') (E 47° 58')	405820 _ KISR
06	Abu Dhabi	(N 24° 25') (E 54° 39')	412170 _ IWEC

Table 21. Thermal properties of RT26 (Rubitherm, 2019)

Melting range (*heating*)	25 – 26 (*peak of 26*)	˚C
Solidification range (*cooling*)	26 – 25 (*peak of 26*)	˚C
Thermal storage capacity*	180 (±7.5%)	kJ/kg
Heat capacity	2	kJ/kg.K
Density	880 (*solid*)	kg/m^3
	750 (*liquid*)	kg/m^3
Thermal conductivity	0.2	W/m.K
Volume expansion	12.5	%

**Combination of latent and sensible heat in a temperature range of 19˚C to 34˚C*

The thermal performance of the developed PAHX system during cooling discharging was determined in terms of heat exchanger (HX) effectiveness in respect of the ambient air temperature as the inlet temperature of the system and the sky temperature as the reference temperature of the energy source (the minimum temperature the system can theoretically reach). Both control operational configurations (config-A (scenario 1 during charging and scenario 6 during discharging), and config-G (scenario 3 during charging and scenario 6 during discharging)) were assessed using the effectiveness criterion. The HX effectiveness (ε) for the designed free cooling application of this study can be defined as:

$$\varepsilon = \frac{T_i - T_o}{T_i - T_r} \times 100\ (\%) \quad (37)$$

where $(T_i - T_o)$ is the achieved reduction in the air temperature by the application of the system (the difference between the ambient air temperature (T_i) and the system outlet air temperature (T_o)), and $(T_i - T_r)$ is the maximum reduction that can theoretically be achieved in respect of the sky temperature (T_r) as an energy source. Equation 37 was only applied during system application (cooling discharging of the system). It is worth mentioning that both the ambient air temperature and the sky temperature were varied according to the location of the city. So, the direct comparison among the applications in the different cities would be inaccurate. Instead, the comparison between the operational configurations within the same city would be applicable and efficient. Figure 88 shows the average values of the ambient air temperature and relative humidity (RH) values during daytime and night-time for each location during the proposed typical summer week. The daytime and night-time periods here are referring to the actual periods of charging and discharging of the system during the application. During the typical summer week, the effectiveness of the PAHX system during cooling discharging was evaluated for both configurations. Figure 89 shows the effectiveness values for the proposed applications. The weekly average outlet air temperature (during only cooling discharging for the configuration of a better performance) was calculated compared with the average ambient air temperature and the average sky temperature. Regarding the difference between the average ambient air temperature and the average outlet air temperature, better performance could be noticed in cities with lower RH values and lower ambient air temperature during discharging. In Kuwait, the high average daytime air temperature affected the performance of the proposed system. However, different system configurations and PCM selection might enhance the performance in this specific location. In Abu Dhabi, the high recorded value of HX effectiveness was due to the relatively high sky temperature and the high RH values which affected the absolute performance of the developed cooling system. The application in Cairo and Asyut achieved the lowest average outlet air temperature promoting the cooling potential of the system to enhance the indoor thermal comfort levels in these locations. The city of Asyut was selected to perform the further investigations as it recorded second better system effectiveness and lower ambient RH values which promote better cooling performance.

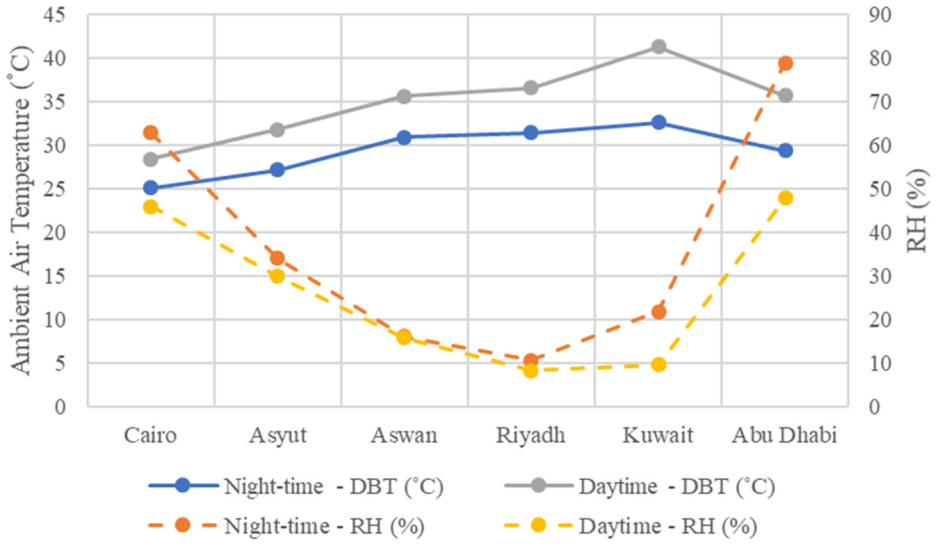

Figure 88. The average values for ambient air temperature and RH for all the proposed locations

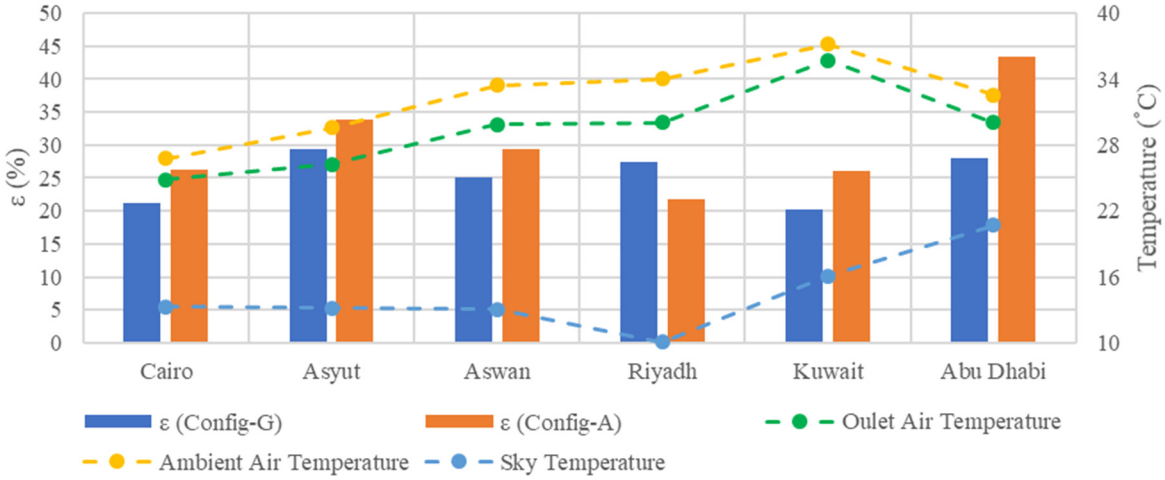

Figure 89. HX effectiveness and outlet air temperature in all the proposed locations

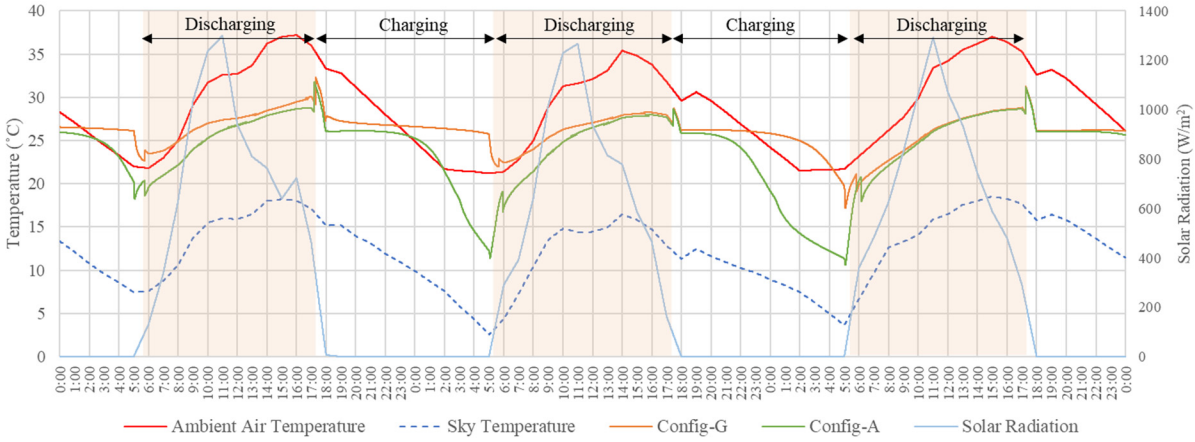

Figure 90. Outlet air temperature during charging and discharging of the PAHX system

In general, the results show that at most cases config-A achieved a higher effectiveness value than config-G. Only in the city of Riyadh with the lowest sky temperature and RH value, the HX effectiveness of config-G was 5.6% higher than config-A. It means that in most cases applying the glazing layer to the system during cooling charging (PCM solidification) affected the system performance during the discharging application. Although the solidification of the PCM was maintained in both configurations, the duration of the solidification in config-A was reduced allowing the system to reach a lower temperature during charging process. However, config-G can be more beneficial in other climates or different duration of the application. Figure 90 shows an example of a 3-days application (June 23rd to June 25th) in the city of Asyut. It can be noticed that the PCM solidification while applying config-A was limited to 4 – 7 hours during the whole charging period which lasted for almost 12 hours. The air temperature inside the channel dropped significantly during charging process which promoted better performance during discharging of the system. On the other hand, the duration of the PCM solidification in config-G was almost doubled which slightly affected the outlet air temperature during the cooling discharging. Accordingly, config-A was nominated to be utilized for further investigations in this study.

5.2.2. Selection of PCM

Several commercially- available PCM types were tested during the proposed typical summer week for the cooling application in the city of Asyut to evaluate the thermal performance of the system while applying different types of PCM. The proposed types of PCM are concluded in Table 22. Config-A was employed applying the control strategy mentioned in Section 5.1.1 while charging and discharging. The HX effectiveness criterion was applied to assess the thermal performance during the cooling discharging. Figure 91 shows a 3-days application of the system (from June 23rd to June 25th) utilizing the proposed types of PCMs. The resulted values of HX effectiveness for different PCM types during the typical summer week application were presented by Figure 92. The results showed that choosing the proper PCT range of the used PCM would be more efficient than applying the PCM with a higher storage capacity. For this specific application, RT25HC recorded the highest value of the HX effectiveness and the minimum average outlet air temperature during cooling discharging. Overall, RT22HC and RT25HC recorded considerable thermal performance for this specific application. It can be noticed that a PCM with a lower range of PCT does not necessarily assure a better performance for the PAHX application (in this case, RT18HC

did not show the best performance). Instead, each location has its own proper range of PCT that promotes a better performance which supports the locality of the PCM-based free cooling applications.

Table 22. Proposed types of PCMs

PCM	PCT Range	Storage Capacity
RT18HC	17˚C – 19˚C	260 kJ/kg
RT22HC	20˚C – 23˚C	190 kJ/kg
RT25HC	22˚C – 26˚C	210 kJ/kg
RT26	25˚C – 26˚C	180 kJ/kg
RT28HC	27˚C – 29˚C	250 kJ/kg
RT31	27˚C – 33˚C	165 kJ/kg

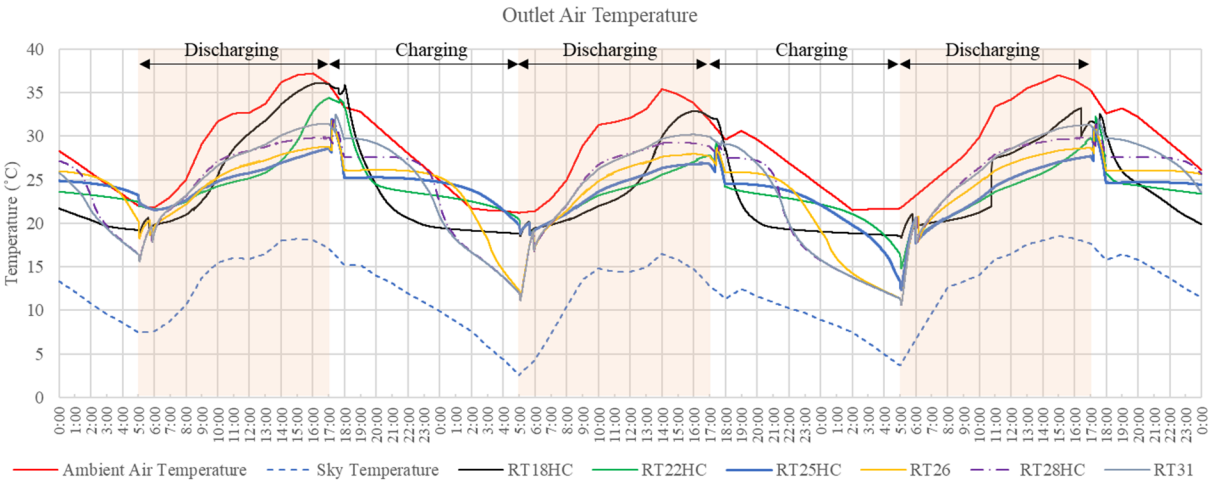

Figure 91. Outlet air temperature while applying various types of PCMs

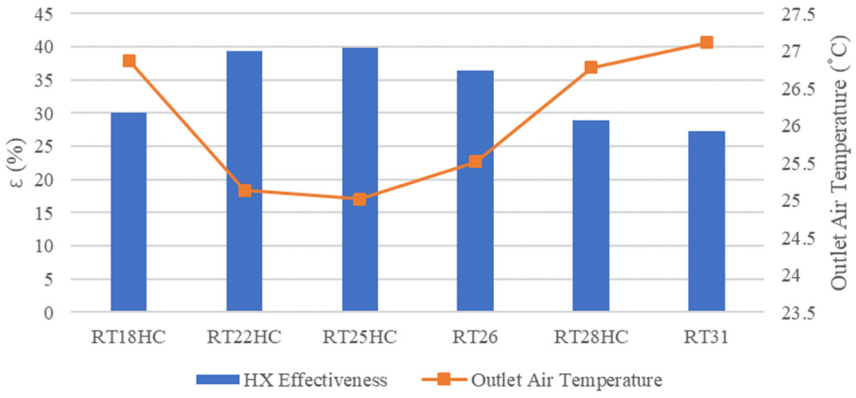

Figure 92. HX effectiveness of applying various types of PCMs

Table 23. Thermal properties of RT25HC (Rubitherm, 2019)

Melting range (*heating*)	22 – 26 (*peak of 25*)	˚C
Solidification range (*cooling*)	26 – 22 (*peak of 25*)	˚C
Thermal storage capacity*	210 (±7.5%)	kJ/kg

Heat capacity	2	kJ/kg.K
Density	880 (*solid*)	kg/m^3
	770 (*liquid*)	kg/m^3
Thermal conductivity	0.2	W/m.K
Volume expansion	12.5	%

**Combination of latent and sensible heat in a temperature range of 19˚C to 34˚C*

Based on the previous investigations, the reference case was identified by the above-mentioned variables applying config-A during cooling charging process. The city of Asyut was selected as the location of the study. PCM RT25HC was selected with the thermal properties indicated in Table 23. The first week of summer was specified as a typical summer week for the study. The effectiveness of the reference case was estimated by 39.8%.

5.2.3. Justification of the Developed PAHX Stand-alone Performance

In order to justify the thermal performance of the developed PAHX system in respect of the improved radiative cooling potential, a comparative study was conducted in the hot desert climate between the developed PAHX system and the conventional PAHX configuration which depends only on the convection cooling potential. The conventional PAHX units utilize the ambient air as an energy source to charge the system. In order to represent the conventional design for PAHXs, scenario 6 (insulated system) was applied during charging and discharging. This means that only convection between the air and the PCM panels was allowed; whereas thermal radiation to the sky was blocked. The configurational and climatic parameters of the reference case were applied to test the feasibility of applying the new PAHX concept in the hot desert climate. For the developed PAHX system, scenario 6 was applied during discharging and scenario 2 was applied during charging to unify the conditions between the two configurations. The air velocity was set to 0.3 m/s for the whole periods of charging and discharging in both configurations. Figure 93 shows the outlet air temperature of the two configurations during the typical summer week application. The improvements in the outlet temperature profile of the improved PAHX system can be easily identified. The weekly average outlet temperature was calculated and recorded 25.6 ˚C and 29.8 ˚C for the improved and the conventional PAHX units respectively. This means that the developed improved PAHX unit achieved a reduction in the average outlet air temperature of 14% than the conventional design.

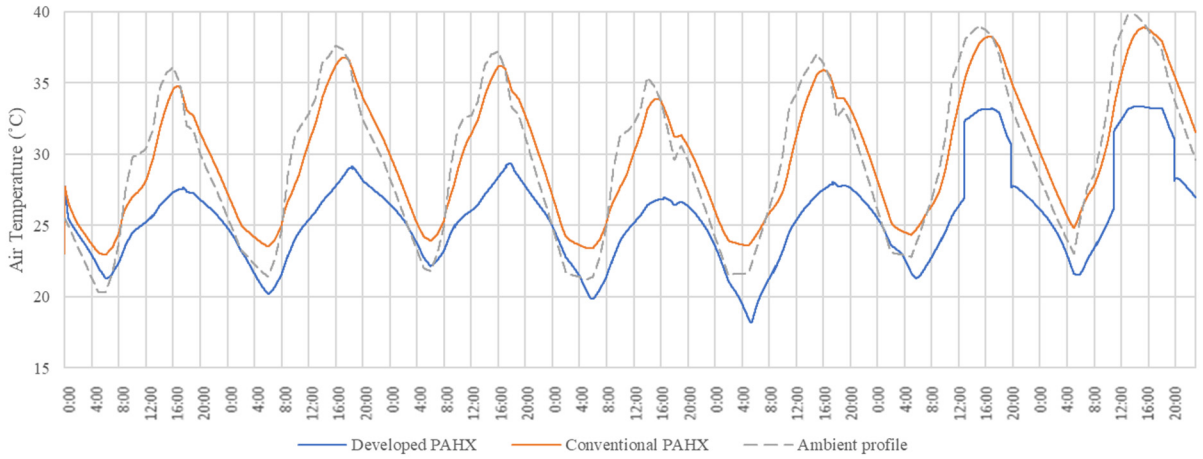

Figure 93. Outlet air temperature of the developed and conventional PAHX configurations

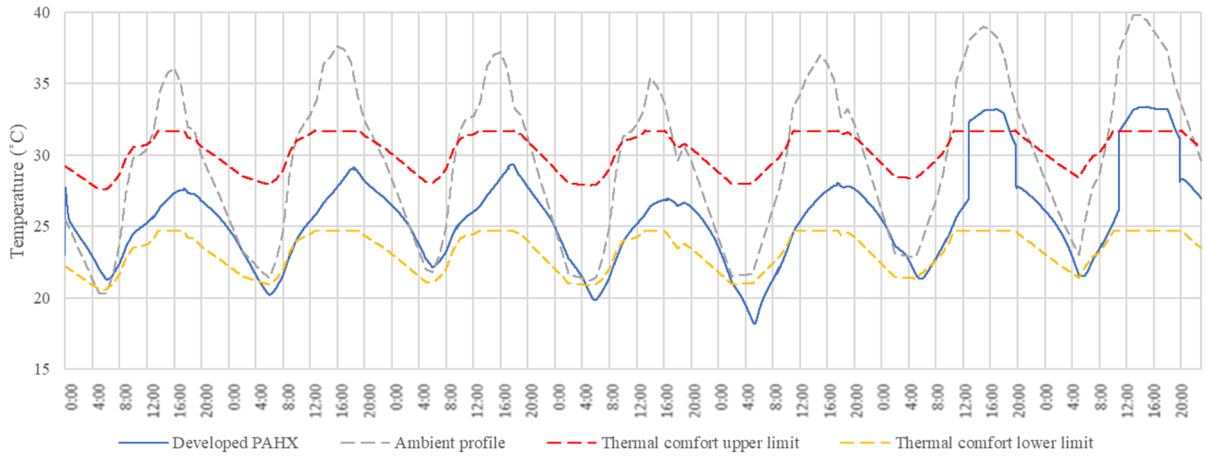

Figure 94. Outlet air temperature in respect of the thermal comfort range

Referring to the adaptive thermal comfort model defined by ASHRAE (2013) and illustrated by Equation (1), the outlet air temperature profile of the developed PAHX was evaluated. While the developed thermal comfort criterion is only applicable for ambient temperature between 10 ˚C and 33.5 ˚C (ASHRAE, 2013), then for higher ambient temperature values, the temperature of 33.5 ˚C was set to define the limits of the comfort range. Figure 94 shows the comparison between the thermal comfort range (based on the ambient profile) and the outlet air temperature of the developed PAHX. It can be noticed that during most of the charging and discharging periods, the outlet air temperature is within the comfort range. Only during 8.5% of the total duration of the weekly application, the outlet air temperature was higher than the upper limit of the comfort range. Moreover, during 14.5% of the application, the outlet air temperature was lower than the lower limit of the comfort range. Whereas the criterion defines the comfort range of the operative

temperatures (not the air temperature), only cooling potential of applying PAHX can be claimed for enhancing the indoor thermal performance.

5.3.Parametric Analysis

In this section, the influences of applying different values for PAHX parameters on the thermal performance of the stand-alone unit were assessed. It is worth mentioning that this parametric analysis is not an optimization study, and it does not aim to reach the optimum variables regarding the system thermal performance. The criterion of the HX effectiveness was used to evaluate the performance of the system regarding various variables. Five parameters were analyzed: the air velocity inside the air channel, the PCM panel thickness, the system length in the direction of airflow, the height of the air channel, and the PCT range of the PCM (using the same type of PCM). Additionally, the multiple-PCM approach was investigated to assess the influence of integrating different types of PCM in series within the same volume of the system. The analysis was conducted applying the configurational and climatic conditions of the reference case. Only the parameters under investigation were applied with various values.

5.3.1. Air Velocity

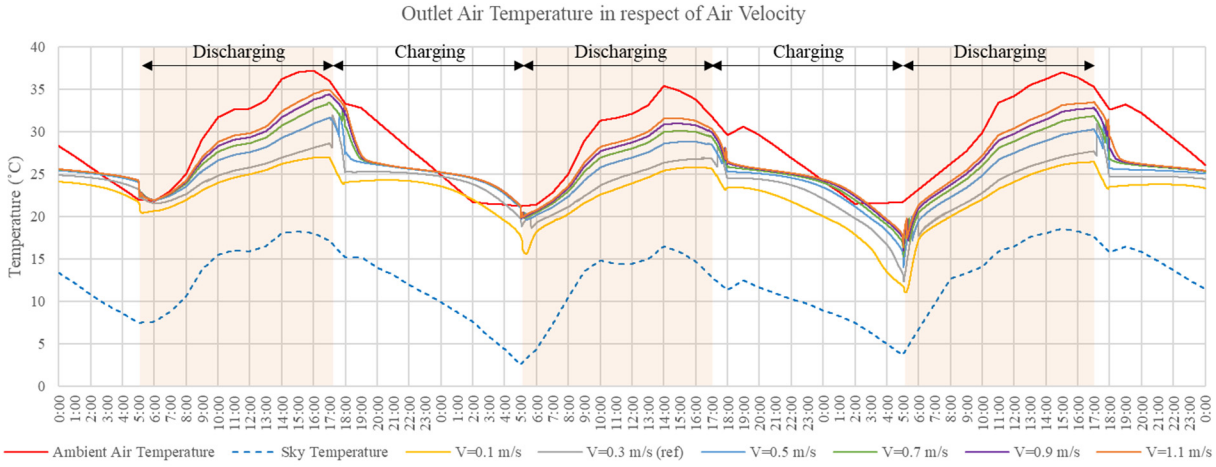

Figure 95. Outlet air temperature in respect of various air velocity values inside the air channel (V)

The air velocity is an essential parameter in determining the thermal performance of the system. Various convection modes (free, forced, and mixed modes) could be applied due to the air velocity value inside the air channel in respect of the height of the air channel. Air velocity values from 0.1 m/s to 1.1 m/s were applied with a step of 0.2 m/s. Figure 95 shows the thermal behavior of the air

temperature in the air channel (at the channel outlet) during charging and discharging. Figure 96 shows the system effectiveness and the average outlet air temperature during the cooling discharging applying the selected air velocity values. The results showed that lower air velocity values provided better system performance applying the proposed air channel height (40 mm) where they delivered lower outlet air temperature during cooling discharging. It is worth mentioning that the air velocity is a critical factor in determining the thermal comfort and the indoor thermal performance.

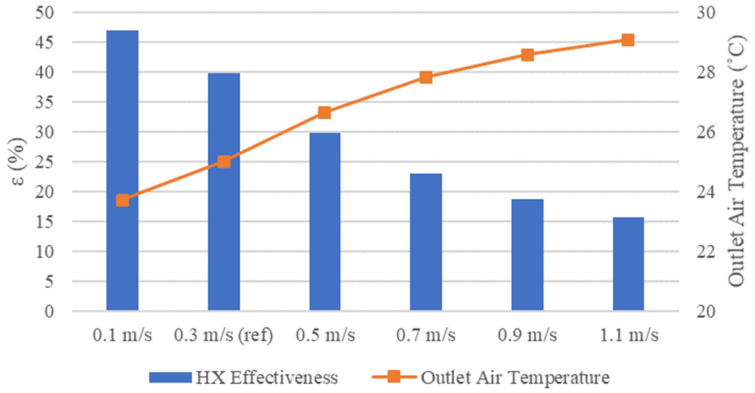

Figure 96. HX effectiveness of applying various air velocity values inside the air channel

5.3.2. PCM Panel Thickness

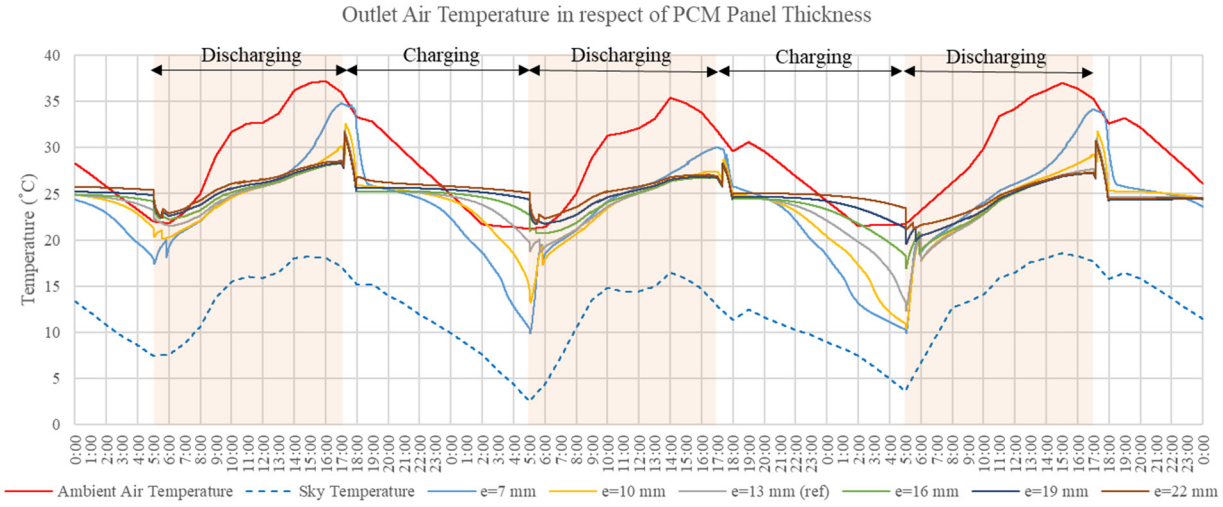

Figure 97. Outlet air temperature in respect of various PCM panel thicknesses (e)

A wide range of PCM thicknesses was tested starting from 7 mm to 22 mm with a step of 3 mm. It is worth mentioning that the number of the PCM nodes in the thickness direction was maintained unchanging during this analysis. Figure 97 shows the thermal behavior of the outlet air temperature of the air channel during charging and discharging regarding PCM panel thickness. Remarkable results were driven from the performance analysis presented in Figure 98. The figure shows that there was an optimal range of thicknesses (between 10 mm and 13 mm) which achieved the best results of thermal performance. Other lower and higher values of PCM thickness affected the resulted thermal performance of the system.

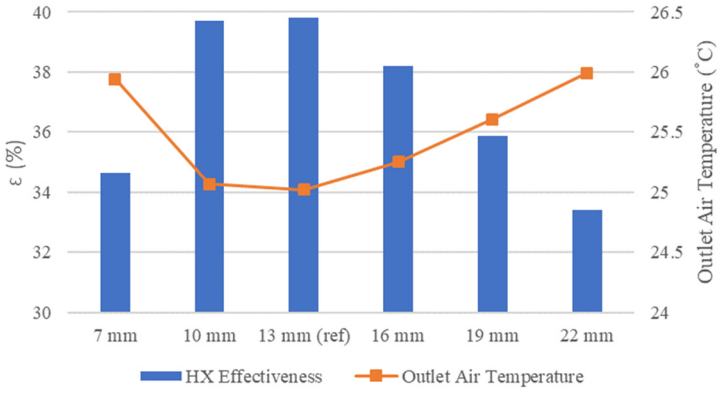

Figure 98. HX effectiveness of applying various thicknesses for the PCM panel

5.3.3. PAHX System Length

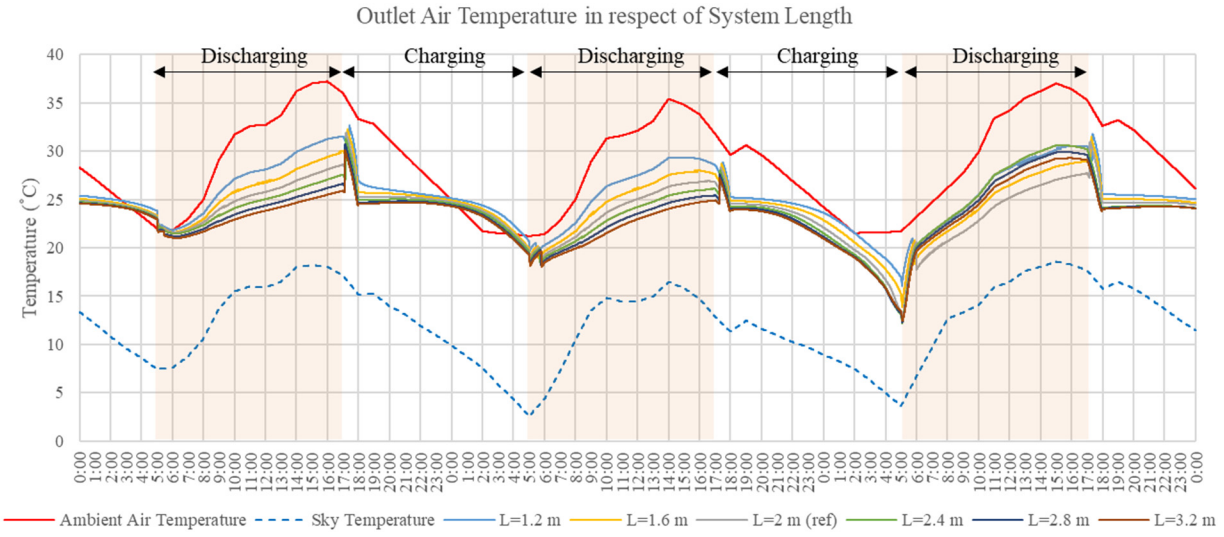

Figure 99. Outlet air temperature in respect of various PAHX system lengths (L)

The length of the PAHX system is the effective dimension of the PCM panels in the direction of the airflow. In all cases, the width of the system was maintained fixed. The system was investigated applying several lengths (from 1.2 m to 3.2 m) with a step of 0.4 m. The results, presented in Figures 99 and 100, showed that higher values of the system length provided better performance. However, after a specific length value (2 m) the improvements in the effectiveness value were limited. It is very important to assess the effect of the system length on the power consumption of the supply fan due to the pressure drop along the system.

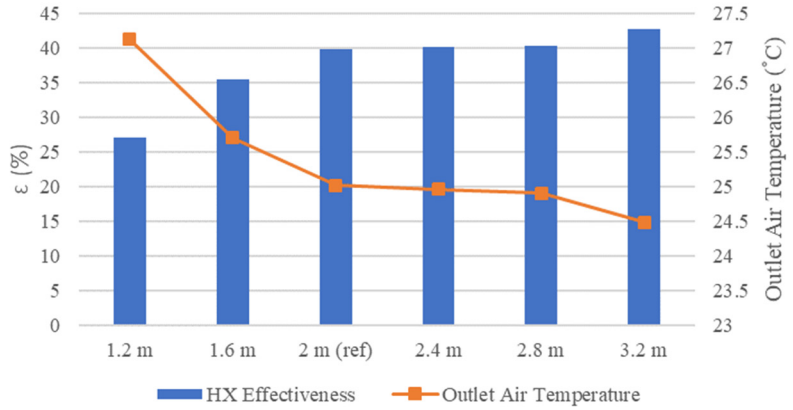

Figure 100. HX effectiveness of applying various values for system length

5.3.4. Air Channel Height

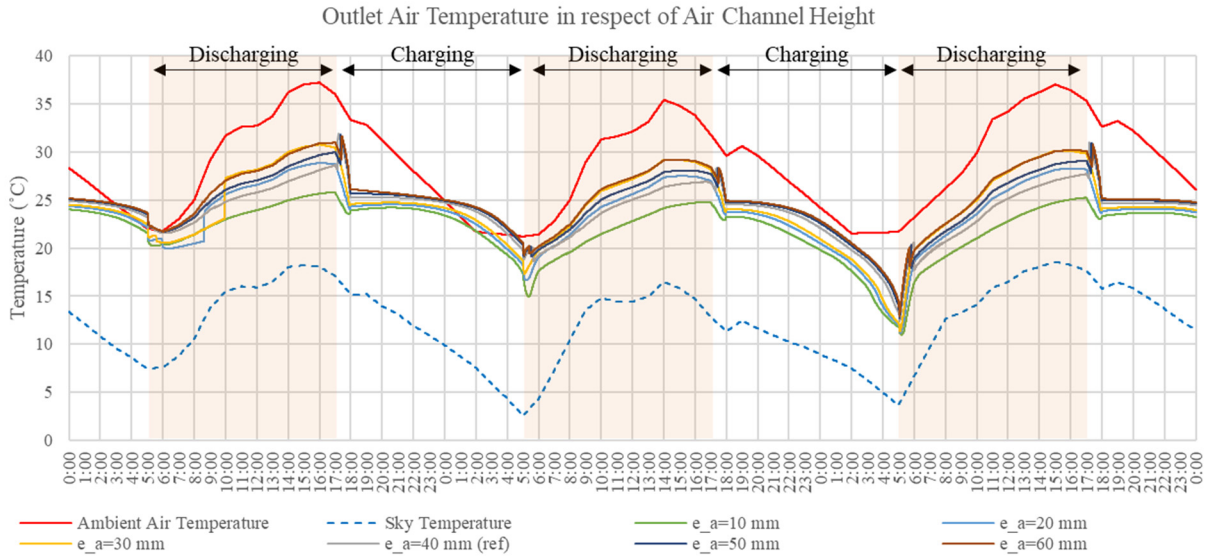

Figure 101. Outlet air temperature in respect of various air channel heights (e_a)

The height of the air channel and the air velocity have the greatest effect on the calculations of the convection model inside the air channel. Under the air velocity of the reference case (0.3 m/s) height values from 10 mm to 60 mm were applied with a step of 10 mm. Results in Figures 101 and 102 showed that a higher thermal performance could be achieved by a smaller air layer height. However, the changes occurred in the flow regimes from turbulent to laminar (starting at the thickness 40 mm) enhanced the thermal performance of the system decreasing the outlet air temperature. Like the system length, the air channel height is very effective in the power consumption of the system supply fan.

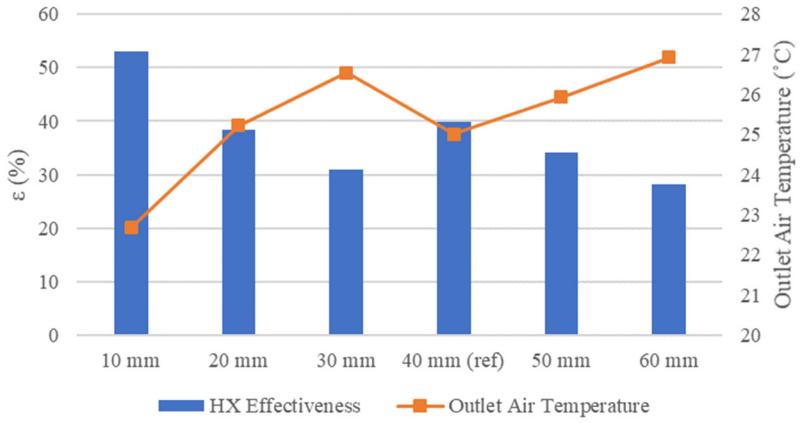

Figure 102. HX effectiveness of applying various values for air channel height

5.3.5. PCT Range

The same thermophysical properties of the PCM RT25HC were applied. A factor of temperature was added to the upper and lower limits of the PCT range of the PCM (22 ˚C – 26 ˚C) to assess the effect of changing only the PCT range applying the same thermal storage capacity (210 kJ/kg). This temperature factor ranged between -4 ˚C and +6 ˚C with a step of 2 ˚C. The results assured the above-mentioned results of PCM selection in Section 5.2.2 that the PCT range is a local-oriented variable that is related to the local climatic conditions. As shown in Figures 103 and 104, a better thermal performance was observed around the PCT range of the reference case. Higher and lower values than ±2 ˚C for the added factor to the PCT range lead to lower values of the system effectiveness.

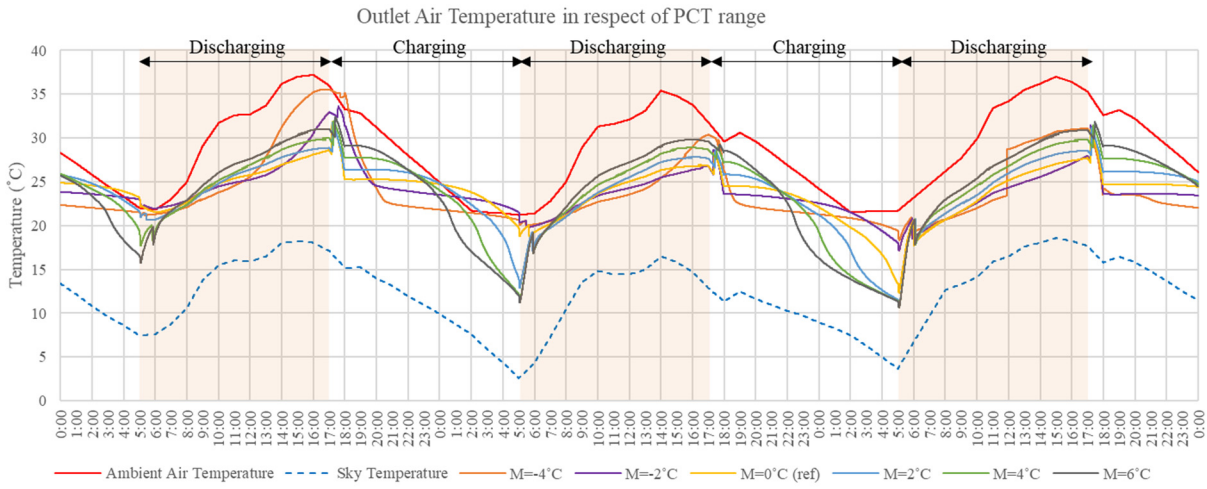

Figure 103. Outlet air temperature in respect of various temperature factors added to PCT range (M)

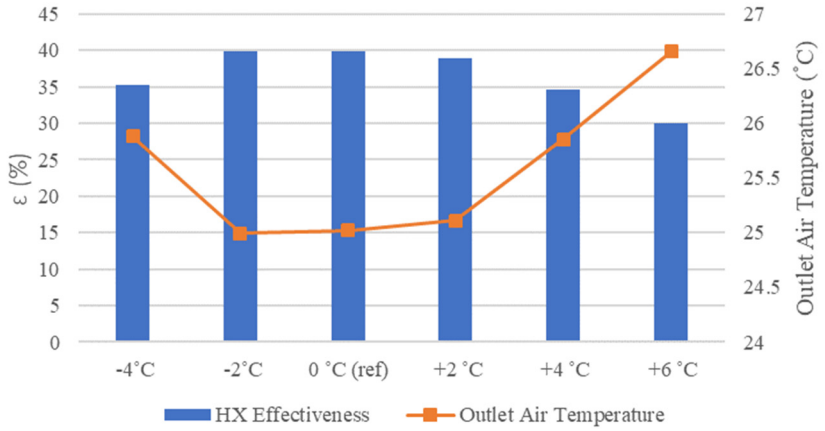

Figure 104. HX effectiveness of applying various PCT ranges

5.3.6. Multi-PCM Approach

The multiple PCM approach was investigated to assess the system thermal performance during applying various PCM types in series. This approach was claimed to achieve a better thermal performance (Mosaffa et al., 2013). In respect of the system length (in the flow direction), the system was divided into three consecutive parts. Various PCM types were applied to the three parts with different compositions considering that the PCM with higher PCT range was applied to the part close to the system inlet. Four different options, presented in Table 24, were designed and compared to the reference case with only one type of PCM (RT25HC). The results, presented in Figures 105 and 106, showed that the thermal performance of the reference case was higher than all the different compositions of the Multi-PCM applications. The lower performance was noticed

in Opt. 01 with applying PCMs with higher PCT ranges. However, applying PCMs with lower PCT ranges achieved better thermal performance. Again, this supports that each location has its own optimum PCT range during the application of the PAHX system.

Table 24. System variables of the reference case

Configuration	Part 1	Part 2	Part 3
Ref. Case	RT25HC	RT25HC	RT25HC
Opt. 01	RT31	RT28HC	RT25HC
Opt. 02	RT31	RT26	RT22HC
Opt. 03	RT28HC	RT25HC	RT22HC
Opt. 04	RT26	RT22HC	RT18HC

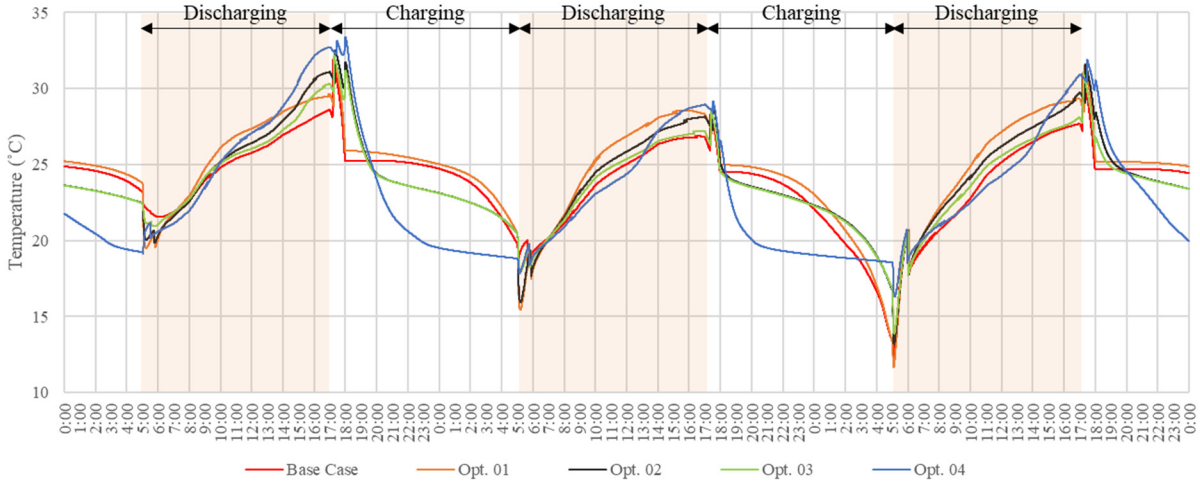

Figure 105. Outlet air temperature in respect of various compositions of PCMs

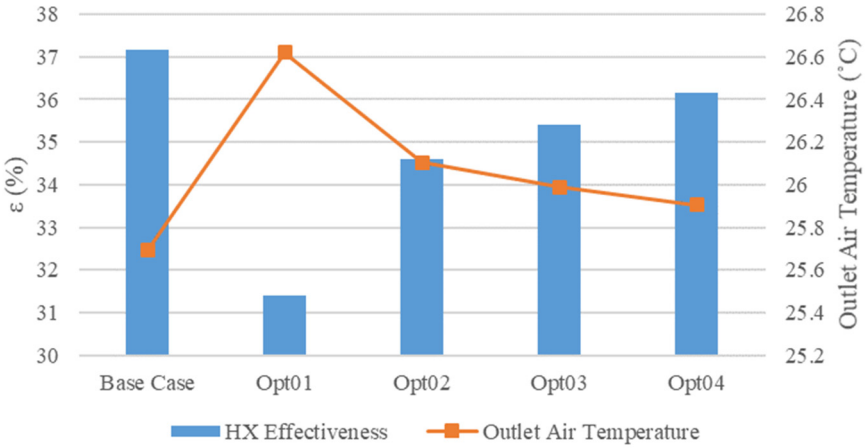

Figure 106. HX effectiveness of applying the multi-PCM approach

5.4.Indoor Thermal Performance

The developed PAHX unit with the assumed variables of the reference case was integrated into a mechanical ventilation system with a cooling unit to assess the effect of this integrating on the indoor thermal performance (in case of direct supply) and the energy consumption (in case the air is supplied to the mechanical cooling unit) for an occupied space. The room under investigation, shown in Figure 107, was assumed to be an office space with a volume of $3 \times 3 \times 2.8$ m^3. TRNSYS simulation was used to model the office space utilizing the building type 56 with the assumptions mentioned in Table 25. The investigation was conducted during the typical summer week (June 21st: June 27th) in the city of Asyut applying the climatic data used in the simulations of the PAHX system reference case. The investigation was focused on (Room_B) as a typical intermediate space. Meanwhile, all rooms were operated under the same conditions. The developed PAHX system was integrated to the building ventilation system as shown in Figure 108. The outlet air of the PAHX unit can be directly supplied to the space to satisfy the indoor cooling loads in free cooling applications. Also, it can be introduced to the mechanical cooling unit before supplying the air to the space to reduce the cooling energy consumption by the mechanical system (energy saving strategy). The MATLAB output file defining the outlet air temperature and the air velocity of the PAHX system was connected to TRNSYS by a data reader type. Furthermore, other important assumptions were proposed. The supply airflow rate and the air temperature of the building ventilation system were considered to be equal to the outlet airflow rate and the outlet air temperature of the PAHX system. Accordingly, the mass flow rate was initially set to 44.58 kg/h. Also, the RH of the outlet air temperature was assumed to be equal to the ambient RH. Four parameters were analyzed to assess the indoor performance: the indoor air temperature, the cooling loads, the thermal comfort level, and the energy consumption of the cooling unit. The indoor thermal comfort was represented by the Predicted Percentage of Dissatisfied (PPD) index which quantitatively predicts the percentage of thermally dissatisfied people. According to ASHRAE standard 55 (2013) the acceptable range of PPD is 10% and below. During free cooling applications, the cooling loads were calculated by the energy required to cool down the air of the space (T_{a_R}) to the set point temperature which was set to 22 ˚C.

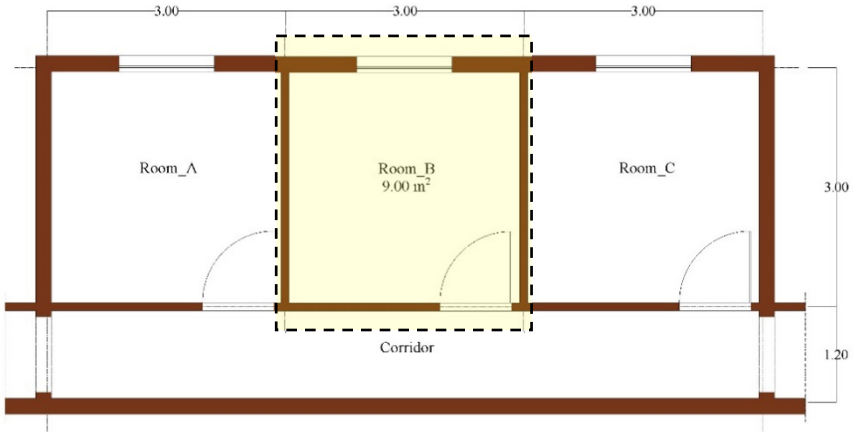

Figure 107. The proposed office space of the study

Table 25. Construction and operational assumptions of the office space

Window to wall ratio		14% (North)
Infiltration		0.2 ACH
Occupation		2 persons / room
Internal gains		14 W/m^2
Clothing factor		0.6 clo
Metabolic rate		1 met
Artificial lighting gains		10 W/m^2
Lighting control (Daylighting plan)	Lower Threshold	120 Lux
	Upper Threshold	200 Lux
Window shading		Fixed horizontal shading (0.4 m in depth)

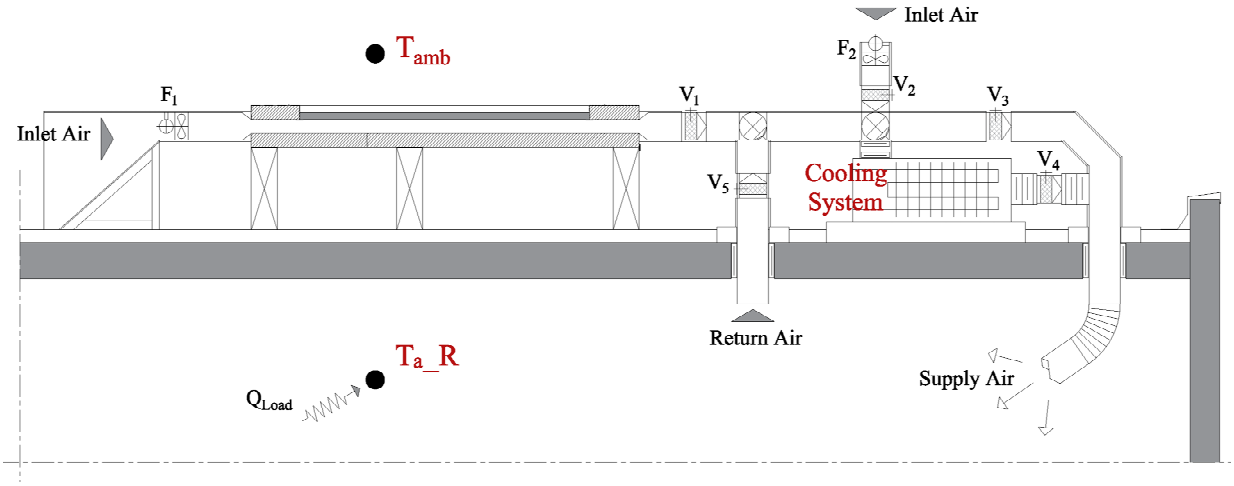

Figure 108. The integrated PAHX system with the building ventilation system and the cooling unit

5.4.1. Operational Modes

The proposed integrated ventilation system was designed to satisfy several operational modes. In most of the operational modes, the assumed ventilation strategy was 100% fresh supply air plan

(no return air was mixed to the supply air). However, in some other modes, the return air was introduced to the space during PAHX charging periods for the sake of comparison between the modes regarding the cooling loads and energy consumption. In Figure 108, two fans (F1 and F2) were planned to control the supply airflow. F1 was installed at the inlet of the PAHX unit; F2 was installed after the PAHX unit at the inlet of the active cooling unit. Five control valves were installed to manipulate the different modes of operation. Table 26 summarizes all the designed operational modes utilizing the proposed fans and control valves. Also, Figure 109 defines the different operational modes regarding the simulation procedure using the utilized TRNSYS types. Modes 1, 2, and 3 represent the free operational conditions of the system without the operation of the mechanical cooling unit. While modes 4, 5, 6, and 7 represent the active cooling operation of the ventilation system operating the mechanical cooling unit. Mode 1 was designed to identify the free running condition of the building where the ambient air was directly driven to the space for ventilation purposes with no mechanical cooling. The free cooling condition was applied using mode 2 where the outlet air of the PAHX unit was continuously directed to the space during charging and discharging (where scenarios 2 and 6 were applied during charging and discharging respectively, as mentioned earlier in Section 5.1.1) without mechanical cooling. Mode 3 applied the free cooling concept while the outlet air temperature of the PAHX unit was directed to the space only during discharging. During charging, the no-airflow condition was applied to the PAHX unit (scenario 1 was applied). In this case, the return air was circulated to the space only during PAHX charging periods. Mode 4 simulated the conventional cooling scenario where the ambient air was actively cooled before it was supplied to the space. To assess the energy saving potential of the PAHX system, mode 5 proposed that the outlet air of the PAHX unit was directed to the cooling unit to reduce its energy consumption before supplying the air to the space. Mode 5 assumed that the air was continuously being directed through the PAHX unit during both charging and discharging at the same air velocity. Modes 6 and 7 followed the previous energy saving concept with applying the operational control of the reference case of the PAHX unit where the airflow was only allowed during the discharging periods. During charging periods where there was no airflow through the PAHX unit (scenario 1)., the return air was delivered to the cooling unit to be resupplied to the space in mode 6. In mode 7, 100% fresh air ventilation strategy was applied introducing the ambient air to the cooling unit during PAHX charging periods. The modes 1, 2, and 3 were assessed by evaluating the thermal comfort levels (percentage of PPD) and the cooling

loads. The modes 4, 5, 6, and 7 were assessed by evaluating the energy consumption of the cooling unit.

Table 26. Operational modes of integrating the proposed PAHX unit with the ventilation system

Operational Mode	Fans		Valves				
	F1	F2	V1	V2	V3	V4	V5
Mode 1 (Free running)	OFF	ON	OFF	ON	ON	OFF	OFF
Mode 2 (Free cooling)	ON	OFF	ON	OFF	ON	OFF	OFF
Mode 3 (Free cooling)-Return	ON/OFF	OFF	ON/OFF	OFF	ON	OFF	OFF/ON
Mode 4 (conventional cooling)	OFF	ON	OFF	ON	OFF	ON	OFF
Mode 5 (Energy savings)	ON	OFF	ON	OFF	OFF	ON	OFF
Mode 6 (Energy savings)-Return	ON/OFF	OFF	ON/OFF	OFF	OFF	ON	OFF/ON
Mode 7 (Energy savings)-Ambient	ON/OFF	OFF/ON	ON/OFF	OFF/ON	OFF	ON	OFF

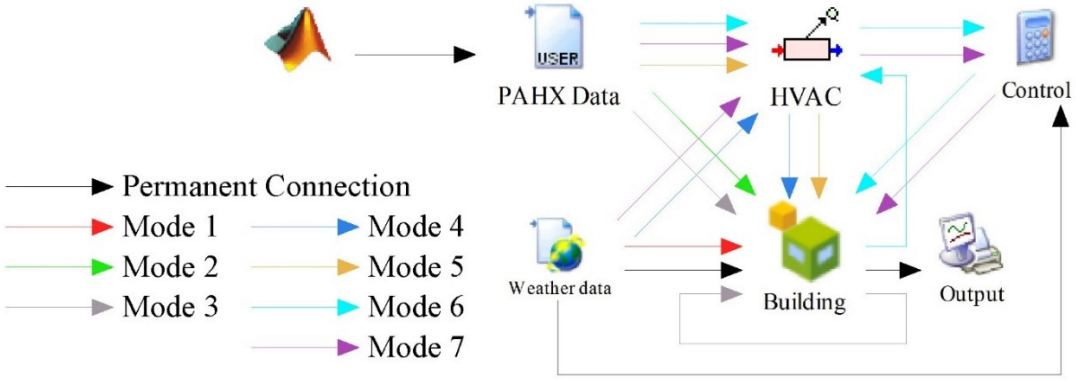

Figure 109. The designed operational modes in respect of the used TRNSYS types

5.4.2. Building Envelope Characteristics

Two different characteristics were defined for the building envelope: Heavyweight and Lightweight construction types. Usually, the heavyweight construction defines the conventional buildings in hot desert region, while the lightweight envelopes are one of the main features of the contemporary construction style. Table 27 summarizes the envelope characteristics of the heavyweight and the lightweight building types. The roof construction and the glazing type were assumed to be similar in both types. The indoor thermal performance was assessed utilizing both building types.

Table 27. Envelope characteristics for the used building types

Roof *U-value (0.324 W/m^{2}K)*	Plaster (innermost layer)	0.02 m
	Concrete slab	0.25 m
	Insulation	0.1 m
	Flooring tiles	0.02 m

Glazing *U-value (5.68 W/m²K)*		Single glazing	0.004 m
Heavyweight	Exterior walls *U-value (1.012 W/m²K)*	Plaster (innermost layer)	0.01 m
		Limestone	0.4 m
		Plaster (outermost layer)	0.015 m
	Interior walls *U-value (1.711 W/m²K)*	Plaster (innermost layer)	0.01 m
		Limestone	0.2 m
		Plaster (outermost layer)	0.01 m
Lightweight	Exterior walls *U-value (0.342 W/m²K)*	Plaster (innermost layer)	0.01 m
		Gypsum boards	0.05 m
		Insulation	0.1 m
		Plaster (outermost layer)	0.015 m
	Interior walls *U-value (0.652 W/m²K)*	Gypsum boards (innermost layer)	0.012 m
		Insulation	0.05 m
		Gypsum boards (outermost layer)	0.012 m

5.4.3. Direct Free Cooling

The three passive operational modes (1, 2, and 3) for the proposed integrated ventilation system were tested without the operation of active cooling. Mode 1 represented the free running condition of the building. Mode 2 represented the direct free cooling mode with an airflow with a velocity of 0.3 m/s during charging and discharging. Mode 3 followed the control strategy of the PAHX reference case (no airflow during charging- airflow with a velocity of 0.3 m/s during discharging). Accordingly, only in mode 3, the return air was recirculated during PAHX charging periods. The airflow rate was the same in all modes which was similar to this of the reference case (44.58 kg/h). The investigation was conducted on both building types. The analysis utilized the average values of the room air temperature, PPD, and cooling loads to evaluate the thermal performance of the building during the typical summer week application.

- *Heavyweight Building Type*

The results of the investigation of the heavyweight building type, shown in Figure 110, showed that mode 2 (direct free cooling) achieved the least average values of the room air temperature (30.77˚C) and the PPD (57.01%). Thus, mode 2 accomplished an enhancement of 16.4% in the PPD level than the free running condition of the building (mode 1). Also, the space recorded less required cooling loads during mode 2 application than mode 1 by 10.4%. However, mode 3 achieved the least required amount of energy for cooling loads (81.38 kWh) with a reduction of 14.5% than mode 1 but with a reduction of only 2.8% in PPD. Figures 111 and 112 show the evolution of the PPD levels and the cooling loads in (kW) respectively during three days (23rd June

– 25th June) of the application. As noticed, mode 2 maintained the least profile for PPD levels. Regarding cooling loads, mode 3 achieved the lowest profile due to the return air strategy during night-time; however, this strategy affected the PPD levels during this period.

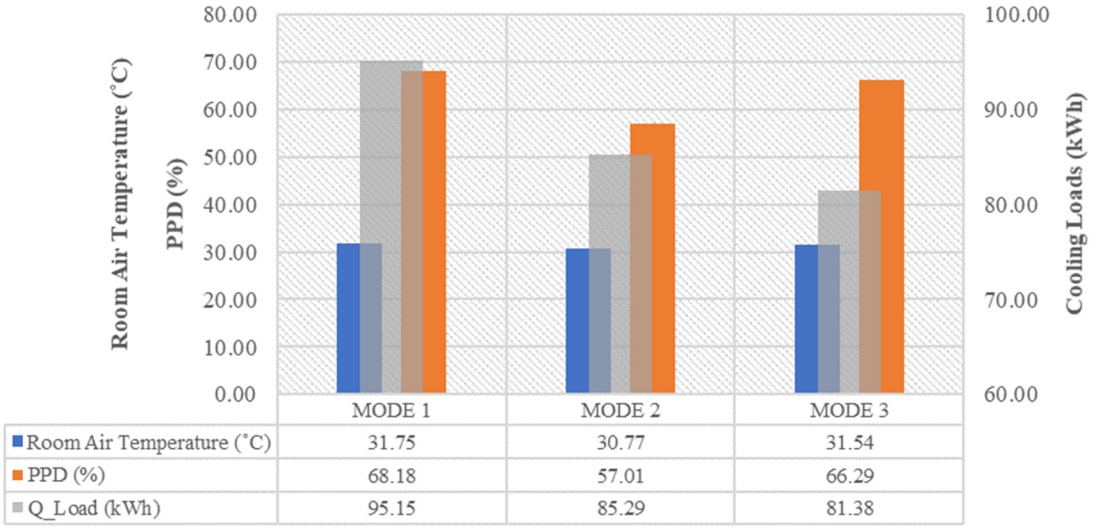

Figure 110. Weekly average values for direct free cooling investigation for heavyweight building

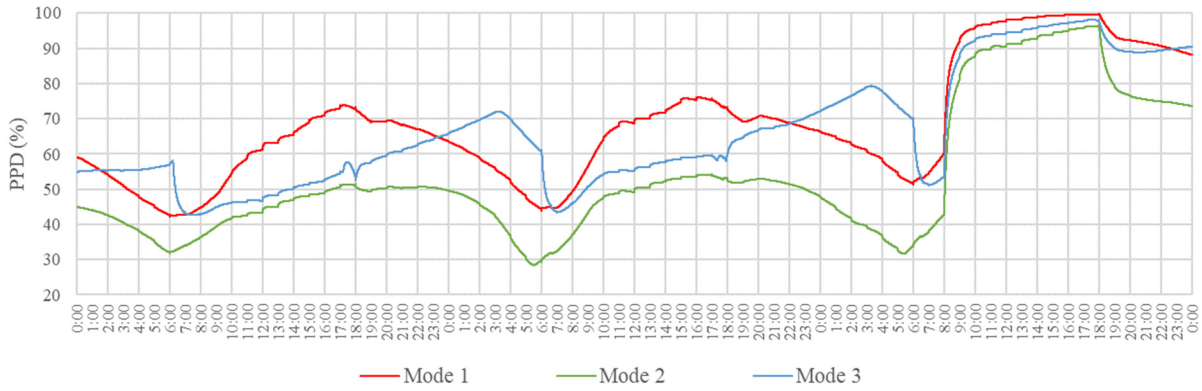

Figure 111. PPD levels during direct free cooling investigation for heavyweight building

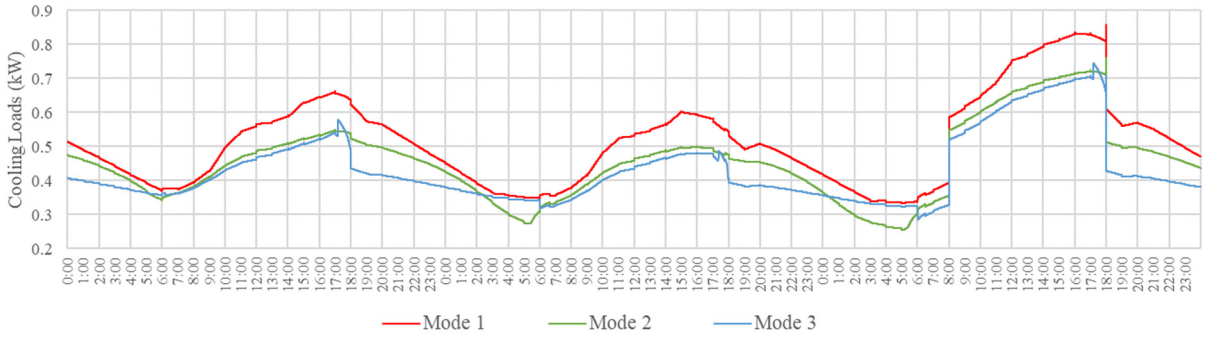

Figure 112. Cooling loads during direct free cooling investigation for heavyweight building

- *Lightweight Building Type*

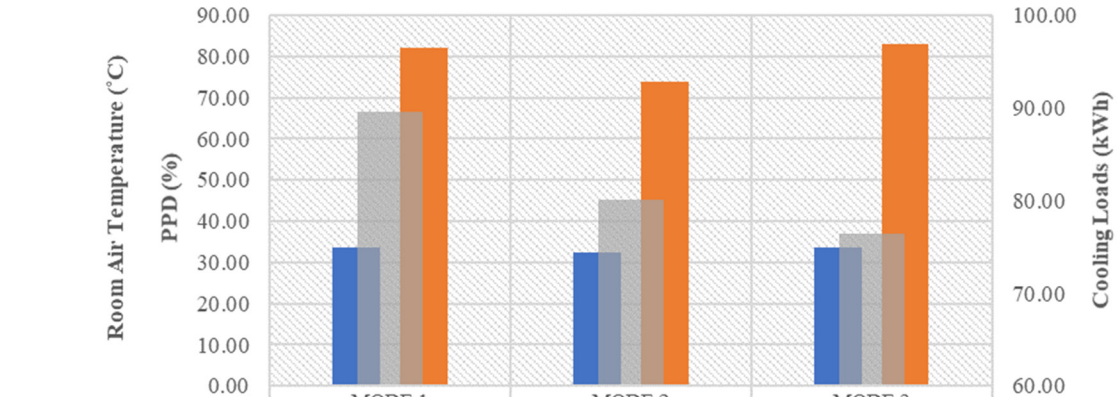

	MODE 1	MODE 2	MODE 3
Room Air Temperature (°C)	33.54	32.36	33.59
PPD (%)	82.19	73.90	83.10
Q_Load (kWh)	89.52	80.12	76.42

Figure 113. Weekly average values for direct free cooling investigation for lightweight building

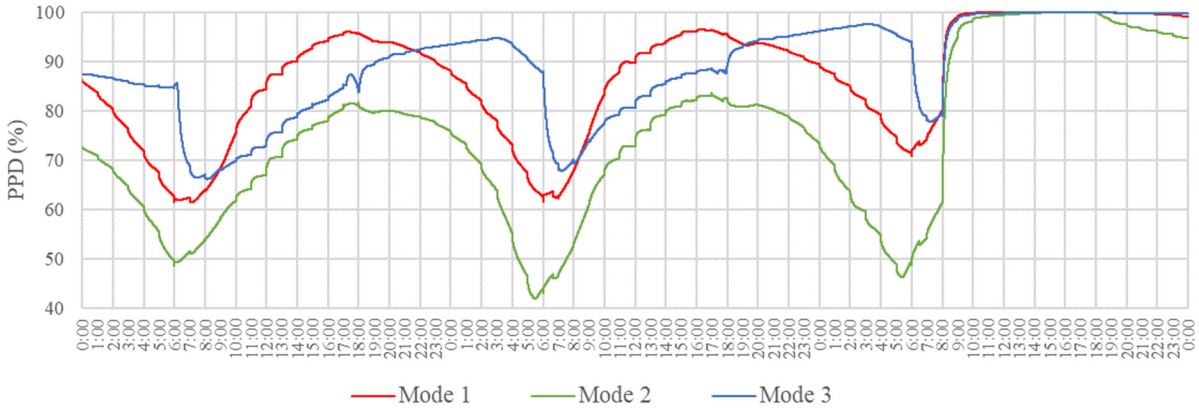

Figure 114. PPD levels during direct free cooling investigation for lightweight building

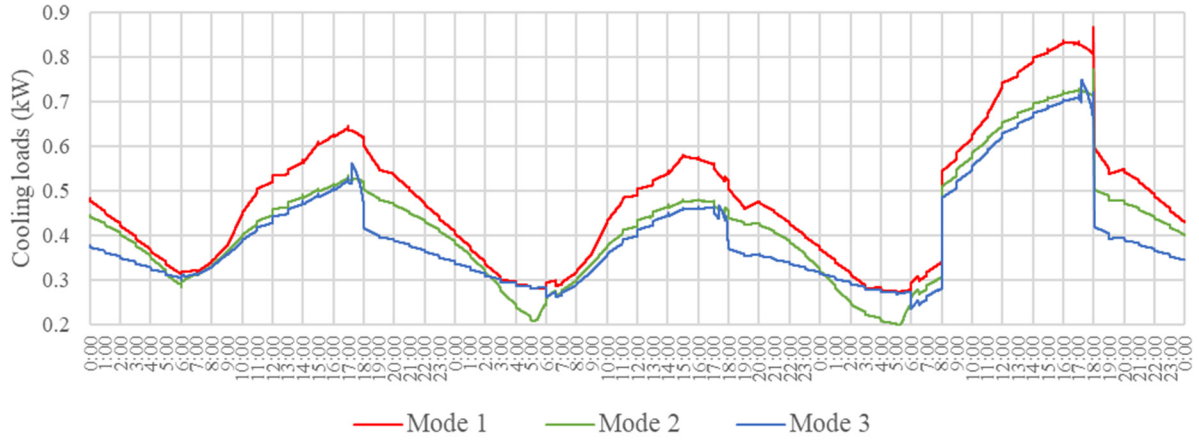

Figure 115. Cooling loads during direct free cooling investigation for lightweight building

Figure 113 shows the analysis of the average values of room air temperature, PPD, and cooling loads for the lightweight building type during the typical summer week. It can be inferred that applying mode 2 (direct free cooling) enhanced the thermal comfort levels than the free running mode (mode 1) by 10.1% with a reduction of the cooling loads of 10.5%. However, applying the control strategy of the PAHX reference case with utilizing the return air during PAHX charging periods (mode 3) achieved a reduction of 14.6% in the cooling loads but without any enhancements in the PPD levels. Figures 114 and 115 show the profiles of the PPD levels and cooling loads respectively during three days of the application of the direct free cooling.

Referring to PPD and cooling loads profile distribution in both building types, it can be inferred that the maximum enhancements were occurred during the peaks of the conventional profiles. This increases the potential of applying the PAHX unit for cooling loads peak shaving applications. Thus, the stored energy in PAHX unit can be preserved till the peak duration, and the system operation can be limited for the peak period providing the required enhancements in loads and comfort profiles for an objective of peak shaving. It can also be noticed that, in general, the thermal comfort levels were enhanced in heavyweight building type than the lightweight type for all the modes. Applying the free cooling mode (mode 2), the analysis shows an enhancement of about 17% in PPD level when heavyweight construction was utilized.

5.4.4. Energy Saving Strategy

Energy saving modes (modes 4, 5, 6, and 7) aimed at the conservation of the cooling energy consumed by the mechanical cooling unit through introducing the PAHX outlet air to the active unit. For all the modes, the set-point temperature of the cooling unit was set to 6˚C with no specified set-point temperature for the space. The indoor thermal performance was evaluated for both building types. The average values of the room air temperature and the PPD were assessed for the typical summer week application. Regardless the applied mode, the average room air temperature recorded 25.7˚C and 26.3˚C for heavyweight and lightweight building types respectively. The average PPD recorded 9.1% and 13.7% in heavyweight and lightweight building types respectively. It can be concluded that better thermal comfort levels could be achieved utilizing the heavyweight construction.

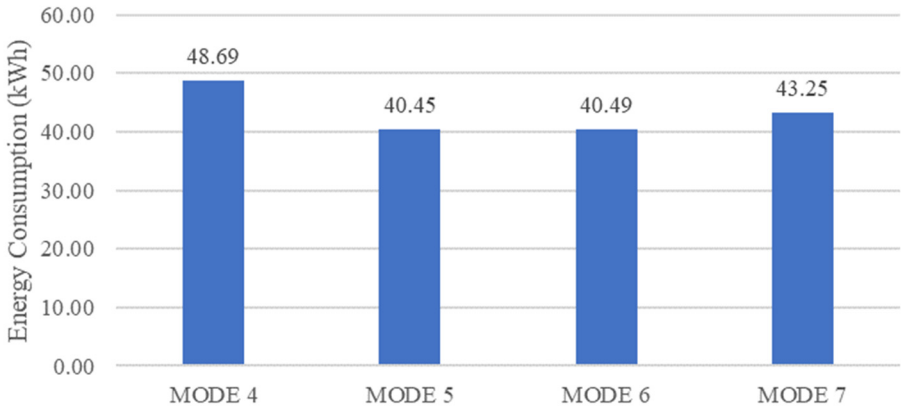

Figure 116. Energy consumption of the energy savings modes during the typical summer week

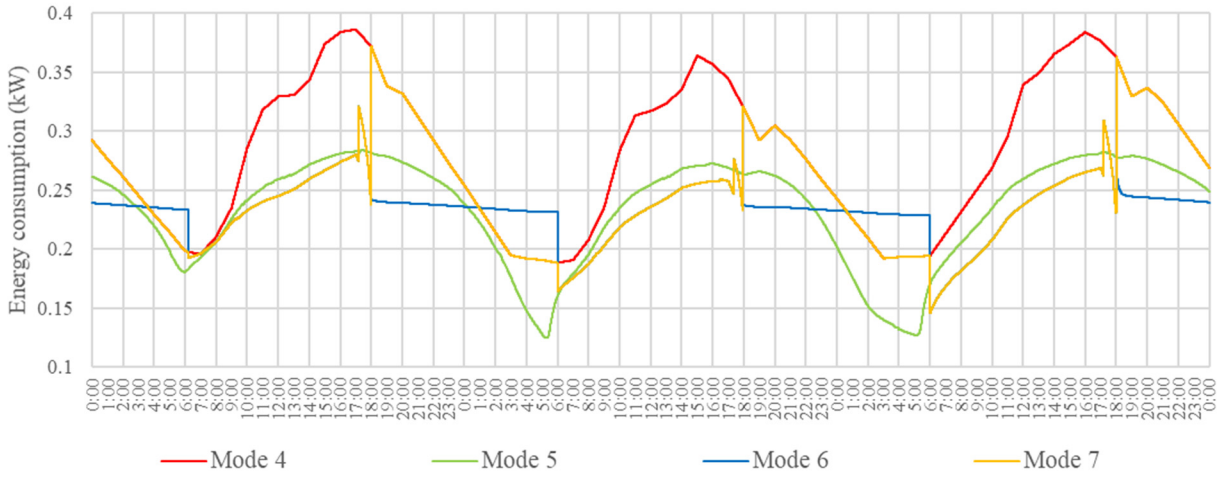

Figure 117. Energy consumption of the mechanical cooling system

Mode 4 simulated the conventional active cooling with 100% supply ambient air. The outlet air of the PAHX unit with a constant airflow rate (44.58 kg/h) during both charging and discharging was introduced to the cooling unit in mode 5 as its inlet air temperature. Modes 6 and 7 followed the control strategy of the PAHX reference case where there was no airflow during charging. Accordingly, the return air from the space and the ambient air were introduced to the cooling unit during charging periods in mode 6 and mode 7 respectively. Figure 116 shows the energy consumption of the cooling system for the four modes during the typical summer week application. Figure 117 illustrates the evolution of the energy consumption distribution profile during three days of the application. It can be inferred that the continuous supply of the PAHX outlet air to the cooling system (mode 5) instead of the ambient air (mode 4) reduced the energy consumption of the cooling unit by 16.9%. However, introducing the return air to the cooling system during PAHX charging periods in mode 6 did not attain more enhancement in energy consumption recording a

reduction of 16.8%. Also, introducing the ambient air during PAHX charging (mode 7) decreased the overall energy consumption by only 11.2%. Referring to the distribution profile, the maximum reduction in energy consumption can be noticed during peak periods. This promotes the peak shaving application of the integrated PAHX unit applying an operational strategy for the system.

5.4.5. Influence of Mass Flow Rate on The Indoor Thermal Performance

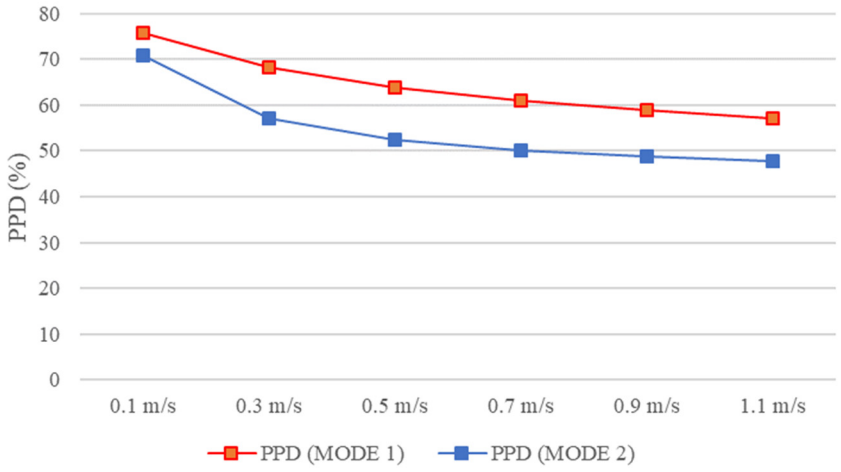

Figure 118. Thermal comfort levels for direct free cooling in respect of various air velocities

Utilizing the application of the heavyweight construction, the influence of applying several mass airflow rates on the indoor thermal comfort levels and the energy consumption of the cooling unit was assessed. The various values of mass airflow rates were similar to those investigated earlier in Section 5.3.1 for the PAHX parametric analysis. Several values for the air velocity (from 0.1 m/s to 1.1 m/s) were applied with a step of 0.2 m/s. The mass flow rate of the ventilation system was considered to equal the mass flow rate through the PAHX system. The set-point temperature of the cooling unit was reset to 18˚C to avoid over cooling effect by the higher air velocities. The PPD levels and the energy consumption were assessed through direct free cooling (mode 2) and energy savings strategy (mode 5) respectively. Regarding the direct free cooling application, the average PPD value for mode 2 during the typical summer week application was compared to the free running condition (mode 1) supplying the ambient air and applying the similar mass flow rates. The results in Figure 118 show that higher air velocity values provided lower PPD values. The application recorded a PPD value of 47.9% with the free cooling application with an air

velocity of 1.1 m/s. Overall, mode 2 achieved an enhancement in thermal comfort levels up to 17.9% (with an air velocity of 0.5 m/s).

The accumulated value of the energy consumption during the typical summer week was evaluated for the energy savings mode (mode 5) and the conventional cooling application (mode 4). Also, the average PPD levels were recorded for all the various cases of the mass flow rates. It can be noticed from Figure 119 that although lower values of mass flow rates achieved lower energy consumption values (with lower PAHX outlet air temperature), however, they could not satisfy the indoor thermal comfort of the space. The thermal comfort levels were maintained within the acceptable range for air velocity values of 0.7 m/s and higher. It is worth mentioning here that the ASHRAE standard 55 does not have a separate criterion for air velocities higher than 0.3 m/s. For the air velocity of 0.7 m/s, the application recorded an average PPD of 8.2% with a reduction of the energy consumption of the cooling system of 10.3 kWh which represented 18.4% of the weekly energy consumption. The reduction in the accumulative energy consumption increased with the elevated air velocity values that reached up to 10.8 kWh for an air velocity of 1.1 m/s.

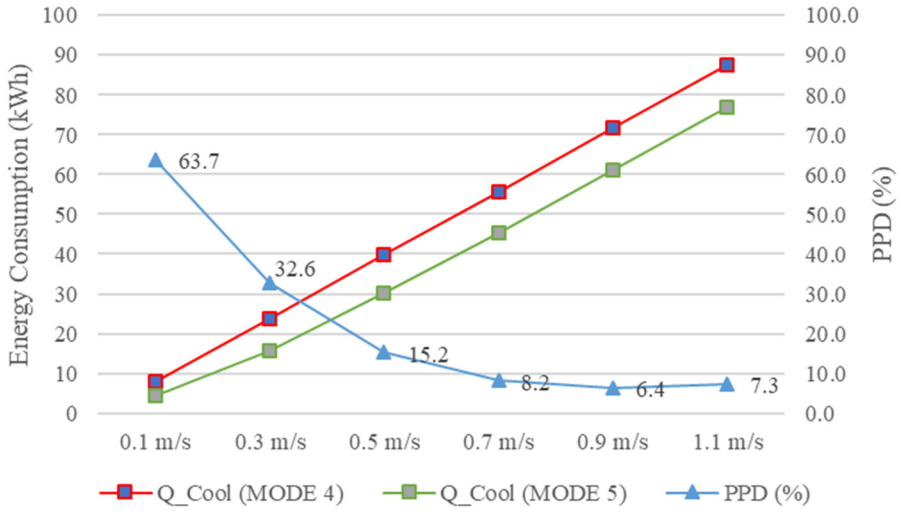

Figure 119. Energy consumption and thermal comfort levels of energy savings modes for elevated air velocities

CHAPTER SIX: CONCLUSION & RECOMMENDATIONS

Utilizing the concept of Latent Heat Thermal Energy Storage (LHTES) using phase change materials (PCMs) has been widely discussed in the literature. In some LHTES systems, the air is used as a heat transfer fluid to charge and discharge the PCM inside a heat exchanger called PCM-to-Air Heat Exchanger (PAHX). In this study, the applications of PAHXs for free cooling applications were comprehensively reviewed and analyzed. Chapter two discussed the potential and constraints of applying PAHXs free cooling systems in building applications. The review pointed out that the governing parameters and most system influencing factors are inlet air temperature, phase change temperature range, and airflow rates. It is worth mentioning that these factors are integrated, cohesive and should be simultaneously analyzed and investigated to better assess the system performance. The review also defined potential approaches that lead to increased system thermal performance, like using multiple PCMs and integration with other passive technologies. However, most of system challenges were related to local climatic conditions. Previous studies reported the insufficient cooling charging energy needed for complete solidification of the PCM in free cooling systems, especially in hot climates, which affects the outlet air temperature and the overall system performance. They also claimed that continuously maintaining PAHX outlet air temperature within the preferred indoor thermal comfort is a system limitation, especially in climates with exceptionally high cooling demand.

For magnifying the system free cooling abilities, the study proposed considering the night-time sky as potential source of radiative cooling for PCM charging process (solidification). Chapter three described the development of an improved PAHX type for building envelope applications. The developed system aimed to increase the cooling charging power of the system through magnifying the radiation thermal losses to the sky, as a cooling source, during the night-time cooling charging process (PCM solidification). Chapter three presented the experimental investigation for two real-scale prototypes of the developed system to monitor the effect of the radiative cooling on the system thermal behavior under real ambient conditions. The cooling charging energy was evaluated for various operational and configurational experimental cases. Two different PCM types were utilized in the two designed prototypes: organic PCM RT44HC (prototype 01), and microencapsulated PCM composite panels (prototype 02). Specific key

performance indicators were defined to better analyze the experimental results and evaluate the charging performance of the experimental cases. The experimental results showed that the system exposure to the clear sky magnifies the thermal losses during cooling charging (PCM solidification). The results also assured the system charging performance when the difference between the ambient charging temperature and the phase change temperature of the system is insufficient to charge the system. However, a control strategy is recommended to manage the convective and radiative losses with respect to the ambient profile (temperature difference between phase change range of the PCM and the ambient temperature) and system configurational and operational modes. The results proved that the cooling charging energy increased by up to 22% under specific conditions of the experiment promoting better overall thermal performance of the system. They also proved the increased cooling potential of the system application in hot dry climates.

A numerical model of the new PAHX type was developed and presented in Chapter four. The developed model consists of four sub-models: the sub-model for thermal storage in the PCM, the thermal radiation sub-model, the conduction sub-model, and the convection sub-model. The model developed new thermal boundaries for long-wave radiation to the sky considering the cloudiness percentage (level of sky clearness) and relative humidity level. The model implemented energy balance equations, which were coded by means of the finite difference method and the implicit time discretization in the MATLAB/SIMULINK environment. The apparent heat capacity method was utilized for the phase change modeling. A detailed description of the convection heat transfer phenomena inside the PAHX system was introduced by the convection sub-model to consider various modes of operation (forced, free, and mixed modes of convection). The obtained experimental data were utilized to validate the numerical model under various operational scenarios. The results of the model validation indicated that the model was in all cases within the accepted calibration range defined by ASHRAE Guideline 14. Further, inter-model validations were conducted to compare the thermal radiation sub-model and the sky temperature sub-model with the existing numerical models. The results were within the accepted calibration range.

Moreover, using the developed validated numerical model, the thermal performance of the developed PAHX system was numerically assessed for an application in the hot desert climate. Chapter five presented the application of the developed PAHX within various locations in the hot

desert climate. Since the RH values, the ambient air profile, and the sky temperature differ from location to location, the performance analysis showed that the free cooling systems are local-based applications and should be carefully designed with respect to the location. The location-based analysis showed that the PAHX configuration and the type of PCM should be determined separately for each location. An operational control plan was proposed to block the solar radiation during the daytime (cooling discharging) and to allow the thermal losses to the clear sky during night-time. A parametric study was conducted to demonstrate the influence of applying various values of the system variables on the stand-alone thermal performance of the system. These parameters included: the air velocity inside the air channel, the PCM panel thickness, the system length, the height of the air channel, and the PCT range of the PCM. Also, the multi-PCM approach was discussed and evaluated utilizing different compositions of the PCM types. Most of the previous studies of the multi-PCM approach applied a fixed inlet air temperature to investigate the thermal performance of the PAHX unit (Mosaffa et al., 2013; Zalba et al., 2004). This study investigated the Multi-PCM approach under real ambient conditions for a typical summer week in the hot desert climate using the new developed PAHX type. The results showed that applying one proper type of PCM was more beneficial to the thermal performance of the stand-alone PAHX unit than operating the system under multiple PCM types. It can be concluded that applying single type of PCM while utilizing the radiative cooling during PCM solidification is more efficient that applying the multi-PCM approach. The outlet air temperature of the stand-alone unit was compared with the thermal comfort range of the naturally conditions spaces. It was shown that during 91.5% of the application duration, the outlet air temperature was within the occupants' thermal comfort range promoting the cooling potential of the developed PAHX unit as an efficient cooling system.

The stand-alone PAHX unit was integrated to a mechanical ventilation system of an office space to evaluate the influence of this integration on the indoor thermal requirements in the hot desert climate. Two building types were analyzed; heavyweight and lightweight constructions. The thermal comfort levels were assessed during the free running and the direct free cooling applications. Also, the energy consumption of the mechanical system was evaluated during the conventional cooling and the energy savings modes. In general, under the investigated conditions and assumptions, the heavyweight construction promoted better thermal comfort levels than the lightweight building type during both free running and conventional cooling modes. Moreover, it

can be concluded that, during the direct free cooling application, the thermal comfort levels were enhanced by 16.4% in the heavyweight building type and 10.1% in the lightweight building type through supplying the PAHX outlet air to the mechanical ventilation system. Through following a control strategy of the air supply during charging and discharging, the cooling loads of the space could be reduced by 14.5% in heavyweight building type and 14.6% in lightweight building type. During the energy savings mode, introducing the outlet air of the PAHX unit to the mechanical cooling unit reduced the energy consumption of the cooling unit by 16.9% saving 8.24 kWh of energy during the weekly application. The influence of increasing the mass airflow rate through the ventilation system was assessed. The results showed that higher air velocity values (up to 1.1 m/s) provided better thermal comfort levels. The direct free cooling application provided an enhancement up to 17.9% in thermal comfort levels. For energy saving applications, lower mass airflow rates provided lower outlet air temperatures of the PAHX unit and lower energy consumption of the integrated cooling system. However, these low rates of mass airflow could not satisfy the indoor thermal comfort requirements. Instead, higher air velocities recorded satisfying performance with respect to the thermal comfort levels achieving a reduction of 18.4% (up to 10.8 kWh/week) in cooling energy consumption than the conventional cooling system.

Based on the experimental results and the performance analysis of the system, it can be inferred that there are some significant influential parameters that control the thermal behavior of the system. From the environmental perspective, the ambient air temperature, which also affects the sky temperature, is the most important aspect in determining the system performance. The ambient air profile during the application also determines the appropriate PCT range of the system. From the operational perspective, the airflow is the most significant parameter as it controls the charging and discharging processes. It also affects the thermal comfort levels and energy consumption of the mechanical ventilation system. The airflow should be carefully designed through an operational plan considering the power consumption of the fan. The most influential parameter from the design perspective is the type of the PCM (PCT range of the application) which determines the thermal performance and controls the outlet air temperature during the application.

In conclusion, the developed PAHX system promotes the energy savings concept when it is integrated with a mechanical ventilation system in the hot desert climate. The study promotes the practical application of the developed PAHX system with respect to the local climatic conditions.

However, the study comes with the following recommendations for future works regarding the current application of the system:

- An optimization study that considers all system parameters (system size, PCM type, etc.), ventilation system operational modes, and control strategy of heat gains and losses to the PAHX unit with the power consumption related to the control plan is highly recommended to reach the optimal thermal performance of the integrated PAHX system to maximize the comfort levels and minimize the cooling loads. The optimization should be a location-based study that depends on the specific climatic characterizations of the location.
- The optimization study should be extended to include the parameters of the whole mechanical ventilation system and variables (operation hours, set-point temperature, airflow, and fans operations) in order to minimize the energy consumption of the entire mechanical system within the building ventilation system.
- A complementary study for system thermal behavior under real applications with limited sky exposure and vertical configuration with surroundings are recommended.

For further applications, developments, and improvements of the system thermal performance, the researcher recommends that the future studies can include:

- The extension of the application duration of the developed PAHX thermal performance to consider the whole cooling season with respect to the location.
- A feasibility study for the year-round operation of the free cooling system potential in hot desert climate is needed to support the practical application focusing on the economic analysis of the PAHX free cooling system.
- A practical investigation for the developed PAHX system under hot and humid conditions.

REFERENCES

Adelard, L., Pignolet-Tardan, F., Mara, T., Lauret, P., Garde, F., and Boyer, H. **1998**. "Sky Temperature Modelisation and Applications in Building Simulation." *Renewable Energy* 15 (1): 418–30. DOI: 10.1016/S0960-1481(98)00198-0.

Agyenim, Francis, Hewitt, Neil, Eames, Philip, and Smyth, Mervyn. **2010**. "A Review of Materials, Heat Transfer and Phase Change Problem Formulation for Latent Heat Thermal Energy Storage Systems (LHTESS)." *Renewable and Sustainable Energy Reviews* 14: 615–28. DOI: 10.1016/j.rser.2009.10.015.

Ali, Ahmed Hamza H. **2013**. "Desiccant Enhanced Nocturnal Radiative Cooling-Solar Collector System for Air Comfort Application in Hot Arid Areas." *Sustainable Energy Technologies and Assessments* 1 (March): 54–62. DOI: 10.1016/j.seta.2013.01.003.

AL-Lami, Alaa M., AL-Salihi, Ali M., and AL-Timimi, Yaseen K.. **2017**. "Parameterization of the Downward Long Wave Radiation under Clear-Sky Condition in Baghdad, Iraq." *Asian Journal of Applied Sciences* 10: 10–17. DOI: 10.3923/ajaps.2017.10.17.

Al-Nimr, M., Tahat, M., and Al-Rashdan, M. **1999**. "A Night Cold Storage System Enhanced by Radiative Cooling - a Modified Australian Cooling System." *Applied Thermal Engineering* 19 (9): 1013–26.

Arkar, C., and Medved, S. **2005**. "Influence of Accuracy of Thermal Property Data of a Phase Change Material on the Result of a Numerical Model of a Packed Bed Latent Heat Storage with Spheres." *Thermochimica Acta* 438: 192–201. DOI: 10.1016/j.tca.2005.08.032.

———. **2007**. "Free Cooling of a Building Using PCM Heat Storage Integrated into the Ventilation System." *Solar Energy* 81 (9): 1078–87. DOI: 10.1016/j.solener.2007.01.010.

Arkar, C., Vidrih, B., and Medved, S. **2007**. "Efficiency of Free Cooling Using Latent Heat Storage Integrated into the Ventilation System of a Low Energy Building." *International Journal of Refrigeration* 30: 134–43. DOI: 10.1016/j.ijrefrig.2006.03.009.

ASHRAE. **2002**. *ASHRAE Guideline - Measurement of Energy and Demand Savings*. Vol. 14.

———. **2009a**. *2009 ASHRAE Handbook - Fundamentals SI Edition*. SI. Atlanta, GA: American Society of Heating, Refrigerating and Air-Conditioning Engineers.

———. **2009b**. "ASHRAE Handbook_Fundamentals." American Society of Heating, Refrigerating and Air-Conditioning Engineers, Inc.

———. **2013**. "ASHRAE Standard 55 - Thermal Environmental Conditions for Human Occupancy." ANSI-ASHRAE.

Bahrar, Myriam. **2018**. "Contribution Au Développement et à l'analyse d'une Enveloppe de

Bâtiment Multifonctionnelle Dans Le Cadre de l'optimisation Du Confort Dans l'habitat." PhD Thesis.

Barzin, Reza, Chen, John J. J., Young, Brent R., and Farid, Mohammed M. **2015**. "Application of PCM Energy Storage in Combination with Night Ventilation for Space Cooling." *Applied Energy* 158: 412–21. DOI: 10.1016/j.apenergy.2015.08.088.

BLOX, USINAGE PLASTIQUES. 2019. *Polymethyl Methacrylate (PMMA)*. Vol. **2019**. (https://www.blox.fr/)

Borderon, Julien. **2012**. "Intégration Des Matériaux à Changement de Phase Comme Système de Régulation Dynamique En Rénovation Thermique." PhD Thesis.

Borderon, Julien, Virgone, Joseph, and Cantin, Richard. **2015**. "Modeling and Simulation of a Phase Change Material System for Improving Summer Comfort in Domestic Residence." *Applied Energy* 140: 288–96. DOI: 10.1016/j.apenergy.2014.11.062.

Budaiwi, I. M. **2001**. "Energy Performance of the Economizer Cycle under Three Climatic Conditions in Saudi Arabia." *International Journal of Ambient Energy* 22 (2): 83–94. DOI: 10.1080/01430750.2001.9675391.

Bulut, Hüsamettin, and Aktacir, Mehmet Azmi. **2011**. "Determination of Free Cooling Potential: A Case Study for İstanbul, Turkey." *Applied Energy* 88 (3). DOI: 10.1016/j.apenergy.2010.08.030.

Butala, Vincenc, and Stritih, Uroš. **2009**. "Experimental Investigation of PCM Cold Storage." *Energy & Buildings* 41: 354–59. DOI: 10.1016/j.enbuild.2008.10.008.

CCES. **2008**. "Residential Buildings Total Energy End Use." Center of Climate and Energy Solutions.

Çengel, Yunus A. **2003**. *Heat Transfer: A Practical Approach*. Illustrated. McGraw-Hill.

Ceylan, İlhan, Ergün, Alper, Acar, Bahadır, and Aydin, Mustafa. **2016**. "Psychometric and Thermodynamic Analysis of New Ground Source Evaporative Cooling System." *Energy & Buildings* 119: 20–27. DOI: 10.1016/j.enbuild.2016.03.017.

Chan, Hoy-Yen, Riffat, Saffa B., and Zhu, Jie. **2010**. "Review of Passive Solar Heating and Cooling Technologies." *Renewable and Sustainable Energy Reviews* 14: 781–89. DOI: 10.1016/j.rser.2009.10.030.

Chandrasekar, M., Rajkumar, S., and Valavan, D. **2015**. "A Review on the Thermal Regulation Techniques for Non-Integrated Flat PV Modules Mounted on Building Top." *Energy & Buildings* 86: 692–97. DOI: 10.1016/j.enbuild.2014.10.071.

Chen, Chao, Guo, Haifeng, Liu, Yuning, Yue, Hailin, and Wang, Chendong. **2008**. "A New Kind of Phase Change Material (PCM) for Energy-Storing Wallboard." *Energy & Buildings* 40: 882–90. DOI: 10.1016/j.enbuild.2007.07.002.

Cole, R. J. **1976**. "The Longwave Radiative Environment around Buildings." *Building and Environment* 11 (1). DOI: 10.1016/0360-1323(76)90014-7.

COMSOL-AB. **2017**. *COMSOL Multiphysics 5.3 (Build: 316)*. Vol. 5.3.

Cuce, Pinar Mert, and Riffat, Saffa. **2016**. "A State of the Art Review of Evaporative Cooling Systems for Building Applications." *Renewable and Sustainable Energy Reviews* 54: 1240–49. DOI: 10.1016/j.rser.2015.10.066.

Cui, X., Chua, K. J., Islam, M. R., and Ng, K. C. **2015**. "Performance Evaluation of an Indirect Pre-Cooling Evaporative Heat Exchanger Operating in Hot and Humid Climate." *Energy Conversion and Management* 102: 140–50. DOI: 10.1016/j.enconman.2015.02.025.

Dardir, Mohamed A. **2017**. *Natural Ventilation Techniques as a Base for Environmental Passive Architecture*. Cairo, Egypt: Noor Publishing.

Dardir, Mohamed, Panchabikesan, Karthik, Haghighat, Fariborz, El Mankibi, Mohamed, and Yuan, Yanping. **2019**. "Opportunities and Challenges of PCM-to-Air Heat Exchangers (PAHXs) for Building Free Cooling Applications—A Comprehensive Review." *Journal of Energy Storage* 22. DOI: 10.1016/j.est.2019.02.011.

Darzi, A. A. R., Moosania, S. M., Tan, F. L. and Farhadi, M. **2013**. "Numerical Investigation of Free-Cooling System Using Plate Type PCM Storage." *International Communications in Heat and Mass Transfer* 48: 155–63. DOI: 10.1016/j.icheatmasstransfer.2013.08.025.

De Gracia, Alvaro, and Cabeza, Luisa F., **2015**. "Phase Change Materials and Thermal Energy Storage for Buildings." *Energy & Buildings* 103: 414–19. DOI: 10.1016/j.enbuild.2015.06.007.

De Gracia, Alvaro, Castell, Albert, Fernández, Cèsar and Cabeza, Luisa F. **2015**. "A Simple Model to Predict the Thermal Performance of a Ventilated Facade with Phase Change Materials." *Energy & Buildings* 93. DOI: 10.1016/j.enbuild.2015.01.069.

De Gracia, Alvaro, David, Damien, Castell, Albert, Cabeza, Luisa F., and Virgone, Joseph. **2013**. "A Correlation of the Convective Heat Transfer Coefficient between an Air Flow and a Phase Change Material Plate." *Applied Thermal Engineering* 51 (1): 1245–54. DOI: 10.1016/j.applthermaleng.2012.11.045.

De Gracia, Alvaro, Navarro, Lidia, Castell, Albert, and Cabeza, Luisa F. **2013**. "Numerical Study on the Thermal Performance of a Ventilated Facade with PCM." *Applied Thermal Engineering* 61 (2): 372–80. DOI: 10.1016/j.applthermaleng.2013.07.035.

———. **2015**. "Energy Performance of a Ventilated Double Skin Facade with PCM under Different Climates." *Energy & Buildings* 91: 37–42. DOI: 10.1016/j.enbuild.2015.01.011.

De Gracia, Alvaro, Navarro, Lidia, Castell, Albert, Ruiz-Pardo, Álvaro, Alvárez, Servando, and Cabeza, Luisa F. **2013**. "Experimental Study of a Ventilated Facade with PCM during

Winter Period." *Energy & Buildings* 58. DOI: 10.1016/j.enbuild.2012.10.026.

De Gracia, Alvaro, Navarro, Lidia, Castell, Albert, Ruiz-Pardo, Álvaro, Álvarez, Servando, and Cabeza, Luisa F. **2013**. "Thermal Analysis of a Ventilated Facade with PCM for Cooling Applications." *Energy & Buildings* 65. DOI: 10.1016/j.enbuild.2013.06.032.

Diarce, G., Á Campos-Celador, K. Martin, A. Urresti, A. García-Romero, and J. M. Sala. **2014**. "A Comparative Study of the CFD Modeling of a Ventilated Active Façade Including Phase Change Materials." *Applied Energy* 126: 307–17. DOI: 10.1016/j.apenergy.2014.03.080.

Del Pero, Claudio, Aste, Niccolò, Paksoy, Halime, Haghighat, Fariborz, Grillo, Samuele, and Leonforte, Fabrizio. **2018**. "Energy Storage Key Performance Indicators for Building Application." *Sustainable Cities and Society* 40. DOI: 10.1016/j.scs.2018.01.052.

Dolado, Pablo, Lazaro, Ana, Marin, Jose M., and Zalba, Belen. **2011**. "Characterization of Melting and Solidification in a Real Scale PCM-Air Heat Exchanger: Numerical Model and Experimental Validation." *Energy Conversion and Management* 52: 1890–1907. DOI: 10.1016/j.enconman.2010.11.017.

Domanski, R., and Fellah, G. **1996**. "Exergy Analysis for the Evaluation of a Thermal Storage System Employing PCMs with Different Melting Temperatures." *Applied Thermal Engineering* 16 (11): 907–19. DOI: 10.1016/1359-4311(96)00003-8.

Dovrtel, Klemen, and Medved, Sašo. **2011**. "Weather-Predicted Control of Building Free Cooling System." *Applied Energy* 88: 3088–96. DOI: 10.1016/j.apenergy.2011.03.010.

———. **2012**. "Multi-Objective Optimization of a Building Free Cooling System, Based on Weather Prediction." *Energy & Buildings* 52: 99–106. DOI: 10.1016/j.enbuild.2012.05.014.

DuPont. **2012**. "DuPont Energain®Data Sheet." DuPont, The miracles of science.

El-Sawi, Azeldin. **2013**. "Centralized Thermal Storage System Model for Buildings of the Future: Development and Validation." PhD Thesis.

El-Sawi, Azeldin, Haghighat, Fariborz, and Akbari, Hashem. **2013**. "Centralized Latent Heat Thermal Energy Storage System: Model Development and Validation." *Energy & Buildings* 65: 260–71. DOI: 10.1016/j.enbuild.2013.05.027.

———. **2014**. "Assessing Long-Term Performance of Centralized Thermal Energy Storage System." *Applied Thermal Engineering* 62: 313–21. DOI: 10.1016/j.applthermaleng.2013.09.047.

EnergyPlus. **2019**. *Weather Data*. Vol. 2019. July.

Evola, G., Marletta, L., and Sicurella, F. **2014**. "Simulation of a Ventilated Cavity to Enhance the Effectiveness of PCM Wallboards for Summer Thermal Comfort in Buildings." *Energy*

& Buildings 70: 480–89. DOI: 10.1016/j.enbuild.2013.11.089.

Fan, Gaochao, Huang, Zaiyin, and Wang, Tenghui. **2013**. "Size Effect on Thermodynamic Properties of CaMoO4 Micro/Nano Materials and Reaction Systems." *Solid State Sciences* 16: 121–24. DOI: 10.1016/j.solidstatesciences.2012.11.006.

Farid, Mohammed M., Khudhair, Amar M., Razack, Siddique Ali K., and Al-Hallaj, Said. **2004**. "Review: A Review on Phase Change Energy Storage: Materials and Applications." *Energy Conversion and Management* 45: 1597–1615. DOI: 10.1016/j.enconman.2003.09.015.

Fleming, Evan, Wen, Shaoyi, Shi, Li, and da Silva, Alexandre K. **2015**. "Experimental and Theoretical Analysis of an Aluminum Foam Enhanced Phase Change Thermal Storage Unit." *International Journal of Heat and Mass Transfer* 82: 273–81. DOI: 10.1016/j.ijheatmasstransfer.2014.11.022.

Frusteri, F., Leonardi, V., Vasta, S., and Restuccia, G. **2005**. "Thermal Conductivity Measurement of a PCM Based Storage System Containing Carbon Fibers." *Applied Thermal Engineering* 25: 1623–33. DOI: 10.1016/j.applthermaleng.2004.10.007.

Fukai, Jun, Kanou, Makoto, Kodama, Yoshikazu, and Miyatake, Osamu. **2000**. "Thermal Conductivity Enhancement of Energy Storage Media Using Carbon Fibers." *Energy Conversion and Management* 41: 1543–56. DOI: 10.1016/S0196-8904(99)00166-1.

Ghiaus, Cristian, and Allard, Francis. **2006**. "Potential for Free-Cooling by Ventilation." *Solar Energy* 80: 402–13. DOI: 10.1016/j.solener.2005.05.019.

Gowreesunker, B. L., Tassou, S. A., and Kolokotroni, M. **2013**. "Coupled TRNSYS-CFD Simulations Evaluating the Performance of PCM Plate Heat Exchangers in an Airport Terminal Building Displacement Conditioning System." *Building and Environment* 65: 132–45. DOI: 10.1016/j.buildenv.2013.04.003.

Haghighat, Fariborz. **2013**. "Applying Energy Storage in Ultra-Low Energy Buildings." IEA - Energy Technology Network - Energy Conservation through Energy Storage.

———. **2018**. "Energy Storage with Energy Efficient Buildings and Districts: Optimization and Automation." International Energy Agency (IEA) - Annex 31.

Halawa, E., Bruno, F., and Saman, W. **2005**. "Numerical Analysis of a PCM Thermal Storage System with Varying Wall Temperature." *Energy Conversion and Management* 46: 2592–2604. DOI: 10.1016/j.enconman.2004.11.003.

Halawa, E., and Saman, W. **2011**. "Thermal Performance Analysis of a Phase Change Thermal Storage Unit for Space Heating." *Renewable Energy* 36: 259–64. DOI: 10.1016/j.renene.2010.06.029.

Halawa, E., Saman, W., and Bruno, F. **2010**. "A Phase Change Processor Method for Solving a One-Dimensional Phase Change Problem with Convection Boundary." *Renewable*

Energy 35: 1688–95. DOI: 10.1016/j.renene.2010.01.016.

IEA, International Energy Agency. **2017a**. "Key World Energy Statistics." International Energy Agency. http://www.iea.org/statistics/.

———. **2017b**. "World Energy Outlook." International Energy Agency. www.iea.org.

Inard, Christian, Pfafferott, Jens, and Ghiaus, Christian. **2011**. "Free-Running Temperature and Potential for Free Cooling by Ventilation: A Case Study." *Energy & Buildings* 43: 2705–11. DOI: 10.1016/j.enbuild.2011.06.017.

Incropera, Frank P., DeWitt, David P., Bergman, Theodore L., and Lavine, Adrienne S. **2007**. *Introduction to Heat Transfer*. 5th ed. the University of Michigan: Wiley.

Jaworski, Maciej. **2014**. "Thermal Performance of Building Element Containing Phase Change Material (PCM) Integrated with Ventilation System – An Experimental Study." *Applied Thermal Engineering* 70: 665–74. DOI: 10.1016/j.applthermaleng.2014.05.093.

Jaworski, Maciej, Łapka, Piotr, and Furmański, Piotr. **2014**. "Numerical Modelling and Experimental Studies of Thermal Behaviour of Building Integrated Thermal Energy Storage Unit in a Form of a Ceiling Panel." *Applied Energy* 113. DOI: 10.1016/j.apenergy.2013.07.068.

Karaipekli, Ali, Sarı, Ahmet, and Kaygusuz, Kamil. **2007**. "Thermal Conductivity Improvement of Stearic Acid Using Expanded Graphite and Carbon Fiber for Energy Storage Applications." *Renewable Energy* 32: 2201–10. DOI: 10.1016/j.renene.2006.11.011.

King Jr., Joseph A. **2010**. "Hydrocarbon-Based PCM Applications.". Thermal Performance of the Exterior Envelopes of Whole Buildings XI International Conference: Thermal Mass VI Workshop.

Kottek, Markus, Grieser, Jorgen, Beck, Christoph, Rudolf, Bruno, and Rubel, Franz. **2006**. "World Map of the Koppen-Geiger Climate Classification Updated." *METEOROLOGISCHE ZEITSCHRIFT* 15 (3): 259–63. DOI: 10.1127/0941-2948/2006/0130.

Kumaresan, V., and Velraj, R. **2012**. "Experimental Investigation of the Thermo-Physical Properties of Water–Ethylene Glycol Mixture Based CNT Nanofluids." *Thermochimica Acta* 545: 180–86. DOI: 10.1016/j.tca.2012.07.017.

Kuznik, Frédéric, and Virgone, Joseph. **2009**. "Experimental Assessment of a Phase Change Material for Wall Building Use." *Applied Energy* 86 (10). DOI: 10.1016/j.apenergy.2009.01.004.

Lacroix, M. **1993**. "Study of the Heat Transfer Behavior of a Latent Heat Thermal Energy Storage Unit with a Finned Tube." *International Journal of Heat and Mass Transfer* 36 (8): 2083–92. DOI: 10.1016/S0017-9310(05)80139-5.

Lamberg, P., Lehtiniemi, R., and Henell, A. M. **2004**. "Numerical and Experimental Investigation of Melting and Freezing Processes in Phase Change Material Storage." *INTERNATIONAL JOURNAL OF THERMAL SCIENCES* 43 (3): 277–87. DOI: 10.1016/j.ijthermalsci.2003.07.001.

Lazaro, Ana, Dolado, Pablo, Marín, Jose M., and Zalba, Belen. **2009**. "PCM–Air Heat Exchangers for Free-Cooling Applications in Buildings: Experimental Results of Two Real-Scale Prototypes." *Energy Conversion and Management* 50 (3). DOI: 10.1016/j.enconman.2008.11.002.

Li, XingYi, Zhang, Zhaoliang, and Chen, Hao. **2013**. "Pharmaceutical Nanotechnology: Development and Evaluation of Fast Forming Nano-Composite Hydrogel for Ocular Delivery of Diclofenac." *International Journal of Pharmaceutics* 448: 96–100. DOI: 10.1016/j.ijpharm.2013.03.024.

Liu, Cheng, Yuan, Yanping, Zhang, Nan, Cao, Xiaoling, and Yang, Xiaojiao. **2014**. "A Novel PCM of Lauric-Myristic-Stearic Acid/Expanded Graphite Composite for Thermal Energy Storage." *Materials Letters* 120: 43–46. DOI: 10.1016/j.matlet.2014.01.051.

Liu, Ran, Liu, Lei, and Liu, Jing. **2009**. "Massive Production of Nanoparticles via Mist Reaction." *Physica E: Low-Dimensional Systems and Nanostructures* 41: 1197–1200. DOI: 10.1016/j.physe.2009.01.012.

Liu, Zhengxuan, Yu, Zhun (Jerry), Yang, Tingting, El Mankibi, Mohamed, Roccamena, Letizia, Sun, Ying, Sun, Pengcheng, Li, Shuisheng, and Zhang, Guoqiang. **2019**. "Experimental and Numerical Study of a Vertical Earth-to-Air Heat Exchanger System Integrated with Annular Phase Change Material." *Energy Conversion and Management* 186 (April): 433–49. DOI: 10.1016/j.enconman.2019.02.069.

LU, S. M., and YAN, W. J. **1995**. "Development and Experimental Validation of a Full-Scale Solar Desiccant Enhanced Radiative Cooling System." *Renewable Energy* 6 (7): 821–27. DOI: 10.1016/0960-1481(95)00069-V.

Marín, José M., Zalba, Belén, Cabeza, Luisa F., and Mehling, Harald. **2005**. "Improvement of a Thermal Energy Storage Using Plates with Paraffin–Graphite Composite." *International Journal of Heat and Mass Transfer* 48: 2561–70. DOI: 10.1016/j.ijheatmasstransfer.2004.11.027.

Medved, Sašo, and Arkar, Ciril. **2008**. "Correlation between the Local Climate and the Free-Cooling Potential of Latent Heat Storage." *Energy & Buildings* 40: 429–37. DOI: 10.1016/j.enbuild.2007.03.011.

Mehling, Harald, and Cabeza, Luisa F. **2008**. *Heat and Cold Storage with PCM an up to Date Introduction into Basics and Applications*. 1st ed. Springer-Verlag Berlin Heidelberg. DOI: 10.1007/978-3-540-68557-9.

Mesalhy, Osama, Lafdi, Khalid, Elgafy, Ahmed, and Bowman, Keith. **2005**. "Numerical Study for Enhancing the Thermal Conductivity of Phase Change Material (PCM) Storage Using

High Thermal Conductivity Porous Matrix." *Energy Conversion and Management* 46: 847–67. DOI: 10.1016/j.enconman.2004.06.010.

Mills, Andrew, Farid, Mohammed, Selman, J. R., and Al-Hallaj, Said. **2006**. "Thermal Conductivity Enhancement of Phase Change Materials Using a Graphite Matrix." *Applied Thermal Engineering* 26: 1652–61. DOI: 10.1016/j.applthermaleng.2005.11.022.

Mosaffa, A. H., Farshi, L. Garousi, Infante Ferreira, C. A., and Rosen, M. A. **2014**. "Energy and Exergy Evaluation of a Multiple-PCM Thermal Storage Unit for Free Cooling Applications." *Renewable Energy* 68: 452–58. DOI: 10.1016/j.renene.2014.02.025.

Mosaffa, A. H., Infante Ferreira, C. A., Rosen, M. A., and Talati, F. **2013**. "Thermal Performance Optimization of Free Cooling Systems Using Enhanced Latent Heat Thermal Storage Unit." *Applied Thermal Engineering* 59 (1). DOI: 10.1016/j.applthermaleng.2013.06.011.

Mosaffa, A. H., Infante Ferreira, C. A., Talati, F., and Rosen, M. A. **2013**. "Thermal Performance of a Multiple PCM Thermal Storage Unit for Free Cooling." *Energy Conversion and Management* 67: 1–7. DOI: 10.1016/j.enconman.2012.10.018.

Muthuvelan, T., Nibhanupudi, K. M., Panchabikesan, K., Ramalingam, V., and Munisamy, R. **2018**. "Experimental Investigation of Free Cooling Using Phase Change Material-Filled Air Heat Exchanger for Energy Efficiency in Buildings." *Advances in Building Energy Research* 12 (2): 139–49. DOI: 10.1080/17512549.2016.1248487.

Nagano, K., Takeda, S., Mochida, T., and Shimakura, K. **2004**. "Thermal Characteristics of a Direct Heat Exchange System between Granules with Phase Change Material and Air." *Applied Thermal Engineering* 24: 2131–44. DOI: 10.1016/j.applthermaleng.2004.02.004.

Nagano, K., Takeda, S., Mochida, T., Shimakura, K., and Nakamura, T. **2006**. "Study of a Floor Supply Air Conditioning System Using Granular Phase Change Material to Augment Building Mass Thermal Storage—Heat Response in Small Scale Experiments." *Energy and Buildings* 38 (5). DOI: 10.1016/j.enbuild.2005.07.010.

Onishi, Masanori, Nakamura, Miki, and Sakai, Satoshi. **2009**. "Radiative Cooling Estimate by Cloudiness, Temperature, and Dewpoint Temperature." In *The Seventh International Conference on Urban Climate*.

Osterman, E., Butala, V., and Stritih, U. **2015**. "PCM Thermal Storage System for 'Free' Heating and Cooling of Buildings." *Energy & Buildings* 106: 125–33. DOI: 10.1016/j.enbuild.2015.04.012.

Paksoy, Halime Ö, SpringerLink, and North Atlantic Treaty Organization. **2007**. *Thermal Energy Storage for Sustainable Energy Consumption*. Vol. 234. Dordrecht: Springer.

Panchabikesan, Karthik. **2017**. "Investigation on The Charging Characteristics of a Phase Change Material Based Free Cooling System Integrated with Evaporative Cooling Unit." PhD Thesis.

Panchabikesan, Karthik, Aroul Raj, Antony V., Abaranji, Sujatha, Vellaichamy, Pandiyarajan, and Ramalingam, Velraj. **2017**. "Effect of Direct Evaporative Cooling during the Charging Process of Phase Change Material Based Storage System for Building Free Cooling Application—A Real Time Experimental Investigation." *Energy & Buildings* 152: 250–63. DOI: 10.1016/j.enbuild.2017.07.037.

Panchabikesan, Karthik, Swami, Muthusamy V., Ramalingam, Velraj, and Haghighat, Fariborz. **2019**. "Influence of PCM Thermal Conductivity and HTF Velocity during Solidification of PCM through the Free Cooling Concept – A Parametric Study." *Journal of Energy Storage* 21. DOI: 10.1016/j.est.2018.11.005.

Panchabikesan, Karthik, Vellaisamy, Kumaresan, and Ramalingam, Velraj. **2017**. "Passive Cooling Potential in Buildings under Various Climatic Conditions in India." *Renewable and Sustainable Energy Reviews* 78: 1236–52. DOI: 10.1016/j.rser.2017.05.030.

Panchabikesan, Karthik, Vincent, Antony Aroul Raj, Ding, Yulong, and Ramalingam, Velraj. **2018**. "Enhancement in Free Cooling Potential through PCM Based Storage System Integrated with Direct Evaporative Cooling (DEC) Unit." *Energy* 144: 443–55. DOI: 10.1016/j.energy.2017.11.117.

Pardo, N., Vatopoulos, K., Krook-Riekkola, A., Moya, J. A., and Perez, A. **2012**. "Heat and Cooling Demand and Market Perspective." Joint Research Centre, Institute for Energy and Transport, European Commission. DOI: 10.2790/56532.

Pasupathy, A., and Velraj, R. **2008**. "Effect of Double Layer Phase Change Material in Building Roof for Year Round Thermal Management." *Energy & Buildings* 40: 193–203. DOI: 10.1016/j.enbuild.2007.02.016.

Peiró, Gerard, Gasia, Jaume, Miró, Laia, and Cabeza, Luisa F. **2015**. "Experimental Evaluation at Pilot Plant Scale of Multiple PCMs (Cascaded) vs. Single PCM Configuration for Thermal Energy Storage." *Renewable Energy* 83: 729–36. DOI: 10.1016/j.renene.2015.05.029.

Rady, Mohamed. **2009a**. "Granular Phase Change Materials for Thermal Energy Storage: Experiments and Numerical Simulations." *Applied Thermal Engineering* 29: 3149–59. DOI: 10.1016/j.applthermaleng.2009.04.018.

———. **2009b**. "Thermal Performance of Packed Bed Thermal Energy Storage Units Using Multiple Granular Phase Change Composites." *Applied Energy* 86: 2704–20. DOI: 10.1016/j.apenergy.2009.04.027.

Raj, V. Antony Aroul, and Velraj, R. **2010**. "Review on Free Cooling of Buildings Using Phase Change Materials." *Renewable and Sustainable Energy Reviews* 14 (9): 2819–29. DOI: 10.1016/j.rser.2010.07.004.

———. **2011**. "Heat Transfer and Pressure Drop Studies on a PCM-Heat Exchanger Module for Free Cooling Applications." *International Journal of Thermal Sciences* 50 (8): 1573–82. DOI: 10.1016/j.ijthermalsci.2011.01.025.

Roccamena, Letizia, El Mankibi, Mohamed, and Stathopoulos, Nikolaos. **2019**. "Development and Validation of the Numerical Model of an Innovative PCM Based Thermal Storage System." *Journal of Energy Storage* 24. DOI: 10.1016/j.est.2019.04.014.

Rouault, Fabien, Bruneau, Denis, Sebastian, Patrick, and Nadeau, Jean-Pierre. **2016**. "Use of a Latent Heat Thermal Energy Storage System for Cooling a Light-Weight Building: Experimentation and Co-Simulation." *Energy & Buildings* 127: 479–87. DOI: 10.1016/j.enbuild.2016.05.082.

Rubitherm, GmbH. **2019**. *PCM-RT Line*. Vol. 2019.

Saman, W., Bruno, F., and Halawa, E. **2005**. "Thermal Performance of PCM Thermal Storage Unit for a Roof Integrated Solar Heating System." *Solar Energy* 78: 341–49. DOI: 10.1016/j.solener.2004.08.017.

Santamouris, Mat, **2007**. *Advances in Passive Cooling*. London, UK: Earthscan.

Santamouris, Mattheos, and Kolokotsa, Dionysia. **2013**. "Review: Passive Cooling Dissipation Techniques for Buildings and Other Structures: The State of the Art." *Energy & Buildings* 57: 74–94. DOI: 10.1016/j.enbuild.2012.11.002.

Sanusi, Omar, Warzoha, Ronald, and Fleischer, Amy S. **2011**. "Energy Storage and Solidification of Paraffin Phase Change Material Embedded with Graphite Nanofibers." *International Journal of Heat and Mass Transfer* 54: 4429–36. DOI: 10.1016/j.ijheatmasstransfer.2011.04.046.

Sharma, Atul, Tyagi, V. V., Chen, C. R., and Buddhi, D. **2009**. "Review on Thermal Energy Storage with Phase Change Materials and Applications." *Renewable & Sustainable Energy Reviews* 13 (2): 318–45. DOI: 10.1016/j.rser.2007.10.005.

Solomon, Gnanadurai Ravikumar, Karthikeyan, S., and Velraj, Ramalingam. **2013**. "Sub Cooling of PCM Due to Various Effects during Solidification in a Vertical Concentric Tube Thermal Storage Unit." *Applied Thermal Engineering* 52: 505–11. DOI: 10.1016/j.applthermaleng.2012.12.030.

Sparrow, E. M., and Wachtler, K. P. **1978**. "Transfer Coefficients on the Surfaces of a Transverse Plate Situated in a Duct Flow." *International Journal of Heat and Mass Transfer* 21 (6): 761–67. DOI: 10.1016/0017-9310(78)90038-8.

Stathopoulos, N., El Mankibi, M., Issoglio, R., Michel, P., and Haghighat, F. **2016**. "Air–PCM Heat Exchanger for Peak Load Management: Experimental and Simulation." *Solar Energy* 132: 453–66. DOI: 10.1016/j.solener.2016.03.030.

Stathopoulos, N., El Mankibi, M., and Santamouris, M. **2017**. "Numerical Calibration and Experimental Validation of a PCM-Air Heat Exchanger Model." *Applied Thermal Engineering* 114: 1064–72. DOI: 10.1016/j.applthermaleng.2016.12.045.

Stritih, U., and Butala, V. **2010**. "Experimental Investigation of Energy Saving in Buildings with

PCM Cold Storage." *International Journal of Refrigeration* 33 (8). DOI: 10.1016/j.ijrefrig.2010.07.017.

Stritih, Uroš. **2003**. "Heat Transfer Enhancement in Latent Heat Thermal Storage System for Buildings." *Energy & Buildings* 35: 1097–1104. DOI: 10.1016/j.enbuild.2003.07.001.

———. **2004**. "An Experimental Study of Enhanced Heat Transfer in Rectangular PCM Thermal Storage." *International Journal of Heat and Mass Transfer* 47: 2841–47. DOI: 10.1016/j.ijheatmasstransfer.2004.02.001.

Stritih, Uroš, and Butala, Vincenc. **2007**. "Energy Saving in Building with PCM Cold Storage." *International Journal of Energy Research* 31 (15): 1532–44. DOI: 10.1002/er.1318.

Swinbank, W. C. **2019**. "Long-Wave Radiation from Clear Skies." *Quarterly Journal of the Royal Meteorological Society* 89 (381): 339–48. DOI: 10.1002/qj.49708938105.

Takeda, S., Nagano, K., Mochida, T., and Shimakura, K. **2004**. "Development of a Ventilation System Utilizing Thermal Energy Storage for Granules Containing Phase Change Material." *Solar Energy* 77: 329–38. DOI: 10.1016/j.solener.2004.04.014.

Tay, N. H. S., Belusko, M., and Bruno, F. **2012**. "Designing a PCM Storage System Using the Effectiveness-Number of Transfer Units Method in Low Energy Cooling of Buildings." *Energy & Buildings* 50: 234–42. DOI: 10.1016/j.enbuild.2012.03.041.

Thambidurai, Muthuvelan, Panchabikesan, Karthik, Mohan N, Krishna, and Ramalingam, Velraj. **2015**. "Review on Phase Change Material Based Free Cooling of Buildings—The Way toward Sustainability." *Journal of Energy Storage* 4 (December): 74–88. DOI: 10.1016/j.est.2015.09.003.

TSI-Incorporated. **2019**. *Air Velocity* Transducers. Vol. 2019. (https://tsi.com/products/ventilation-test-instruments/air-velocity-transducers/)

Turnpenny, J. R., Etheridge, D. W., and Reay, D. A. **2000**. "Novel Ventilation Cooling System for Reducing Air Conditioning in Buildings. Part I: Testing and Theoretical Modelling." *Applied Thermal Engineering* 20 (11): 1019–37. DOI: 10.1016/S1359-4311(99)00068-X.

———. **2001**. "Novel Ventilation System for Reducing Air Conditioning in Buildings. Part II: Testing of Prototype." *Applied Thermal Engineering* 21: 1203–17. https://doi.org/10.1016/S1359-4311(01)00003-5.

Vakilaltojjar, S. M., and Saman, W. **2001**. "Analysis and Modelling of a Phase Change Storage System for Air Conditioning Applications." *Applied Thermal Engineering* 21: 249–63. DOI: 10.1016/S1359-4311(00)00037-5.

Vaulx-en-Velin, France Station IDMP: **2019**. *Station IDMP: Measures*. Vol. 2019. 04/04.

Velraj, R., Seeniraj, R. V., Hafner, B., Faber, C., and Schwarzer, K. **1997**. "Experimental Analysis and Numerical Modelling of Inward Solidification on a Finned Vertical Tube

for a Latent Heat Storage Unit." *Solar Energy* 60 (5). DOI: 10.1016/S0038-092X(96)00167-3.

———. **1999**. "HEAT TRANSFER ENHANCEMENT IN A LATENT HEAT STORAGE SYSTEM.". Paper Presented at the ISES Solar World Congress, Taejon, South Korea, 24–29 August 1997.1. *Solar Energy* 65 (3). DOI: 10.1016/S0038-092X(98)00128-5.

Walsh, Brendan P., Murray, Sean N., and O'Sullivan, D. T. J. **2013**. "Free-Cooling Thermal Energy Storage Using Phase Change Materials in an Evaporative Cooling System." *Applied Thermal Engineering* 59: 618–26. DOI: 10.1016/j.applthermaleng.2013.06.008.

Wang, Wenbo, and Wang, Aiqin. **2009**. "Preparation, Characterization and Properties of Superabsorbent Nanocomposites Based on Natural Guar Gum and Modified Rectorite." *Carbohydrate Polymers* 77: 891–97. DOI: 10.1016/j.carbpol.2009.03.012.

Waqas, A., and Kumar, S. **2011**. "Utilization of Latent Heat Storage Unit for Comfort Ventilation of Buildings in Hot and Dry Climates." *INTERNATIONAL JOURNAL OF GREEN ENERGY* 8 (1): 1–24. DOI: 10.1080/15435075.2010.529406.

Waqas, Adeel, and Ud Din, Zia. **2013**. "Phase Change Material (PCM) Storage for Free Cooling of Buildings—A Review." *Renewable and Sustainable Energy Reviews* 18. DOI: 10.1016/j.rser.2012.10.034.

Waqas, Adeel, and Kumar, S. **2011**. "Thermal Performance of Latent Heat Storage for Free Cooling of Buildings in a Dry and Hot Climate: An Experimental Study." *Energy and Buildings* 43 (10). DOI: 10.1016/j.enbuild.2011.06.015.

———. **2013**. "Phase Change Material (Pcm)-Based Solar Air Heating System For Residential Space Heating In Winter." *International Journal of Green Energy* 10 (4): 402–26. DOI: 10.1080/15435075.2012.673518.

Yamaha, Motoi, and Misaki, Shinya. **2006**. "The Evaluation of Peak Shaving by a Thermal Storage System Using Phase-Change Materials in Air Distribution Systems." *HVAC&R Research* 12 (3): 861–69. DOI: 10.1080/10789669.2006.10391213.

Yanbing, Kang, Yi, Jiang, and Yinping, Zhang. **2003**. "Modeling and Experimental Study on an Innovative Passive Cooling System—NVP System." *Energy & Buildings* 35: 417–25. DOI: 10.1016/S0378-7788(02)00141-X.

Yanbing, Kang, Yinping, Zhang, Yi, Jiang, and Yingxin, Zhu. **1999**. "A General Model for Analyzing the Thermal Characteristics of a Class of Latent Heat Thermal Energy Storage Systems." *Journal of Solar Energy Engineering* 121 (4): 185–93. DOI: 10.1115/1.2888165.

Zalba, Belén, Mari´n, José M., Cabeza, Luisa F., and Mehling, Harald. **2004**. "Free-Cooling of Buildings with Phase Change Materials." *International Journal of Refrigeration* 27: 839–49. DOI: 10.1016/j.ijrefrig.2004.03.015.

Zalba, Belén, Marín, José M., Cabeza, Luisa F., and Mehling, Harald. **2003**. "Review on Thermal Energy Storage with Phase Change: Materials, Heat Transfer Analysis and Applications." *Applied Thermal Engineering* 23 (3): 251–83. DOI: 10.1016/S1359-4311(02)00192-8.

Zeng, J. L., Cao, Z., Yang, D. W., Sun, L. X., and Zhang, L. **2010**. "Thermal Conductivity Enhancement of Ag Nanowires on an Organic Phase Change Material." *Journal of Thermal Analysis & Calorimetry* 101 (1): 385–89. DOI:10.1007/s10973-009-0472-y.

Zhang, Shuo, and Niu, Jianlei. **2012**. "Cooling Performance of Nocturnal Radiative Cooling Combined with Microencapsulated Phase Change Material (MPCM) Slurry Storage." *Energy & Buildings* 54: 122–30. DOI: 10.1016/j.enbuild.2012.07.041.

Zhou, Guobing, Yang, Yongping, Wang, Xin, and Zhou, Shaoxiang. **2009**. "Numerical Analysis of Effect of Shape-Stabilized Phase Change Material Plates in a Building Combined with Night Ventilation." *Applied Energy* 86: 52–59. DOI: 10.1016/j.apenergy.2008.03.020.

APPENDIX – A: ENERGY BALANCE EQUATIONS

Finite difference method was conducted to approximate the energy equations utilizing the implicit technique for solving the set of matrices which provides model stability regardless the value of time step. The average temperature method was introduced to identify the unknown temperature after specified time interval. All energy equations are formulated as a function of the average temperature. In this appendix, the energy balance equations for the heat transfer media of a complete system (config-G) are presented and solved referring to the thermal network in Section 4.3.2.

1- Internal air channel

$$\frac{2\,.\rho_a\,.\,Cp_a\,.\,V_a}{dt}(T_{a,i}\text{-}T_{a,i}^{t\text{-}dt})=\dot{m}\,.\,Cp_a\,.(T_{a,i+1}\text{-}T_{a,i})+h_{in}.\,S\,.(T_{p,i}\text{-}T_{a,i})$$

Where ρ_a is the air density which is calculated as $\frac{\rho_a^{0.0^{\circ}C}\times 273.15}{273.15+T_{(1:n)}}$, Cp_a is the air heat capacity, V_a is the air node volume, dt is the time step, $\dot{m}$ is the mass flow rate, h_{in} is the convective heat transfer coefficient for inner cavity, S is the node surface area, and $T_{location}^{time\ step}$ is the node temperature. The previous equation can be rewritten as:

$$T_{a,i}^{t\text{-}dt}=aa.\,T_{a,i}\text{-}ba.T_{a,i+1}\text{-}ca.\,T_{p,i}$$

Where $(ba=\dot{m}\,dt/2\,\rho_a\,V_a)$, $(ca=h_{in}\,S\,dt/2\,\rho_a\,Cp_a\,V_a)$, and $(aa=1+ba+ca)$

Referring to the thermal network, the system was discretized into n number of nodes in X direction. All the energy balance equations for the nodes of the internal air channel can be combined and represented in matrices form:

$$\begin{bmatrix} T_{a,1}^{t-dt} \\ T_{a,2}^{t-dt} \\ T_{a,3}^{t-dt} \\ \vdots \\ T_{a,n}^{t-dt} \end{bmatrix} = \begin{bmatrix} aa & -ba & 0 & \dots & 0 \\ 0 & aa & -ba & 0 & 0 \\ \vdots & 0 & aa & -ba & \vdots \\ \vdots & \dots & 0 & \ddots & -ba \\ 0 & \dots & \dots & 0 & aa \end{bmatrix} . \begin{bmatrix} T_{a,1} \\ T_{a,2} \\ T_{a,3} \\ \vdots \\ T_{a,n} \end{bmatrix} + \begin{bmatrix} -ca & 0 & 0 & \dots & 0 \\ 0 & -ca & 0 & 0 & 0 \\ \vdots & 0 & -ca & 0 & \vdots \\ \vdots & \dots & 0 & \ddots & 0 \\ 0 & \dots & \dots & 0 & -ca \end{bmatrix} . \begin{bmatrix} T_{p,1} \\ T_{p,2} \\ T_{p,3} \\ \vdots \\ T_{p,n} \end{bmatrix} + \begin{bmatrix} -ba \, . T_{amb} \\ 0 \\ 0 \\ \vdots \\ 0 \end{bmatrix}$$

First node: $T_{a,1}^{t-dt} = aa.\ T_{a,1} - ba.T_{a,2} - ca.\ T_{p,1} - ba.\ T_{amb}$

Middle nodes: $T_{a,i}^{t-dt} = aa.\ T_{a,i} - ba.T_{a,i+1} - ca.\ T_{p,i}$

Last node: $T_{a,n}^{t-dt} = aa.\ T_{a,n} - ca.\ T_{p,n}$

2- Internal air channel (in case of no flow)

$$\frac{2 \, . \rho_a \, . \, Cp_a \, . \, V_a}{dt} (T_{a,i} - T_{a,i}^{t-dt}) = \frac{T_{a,i-1} - 2 \, . T_{a,i} + T_{a,i+1}}{R_a} + h_{in} . \, S \, . (T_{p,i} - T_{a,i})$$

Where $R_a = dx / (S_a * K_{in})$, dx is discretization length in X direction, S_a is the cross sectional area of air channel node ($Y*Z$), K_{in} is the air thermal conductivity inside air channel. The previous equation can be rewritten as:

$$T_{a,i}^{t-dt} = aa.\ T_{a,i} - ba.T_{a,i-1} - ba.T_{a,i+1} - ca.\ T_{p,i}$$

Where ($ba = dt / 2 \, \rho_a \, Cp_a \, V_a \, R_a$), ($ca = h_{in} \, S \, dt / 2 \, \rho_a \, Cp_a \, V_a$), and ($aa = 1 + 2.ba + ca$)

All the energy balance equations for the nodes of the internal air channel in case of no airflow can be combined and represented in matrices form:

$$\begin{bmatrix} T_{a,1}^{t-dt} \\ T_{a,2}^{t-dt} \\ T_{a,3}^{t-dt} \\ \vdots \\ T_{a,n}^{t-dt} \end{bmatrix} = \begin{bmatrix} aa & -ba & 0 & \dots & 0 \\ -ba & aa & -ba & 0 & 0 \\ \vdots & -ba & aa & -ba & \vdots \\ \vdots & \dots & -ba & \ddots & -ba \\ 0 & \dots & \dots & -ba & aa \end{bmatrix} . \begin{bmatrix} T_{a,1} \\ T_{a,2} \\ T_{a,3} \\ \vdots \\ T_{a,n} \end{bmatrix} + \begin{bmatrix} -ca & 0 & 0 & \dots & 0 \\ 0 & -ca & 0 & 0 & 0 \\ \vdots & 0 & -ca & 0 & \vdots \\ \vdots & \dots & 0 & \ddots & 0 \\ 0 & \dots & \dots & 0 & -ca \end{bmatrix} . \begin{bmatrix} T_{p,1} \\ T_{p,2} \\ T_{p,3} \\ \vdots \\ T_{p,n} \end{bmatrix}$$

First node: $T_{a,1}^{t-dt}=aa.\ T_{a,1}\ -ba.T_{a,2}\ -ca.\ T_{p,1}$

Middle nodes: $T_{a,i}^{t-dt}=aa.\ T_{a,i}\ -ba.T_{a,i-1}\ -ba.T_{a,i+1}\ -ca.\ T_{p,i}$

Last node: $T_{a,n}^{t-dt}=aa.\ T_{a,n}\ -ba.T_{a,n-1}\ -ca.\ T_{p,n}$

3- Inner encapsulation layer

$$\frac{2\ .\rho_p\ .\ Cp_p\ .\ V_p}{dt}(T_{p,i}-T_{p,i}^{t-dt})=\frac{T_{a,i}-T_{p,i}}{R_{p_{-1}}}+\frac{T_{p,i-1}-2\ .T_{p,i}+T_{p,i+1}}{R_{p_{-2}}}+\frac{T_{m,i}-T_{p,i}}{R_{p-3}}$$

Where ρ_p is the encapsulation density, Cp_p is the encapsulation heat capacity, V_p is the encapsulation node volume, $R_{p-1} = dy_p / (2*S*K_p)+1/(S*h_{in})$, $R_{p-2} = dx / (S_p*K_p)$, $R_{p-3} = dy_p / (2*S*K_p)+ dy_m / (2*S*K_m)$ where dy_p, dy_m are the discretization lengths in Y direction for encapsualtion and PCM respectively, K_p, K_m are encapsulation and PCM thermal conductivity, and S_p is the cross sectional area of encapsulation node ($Y*Z$). The previous equation can be rewritten as:

$$T_{p,i}^{t-dt}=ap.\ T_{p,i}\ -cp.T_{a,i}\ -bp.T_{p,i+1}\ -bp.T_{p,i-1}\ -dp.\ T_{m,i}$$

Where $(cp=\ dt/2\ \rho_a\ Cp_a\ V_a\ R_{p\_1})$, $(bp=\ dt/2\ \rho_a\ Cp_a\ V_a\ R_{p\_2})$, $(dp=\ dt/2\ \rho_a\ Cp_a\ V_a\ R_{p\_3})$, $(ap=1+cp+2.bp+dp)$, and $(ap_1=1+cp+bp+dp)$.

All the energy balance equations for the inner encapsulation layer can be combined and represented in matrices form:

$$\begin{bmatrix} T_{p,1}^{t-dt} \\ T_{p,2}^{t-dt} \\ T_{p,3}^{t-dt} \\ \vdots \\ T_{p,n}^{t-dt} \end{bmatrix} = \begin{bmatrix} ap_1 & -bp & 0 & \dots & 0 \\ -bp & ap & -bp & 0 & 0 \\ \vdots & -bp & ap & -bp & \vdots \\ \vdots & \dots & -bp & \ddots & -bp \\ 0 & \dots & \dots & -bp & ap_1 \end{bmatrix} . \begin{bmatrix} T_{p,1} \\ T_{p,2} \\ T_{p,3} \\ \vdots \\ T_{p,n} \end{bmatrix} + \begin{bmatrix} -cp & 0 & 0 & \dots & 0 \\ 0 & -cp & 0 & 0 & 0 \\ \vdots & 0 & -cp & 0 & \vdots \\ \vdots & \dots & 0 & \ddots & 0 \\ 0 & \dots & \dots & 0 & -cp \end{bmatrix} . \begin{bmatrix} T_{a,1} \\ T_{a,2} \\ T_{a,3} \\ \vdots \\ T_{a,n} \end{bmatrix} +$$

$$\begin{bmatrix} -dp & 0 & 0 & \dots & 0 \\ 0 & -dp & 0 & 0 & 0 \\ \vdots & 0 & -dp & 0 & \vdots \\ \vdots & \dots & 0 & \ddots & 0 \\ 0 & \dots & \dots & 0 & -dp \end{bmatrix} . \begin{bmatrix} T_{m,i1} \\ T_{m,i2} \\ T_{m,i3} \\ \vdots \\ T_{m,in} \end{bmatrix}$$

First node: $T_{p,1}^{t-dt}=ap_1.\ T_{p,1}\ -bp.\ T_{p,2}-cp.T_{a,1}\ -dp.\ T_{m,i1}$

Middle nodes: $T_{p,i}^{t-dt}=ap\ .\ T_{p,i}\ -bp.\ T_{p,i-1}-bp.\ T_{p,i+1}-cp.T_{a,i}\ -dp.\ T_{m,i}$

Last node: $T_{p,n}^{t-dt}=ap_1.\ T_{p,n}\ -bp.\ T_{p,n-1}-cp.T_{a,n}\ -dp.\ T_{m,in}$

4- PCM layer

- **PCM (Inner row)**

$$\frac{2\ .\rho_m\ .\ Cp_m\ .\ V_m}{dt}(T_{m,i}-T_{m,i}^{t-dt})=\frac{T_{p,i}-T_{m,i}}{R_{p_{-3}}}+\frac{T_{m,i-1}-2\ .T_{m,i}+T_{m,i+1}}{R_{mx}}+\frac{T_{m,j}-T_{m,i}}{R_{my}}$$

Where ρ_m is the PCM density, Cp_m is the PCM heat capacity, V_m is the PCM node volume, $R_{mx} = dx/(S_m*K_m)$, $R_{my} = dy_m/(S*K_m)$, $T_{m,i}$ is the inner row nodes, $T_{m,j}$ is the middle rows nodes, and $T_{m,q}$ is the outer row nodes. The previous equation can be rewritten as:

$$T_{m,i}^{t-dt}=am.\ T_{m,i}\ -cm.T_{p,i}\ -bm.T_{m,i+1}\ -bm.T_{m,i-1}\ -dm.\ T_{m,j}$$

Where ($cm= dt/2\ \rho_m\ Cp_m\ V_m\ R_{p\_3}$), ($bm= dt/2\ \rho_m\ Cp_m\ V_m\ R_{mx}$),
($dm= dt/2\ \rho_m\ Cp_m\ V_m\ R_{my}$), ($am=1+cm+2.bm+dm$), and ($am_1=1+cm+bm+dm$)

All the energy balance equations for the inner row for PCM layer can be combined and represented in matrices form:

$$\begin{bmatrix}T_{m,i1}^{t-dt}\\T_{m,i2}^{t-dt}\\T_{m,i3}^{t-dt}\\\vdots\\T_{m,in}^{t-dt}\end{bmatrix}=\begin{bmatrix}am_1 & -bm & 0 & \dots & 0\\-bm & am & -bm & 0 & 0\\\vdots & -bm & am & -bm & \vdots\\\vdots & \dots & -bm & \ddots & -bm\\0 & \dots & \dots & -bm & am_1\end{bmatrix}.\begin{bmatrix}T_{m,i1}\\T_{m,i2}\\T_{m,i3}\\\vdots\\T_{m,in}\end{bmatrix}+\begin{bmatrix}-cm & 0 & 0 & \dots & 0\\0 & -cm & 0 & 0 & 0\\\vdots & 0 & -cm & 0 & \vdots\\\vdots & \dots & 0 & \ddots & 0\\0 & \dots & \dots & 0 & -cm\end{bmatrix}.\begin{bmatrix}T_{p,1}\\T_{p,2}\\T_{p,3}\\\vdots\\T_{p,n}\end{bmatrix}+$$

$$\begin{bmatrix}-dm & 0 & 0 & \dots & 0\\0 & -dm & 0 & 0 & 0\\\vdots & 0 & -dm & 0 & \vdots\\\vdots & \dots & 0 & \ddots & 0\\0 & \dots & \dots & 0 & -dm\end{bmatrix}.\begin{bmatrix}T_{m,j1}\\T_{m,j2}\\T_{m,j3}\\\vdots\\T_{m,jn}\end{bmatrix}$$

First node: $T_{m,i1}^{t-dt}=am_1.\ T_{m,i1}\ -bm.\ T_{m,i2}-cm.T_{p,1}\ -dm.\ T_{m,j1}$

Middle nodes: $T_{m,i}^{t-dt}=am\ .\ T_{m,i}\ -bm.\ T_{m,i-1}-bm.\ T_{m,i+1}-cm.T_{p,i}\ -dm.\ T_{m,j}$

Last node: $T^{t-dt}_{m,in}=am_1.\ T_{m,in}\ -bm.\ T_{m,in-1}-cm.T_{p,n}\ -dm.\ T_{m,jn}$

- **PCM (Middle row)**

$$\frac{2\ .\rho_m\ .\ Cp_m\ .\ V_m}{dt}\ (T_{m,j}-T^{t-dt}_{m,j})=\frac{T_{m,j-1}-2\ .T_{m,j}+T_{m,j+1}}{R_{mx}}+\frac{T_{m,i}-2\ .T_{m,j}+T_{m,q}}{R_{my}}$$

The previous equation can be rewritten as:

$$T^{t-dt}_{m,j}=am_j.\ T_{m,i}\ -bm.T_{m,i+1}\ -bm.T_{m,i-1}\ -dm.\ T_{m,i}\ -dm.\ T_{m,q}$$

Where ($am_j=1+2.bm+2.dm$), and ($am_{j1}=1+bm+2.dm$).

All the energy balance equations for the middle row for PCM layer can be combined and represented in matrices form:

$$\begin{bmatrix} T^{t-dt}_{m,j1} \\ T^{t-dt}_{m,j2} \\ T^{t-dt}_{m,j3} \\ \vdots \\ T^{t-dt}_{m,jn} \end{bmatrix} = \begin{bmatrix} am_{j1} & -bm & 0 & \dots & 0 \\ -bm & am_j & -bm & 0 & 0 \\ \vdots & -bm & am_j & -bm & \vdots \\ \vdots & \dots & -bm & \ddots & -bm \\ 0 & \dots & \dots & -bm & am_{j1} \end{bmatrix} . \begin{bmatrix} T_{m,j1} \\ T_{m,j2} \\ T_{m,j3} \\ \vdots \\ T_{m,jn} \end{bmatrix} + \begin{bmatrix} -dm & 0 & 0 & \dots & 0 \\ 0 & -dm & 0 & 0 & 0 \\ \vdots & 0 & -dm & 0 & \vdots \\ \vdots & \dots & 0 & \ddots & 0 \\ 0 & \dots & \dots & 0 & -dm \end{bmatrix} . \begin{bmatrix} T_{m,i1} \\ T_{m,i2} \\ T_{m,i3} \\ \vdots \\ T_{m,in} \end{bmatrix} +$$

$$\begin{bmatrix} -dm & 0 & 0 & \dots & 0 \\ 0 & -dm & 0 & 0 & 0 \\ \vdots & 0 & -dm & 0 & \vdots \\ \vdots & \dots & 0 & \ddots & 0 \\ 0 & \dots & \dots & 0 & -dm \end{bmatrix} . \begin{bmatrix} T_{m,q1} \\ T_{m,q2} \\ T_{m,q3} \\ \vdots \\ T_{m,qn} \end{bmatrix}$$

First node: $T^{t-dt}_{m,j1}=am_{j1}.\ T_{m,j1}\ -bm.\ T_{m,j2}-dm.T_{m,i1}\ -dm.\ T_{m,q1}$

Middle nodes: $T^{t-dt}_{m,j}=am_j\ .\ T_{m,j}\ -bm.\ T_{m,j-1}-bm.\ T_{m,j+1}-dm.T_{m,i}\ -dm.\ T_{m,q}$

Last node: $T^{t-dt}_{m,jn}=am_{j1}.\ T_{m,jn}\ -bm.\ T_{m,jn-1}-dm.T_{m,in}\ -dm.\ T_{m,qn}$

- **PCM (Outer row)**

$$\frac{2\ .\rho_m\ .\ Cp_m\ .\ V_m}{dt}\ (T_{m,q}-T^{t-dt}_{m,q})=\frac{T_{p,j}-T_{m,q}}{R_{p_{-3}}}\ +\frac{T_{m,q-1}-2\ .T_{m,q}+T_{m,q+1}}{R_{mx}}+\frac{T_{m,j}-T_{m,q}}{R_{my}}$$

The previous equation can be rewritten as:

$$T^{t-dt}_{m,q}=am_q.\ T_{m,q}\ -bm.T_{m,q+1}\ -bm.T_{m,q-1}\ -dm.\ T_{m,j}\ -em.\ T_{p,j}$$

Where ($am_q=1+2.bm+dm+em$), and ($am_{q1}=1+bm+dm+em$).

All the energy balance equations for the outer row for PCM layer can be combined and represented in matrices form:

$$\begin{bmatrix} T^{t-dt}_{m,q1} \\ T^{t-dt}_{m,q2} \\ T^{t-dt}_{m,q3} \\ \vdots \\ T^{t-dt}_{m,qn} \end{bmatrix} = \begin{bmatrix} am_{q1} & -bm & 0 & \dots & 0 \\ -bm & am_q & -bm & 0 & 0 \\ \vdots & -bm & am_q & -bm & \vdots \\ \vdots & \dots & -bm & \ddots & -bm \\ 0 & \dots & \dots & -bm & am_{q1} \end{bmatrix} . \begin{bmatrix} T_{m,q1} \\ T_{m,q2} \\ T_{m,q3} \\ \vdots \\ T_{m,qn} \end{bmatrix} + \begin{bmatrix} -dm & 0 & 0 & \dots & 0 \\ 0 & -dm & 0 & 0 & 0 \\ \vdots & 0 & -dm & 0 & \vdots \\ \vdots & \dots & 0 & \ddots & 0 \\ 0 & \dots & \dots & 0 & -dm \end{bmatrix} .$$

$$\begin{bmatrix} T_{m,j1} \\ T_{m,j2} \\ T_{m,j3} \\ \vdots \\ T_{m,jn} \end{bmatrix} + \begin{bmatrix} -em & 0 & 0 & \dots & 0 \\ 0 & -em & 0 & 0 & 0 \\ \vdots & 0 & -em & 0 & \vdots \\ \vdots & \dots & 0 & \ddots & 0 \\ 0 & \dots & \dots & 0 & -em \end{bmatrix} . \begin{bmatrix} T_{p,j1} \\ T_{p,j2} \\ T_{p,j3} \\ \vdots \\ T_{p,jn} \end{bmatrix}$$

First node: $T^{t-dt}_{m,q1}=am_{q1}.\ T_{m,q1}\ -bm.\ T_{m,q2}-dm.T_{m,j1}\ -em.\ T_{p,j1}$

Middle nodes: $T^{t-dt}_{m,q}=am_q\ .\ T_{m,q}\ -bm.\ T_{m,q-1}-bm.\ T_{m,q+1}-dm.T_{m,j}\ -em.\ T_{p,j}$

Last node: $T^{t-dt}_{m,qn}=am_{q1}.\ T_{m,qn}\ -bm.\ T_{m,qn-1}-dm.T_{m,jn}\ -em.\ T_{p,jn}$

5- Outer encapsulation layer

$$\frac{2\ .\rho_p\ .\ Cp_p\ .\ V_p}{dt}(T_{p,j}-T^{t-dt}_{p,j}) =$$

$$\frac{T_{m,q}-T_{p,j}}{R_{p_{-3}}} + \frac{T_{p,j-1}-2\ .T_{p,j}+T_{p,j+1}}{R_{p_{-2}}} + \frac{T_{a,j}-T_{p,j}}{R_{pout}} + \frac{T_{sky}-T_{p,j}}{R_r} + \frac{T_{g,i}-T_{p,j}}{R_w} + (sol.Q_s.\alpha_s.\tau_s)$$

Where R_{pout} = $1/(S*h_{cav})+dy_p/(2*S*K_p)$, $R_r = 1/(\pi*S*h_r)+dy_p/(2*S*K_p)$, $R_w = 1/(\pi*S*h_w) +dy_p/(2*S*K_p)$, h_{cav} is the convective heat transfer coefficient for external cavity, h_r is the radiative heat transfer coefficient to sky component (in case of long-wave transmittance value of glazing), h_w is the radiative heat transfer coefficient to glazing layer, Q_s is the solar gain (W/m^2), α_s is the solar absorptance, and τ_s is the solar transmittance of glazing. The previous equation can be rewritten as:

$$T_{p,j}^{t-dt} = kp.\ T_{p,j} - jp.T_{m,q} - hp.T_{p,j+1} - hp.T_{p,j-1} - gp_1.\ T_{a,j} - gp_2.\ T_{sky} - gp\ .\ T_{g,i} - sol.Q_s.\alpha_s.\tau_s$$

Where $(jp = dt/2\ \rho_p\ Cp_p\ V_p\ R_{p_3})$, $(hp = dt/2\ \rho_p\ Cp_p\ V_p\ R_{p_2})$, $(gp_1 = dt/2\ \rho_p\ Cp_p\ V_p\ R_{pout})$, $(gp_2 = dt/2\ \rho_p\ Cp_p\ V_p\ R_r)$, $(gp = dt/2\ \rho_p\ Cp_p\ V_p\ R_w)$, $(sol = S*dt/\ \rho_p\ Cp_p\ V_p\ )$, $(kp = 1+jp+2.hp+gp_1+gp_2+gp\ )$, and $(kp_1 = 1+jp+hp+gp_1+gp_2+gp\ )$.

All the energy balance equations for the outer encapsulation layer can be combined and represented in matrices form:

$$\begin{bmatrix} T_{p,j1}^{t-dt} \\ T_{p,j2}^{t-dt} \\ T_{p,j3}^{t-dt} \\ \vdots \\ T_{p,jn}^{t-dt} \end{bmatrix} = \begin{bmatrix} kp_1 & -hp & 0 & \dots & 0 \\ -hp & kp & -hp & 0 & 0 \\ \vdots & -hp & kp & -hp & \vdots \\ \vdots & \dots & -hp & \ddots & -hp \\ 0 & \dots & \dots & -hp & kp_1 \end{bmatrix} . \begin{bmatrix} T_{p,j1} \\ T_{p,j2} \\ T_{p,j3} \\ \vdots \\ T_{p,jn} \end{bmatrix} + \begin{bmatrix} -jp & 0 & 0 & \dots & 0 \\ 0 & -jp & 0 & 0 & 0 \\ \vdots & 0 & -jp & 0 & \vdots \\ \vdots & \dots & 0 & \ddots & 0 \\ 0 & \dots & \dots & 0 & -jp \end{bmatrix} . \begin{bmatrix} T_{m,q1} \\ T_{m,q2} \\ T_{m,q3} \\ \vdots \\ T_{m,qn} \end{bmatrix} +$$

$$\begin{bmatrix} -gp_1 & 0 & 0 & \dots & 0 \\ 0 & -gp_1 & 0 & 0 & 0 \\ \vdots & 0 & -gp_1 & 0 & \vdots \\ \vdots & \dots & 0 & \ddots & 0 \\ 0 & \dots & \dots & 0 & -gp_1 \end{bmatrix} . \begin{bmatrix} T_{a,j1} \\ T_{a,j2} \\ T_{a,j3} \\ \vdots \\ T_{a,jn} \end{bmatrix} + \begin{bmatrix} -gp_2 & 0 & 0 & \dots & 0 \\ 0 & -gp_2 & 0 & 0 & 0 \\ \vdots & 0 & -gp_2 & 0 & \vdots \\ \vdots & \dots & 0 & \ddots & 0 \\ 0 & \dots & \dots & 0 & -gp_2 \end{bmatrix} . \begin{bmatrix} T_{sky} \\ T_{sky} \\ T_{sky} \\ \vdots \\ T_{sky} \end{bmatrix} +$$

$$\begin{bmatrix} -gp & 0 & 0 & \dots & 0 \\ 0 & -gp & 0 & 0 & 0 \\ \vdots & 0 & -gp & 0 & \vdots \\ \vdots & \dots & 0 & \ddots & 0 \\ 0 & \dots & \dots & 0 & -gp \end{bmatrix} . \begin{bmatrix} T_{g,i} \\ T_{g,i} \\ T_{g,i} \\ \vdots \\ T_{g,i} \end{bmatrix} + \begin{bmatrix} sol.Q_s.\alpha_s.\tau_s \\ sol.Q_s.\alpha_s.\tau_s \\ sol.Q_s.\alpha_s.\tau_s \\ \vdots \\ sol.Q_s.\alpha_s.\tau_s \end{bmatrix}$$

It is worth mentioning that in case of config-A, in the calculations of the external convective component, the external air cavity temperature $(T_{a,j})$ will be replaced with the ambient temperature (T_{amb}).

First node: $T_{p,j1}^{t-dt} = kp_1.\ T_{p,j1} - hp.\ T_{p,j2} - jp.T_{m,q1} - gp_1.\ T_{a,j1} - gp_2.\ T_{sky} - gp\ .\ T_{g,i1} - sol.Q_s.\alpha_s.\tau_s$

Middle nodes: $T_{p,j}^{t-dt} = kp\ .\ T_{p,j} - hp.\ T_{p,j-1} - hp.\ T_{p,j+1} - jp.T_{m,q} - gp_1.\ T_{a,j} - gp_2.T_{sky} - gp\ .\ T_{g,i} - sol.Q_s.\alpha_s.\tau_s$

Last node: $T_{p,jn}^{t-dt} = kp_1.\ T_{p,jn} - hp.\ T_{p,jn-1} - jp.T_{m,qn} - gp_1.\ T_{a,jn} - gp_2.\ T_{sky} - gp\ .T_{g,in} - sol.Q_s.\alpha_s.\tau_s$

6- External air cavity layer

$$\frac{2\,.\rho_a\,.\,Cp_a\,.\,V_a}{dt}(T_{a,j}-T_{a,j}^{t-dt})=\frac{T_{p,j}-T_{a,j}}{R_{pout}}+\frac{T_{a,j-1}-2\,.T_{a,j}+T_{a,j+1}}{R_{cav}}+\frac{T_{g,i}-T_{a,j}}{R_{g\text{-}cav}}$$

Where $R_{g-cav} = 1/(S*h_{cav})+dy_g/(2*S*K_g)$, $R_{cav} = dx/(S_{cav}*K_{out})$, where dy_g is the discretization length in Y direction, K_g is the glazing thermal conductivity, S_{cav} is the cross sectional area for air cavity, K_{out} is the air thermal conductivity of the air cavity. The previous equation can be rewritten as:

$$T_{a,j}^{t-dt}=aac.\,T_{a,j}\,-da.T_{a,j-1}\,-da.T_{a,j+1}\,-va.\,T_{p,j}\,-wa.\,T_{g,i}$$

Where ($da= dt/2\,\rho_a\,Cp_a\,V_a\,R_{cav}$), ($va= dt/2\,\rho_a\,Cp_a\,V_a\,R_{pout}$), ($va= dt/2\,\rho_a\,Cp_a\,V_a\,R_{g\text{-}cav}$), ($aac=1+2.da+va+wa$), and ($aac_1=1+da+va+wa$).

All the energy balance equations for the external air cavity layer can be combined and represented in matrices form:

$$\begin{bmatrix}T_{a,j1}^{t-dt}\\T_{a,j2}^{t-dt}\\T_{a,j3}^{t-dt}\\\vdots\\T_{a,jn}^{t-dt}\end{bmatrix}=\begin{bmatrix}aac_1 & -da & 0 & \dots & 0\\ -da & aac & -da & 0 & 0\\ \vdots & -da & aac & -da & \vdots\\ \vdots & \dots & -da & \ddots & -da\\ 0 & \dots & \dots & -da & aac_1\end{bmatrix}.\begin{bmatrix}T_{a,j1}\\T_{a,j2}\\T_{a,j3}\\\vdots\\T_{a,jn}\end{bmatrix}+\begin{bmatrix}-va & 0 & 0 & \dots & 0\\ 0 & -va & 0 & 0 & 0\\ \vdots & 0 & -va & 0 & \vdots\\ \vdots & \dots & 0 & \ddots & 0\\ 0 & \dots & \dots & 0 & -va\end{bmatrix}.\begin{bmatrix}T_{p,j1}\\T_{p,j2}\\T_{p,j3}\\\vdots\\T_{p,jn}\end{bmatrix}+$$

$$\begin{bmatrix}-wa & 0 & 0 & \dots & 0\\ 0 & -wa & 0 & 0 & 0\\ \vdots & 0 & -wa & 0 & \vdots\\ \vdots & \dots & 0 & \ddots & 0\\ 0 & \dots & \dots & 0 & -wa\end{bmatrix}.\begin{bmatrix}T_{g,i1}\\T_{g,i2}\\T_{g,i3}\\\vdots\\T_{g,in}\end{bmatrix}$$

First node: $T_{a,j1}^{t-dt}=aac_1.\,T_{a,j1}\,-da.\,T_{a,j2}-va.T_{p,j1}\,-wa.\,T_{g,i1}$

Middle nodes: $T_{a,j}^{t-dt}=aac\;.\,T_{a,j}\,-da.\,T_{a,j-1}-da.\,T_{a,j+1}-va.T_{p,j}\,-wa.\,T_{g,i}$

Last node: $T_{a,jn}^{t-dt}=aac_1.\,T_{a,jn}\,-da.\,T_{a,jn-1}-va.T_{p,jn}\,-wa.\,T_{g,in}$

7- Glazing layer

$$\frac{2 .\rho_g . Cp_g . V_g}{dt}(T_{g,i}-T_{g,i}^{t-dt})=$$
$$\frac{T_{amb}-T_{g,i}}{R_{amb}}+\frac{T_{g,i-1}-2 .T_{g,i}+T_{g,i+1}}{R_{gl}}+\frac{T_{a,j}-T_{g,i}}{R_{g-cav}}+\frac{T_{p,j}-T_{g,i}}{R_g}+\frac{T_{sky}-T_{g,i}}{R_{sky}}+sol_2.Q_s.\alpha_s$$

Where ρ_g is the glazing density, Cp_g is the glazing heat capacity, V_g is the glazing node volume, $R_{amb} = 1/(S*h_{out})+dy_g/(2*S*K_g)$, $R_g = 1/(\pi*S*h_w)+dy_g/(2*S*K_g)$, $R_{sky} = 1/(\pi*S*h_g)$, $R_{gl} = dx/(S_g*K_g)$, where h_{out} is the convective heat transfer coefficient for the ambient air, h_g is the radiative heat transfer coefficient to the sky temperature, α_s is the glazing solar absorptance, and S_g is the cross sectional area for glazing layer. The previous equation can be rewritten as:

$$T_{g,i}^{t-dt}=ag. T_{g,i} -dg.T_{g,i-1} -dg.T_{g,i+1} -bg. T_{a,j} -cg. T_{amb} -wg. T_{p,i}-eg. T_{sky}-sol_2.Q_s.\alpha_s$$

Where ($dg= dt/2\ \rho_g\ Cp_g\ V_g\ R_{gl}$), ($bg= dt/2\ \rho_g\ Cp_g\ V_g\ R_{g-cav}$), ($cg= dt/2\ \rho_g\ Cp_g\ V_g\ R_{amb}$), ($wg= dt/2\ \rho_g\ Cp_g\ V_g\ R_g$), ($eg= dt/2\ \rho_g\ Cp_g\ V_g\ R_{sky}$), ($sol_2= S*dt/\ \rho_g\ Cp_g\ V_g$), ($ag=1+2.dg+bg+cg+wg+eg$), and ($ag_1=1+dg+bg+cg+wg+eg$).

All the energy balance equations for the glazing layer can be combined and represented in matrices form:

$$\begin{bmatrix} T_{g,i1}^{t-dt} \\ T_{g,i2}^{t-dt} \\ T_{g,i3}^{t-dt} \\ \vdots \\ T_{g,in}^{t-dt} \end{bmatrix} = \begin{bmatrix} ag_1 & -dg & 0 & \dots & 0 \\ -dg & ag & -dg & 0 & 0 \\ \vdots & -dg & ag & -dg & \vdots \\ \vdots & \dots & -dg & \ddots & -dg \\ 0 & \dots & \dots & -dg & ag_1 \end{bmatrix} . \begin{bmatrix} T_{g,i1} \\ T_{g,i2} \\ T_{g,i3} \\ \vdots \\ T_{g,in} \end{bmatrix} + \begin{bmatrix} -bg & 0 & 0 & \dots & 0 \\ 0 & -bg & 0 & 0 & 0 \\ \vdots & 0 & -bg & 0 & \vdots \\ \vdots & \dots & 0 & \ddots & 0 \\ 0 & \dots & \dots & 0 & -bg \end{bmatrix} . \begin{bmatrix} T_{a,j1} \\ T_{a,j2} \\ T_{a,j3} \\ \vdots \\ T_{a,jn} \end{bmatrix} +$$

$$\begin{bmatrix} -cg & 0 & 0 & \dots & 0 \\ 0 & -cg & 0 & 0 & 0 \\ \vdots & 0 & -cg & 0 & \vdots \\ \vdots & \dots & 0 & \ddots & 0 \\ 0 & \dots & \dots & 0 & -cg \end{bmatrix} . \begin{bmatrix} T_{amb} \\ T_{amb} \\ T_{amb} \\ \vdots \\ T_{amb} \end{bmatrix} + \begin{bmatrix} -wg & 0 & 0 & \dots & 0 \\ 0 & -wg & 0 & 0 & 0 \\ \vdots & 0 & -wg & 0 & \vdots \\ \vdots & \dots & 0 & \ddots & 0 \\ 0 & \dots & \dots & 0 & -wg \end{bmatrix} .$$

$$\begin{bmatrix} T_{p,i} \\ T_{p,i} \\ T_{p,i} \\ \vdots \\ T_{p,i} \end{bmatrix} + \begin{bmatrix} -eg & 0 & 0 & \dots & 0 \\ 0 & -eg & 0 & 0 & 0 \\ \vdots & 0 & -eg & 0 & \vdots \\ \vdots & \dots & 0 & \ddots & 0 \\ 0 & \dots & \dots & 0 & -eg \end{bmatrix} . \begin{bmatrix} T_{sky} \\ T_{sky} \\ T_{sky} \\ \vdots \\ T_{sky} \end{bmatrix} + \begin{bmatrix} sol.Q_s.\alpha_s \\ sol.Q_s.\alpha_s \\ sol.Q_s.\alpha_s \\ \vdots \\ sol.Q_s.\alpha_s \end{bmatrix}$$

First node: $T_{g,i1}^{t-dt} = ag_1 . T_{g,i1} - dg . T_{g,i2} - bg . T_{a,j1} - cg . T_{amb} - wg . T_{p,i1} - eg . T_{sky} - sol_2 . Q_s . \alpha_s$

Middle nodes: $T_{g,i}^{t-dt} = ag . T_{g,i} - dg . T_{g,i-1} - dg . T_{g,i+1} - bg . T_{a,j} - cg . T_{amb} - wg . T_{p,i} - eg . T_{sky} - sol_2 . Q_s . \alpha_s$

Last node: $T_{g,in}^{t-dt} = ag_1 . T_{g,in} - dg . T_{g,in-1} - bg . T_{a,jn} - cg . T_{amb} - wg . T_{p,in} - eg . T_{sky} - sol_2 . Q_s . \alpha_s$